Probing the thermodynamics of SU(N)-symmetric Fermi gases with ultracold atoms

Giulio Pasqualetti

SIGILL:UNIVERSITAT:LUDOVIC:MAXIM:

München 2023

Probing the thermodynamics of SU(N)-symmetric Fermi gases with ultracold atoms

Dissertation an der Fakultät für Physik
Ludwig-Maximilians-Universität München

vorgelegt von

Giulio Pasqualetti

aus Pontedera, Italien

München, den 7. Juni 2023

Tag der mündlichen Prüfung: 21. Juli 2023

Erstgutachter: Prof. Immanuel Bloch

Zweitgutachter: Prof. Jan von Delft

Zusammenfassung

In dieser Arbeit wird die Thermodynamik von SU(N)-Fermi-Gasen in einer Quasi-2D-Geometrie untersucht. Unser System besteht aus Ytterbium-Atomen mit einer abstimmbaren SU($N \leq 6$)-Symmetrie in der zentralen Ebene eines vertikalen optischen Gitters. Wir charakterisieren die Zustandsgleichung (ZG) durch Messung der lokalen Dichteprofile mit hochauflösender Absorptionsabbildung sowohl in einer harmonischen Falle als auch in einem quadratischen Gitter. In der harmonischen Falle charakterisieren wir das tief entartete Regime und den Einfluss schwacher Wechselwirkungen auf die Bestimmung der ZG. Mittels optischer Gitter realisieren wir das 2D-SU(N)-Fermi-Hubbard-Modell und untersuchen den Übergang von der metallischen zur Mott-isolierenden Phase oberhalb der Superexchange-Temperatur. Insbesondere untersuchen wir die Dichte, die Kompressibilität, die Besetzungszahlen und die Dichtefluktuationen als Funktionen der Wechselwirkungsstärke, der Dichte und der Temperatur für $N = 3, 4$ und 6. Mit den Messungen vergleichen wir die Ergebnisse aktueller numerischen Methoden, insbesondere Determinant Quantum Monte Carlo (DQMC) und Numerical Linked-Cluster Expansion (NLCE). Durch Anwendung des Fluktuations-Dissipations-Theorems bestimmen wir die Temperatur des Systems mit einer theoriefreien Methode und validieren die Ergebnisse der ZS-Bestimmung.

Abstract

This thesis reports on probing the thermodynamics of SU(N) Fermi gases in a quasi-2D geometry. Our system consists of degenerate ytterbium atoms with a tunable SU($N \leq 6$) symmetry in the central plane of a vertical optical lattice. We characterize the equation of state (EoS) by measuring the local density profiles with high-resolution absorption imaging both in a harmonic trap and a square lattice. In the harmonic trap, we characterize the deeply degenerate regime and the effect of the weak interactions on the determination of the EoS. By loading the gas into a square in-plane optical lattice, we realize the 2D SU(N) Fermi-Hubbard model and probe the transition from the metallic to the Mott insulating phases above the superexchange temperature. In particular, we probe the density, the compressibility, the occupation probabilities, and the local density fluctuations as functions of the interaction strength, the filling, and the temperature for $N = 3, 4$, and 6. Our measurements are used as a benchmark for state-of-the-art theoretical methods, including determinant quantum Monte Carlo (DQMC) and numerical linked-cluster expansion (NLCE). By applying the fluctuation-dissipation theorem, we determine the system's temperature with a theory-free method and validate the results of the numerical fits to the EoS.

Contents

Introduction

A central problem of contemporary physics is understanding the relation between elementary quantum systems and macroscopic emergent phenomena, which cannot be trivially explained by the properties of the constituents [1]. In condensed-matter physics, two paradigmatic examples are the BCS superconductivity [2] and the Kondo effect [3]. These two phenomena have both been experimentally discovered by investigating the resistivity of metals as a function of temperature. In the case of superconductivity, the resistivity vanishes below a critical temperature [4], while in the case of the Kondo effect, the resistivity shows a minimum at low temperatures [5]. The two phenomena are quite different, but they can both be understood as quantum many-body effects due to the strong interaction between electrons in a metal: with phonons in the former case and with localized magnetic impurities in the latter case [6]. The development of theories to explain these phenomena with a microscopic model has required decades of work and can be considered a major achievement of physics in the second half of the twentieth century [6].

However, many other systems and phenomena in condensed-matter physics still lack a comparable understanding. Particularly intriguing is the case of some exotic classes of strongly-correlated materials [7–10] exhibiting a variety of emergent phenomena, such as high-temperature non-BCS superconductivity [11–13], colossal magnetoresistance [14], and metal-insulator transitions [15].

From a theoretical point of view, a typical ansatz to investigate the properties of a material consists in starting from a microscopic simplified model and trying to reproduce the key experimental observations. A paradigmatic model in this regard is the so-called Fermi-Hubbard model, which describes electrons moving in a lattice and interacting with each other through a local interaction [16]. This model allows for the description of a variety of phenomena, such as the metal-to-Mott insulator crossover and antiferromagnetic ordering [17], and it is believed to capture the essential physics of cuprates and the emergence of high-temperature non-BCS superconductivity [11, 18, 19].

However, some of the strongly-correlated materials are inherently multi-orbital, and the Fermi-Hubbard model is not able to capture the full complexity of their electronic structure. In these cases, a possible approach is to consider a multi-orbital generalization or, as an additional simplification, a single-orbital model with particles more complex than electrons, such as fermions with a larger number of spin components $N > 2$. In the case of these particles interacting symmetrically with each other, the model is called SU(N) Fermi-Hubbard model [20–22], SU(2) being the symmetry group of the usual spin-1/2 electrons. Large-N systems are believed to be an effective approximation in describing the physics of transition-metal oxides [7, 14, 23] and heavy-fermion compounds [24], as well as other interesting phenomena, such as orbitally-selective Mott transitions [25–27], graphene's SU(4) spin-valley symmetry [28], twisted bilayer graphene [29–31] and robust itinerant ferromagnetism [32–34]. In many of these cases, the effective models are characterized by a 2D geometry. The 2D regime is special because the Mermin-Wagner theorem [35] forbids the spontaneous breaking of a continuous symmetry at finite temperature, and thermal fluctuations tend to destroy long-range order. Furthermore, large N contributes to stabilizing quantum fluctuations [36].

Several studies have shown the existence of a rich phase diagram with exotic phases and properties for both the SU($N > 2$) Fermi-Hubbard model [21, 32, 37–51] and its strongly-interacting version at integer filling, the SU($N > 2$) Heisenberg model [20–23, 36, 52–59]. However, a general understanding of the models for arbitrary interaction strength, filling, temperature, and number of spin components is still far from being achieved. Numerical simulations of large-N systems are indeed particularly challenging due to the exponential growth of the Hilbert space with N and the increased severity of the sign problem [60].

A complementary approach to study these strongly-correlated systems is the use of quantum simulators. Ultracold atoms in optical lattices, in particular, can be a versatile platform for the simulation of other quantum systems by engineering Hamiltonians to mimic the target system's behavior [61–64]. These simulators allow for excellent control of the state preparation and the parameters of the Hamiltonian, and they can be used to investigate the properties of a quantum system in a controlled environment.

In the last decade, experiments with alkaline-earth-like atoms such as ^{173}Yb and ^{87}Sr have proven to be valuable candidates for quantum simulation of multi-orbital systems [65]. These atoms feature an almost perfect decoupling of the nuclear spin from the electronic degree of freedom in the ground state, naturally leading to an SU(N) symmetry up to $N = 6$ and $N = 10$, respectively [66–69]. This has allowed, among others, for the realization of an SU(6) Mott insulator [70], the spectroscopic verification of the existence of the SU(N) symmetry [71], the observation of SU($N \leq 6$) quantum magnetism in 1D [72], the measurement of the equation of state for SU(3) and SU(6) in 3D [73], the observation of antiferromagnetic correlations in dimerized 3D lattices for SU(4) [74] and in uniform 1D, 2D, and 3D lattice for SU(6) [75], and the observation of flavor-selective symmetry breaking for SU(3) [76].

These investigations have been performed in a variety of geometries. However, until now, no quantum simulation has been performed with fermionic alkaline-earth-like atoms in a single 2D plane geometry, which offers a pristine environment where local properties of the system can be easily accessed and probed with high accuracy.

The main subject of this thesis is the investigation of SU(N) Fermi gases with ^{173}Yb atoms in a single 2D plane geometry. In particular, we investigate their thermodynamics and measure their equation of state (EoS) in a harmonic trap and a square lattice. We probe the density profiles of the gas, the site occupation probabilities (in the lattice), the compressibility, and the local density fluctuations. We do so as a function of the temperature, the interaction strength (in the lattice) and the filling for $N = 3, 4$ and 6 and entropy per particle $\gtrsim 1\,k_\mathrm{B}$.

In the case of the harmonic trap, we investigate the role of weak interactions in determining the EoS. In the case of the lattice, which corresponds to the probing of the 2D SU(N) Fermi-Hubbard model, we characterize the EoS by fitting state-of-the-art numerical methods [50]. By applying the fluctuation-dissipation theorem, we develop a method to determine the temperature in a theory-independent way, which allows for verifying the EoS fitted to the data. This method can also be applied to regimes difficult to access with numerical methods, with promising perspectives for additional investigations of SU(N) Fermi gases in our quantum simulator in the future.

In addition to the SU(N) symmetry, alkaline-earth-like atoms feature other interesting properties for quantum simulation. In particular, they have a metastable excited state with a lifetime of the order of seconds [77], which can be used to mimic an additional orbital degree of freedom [67]. Moreover, the different polarizability between the ground and the metastable state allows for the implementation of state-dependent lattices [78], which can be used to engineer Hamiltonians with localized particles in the metastable state interacting with a spin-exchange interaction [67] with the ground state atoms. The spin-exchange has already been observed in experiments [78–82] and could soon allow for the probing of Kondo-type physics, both in the single-impurity form [83, 84], and in the so-called Kondo lattice model [67–69, 85], which is believed to be relevant for the description of heavy-fermion compounds [86].

Outline

This thesis is organized as follows.

In Chap. 1, we introduce ytterbium and its relevant properties for quantum simulation. We describe its electronic structure and its naturally featured SU(N) symmetry in the ground state. We then present the most relevant theoretical models from condensed-matter physics that we would like to simulate and how their Hamiltonians can be mapped to our quantum simulator. We also discuss the metastable clock state and its properties, which can be used to engineer more complex Hamiltonians. Finally, we describe the experimental techniques for preparing tunable SU(N) degenerate Fermi gases in a 3D geometry.

In Chap. 2, we describe the new optical lattice that we have recently implemented in our experiment and allows for the realization of a single 2D plane geometry. We present the technical setup and the experimental procedures for preparing degenerate Fermi gases in a single plane. Finally, we discuss the detection techniques and the calibration of the imaging system.

In Chap. 3, we present the measurement of the equation of state of weakly-interacting SU(N) Fermi gases in a single 2D plane with harmonic confinement. We first review the physics of quasi-2D SU(N) Fermi gases in the non-interacting and weakly-interacting regime. We then benchmark the weakly-interacting model with the experimental data. Finally, we describe the measurement of local density fluctuations both in the thermal and deeply-degenerate regimes.

In Chap. 4, we describe the SU(N) Fermi-Hubbard model on a square lattice. We review its symmetries and thermodynamic properties at temperatures above the superexchange energy. We introduce the relevant numerical methods to simulate the model which will be used in the following chapters to benchmark the experimental data.

In Chap. 5, we present the measurement of the equation of state of the SU(N) Fermi-Hubbard model in a square lattice. We describe the optical lattice setup and the observables we can access. We then fit the theoretical models described in Chapter 4 to the experimental data. We develop a theory-free method to measure the system's temperature based on the fluctuation-dissipation theorem, which allows us to validate the results of the numerics. Finally, we offer a detailed discussion the systematic errors that affect the measurement.

In the final chapter, we summarize the results of this thesis and discuss possible future directions.

Publications

The central results presented in this thesis have been published in the following reference:

- **G. Pasqualetti**, O. Bettermann, N. Darkwah Oppong, E. Ibarra-García-Padilla, S. Dasgupta, R. T. Scalettar, K. R. A. Hazzard, I. Bloch, and S. Fölling, *Equation of State and Thermometry of the 2D* SU(N) *Fermi-Hubbard Model*, Phys. Rev. Lett. **132**, 083401 (2024).

During the course of this thesis, the following additional research articles have been published:

- E. Ibarra-García-Padilla, C. Feng, **G. Pasqualetti**, S. Fölling, R. T. Scalettar, E. Khatami, and K. R. A. Hazzard, *Metal-insulator Transition and Magnetism of* SU(3) *Fermions in the Square Lattice*, Phys. Rev. A **108**, 053312 (2023).

- O. Bettermann, N. Darkwah Oppong*, **G. Pasqualetti***, L. Riegger, I. Bloch, and S. Fölling, *Clock-Line Photoassociation of Strongly Bound Dimers in a Magic-Wavelength Lattice*, Phys. Rev. A **108**, L041302 (2023) (* equal contribution).

- N. Darkwah Oppong, **G. Pasqualetti**, O. Bettermann, P. Zechmann, M. Knap, I. Bloch, and S. Fölling, *Probing Transport and Slow Relaxation in the Mass-Imbalanced Fermi-Hubbard Model*, Phys. Rev. X **12**, 031026 (2022).

CHAPTER 1

Ultracold ytterbium for quantum simulation of multiorbital physics

In this chapter, we lay the foundation for the description of our experiment and the physics we can study with it. The chapter is organized as follows. We start by introducing the element ytterbium, its isotopes, and its electronic structure. Restricting ourselves to the ground state, we describe the arising of the SU(N) symmetry between its Zeeman states, and we discuss the physics that can be probed by exploiting this symmetry. In particular, we focus on both SU(N) Fermi liquids and the SU(N) Fermi-Hubbard model. Then, we consider the clock transition, we describe interorbital interactions and how they can be exploited for quantum simulation of multiorbital physics, particularly the mass-imbalanced Fermi-Hubbard model and Kondo-type physics. Finally, we present the experimental setup and techniques to prepare degenerate Fermi gases of ytterbium atoms and obtain SU(N) mixtures with variable N.

1.1 Properties of ytterbium relevant for cold atom experiments

1.1.1 Isotopic properties

Ytterbium is an alkaline-earth-like element with the atomic number $Z = 70$ and seven stable isotopes. Five exhibit bosonic statistics (nuclear spin $I = 0$): ^{168}Yb, ^{170}Yb, ^{172}Yb, ^{174}Yb, ^{176}Yb, and two have fermionic statistics: ^{171}Yb ($I = 1/2$) and ^{173}Yb ($I = 5/2$). The isotopes have natural abundances between 0.13 % and 32 % [90], and they have all been used and at least partially characterized in experiments with ultracold atoms, either alone or in mixtures [91–93]. In our experiment, we mainly work with the isotopes ^{171}Yb, ^{173}Yb, and ^{174}Yb. The content of this thesis, except for this chapter, focuses on experiments conducted with ^{173}Yb.

1.1.2 Electronic properties

Ytterbium has an electronic configuration [Xe] $4\mathrm{f}^{14}\,6\mathrm{s}^{2}$. The f-shell is complete, and the electronic properties are primarily determined by the two outer valence electrons in the s-shell. In this regard, the electronic structure resembles the one of helium. In first approx-

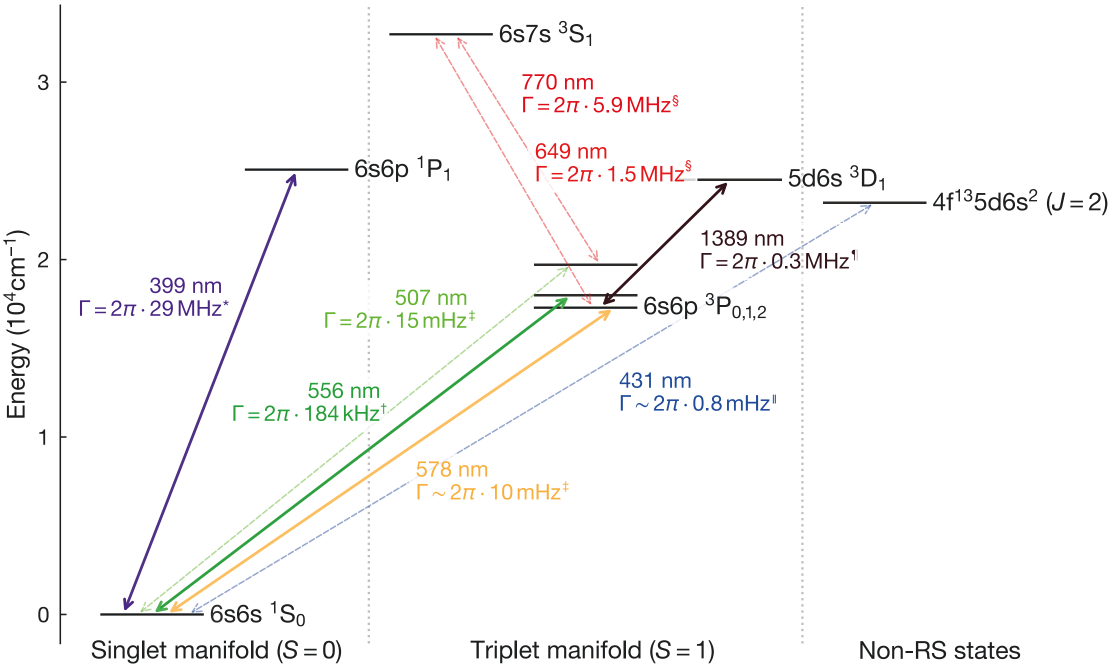

Figure 1.1 | Partial electronic structure of ytterbium. The states are labeled according to the Russell-Saunders (RS) notation when the f-shell is closed and in terms of total angular momentum J when the f-shell is open. The wavelength λ and the linewidth Γ are specified for each transition. Continuous lines: transitions driven in our experiment. Dashed lines: other transitions of general interest mentioned in the main text. References for the values of the linewidths: *[104], †[105], ‡[106], §[107], ¶[108], ‖[109, 110].

imation, it can be described with Russell-Saunders symbols in terms of LS coupling eigenstates of the form $^{2S+1}L_J$, where L is the orbital angular momentum, S is the electronic spin and J the total electronic angular momentum [94]. We can therefore define, as in helium, a singlet ($S = 0$) and a triplet ($S = 1$) manifold. The ground state lies in the singlet manifold, and it is denoted as $^1S_0$. The lowest-lying excited state is the triplet state $^3P_0$. In helium, the transition between these two levels is forbidden, but in ytterbium, the Russell-Saunders description is imperfect because of the internal-shell structure. Therefore, spin-orbit coupling and electrostatic interactions allow for an ultra-narrow transitions between the two states [95]. Similar effects also repeat for other transitions, making the electronic structure of ytterbium more complex than the one of helium. The additional degrees of freedom, and in particular the presence of ultranarrow transitions, make ytterbium an exciting candidate for metrology [96–98], quantum information [99–103], and quantum simulation [65].

In Fig. 1.1, we show ytterbium's low-lying and relevant electronic states. Here, we will briefly comment on the most significant levels and transitions for this thesis and future experiments.

The blue imaging and cooling transition. The $^1S_0 \rightarrow {}^1P_1$ transition at $\lambda = 399\,\text{nm}$ [111] is a broad transition with a linewidth $\Gamma \approx 2\pi \cdot 29\,\text{MHz}$ [104] and a saturation intensity $I_{\text{sat}} = \pi hc\Gamma/(3\lambda^3)$ of about $60\,\text{mW/cm}^2$. In our experiment, we use it as a cycling transition for Zeeman-slowing the atomic beam at the beginning of the experimental sequence.

Moreover, we use it for imaging the atoms with short pulses with both in-situ and time-of-flight techniques (see Sec. 2.3).

The green intercombination line. The $^1S_0 \rightarrow {}^3P_1$ transition at $\lambda = 556\,\text{nm}$ [105] is a narrow transition with a linewidth of $2\pi \cdot 184\,\text{kHz}$ [105] and a saturation intensity of about $0.139\,\text{mW/cm}^2$. It is often referred to as the *intercombination line* in the literature. This transition is characterized by $\Delta S = 1$, which should therefore be forbidden according to the LS selection rules. However, because of the complex internal structure of ytterbium, spin-orbit coupling partially mixes the $^1P_1$ and ^3P_j levels [112] and originates the narrow$^1S_0 \rightarrow {}^3P_1$ transition. In our experiment, we use this transition for cooling the atoms in the magneto-optical trap (MOT) near the Doppler limit of $\hbar\Gamma/(2k_B)$ of $\approx 4.4\,\mu\text{K}$. Moreover, we use it for manipulating atoms in the different Zeeman levels of the ground state. In particular, we use it for optical pumping (see Sec. 1.7.1), the optical Stern-Gerlach technique (see Sec. 1.7.2), and for photoassociation (see Sec. 5.2).

The yellow clock transition. The $^1S_0 \rightarrow {}^3P_0$ transition at $\lambda = 578\,\text{nm}$ is a ultra-narrow transition with a linewidth of a few mHz [106]. Because of its narrowness and extremely large quality factor $Q \sim 10^{17}$, it is used in today's most precise and accurate optical lattice clocks [77, 97], and it is therefore usually referred to as the *clock transition*. Similarly, the $^3P_0$ state is also called the *clock state*. The transition should be doubly forbidden according to the LS selection rules because $\Delta S = 1$ and because for both the initial and final states $J = 0$. However, in fermionic ytterbium, a hyperfine interaction generates a small admixture between the ^3P_j states [112]. The clock transition originates from this admixture and the coupling between the $^1P_1$ and $^3P_1$ states described above. In bosonic ytterbium, the transition can be induced with an external magnetic field [113].

The clock state has a lifetime $\gg 10\,\text{s}$. For the typical time scales of cold atom experiments, the clock state can, therefore, be considered metastable and an excellent resource for implementing an additional degree of freedom for quantum simulation of complex models [65, 67].

The repumping transitions. When working with the clock transition, it is sometimes helpful to use a *repumping* scheme to incoherently transfer nearly all the atoms in the clock state back to the ground state without driving the clock transition again*.

A possible repumping scheme [114] consists in driving simultaneously the two transitions $^3P_0 \rightarrow {}^3S_1$ and $^3P_2 \rightarrow {}^3S_1$ at $\lambda = 649\,\text{nm}$ and $770\,\text{nm}$, respectively [114]. Atoms in the $^3S_1$ state decay to the $^3P_{0,1,2}$ state with a branching ratio of 1:3:4 [115]. Atoms in the $^3P_0$ and $^3P_2$ states get repumped back to the $^3S_1$, while atoms in the $^3P_1$ state decay to the ground state.

An alternative scheme [108, 116] consists in driving the transition $^3P_1 \rightarrow {}^3D_1$ at $\lambda = 1388\,\text{nm}$ [117]. From the $^3D_1$ state, the branching ratio to the $^3P_{0,1,2}$ states is about 64:35:1 [108]. Similarly to the other scheme, the decay to the ground state happens mainly through the intermediate $^3P_1$ state [108]. In our experiment, we implement this method. More technical details about the implementation are reported in Ref. [118].

The other clock transitions. In addition to the $^1S_0 \rightarrow {}^3P_0$ transition at $\lambda = 578\,\text{nm}$,

---

*Because the exact frequency for a π-pulse might not be exactly known, or because the presence of energy shifts might require complex multipulse sequences.

the complex internal electronic structure of ytterbium allows for additional ultranarrow transitions, which can be used for high-precision spectroscopy, metrology, or in complex quantum simulations.

The $^3\mathrm{P}_2$ state has a lifetime of about 15 s and the transition to the ground state ($\lambda = 507\,\mathrm{nm}$) has a similar linewidth as the $^3\mathrm{P}_0$ [119]. In contrast to the $^3\mathrm{P}_0$ state, however, the $^3\mathrm{P}_2$ state shows strong magnetic field sensitivity, making its use as a clock transition more challenging [97]. Its atomic properties have been largely characterized [119–122] and used for spectroscopy [123–125].

In addition to the $^1\mathrm{S}_0 - {}^3\mathrm{P}_2$ transition, an ultranarrow transition from the ground state to the $4\mathrm{f}^{13}\,5d\,6\mathrm{s}^2$ ($J = 2$) state at 431 nm [109, 110] has been recently measured [126, 127]. This state originates from the excitation of one of the electrons in the 4f shell and cannot be described by the simple *LS* coupling scheme and RS notation. The transition has a sub-mHz linewidth with an expected lifetime up to 200 s[†] [110]. Theory models also predict ultranarrow clock transitions between the $4\mathrm{f}^{13}\,5d\,6\mathrm{s}^2$ state and the $^3\mathrm{P}_0$ ($\lambda = 1695\,\mathrm{nm}$, $\Gamma \sim 2\pi \cdot 1\,\mathrm{mHz}$) [109, 128] and the $^3\mathrm{P}_2$ states ($\lambda = 2875\,\mathrm{nm}$, $\Gamma \sim 2\pi \cdot 10\,\mathrm{mHz}$) [128].

We anticipate that the ability to access these states, combining multiple ultranarrow transitions in the same experiment and comparing their frequencies against external perturbation will soon allow for a wide range of applications, including searches for the time variation of fundamental constants [129], ultralight dark matter [130–134], atomic parity violation [135], and new physics [136–139]. Moreover, it could allow for the implementation of more complex quantum simulations [140, 141], advanced manipulation and readout of simulated states [142], and for quantum information processing [99, 143–145].

1.2 Nuclear spin states and SU(*N*) symmetry

In the ground state, ytterbium is characterized by $J = 0$. This means that the quantum number $F = J + I = I$ and, for fermionic ytterbium ($I \neq 0$), there is a decoupling between the electronic configuration and the nuclear spin. As a consequence, a single parameter can parametrize the interaction between the $N = 2F + 1$ Zeeman states, and collisions in a mixture of different states exhibit an SU(N) symmetry [67], which is SU(6) for ^{173}Yb ($I = 5/2$) and SU(2) for ^{171}Yb ($I = 1/2$).

This effect can be better understood by looking at the scattering properties of the system. For two spin-1/2 particles colliding elastically with each other, the wavefunction in the center-of-mass frame after the collision can be described in terms of the relative coordinate $\boldsymbol{r}$ and incident wavevector $\boldsymbol{k}$ as [146]

$$\psi(\boldsymbol{r}) \sim e^{i\boldsymbol{k}\cdot\boldsymbol{r}} + f(\boldsymbol{k},\theta)\frac{e^{ikr}}{r}, \tag{1.1}$$

where the incoming plane wave is described by the first term and the scattered wave by

---

[†] For even isotopes [110].

the second one. In the s-wave regime ($k \to 0$ and spherical outgoing wave) the scattering amplitude $f(\boldsymbol{k},\theta)$ becomes [146]‡

$$f(\boldsymbol{k},\theta) \simeq -\frac{1}{1/a + ik}, \tag{1.2}$$

where a is the s-wave scattering length associated with the interaction potential. Remarkably, it has been shown that the scattering problem can be equivalently solved by replacing the real interatomic potential with a pseudopotential of the form [146]

$$V(\boldsymbol{r}) = \frac{4\pi\hbar^2 a}{m}\delta(\boldsymbol{r}), \tag{1.3}$$

where m is the mass of the particles and $\delta(\boldsymbol{r})$ is the Dirac delta function. In s-wave scattering, the orbital angular momentum is zero, the internal angular momentum of the pair and its projection on the quantized axis are conserved, and an SU(2) symmetry emerges as a consequence of the rotational invariance of the interatomic potential [94]. In the case of particles with a larger spin, Eq. (1.3) can be generalized to [147, 148]

$$V(\boldsymbol{r}) = \frac{4\pi\hbar^2}{m} \sum_{\text{even } F_{\text{pair}}=0}^{2F+1} a_{F_{\text{pair}}} \mathscr{P}_{F_{\text{pair}}} \delta(\boldsymbol{r}). \tag{1.4}$$

Here, $\mathscr{P}_{F_{\text{pair}}}$ is the projection operator of the initial states $|F, m_{F_1}\rangle$ and $|F, m_{F_2}\rangle$ on the subspace with total spin $\boldsymbol{F}_{\text{pair}} = 2\boldsymbol{F}$, $F_{\text{pair}} = |\boldsymbol{F}_{\text{pair}}|$ and $a_{F_{\text{pair}}}$ is the scattering length associated to the pair. The sum runs on even indices because of quantum statistic symmetries§. Eq. (1.4) implies that starting from $|F, m_{F_1}\rangle$, $|F, m_{F_2}\rangle$, collisions can also lead to spin scrambling with final m_F values different from m_{F_1} and m_{F_2}. For $2F + 1 = N$ spin components, $N/2$ scattering lengths are, therefore, necessary to describe all the collision channels in the general case. The symmetry of the interaction is $\otimes_{(2F+1)/2}\mathrm{SU}(2)$.

In the case of alkaline-earth-like (AEL) atoms, $J = 0$ and $F = I$. This means that the electronic configuration, which is mainly responsible for differences between the different scattering channels, becomes irrelevant, and the scattering lengths are the same for all the pairs [66, 91]. The result is an enhanced symmetry, namely, an SU(N) symmetry, which conserves not only F_{pair} and its projection but also the projection of each fermion. This means that no spin scrambling is possible, and the population of each spin component is conserved during collisions. Moreover, by preparing the system with $N' < N$ spin components in the initial state, the system is characterized by an SU(N') symmetry.

For ^{173}Yb, the scattering length is $a = 199.4(2.1)\,a_0$ [91], where a_0 is the Bohr radius, while for ^{171}Yb, $a = -2.8(3.6)\,a_0$ [91]. Signatures confirming the SU(N) symmetry have been observed in several experiments with AEL atoms [70–73, 149, 150]. The SU(N)

[‡] We neglect here the effective range, which might give non-negligible contributions. For more details on scattering in ultracold atoms and the assumptions that we make in the derivation of Eqs. (1.1), (1.2), and (1.3), we refer the reader to Ref. [146].

[§] Under particle exchange, the total wavefunction should change by a factor $(-1)^{2F}$. By the same exchange, the spin and the orbital parts of the wavefunction change by $(-1)^{F_{\text{pair}}}$ and $(-1)^{L_{\text{pair}}}$, respectively. To be consistent, $(-1)^{2F} = (-1)^{F_{\text{pair}}+2F}(-1)^{L_{\text{pair}}}$. For s-wave scattering $L_{\text{pair}} = 0$, which implies that F_{pair} must be even [148].

symmetry has been predicted to be almost exact, with relative differences of 10^{-9} in the scattering length between different channels [67].

Finally, we mention here that in AEL atoms, the SU(N) symmetry is not only present in the ground state but also in the clock state, which is also characterized by $J = 0$ [67]. We will return to this point in Secs. 1.4 and 1.5, where we consider multiorbital SU(N) systems.

1.3 Probing magnetism with SU(*N*) Fermi gases

We now turn our attention to the physics that we can probe with an SU(N) gas of ytterbium atoms in the ground state. Two systems are particularly interesting: the first one are SU(N) Fermi liquids, which can be studied with atoms trapped in harmonic or homogeneous potentials. The second one is the SU(N) Fermi-Hubbard model (FHM), which can be studied in an optical lattice. In this section, we review some of the most interesting features which arise in SU(N) gases, with particular emphasis on quantum magnetism.

1.3.1 SU(*N*) Fermi liquids and itinerant ferromagnetism

Itinerant ferromagnetism describes the formation of spin-polarized domains in repulsive Fermi gases [151, 152]. A quantum magnetic phase transition is predicted in the absence of any crystal pattern and any magnetic field [153], but similar physics is also featured in Hubbard-type models [154][¶]. In the case of spin-1/2 particles, itinerant ferromagnetism has already been investigated in the context of ultracold atoms [155–157], although its unambiguous observation remains elusive because of competing molecular formation mechanisms [158, 159].

In the last few years, the interest for itinerant ferromagnetism in Fermi liquids with multiple spin components and larger symmetries such as SU(N) has been growing [33, 34, 66, 153, 160–163]. In particular, it has been observed that the formation of spin-polarized domains requires the spontaneous breaking of the SU(N) symmetry, but the exact breaking mechanism is still under debate [66]. Furthermore, it has been shown that the transition from the paramagnetic to the ferromagnetic phase is predicted to be of first order, in contrast with the second order phase transition observed in the spin-1/2 case [66, 153][‖]. Alkaline-earth-like atoms might allow in the future the quantum simulation of these phenomena. In Chap. 3, we will review in detail the properties of non-interacting and weakly-interacting SU(N) Fermi gases and present a measurement of the equation of state for $N = 3, 4$ and 6 in the 2D weakly-interacting regime. Further studies in the direction of itinerant ferromagnetism would require tuning the interaction strength between the gas components. This is challenging in alkaline-earth-like atoms because of the lack of a magnetic Feshbach resonance in the ground state (because $J = 0$). Optical alternatives

---

[¶] John Hubbard was two years old when Edmund Stoner published his seminal paper on itinerant ferromagnetism, and the Hubbard models as we know them today had not been formalized yet.

[‖] These results concern the 3D case. In 2D and for spin-1/2 particles, the signatures of ferromagnetic phases have been predicted to be enhanced, but the phase diagram should also look different [164]. For the SU($N > 2$) case, the phase diagram is, to our knowledge, still largely unknown.

have been proposed [165, 166] and demonstrated [167, 168], but their implementation for quantum simulation purposes has been challenging because of the high losses [168]. Nevertheless, the ability to tune the interaction strength might pave the way to probe additional properties of SU(N) Fermi liquids and learn more about the interplay between symmetry breaking and magnetism.

1.3.2 SU(*N*) Fermi-Hubbard model

The Fermi-Hubbard model (FHM) is a paradigmatic model for strongly-correlated systems. It describes fermionic particles hopping on a lattice and interacting with each other through an on-site interaction. The Hamiltonian of the FHM reads

$$\hat{H} = -t \sum_{\langle i,j \rangle, \sigma} \left(\hat{c}^{\dagger}_{i\sigma} \hat{c}_{j\sigma} + \text{h.c.} \right) + \frac{U}{2} \sum_{i, \sigma \neq \tau} \hat{n}_{i\sigma} \hat{n}_{i\tau}, \tag{1.5}$$

where $\hat{c}^{\dagger}_{i\sigma}$ and $\hat{c}_{i\sigma}$ represent the fermionic creation and annihilation operators at site i with spin $\sigma \in \{1 \dots N\}$, $\hat{n}_{i\sigma} = \hat{c}^{\dagger}_{i\sigma}\hat{c}_{i\sigma}$ is the number operator, $\langle i,j \rangle$ denotes next-neighbor lattice sites, t is the hopping amplitude and U is the on-site interaction strength.

The FHM is often studied in the SU($N = 2$) case, where the particles are spin-1/2 fermions and mimic the physics of electrons in a solid. The SU(2) FHM captures many of the features of strongly-correlated systems, such as the Mott insulator transition and antiferromagnetic ordering [17] [see Fig. 1.2(a)], and it is believed to describe some form of high-temperature superconductivity similar to the one observed in cuprates [11, 15, 18, 19]. However, it remains a minimal model and cannot capture the full complexity of real materials. Among the limitations of the SU(2) FHM, we mention, for example, the absence of orbital degrees of freedom. A natural extension in this direction can be considered the SU($N > 2$)-symmetric generalization of the FHM, where the particles have a larger spin with N components. The choice of a larger symmetry can be beneficial for a better description of real materials [169]. Some materials are characterized by quasi-degenerate orbitals, which can be approximately described as degenerate orbitals or a single orbital with a larger spin. For example, the SU(4) FHM can be used to describe a degenerate two-band Hubbard model for spin-1/2 particles [23]. An intriguing example in this regard is the case of cerium volume collapse, where there is a long-standing debate whether the single orbital Hubbard model ($N = 2$) or the double-orbital Hubbard model ($N = 4$) [170–173] is the correct description. Moreover, a larger N is believed to be relevant to describe other exotic materials and phenomena, such as transition-metal oxides [7, 23] and colossal magnetoresistance [14], orbitally-selective Mott transitions [25–27, 174], graphene's SU(4) spin valley symmetry [28], and twisted-bilayer graphene [29–31, 175]. The SU(N) symmetry is also relevant in the context of Kondo-type physics, which will be discussed separately in Sec. 1.5.2.

In addition to these condensed-matter systems, where the SU(N) symmetry is usually imperfect and only approximately realized, the SU(N) FHM is also interesting to study as an elegant model with a larger symmetry. The first theoretical studies of the SU(N) FHM date indeed back to the 1980s as a mathematical technique in the context of the large-N expansion [20, 176–178] Starting from a pioneering intuition by Anderson [179], it was indeed found that the partition function and the correlation functions computed by expanding perturbatively in $1/N$ better approximate the behavior of magnetic alloys [177].

The physics of the SU(N) FHM is richer than the SU(2) case, and it is still largely unexplored. Above the magnetic ordering temperature, the repulsive SU(N) FHM shows a transition between a metallic phase and a Mott insulating phase qualitatively similar to the SU(2) case[**]. However, remarkable properties emerge when comparing systems with different values of N, such as Pomeranchuk cooling [70] and universal scaling laws for some observables [50]. The details of the system's behavior in this regime, one of this thesis's main topics, will be discussed in greater detail in Chaps. 4 and 5.

At lower temperatures, the SU(N) FHM shows a rich phase diagram. Here, we will discuss the system's expected behavior below the magnetic ordering temperature for repulsive interactions. Moreover, we will mainly focus on the square lattice, the most relevant case for the experiments discussed in this thesis. In this case, temperatures necessary to observe some form of magnetic ordering are predicted to be within one order of magnitude compared to those that we can currently reach [37].

At half filling[††], the ground state of the SU(2) FHM is a spin-density wave with long-range antiferromagnetic (AFM) ordering [17, 182]. It has been proposed that for $N = 3$, a similar type of ordering appears in the form of a *flavor density wave*, which breaks the SU(3) symmetry, causing a redistribution of the particles in two sublattices, such that two components prefer one sublattice and the third one the other [37]. For $N = 4$, a long-range AFM order should still survive with a much smaller Neel moment value than SU(2) [39]. For $N = 6$, numerical studies report that the residual Neel moments are absent or extremely small [37, 39]. For $N > 6$, the ground state has been proposed to be a staggered flux phase, where atom currents circulate in opposite directions in neighboring plaquettes. In this case, time-reversal and lattice translation symmetries are expected to be broken but not the SU(N) symmetry. [37, 66].

At finite temperatures and in the intermediate-to-strong interaction regime, the system is expected to go from the ground state to the paramagnetic phase through different phases. In particular, the phase diagram for SU(3) and filling $\langle \hat{n} \rangle = 1$ seems to show 3-sublattice AFM ordering at low temperatures and 2-sublattice AFM ordering for higher temperatures [41, 43, 183] [see Fig. 1.2(b-c)]. For $N = 4$ on a square lattice and filling $\langle \hat{n} \rangle = 1$, the system should similarly show a competition between 2-sublattice ordering and plaquette-ordered AFM [51] [see Fig. 1.2(d-e)]. For $N = 6$ on a square lattice, little is known about the phase diagram, but it has been proposed that at half-filling, the system moves from a Mott AFM ordering to a valence bond solid (VBS) ordering as a function of the interaction [48].

In the strong coupling regime, the SU(N) FHM can be mapped to the Heisenberg model, which describes a system of localized spins interacting with each other through an exchange interaction. The SU(N) Heisenberg model, also far from being completely understood,

---

[**] In SU(2) there is a crossover between the two phases. However, this is not the case in SU(N) for arbitrary filling, where phase transitions have also been predicted [44].

[††] In the SU(N) generalization, half-filling is defined as $\langle \hat{n} \rangle = N/2$.

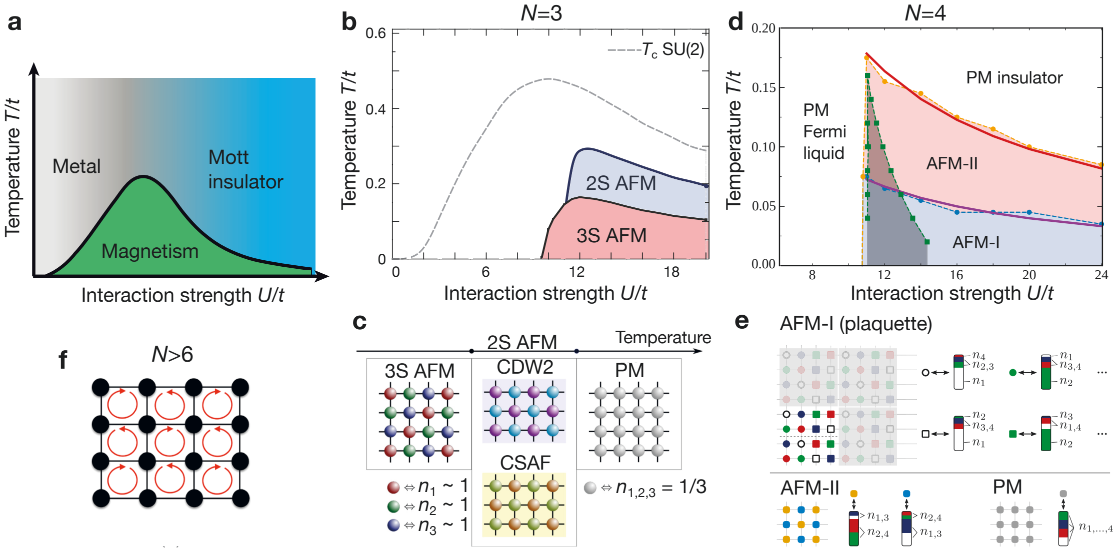

Figure 1.2 | Phase diagram of the SU(N) FHM. (**a**) At high temperatures, the system transitions from a metallic phase to a Mott insulating phase as a function of the interaction strength. At low temperatures, quantum magnetism emerges. Subfigure adapted from Ref. [180]. (**b**) For $N = 3$ at $\langle \hat{n} \rangle = 1$ in a cubic lattice, for low temperatures and intermediate-to-strong interactions, the system is believed to show two different antiferromagnetic (AFM) phases. A similar phase diagram with smaller temperatures for the phase transitions is expected for the square lattice [43]. Subfigure adapted from Ref. [43]. (**c**) The two AFM phases for $N = 3$ are characterized by a 3-sublattice ordering at low temperature and different types of 2-sublattice ordering at intermediate temperature (color density wave and color selective antiferromagnetic state), breaking the SU(3) symmetry. Subfigure adapted from Ref. [43]. (**d**) For $N = 4$ at $\langle \hat{n} \rangle = 1$ in a square lattice, for low temperatures and intermediate-to-strong interactions, the system is believed to show two different AFM phases. Subfigure adapted from Ref. [51]. (**e**) The two AFM phases for $N = 4$ are characterized by plaquette ordering (AFM-I) at low temperatures and 2-sublattice ordering (AFM-II) at intermediate temperatures. In interpreting the colored symbols, the length of the whole vertical bar corresponds to $n = 1$. At the same time, its relative filling by different colors indicates the fraction n_α of the components on the lattice site. Subfigure adapted from Ref. [51]. (**f**) For $N > 6$, it has been proposed that the ground state shows a staggered flux phase containing alternating phase currents. Subfigure adapted from Ref. [181].

has been the subject of several theoretical studies and shows a rich phase diagram with additional exotic phases [36, 37, 54, 55, 57, 58].

The SU(N) Fermi-Hubbard model with ultracold atoms

The FHM can be realized experimentally with ultracold atoms in optical lattices [63]. In an optical lattice, the hopping energy t is given by

$$t = -\int \mathrm{d}\boldsymbol{r}\, w^*(\boldsymbol{r}) \left(-\frac{\hbar^2}{2m}\nabla^2 + V_{\mathrm{lat}}(\boldsymbol{r}) \right) w(\boldsymbol{r}), \tag{1.6}$$

where $V_{\mathrm{lat}}(\boldsymbol{r})$ is the periodic lattice potential, m is the atomic mass, and $w(\boldsymbol{r})$ are the Wannier functions of the lattice [184]. The on-site interaction energy U describes the interaction energy of two atoms occupying the same lattice site and is given by

$$U = \frac{4\pi\hbar^2 a}{m} \int \mathrm{d}\boldsymbol{r}\, |w(\boldsymbol{r})|^4, \tag{1.7}$$

where a is the s-wave scattering length. The ratio U/t can be tuned with the lattice depth V_{lat}. We will return to the determination and calibration of the Hubbard parameters in our experiment in Chap. 5.

In the SU($N > 2$) case, the FHM has already been the object of several experimental studies. A substantial effort has been placed in probing the thermodynamics and the short-range correlations of the model for different spin degeneracies and lattice geometries [70, 73–76, 185]. However, the SU(N) generalization remains much less explored and understood compared to the SU(2) case [65]. This is particularly true in two dimensions, where the thermodynamics of the SU(2) FHM at intermediate temperatures have been studied extensively [186–202]. The characterization and probing of the SU($N > 2$) FHM in two dimensions and for intermediate temperatures will be the main focus of Chaps. 4 and 5.

1.4 Interorbital physics

The SU(N) models presented in Sec. 1.3 can be simulated with ultracold ytterbium atoms in the ground state. In the following chapters, the clock transition will mainly appear as a diagnostic and calibration tool. However, it can also allow for quantum simulation of more complex systems, such as the multiorbital Fermi-Hubbard models, as we will see in Sec. 1.5, or to implement spin shelving techniques and sophisticated readout schemes [99]. Furthermore, the clock transition can be used in principle to probe the occupancies of the SU(N) FHM in alternative to the photoassociation technique that we will present in Sec. 5.2. In this section, we will review some essential properties of the clock transition for the two fermionic isotopes of ytterbium, ^{171}Yb and ^{173}Yb.

Polarizability and state-(in)dependent lattices. The optical potential seen by an atom is proportional to the intensity of the lattice beams. The proportionality constant is given by the polarizability α, which depends on the electronic state of the atom. This means that the potential seen by atoms in the ground state $^1\mathrm{S}_0 \equiv |g\rangle$ can be different from that seen by atoms in the excited state $^3\mathrm{P}_0 \equiv |e\rangle$, and the wavelength of the light can control their amplitudes. Fig. 1.3 shows the ratio of the polarizability of the clock and ground states of ^{173}Yb as a function of the wavelength calculated in *LS* coupling [203]. The ratio between the polarizability of the clock and the ground states is important for quantum simulation because it defines the mobility of the atoms in the two states. When the ratio of the polarizability is one, the atoms in the two states see the same potential and are equally mobile. In this case, the wavelength is called *magic*. Magic lattices are particularly suitable for metrology and clock-line spectroscopy because the differential spectroscopic shifts due

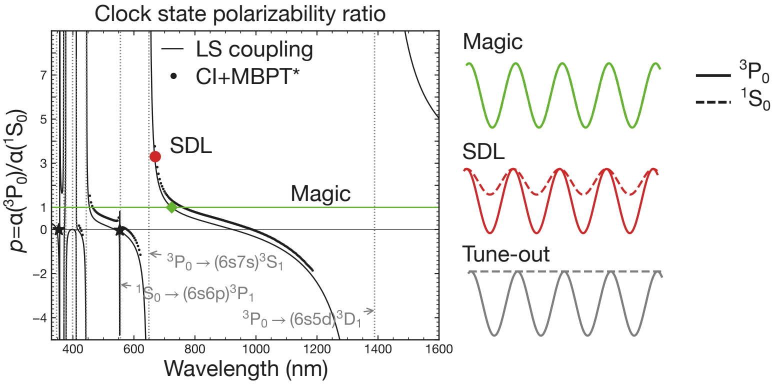

Figure 1.3 | Ratio between the polarizability in the clock and ground state of ^{173}Yb as a function of the wavelength. The figure shows the polarizability calculated in *LS* coupling (black lines) [203], and a comparison with a more advanced ab-initio calculation from (*) Dzuba *et al.* [204] (circles). Grey lines indicate atomic resonances. A polarizability ratio of 1 defines a *magic* wavelength. Green diamond: magic wavelength at λ = 760 nm implemented in our experiment. Red point: SDL at λ = 670 nm implemented in our experiment. On the right, we sketch the potential seen by the ground atoms (dashed lines) and the clock atoms (solid lines) in the magic lattice (green), in the SDL (red), and in a tune-out lattice (grey). Figure adapted from Ref. [203].

to the light intensity are minimized [96, 97]. In our experiment, we use lattices at the magic wavelength of $\lambda \simeq 759\,\mathrm{nm}$ [96]. When the ratio is different from one, the atoms in the two states see different potentials and are not equally mobile. We talk in this case of *state-dependent* lattices (SDL). State-dependent lattices are particularly suitable for the study of mass-imbalanced mixtures (see Sec. 1.5.1) or Kondo-type physics (see Sec. 1.5.2), where one of the species is localized, and the other one is mobile. In our experiment, we have an SDL at the wavelength of 670 nm, where the atoms in the clock state are more localized than the ones in the ground state with a polarizability ratio of about 3.3 [203]. Another interesting limit is given by the *tune-out* wavelengths, where the polarizability for one of the two states is zero. Tune-out wavelengths have been recently demonstrated for both strontium and ytterbium [205, 206] and could represent in the future a valuable resource for quantum simulation [67, 99].

Interorbital interactions. Atoms in different electronic states interact with each other with short-range (in bulk) or on-site (in lattice) interactions. Here, we will focus on the interorbital interactions in a deep optical lattice between only two spin components, such as $m_F = \pm 1/2$ in ^{171}Yb or $m_F = \pm 5/2$ in ^{173}Yb, each of which in different orbitals $|g\rangle$ and $|e\rangle$. We simplify the notation by indicating the spin with $|\uparrow\rangle$ and $|\downarrow\rangle$. In the absence of a magnetic field, the eigenstates of the system are given by the total antisymmetric combination of the electronic and spin degrees of freedom:

$$|eg^{\pm}\rangle = \frac{1}{2}\Big(|ge\rangle \pm |eg\rangle\Big) \otimes \Big(|\uparrow\downarrow\rangle \mp |\downarrow\uparrow\rangle\Big). \tag{1.8}$$

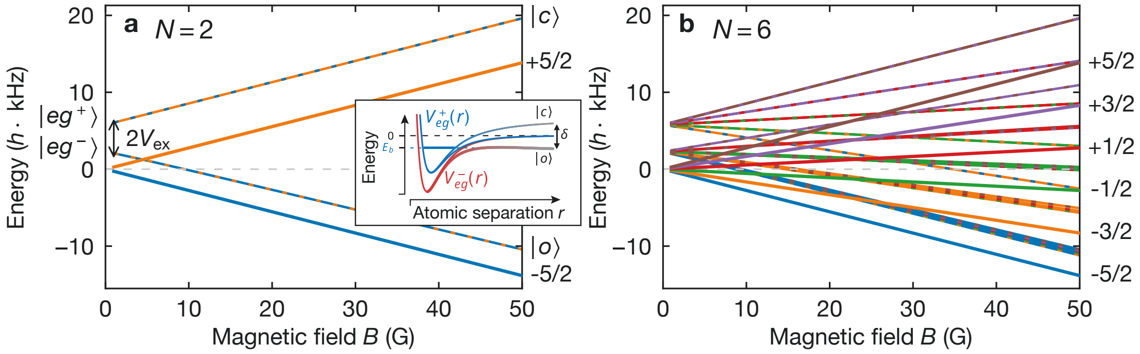

Figure 1.4 | Interaction spectrum for ^{173}Yb. (**a**) Spectrum for $N = 2$ with $m_F = \pm 5/2$. (**b**) Spectrum for $N = 6$ with all the m_F components. Continuous lines represent single-particle transitions (the m_F components are indicated on the right). In the case of $N = 2$, they correspond to $|e\uparrow\rangle$ and $|e\downarrow\rangle$. Interaction energy shifts are indicated by continuous-dashed lines with the color mixture corresponding to the m_F components. For $N = 2$, the two interaction branches are given by $|eg^{\pm}\rangle$ at zero magnetic field, split by an energy $2V_{\text{ex}}$. As a function of the magnetic field, they continuously evolve to $|c\rangle$ and $|o\rangle$. For $N = 6$, the spectrum is more complex, making clock-line spectroscopy more challenging. The strength of the transition, which varies among the branches, is not indicated. The spectrum has been calculated for a quasi-2D configuration corresponding to the vertical lattice presented in Chap. 2 and a square lattice with in-plane lattice depth of $V_{\text{lat}} = 30\,E_{\text{rec}}$ ($\lambda = 760\,\text{nm}$) per axis. **Inset of (a)**: Illustration of the interatomic potentials and how the differential Zeeman shift induces a detuning between $|o\rangle$ and $|c\rangle$ and originates the orbital Feshbach resonance.

Similar to the intraorbital case of Eq. (1.7), each interorbital state is characterized by an interaction energy

$$U_{eg}^{\pm} = \frac{4\pi\hbar^2 a_{eg}^{\pm}}{m} \int \mathrm{d}\boldsymbol{r}\, |w_e(\boldsymbol{r})|^2 |w_g(\boldsymbol{r})|^2, \tag{1.9}$$

where $a_{eg}^{\pm}$ are the associated interorbital scattering lengths and $w_{e,g}(\boldsymbol{r})$ are the Wannier functions of the two orbitals.

At finite magnetic field, the differential Zeeman shift Δ_B[‡‡] mixes the two eigenstates $|eg^{\pm}\rangle$ according to the Hamiltonian[§§] [209]

$$\hat{H} = \begin{pmatrix} U_{eg}^{+} & \Delta_B \\ \Delta_B & U_{eg}^{-} \end{pmatrix}, \tag{1.10}$$

which results in two eigenenergy branches

$$E_{\pm} = V_{\text{dir}} \pm \sqrt{V_{\text{ex}}^2 + \Delta_B^2}, \tag{1.11}$$

[‡‡] In both the ground and clock states, the Zeeman shift should be the same because $J = 0$ and therefore proportional to the nuclear magnetic moment. However, because of a spin-induced mixing with the $^3\text{P}_1$ state, there is a *differential* Zeeman shift $\Delta_B = \delta g \Delta m_F \mu_\text{B}$, where μ_B is the Bohr magneton and $\delta g \simeq 111\,\text{Hz/G}$ for ^{173}Yb [207] and $\simeq -399\,\text{Hz/G}$ for ^{171}Yb [82]. Furthermore, for more precise studies, an m_F-independent quadratic Zeeman shift originating from the Zeeman coupling of the $^3\text{P}_0$ and $^3\text{P}_1$ states should also be taken into account [203, 208].

[§§] In the $\{|eg^+\rangle, |eg^-\rangle\}$ basis.

with $V_{\mathrm{dir}} = \frac{1}{2}\left(U_{eg}^{+} + U_{\mathrm{eg}}^{-}\right)$ and $V_{\mathrm{ex}} = \frac{1}{2}\left(U_{eg}^{+} - U_{\mathrm{eg}}^{-}\right)$. These two terms are also known as direct and exchange interaction, respectively. In Fig. 1.4(a), we show the spectrum for a two-component mixture of ^{173}Yb. The characterization of the interorbital interactions for ^{173}Yb (^{171}Yb) has been reported in Refs. [210, 211] (Refs. [82, 212]) and is described in more detail in Ref. [213] (Ref. [208]). Remarkably, it has been found that the two isotopes show a different sign of the spin-exchange interaction V_{ex}, which is positive (negative) for ^{173}Yb (^{171}Yb). A negative (positive) sign means that the formation of the spin-singlet (triplet) state is energetically favored. This is particularly relevant for the probing of Kondo-type physics, as we will see in Sec. 1.5.2, because it allows the probing of different regimes with the same experimental setup by simply changing the isotope.

Orbital Feshbach resonance. At large magnetic field, the two eigenstates of Eq. (1.8) become

$$|o\rangle = \frac{1}{\sqrt{2}}\Big(|g\uparrow\rangle\otimes|e\downarrow\rangle - |e\downarrow\rangle\otimes|g\uparrow\rangle\Big) = \frac{1}{\sqrt{2}}\Big(|eg^{+}\rangle + |eg^{-}\rangle\Big) \tag{1.12}$$

$$|c\rangle = \frac{1}{\sqrt{2}}\Big(|e\uparrow\rangle\otimes|g\downarrow\rangle - |g\downarrow\rangle\otimes|e\uparrow\rangle\Big) = \frac{1}{\sqrt{2}}\Big(|eg^{+}\rangle - |eg^{-}\rangle\Big). \tag{1.13}$$

If we focus on the scattering properties of the system, as the magnetic field increases, the molecular potentials associated with the two states $|o\rangle$ and $|c\rangle$ detune from each other, as shown in the inset of Fig. 1.4(a). At a particular magnetic field, the potential associated with the state $|o\rangle$ is brought into resonance with the first bound state, giving rise to an orbital Feshbach resonance (OFR) [214]. As the resonance is approached, the scattering properties of the system change, and the scattering length can be freely tuned by varying the magnetic field as in a magnetic Feshbach resonance [214]. In ^{173}Yb, the OFR is located at about 40 G [210, 211], while in ^{171}Yb the OFR is located at about 1300 G [82]. The difference between the two isotopes is exciting from a quantum simulation point of view, as it makes the properties of the two isotopes to some extent complementary and facilitates the study of different interaction regimes. More details about the physics of the OFR and their characterization in the cases of ^{173}Yb and ^{171}Yb can be found in Ref. [211] and Ref. [208], respectively.

Addressing the clock transition. From a technical point of view, selectively addressing the clock transition and performing coherent manipulations of the system requires a narrow laser. This is particularly critical for clock-line spectroscopy of mixtures with more than two components, where the spectrum can be particularly complex [see Fig. 1.4(b)]. Moreover, both short and long-term stability are necessary for coherent addressing and reproducibility of initial conditions for measurements requiring many repetitions. In our experiment, we use a fully commercial laser system[¶¶] combined with an external, home-build cavity for frequency-doubling, locked to a commercial ultra-low-expansion (ULE) cavity through a Pound-Drever-Hall lock. This allows for Fourier-limited pulses with full-width at half maximum of approximately 200 Hz, day-to-day drifts of about 100 Hz[***], and Rabi oscillations

---

[¶¶] Toptica TA Pro.

[***] After compensating for the linear drift of the cavity using feed forward.

with frequencies up to $2\pi \cdot 10\,\mathrm{kHz}$. More details about the technical implementation of the clock laser system can be found in Refs. [208, 209, 215].

1.5 Multiorbital Fermi-Hubbard model

The clock state can be used as an additional degree of freedom to realize a multiorbital Fermi-Hubbard model [67–69]. In this case, the Hamiltonian contains a single-band description for each orbital and additional interorbital terms. More concretely [67],

$$\begin{aligned}\hat{H} = -t_g \sum_{\langle i,j\rangle,\sigma} \left(\hat{c}^\dagger_{ig\sigma}\hat{c}_{jg\sigma} + \text{h.c.}\right) + \frac{U_{gg}}{2} \sum_{i,\sigma\neq\tau} \hat{n}_{ig\sigma}\hat{n}_{ig\tau} - \sum_{i,\sigma} \mu_{ig}\hat{n}_{ig\sigma} \\ -t_e \sum_{\langle i,j\rangle,\sigma} \left(\hat{c}^\dagger_{ie\sigma}\hat{c}_{je\sigma} + \text{h.c.}\right) + \frac{U_{ee}}{2} \sum_{i,\sigma\neq\tau} \hat{n}_{ie\sigma}\hat{n}_{ie\tau} - \sum_{i,\sigma} \mu_{ie}\hat{n}_{ie\sigma} \\ + V_{\text{ex}} \sum_{i,\sigma\neq\tau} \hat{c}^\dagger_{ig\tau}\hat{c}^\dagger_{ie\sigma}\hat{c}_{ig\sigma}\hat{c}_{ie\tau} + V_{\text{dir}} \sum_{i,\sigma,\tau} \hat{n}_{ig\sigma}\hat{n}_{ie\tau},\end{aligned} \tag{1.14}$$

where $\hat{c}^\dagger_{i\alpha\sigma}$, $\hat{c}_{i\alpha\sigma}$, $\hat{n}_{i\alpha\sigma}$, t_α, $U_{\alpha\alpha}$ and $\mu_{i\alpha}$ represent the fermionic creation and annihilation operators, the number operator, the hopping amplitude, the on-site interaction strength and the chemical potential for the ground state ($\alpha = g$) and the clock state ($\alpha = e$), respectively. σ and τ are the spin indices. In addition to the couple of intraorbital terms $(t_\alpha, U_{\alpha\alpha})$ analogous to the single-orbital case, the Hamiltonian contains the on-site interorbital spin-exchange interaction V_{ex} and the on-site direct interorbital interaction V_{dir} which we have derived at the beginning of this section. The Hamiltonian allows for the realization of more complex models to the single-orbital case, in principle, closer to the real behavior of condensed matter systems. The atoms in one of the orbitals can indeed be mapped to the conduction electrons, while the atoms in the other orbital can be mapped to other types of particles, such as electrons in internal shells (f-shell or d-shell), or impurities [67]. Furthermore, each orbital is characterized by an SU(N) symmetry, and the coupling between the two orbitals can be tuned by exploiting the orbital Feshbach resonance [but the SU(N) degeneracy is lifted by the magnetic field].

In the following two subsections, we will briefly describe two of the most interesting systems that can be realized with the multiorbital FHM, namely the mass-imbalanced FHM and Kondo-type models.

1.5.1 Mass-imbalanced Fermi-Hubbard model

Starting from Eq. (1.14), by choosing the right initial state and tuning the interaction parameters in a controlled way, it is possible to realize a mass-imbalanced Fermi-Hubbard model:

$$\hat{H} = -\sum_{\langle i,j\rangle,\alpha\in\{g,e\}} t_\alpha \left[\hat{c}^\dagger_{i\alpha}\hat{c}_{j\alpha} + \text{h.c.}\right] + U_{eg}(B) \sum_i \hat{n}_{ig}\hat{n}_{ie}. \tag{1.15}$$

This limit can be achieved by initializing the system in two $|g,\sigma\rangle$ and $|e,\tau\rangle$ states (spin $\sigma \neq \tau$) in the open channel of the Feshbach resonance described in Sec. 1.4 and tuning the magnetic field to a high value. As a function of the magnetic field, the spin exchange is suppressed, and U_{eg} becomes the dominant interorbital interaction. With only one state per orbital, the intraorbital interactions U_{gg} and U_{ee} can be neglected and the Hamiltonian reduces to Eq. (1.15). By operating in a state-dependent lattice potential, the deep potential seen by the $|e\rangle$ atoms compared to the $|g\rangle$ atoms translates to a larger effective mass, and we can designate the $|e\rangle$ atoms as *heavy* and the $|g\rangle$ atoms as *light*.

Heavy-light mixtures such as the one described in the mass-imbalanced Fermi-Hubbard model are appealing to study in the context of thermalization and ergodicity of non-integrable quantum systems. Some special closed quantum systems experience a failure of thermalization and show non-ergodic behavior. Non-ergodicity arises, for example, due to many-body localization (MBL) in the presence of disorder [216–219]. In recent years, particular attention has been put into trying to understand if other mechanisms can lead to non-ergodicity in closed quantum systems [219–223]. In particular, the question of whether thermalization can be evaded in heavy-light mixtures where the light particles get localized through the interaction with the heavy particles has been the object of several theoretical studies. This situation has been first studied in the context of helium mixtures. In particular, it has been observed that in a mixture where few ^{3}He particles diffuse in a crystalline structure of ^{4}He, the ^{3}He particles can form local immobile clusters through interactions [220]. In this context, the mass-imbalanced Fermi-Hubbard model can be used as a toy model to study how the interplay between interactions and mass imbalance affects thermalization [220–223]. Several studies have shown how a dynamical type of MBL is possible in these systems, although other studies suggest that a very slow relaxation at late times is actually expected [221, 222, 224–226]. Numerical simulations are particularly challenging because of the unfavorable scaling of the Hilbert space and finite-size effects. Therefore, experimental realizations with cold atoms are extremely valuable to study this model. In particular, transport properties can be probed with the help of an optical gradient displacing the equilibrium position and by observing the system's relaxation as a function of time, the interaction strength, and the mass imbalance ratio. This model has been recently probed in our experiment [89], and the interested reader can find more information about the implementation and results in Ref. [227].

1.5.2 Kondo-type physics

The existence of a spin-exchange mechanism between the two orbitals makes alkaline-earth-like atoms a promising platform to study Kondo-type physics. Kondo physics is a paradigmatic model for strongly correlated systems, and its demonstration with ultracold atoms would be of great interest and an important step toward extending the toolbox of quantum simulators beyond Hubbard-like models. Although there have been attempts at realizing Kondo-type systems with ultracold alkali atoms [36, 37, 228], the lack of a suitable spin-exchange mechanism has so far prevented the observation of the Kondo effect. On the other hand, the spin-exchange mechanism described in Sec. 1.4 makes alkaline-earth-like atoms promising candidates [67–69]. Several theoretical works have already studied the possibility of probing Kondo-type physics in these systems, both in its single-impurity and Kondo lattice models [67–69, 84, 141, 229–232].

From an experimental point of view, the spin exchange mechanism has been demonstrated and characterized for both fermionic isotopes [79, 80, 82, 212]. Moreover, a confinement-based mechanism for tuning the spin exchange has also been demonstrated [78].

Single-impurity Kondo model

The Kondo effect is a many-body phenomenon arising from a spin-exchange interaction between a localized spin (the impurity) and the conduction electrons [3, 24, 233]. Originally, the Kondo effect was first observed in metals containing magnetic impurities, such as Cu or Au doped with Mn or Fe. In these materials, it was observed that below a critical temperature, the resistivity of the material increases logarithmically with decreasing temperature [5], which is in contrast with the otherwise expected monotonic power-law behavior [184]. The mechanism at the origin of this behavior was explained first by Jun Kondo in 1964 [3]. The localized spin is screened by the conduction electrons, which form a singlet state with the localized spin. The corresponding Hamiltonian is [24]

$$\hat{H} = \sum_{\boldsymbol{k},\tau} \epsilon_{\boldsymbol{k}} \hat{c}^{\dagger}_{\boldsymbol{k}\tau} \hat{c}_{\boldsymbol{k}\tau} + J\boldsymbol{S} \cdot \sum_{\boldsymbol{k},\boldsymbol{k}'} \hat{c}^{\dagger}_{\boldsymbol{k}\tau} \sigma_{\tau\tau'} \hat{c}_{\boldsymbol{k}'\tau'}, \tag{1.16}$$

where $\hat{c}^{\dagger}_{\boldsymbol{k}\tau}$ ($\hat{c}_{\boldsymbol{k}\tau}$) creates (annihilates) a conduction electron with momentum $\boldsymbol{k}$ and spin τ, $\epsilon_{\boldsymbol{k}}$ is the energy of the conduction electrons, $\boldsymbol{S}$ is the localized spin, σ the Pauli matrices and J is the spin-exchange coupling constant.

The multiorbital FHM Hamiltonian of Eq. (1.14) can be mapped to the single-impurity Kondo model of Eq. (1.16) [83, 84, 89]. This can be done by identifying the localized spin with a particle in the clock state and the conduction electrons with particles in the ground state in a state-dependent lattice suppressing the mobility of the clock state ($t_e \approx 0$). Furthermore, J maps to V_{ex} and, in ^{171}Yb, U_{gg} can be considered negligible. However, in addition to the terms in Eq. (1.16), the cold atoms Hamiltonian also contains a term $\propto (V_{\text{dir}} - V_{\text{ex}}) \sum_{\sigma} \hat{n}_{g\sigma}$ [89]. This term makes quantum simulation more difficult because it suppresses the coupling between the impurity and the conduction electrons and makes detecting the Kondo effect more challenging [89]. Potential-shaping manipulation around the impurity site might nevertheless allow the suppression of this term in our experiment [84, 89].

Kondo Lattice Model

The single-impurity Kondo model can be extended to a lattice of localized spins, which interact with a bath of conduction electrons with a spin-exchange mechanism. This model is known as the Kondo Lattice Model (KLM) [85]. This model is believed to describe the physics of heavy fermions, a special class of materials, some of which present unconventional superconductivity and non-Fermi liquid behavior at low temperatures [8, 24, 86].

In these materials, the conduction electrons are strongly coupled to a lattice of localized d- or f-shell electrons. The Hamiltonian of the KLM reads [85]

$$\hat{H} = -t \sum_{\langle i,j\rangle,\sigma} \hat{c}^{\dagger}_{i\sigma}\hat{c}_{j\sigma} + J \sum_{i,\sigma,\tau} \hat{c}^{\dagger}_{i\sigma}\hat{f}^{\dagger}_{i\tau}\hat{c}_{i\tau}\hat{f}_{i\sigma}, \tag{1.17}$$

where $\hat{c}^{\dagger}_{i\sigma}$ ($\hat{c}_{i\sigma}$) creates (annihilates) a conduction electron with spin σ at site i, $\hat{f}^{\dagger}_{i\sigma}$ ($\hat{f}_{i\sigma}$) creates (annihilates) a localized electron with spin σ at site i, t is the hopping amplitude between nearest-neighbor sites and J is the spin-exchange coupling constant.

In the KLM, the Kondo effect competes with the Ruderman-Kittel-Kasuya-Yosida (RKKY) interaction [234–236], which is a long-range interaction between the localized spins mediated by the conduction electrons. The phase diagram of the KLM is very rich and presents a variety of phases [8, 24, 86]. The RKKY interaction scales as $E_{\mathrm{RKKY}} \sim J^2\rho$, while the Kondo-screening scales as $E_{\mathrm{K}} \sim \exp\left[-1/(J\rho)\right]$, where ρ the density of states of the conduction electrons at the Fermi energy [85, 237]. The RKKY interaction is therefore dominant at small couplings, where magnetic order is favored, while the Kondo effect dominates at large couplings, where a Fermi liquid phase is stabilized [238]. At low temperatures and near the quantum critical point at $E_{\mathrm{RKKY}} \sim E_{\mathrm{K}}$, the competition between the Kondo effect and the RKKY interaction is believed to give rise to the unconventional superconductivity observed in heavy fermions such as $\mathrm{CeCu_2Si_2}$ (critical temperature $T_c \simeq 0.7\,\mathrm{K}$ [239]) and $\mathrm{CeCoIn_5}$ ($T_c \simeq 2.3\,\mathrm{K}$ [240]) [12].

The KLM can explain many of the properties of heavy fermions, but the model is not yet fully understood [86]. It is, therefore, desirable to implement the KLM in a quantum simulator and study its properties in a controlled environment [65]. As in the case of single-impurity Kondo models, the KLM could be simulated with ultracold atoms starting from the Hamiltonian of Eq. (1.14) by mapping the conduction electrons to atoms in the ground state, d- or f-shell electrons to the clock state, J to V_{ex} and setting $t_e = U_{gg} = 0$ with an opportune choice of the lattice and the isotope [67–69]. Furthermore, in the KLM, the term proportional to V_{dir} becomes a global energy shift and can be neglected.

The KLM can also be generalized to the SU(N) case. This extension has been originally treated in the context of the $1/N$ expansion [241] to describe systems with rare earth impurities, particularly cerium and ytterbium [24]. In the SU(N)-symmetric extension, it has been pointed out that the RKKY interaction scales as $1/N$, while the Kondo effect is largely N-independent [231]. Pioneering proposals of simulating the SU(N) KLM with ultracold alkaline-earth-like atoms [67, 68] have recently been complemented by more detailed analysis [231, 232].

1.6 Preparation of 3D SU(*N*) degenerate Fermi gases

This section briefly summarizes the first part of the experimental sequence, which is common to all the experiments presented in the following, and which consists of capturing and cooling ^{173}Yb atoms to quantum degeneracy in a 3D optical, far-detuned dipole trap. In

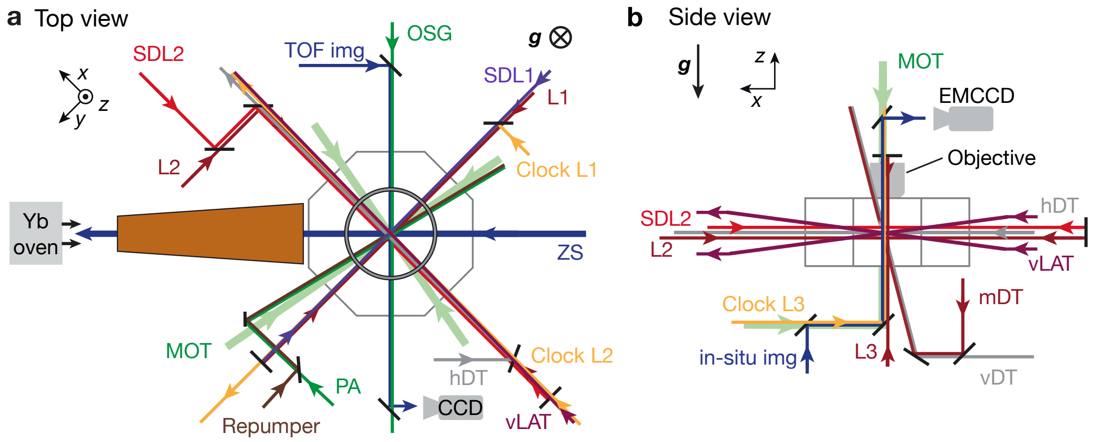

Figure 1.5 | Schematic of the experiment setup, including relevant laser beams. ZS is the Zeeman slower beam at 399 nm. The MOT beams are at 556 nm and are six (four horizontal and two vertical). PA and OSG are the photoassociation and optical Stern-Gerlach beams at 556 nm, respectively. L1, L2 and L3 are retro-reflected lattices at $\lambda = 760$ nm. SDL1 and SDL2 are retro-reflected lattices at $\lambda = 670$ nm. vLAT is the new vertical lattice with a shallow angle at $\lambda = 760$ nm and spacing 3.9 μm. The crossed dipole trap is composed of hDT and mDT. hDT is the horizontal dipole trap at 1064 nm. mDT is the vertical dipole trap at 760 nm. vDT is the vertical dipole trap at 1064 nm used for tilted evaporation (see Chap. 2). The clock excitation can be performed on all three principal optical axes given by L1, L2, and L3. The repumper beam is at 1389 nm. In-situ absorption imaging is performed along the vertical axis through a multiplet objective to an EMCCD camera at 399 nm. Time-of-flight (tof) absorption imaging is performed with a horizontal beam at 399 nm. Sketches adapted and updated from Ref. [203].

Fig. 1.5, we show a schematic of our experimental setup with the geometry of the most relevant laser beams. The laser system and this part of the experimental sequence are very similar to what has already been described in the theses of other Ph.D. students (see Refs. [180, 203, 208, 209, 211, 227]) and it has not been significantly changed from a technical point of view. Therefore, we refer the reader to these works for a more detailed description of the experimental setup and sequence. In Chap. 2, we will describe the most important technical updates made to the experimental setup, namely a vertical lattice with large spacing, which allows the loading of the atoms into a single layer. In the same chapter, we will also describe the second part of the experimental sequence, which consists of preparing a 2D degenerate Fermi gas as in the new single-plane geometry and the readout techniques.

In our experiment, we first capture oven-heated ^{173}Yb atoms with a Zeeman slower on the broad blue $^1\mathrm{S}_0 \rightarrow {}^1\mathrm{P}_1$ transition and cool them down with a 3D magneto-optical trap (MOT) on the narrow intercombination $^1\mathrm{S}_0 \rightarrow {}^1\mathrm{P}_3$ transition. This sequence part lasts about 8.5 s. We then load about 1.6×10^6 atoms into a far-off-resonant crossed dipole trap consisting of a 1064 nm horizontal beam (hDT) and a 760 nm vertical beam (mDT). With forced evaporation, we cool down the cloud to the deep quantum degenerate regime in about 16 s. At the end of this stage of the evaporation, we obtain a spin-unpolarized mixture of about 20×10^3 atoms at $T/T_\mathrm{F} \approx 0.10$ in a 3D harmonic trap with typical frequencies $(\omega_x, \omega_y, \omega_z) \simeq 2\pi \cdot (22, 33, 191)$ Hz. In Fig. 1.6, we show the measurement of the equation of state (EoS) of the gas in this configuration for $N = 3, 4$ and 6. The $N = 6$ case corresponds

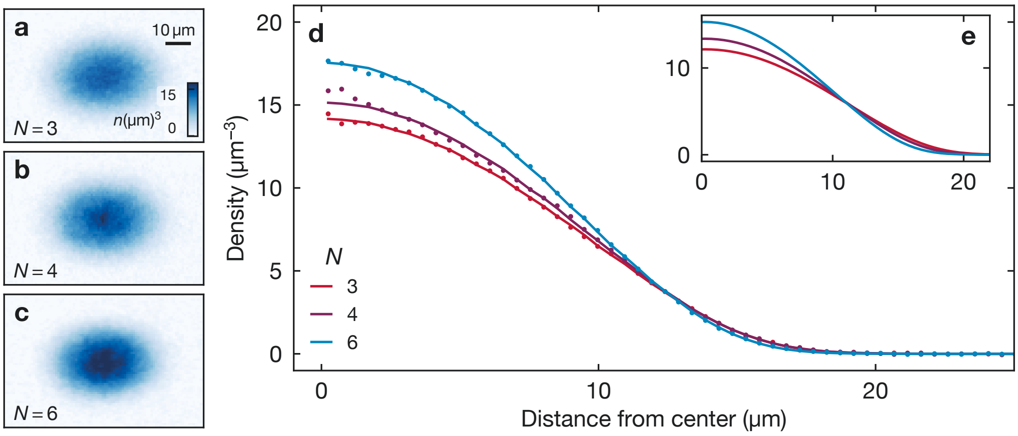

Figure 1.6 | SU(N) Fermi gas in a 3D harmonic trap. (**a**)-(**c**) Measured density profiles for $N = 3, 4$ and 6 clouds with comparable total atom number $N_p = 14.5(5) \times 10^3$ and temperature $T/T_\mathrm{F} = 0.125(5)$. Each image is the average of two realizations postselected according to similar parameters after c.o.m. alignment. (**d**) Radial profiles of the data in (**a**)-(**c**) and fit of a non-interacting Fermi model. (**e**) Simulation of the radial profile of non-interacting Fermi gases with the same N_p and T/T_F (among each other) in a harmonic trap with $(\omega_x, \omega_y, \omega_z) = 2\pi \cdot (22, 33, 191)\,\mathrm{Hz}$. More details on the fit model can be found in Appendix B.2.

to the spin-unpolarized case. The other two cases have been obtained by applying optical pumping in the early evaporation stage, as described in Sec. 1.7.1.

We emphasize that the cooling scheme we described is for ^{173}Yb. The presence of six Zeeman levels in the ground state interacting with each other with a large scattering length makes the evaporative cooling of ^{173}Yb efficient. On the other hand, ^{171}Yb is characterized by an almost vanishing scattering length in the ground state, which makes evaporative cooling much more inefficient. Consequently, we sympathetically cool ^{171}Yb with ^{174}Yb, which has a larger scattering length (both intraspecies and interspecies with ^{171}Yb). The scheme for preparing a degenerate ^{171}Yb gas is described in detail in Refs. [208, 242].

The end of the forced evaporation in the crossed dipole trap constitutes the usual starting point for all our experiments. Afterward, we typically load the atoms to different lattice geometries depending on the specific project. In addition to the new vertical lattice with large spacing that we will describe in Chap. 2, we also dispose of three orthogonal retro-reflected lattices at $\lambda = 760\,\mathrm{nm}$ (L1, L2 and L3 in Fig. 1.5) and two retro-reflected state-dependent optical lattices at $\lambda = 670\,\mathrm{nm}$ (SDL1 and SDL2 in Fig. 1.5). Combining these lattices allows us to prepare various lattice geometries, including 3D cubic lattices, stacks of 2D planes, and ensembles of 1D tubes. L1 and L2 will be used in Chap. 5 to generate the in-plane lattices to probe the 2D SU(N) Fermi-Hubbard model.

1.7 Preparing SU(N) mixtures

The cooling scheme described in the previous section allows us to prepare a degenerate Fermi gas of ^{173}Yb atoms in the spin-unpolarized ($N = 6$) case. In order to prepare different

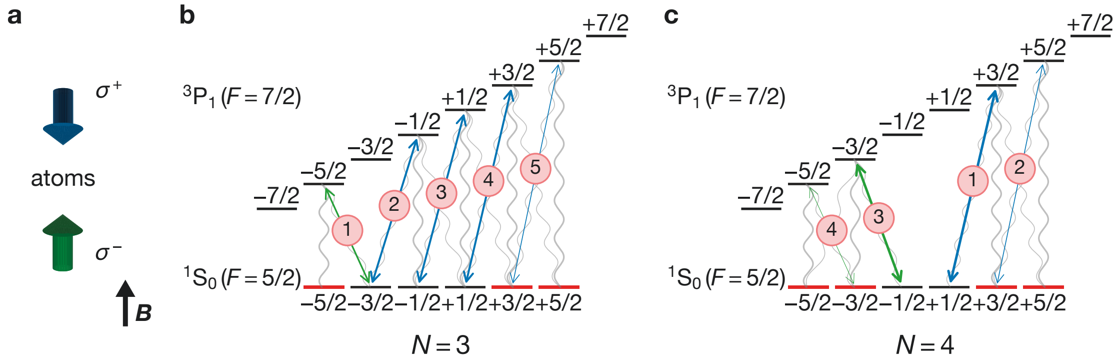

Figure 1.7 | Optical pumping scheme for preparing SU(3) and SU(4) mixtures in ^{173}Yb. (**a**) Optical pumping is done by driving the $^1S_0(F = 5/2) \rightarrow {}^3P_1(F = 7/2)$ transition with circularly polarized light. σ^+ light comes from the top, σ^- light from the bottom. A magnetic field of 50 G lifts the degeneracy of the m_F states. (**b**) Scheme for the preparation of the $N = 3$, $m_F = \{-5/2, +3/2, +5/2\}$ state. We drive five transitions in the order indicated by the number on each arrow. (**c**) Scheme for the preparation of the $N = 4$, $m_F = \{-5/2, -3/2, +3/2, +5/2\}$ state. We drive four transitions (straight arrows) in the order indicated by the number on each arrow. Atoms decay back to the ground state through different channels (curved arrows). The duration of each pulse is finely tuned to achieve a final balanced mixture. The width of each transition indicates a qualitative measure of the pulse duration. Green arrows correspond to σ^- pulses, blue arrows to σ^+ pulses.

spin mixtures, we need to apply a spin-selective optical pumping scheme. The preparation of $N < 6$ mixtures is done in the first part of the sequence before the evaporation. In this section, we describe the optical pumping scheme we use to prepare mixtures of atoms in the $N = 3$ and $N = 4$ cases. Moreover, we describe the detection scheme to measure the number of atoms in each spin state and calibrate their population imbalance.

1.7.1 Optical pumping

In the case of fermionic isotopes, the gas in the crossed dipole trap is a spin-unpolarized mixture. The balancing is expected as a consequence of the quench of the magnetic field when transferring the atoms from the MOT. The diabatic switching of the field projects the original spin mixture into superpositions of spin states, which then dephase during the evaporation [209].

Other spin mixtures can be prepared with an *optical pumping* scheme. In our experiment, the optical pumping is performed with circularly polarized beams on the intercombination line in the presence of a magnetic field which lifts the degeneracy of the m_F states and allows for m_F-selective transitions [see Fig. 1.7(a)]. Here, we will describe the optical pumping scheme for ^{173}Yb, which is most relevant for the experiments described in the following chapters. The optical pumping scheme for ^{171}Yb is qualitatively similar, and the technical details are described in Ref. [208].

In ^{173}Yb, we drive $\sigma^{\pm}$ pulses on the $^1S_0(F = 5/2) \rightarrow {}^3P_1(F = 7/2)$ manifold. The Zeeman splitting in the $^3P_1$ state is of about 600 kHz/G/m_F [203] and a magnetic field of 50 G in the vertical direction ensures a lift of the degeneracy of the m_F states large enough to enable selective transitions $m_F \rightarrow m_F \pm 1$ with the narrow intercombination line. The pump-

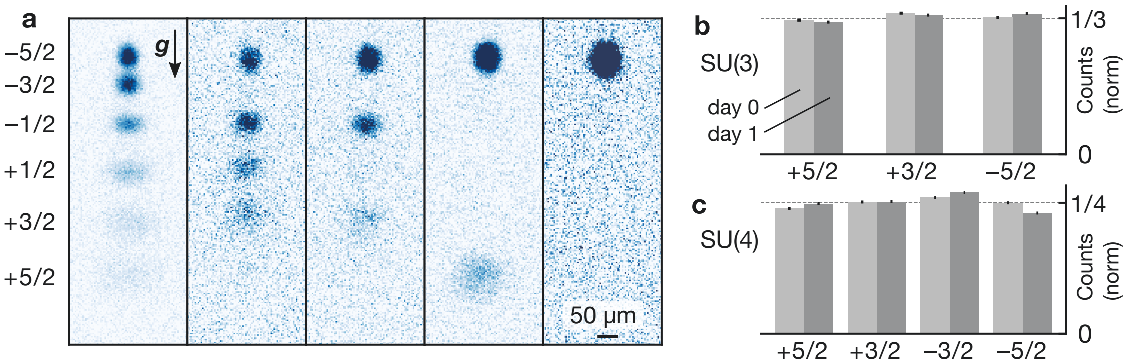

Figure 1.8 | Optical Stern-Gerlach (OSG) technique for the detection of the population of the different spin components. (**a**) Detection of different spin-balanced mixtures. From left to right: $N = 6$, $N = 4$ for $m_F = \{-5/2, -1/2, +1/2, +3/2\}$, $N = 3$ for $m_F = \{-5/2, -1/2, +3/2\}$, $N = 2$ for $m_F = \{-5/2, +5/2\}$, $N = 1$ for $m_F = \{-5/2\}$. The time of flight is 10 ms. The color scale is the same for all images and has been normalized to the total atom number. (**b**) Measurement of the spin population for a $N = 3$, $m_F = \{-5/2, +3/2, +5/2\}$ mixture (normalized fraction). (**b**) Measurement of the spin population for a $N = 4$, $m_F = \{-5/2, -3/2, +3/2, +5/2\}$ mixture (normalized fraction). The measurements of (**b**) and (**c**) have been performed directly before (light grey) and after (dark grey) the measurements shown in Fig. 5.4.

ing scheme is based on the fact that, after the excitation, the decay channels from the $^3P_1$ states favor the preservation of the m_F number [243]†††. In our sequence, we implement the optical pumping in the crossed dipole trap before the beginning of the 3D evaporation (see Sec. 1.6). The sequence consists of multiple intensity-stabilized pulses in a specific order and with different durations (between few µs and 100 ms), which are finely tuned to achieve a final balanced mixture. In Fig. 1.7(b-c), we show the optical pumping scheme for preparing the $N = 3$ and $N = 4$ mixtures. The balancing of the mixture is controlled by measuring the population of each spin component with an optical Stern-Gerlach technique, which is the topic of the next section.

1.7.2 Optical Stern-Gerlach

The distribution of the ground state population in the different spin components can be measured using an optical Stern-Gerlach (OSG) technique [149, 244]. This technique consists in shining an intense m_F-dependent beam on the atoms, which transfers different amounts of momentum to the different spin components. After a time-of-flight (tof), the momentum distribution maps to a spatial distribution, and the population of each spin component can be measured by absorption imaging. In our case, the spin-dependent force is provided by a horizontal beam on the green intercombination line. The beam is circularly (σ^+) polarized, and it is closely detuned with respect to the transition‡‡‡. In this regime, the light shift is dominated by the vector light shift, which depends on m_F§§§. For ^{173}Yb, we typically use a pulse of 1 ms in the presence of a transverse magnetic field of

---

[†††] The Clebsch-Gordan coefficients and branching ratio for this transition can be found in Ref. [203].

[‡‡‡] $^1S_0(F = 5/2) \rightarrow {}^3P_1(F = 7/2)$ for ^{173}Yb and $^1S_0(F = 1/2) \rightarrow {}^3P_1(F = 3/2)$ for ^{171}Yb.

[§§§] See Ref. [203] for the m_F-dependency of the polarizability for the $^3P_1$ state of ^{173}Yb estimated in LS coupling.

20 G and a bias vertical field of 1 G. We detune the beam by 100 MHz and choose a large beam size so that inhomogeneities in the beam profile do not significantly affect the force applied throughout the cloud.

In Fig. 1.8(a), we show the OSG detection images for different spin mixtures after a time of flight. The OSG detection is usually done in the 3D dipole trap, where the atom number and the signal-to-noise ratio are higher. By counting the number of atoms in the ROI corresponding to each spin component, we can optimize the optical pumping (see Sec. 1.7.1) to obtain spin-balanced mixtures. Fig. 1.8(b-c) shows the fraction of total atoms per spin component for calibrated SU(3) and SU(4) mixtures, respectively. We find that after calibration, the standard deviation of the population of the selected spin components is typically below 5 % per component for $N = 6$ and $N = 3$ and below 8 % for $N = 4$. The residual fraction of unwanted spin components is below 5 % per component. Moreover, the calibration is stable over time, as shown in Fig. 1.8(b-c) where we show the results of two OSG measurements performed on consecutive days with unchanged calibration.

In principle, we can also tune the ratio between the spin components to arbitrary values. This might allow future studies of the SU(N) symmetry breaking in the models of interest, including orbital-selective Mott transitions [76, 245–247] and itinerant ferromagnetism [153].

CHAPTER 2

Preparation and detection techniques of quasi-2D SU(N) Fermi gases

This chapter discusses the experimental methods for preparing and detecting SU(N) Fermi gases in a single layer. We begin by describing the new vertical lattice setup and the technical upgrades enabling its implementation in Sec. 2.1. Next, in Sec. 2.2, we cover the loading of atoms into a single plane, the calibration of the vertical lattice properties based on atomic responses, and the optimization of the loading procedure to obtain a cold sample. Finally, in Sec. 2.3, we review the techniques to detect atoms in the single plane and calibrate the imaging system. The techniques described in this chapter serve as the foundation for the state preparation and detection of the results presented in Chap. 3 and 5.

2.1 The new vertical lattice

In previous projects, our experiment investigated physics in different geometries, including a 3D cubic lattice [73, 78, 80, 82, 211], stacks of 2D planes [80, 82, 207] and ensembles of 1D tubes [78, 89]. In most cases, we used a retro-reflected vertical lattice at $\lambda = 760\,\mathrm{nm}$ with a spacing of $\lambda/2$. Retro-reflected lattices are convenient to set up and stabilize, but the small spacing makes it difficult to load atoms into a single plane and probe gases in a pure 2D geometry. In particular, we could typically load 7-10 planes depending on temperature, total atom number, and loading scheme [209].

Several techniques have been proposed and implemented to study atomic gases in a single 2D plane in the ultracold quantum gases community. These include the increase of the confinement of the gas before loading into the central plane of a vertical lattice, either magnetically [248] or optically [249, 250], the removal of atoms from undesired planes by exploiting or inducing some form of local addressability [123, 251–253], the use of evanescent wave surface traps [254–256], the loading into a lattice with large spacing, either retro-reflected [257] or generated by two beams interfering with a small angle [258] (also with a tunable spacing [259, 260]) and the preparation of a minimum of a potential along the vertical direction by using non-Gaussian beam profiles [249].

In our case, implementing compression-based techniques in the old retro-reflected lattice is particularly challenging because of the Fermi pressure. Consequently, we have opted

Parameter		Value
Wavelength	λ	760 nm
Half-angle	θ	$5.6(4)^\circ$
Lattice spacing	d_{lat}	3.9(3) µm
Beam waists	(w_h, w_v)	[248(13), 32(2)] µm
Maximal power	P^{max}	1.8 W
Maximal depth	U_0	$\simeq 103\,E_{\mathrm{rec}}$
Vertical bandgap	Δ_z	$2\pi \cdot 3.95(1)\,\mathrm{kHz}$
In-plane confinement	(ω_x, ω_y)	$2\pi \cdot [23.5(9), 30(1)]\,\mathrm{Hz}$
Maximal atom number in single plane	N_p^{max}	$\lesssim 11 \times 10^3$

Table 2.1 | Summary of the most relevant calibrated parameters for the new vertical lattice. The depth, bandgap, and confinement are calculated for the maximal power P^{max}. The recoil energy is $E_{\mathrm{rec}} = \hbar^2/(2m\lambda^2)$.

for a new lattice with larger spacing generated from two beams intersecting at a small half-angle θ and producing a standing wave with $\lambda_{\mathrm{eff}} = \lambda/\sin\theta$. In this way, we can maintain the wavelength $\lambda = 760\,\mathrm{nm}$, which is magic for the ${}^1\mathrm{S}_0 \to {}^3\mathrm{P}_0$ transition and, therefore, suitable for clock-line spectroscopy. At the same time, the larger spacing enables the loading of all the atoms to the central plane without any additional "slicing" process selectively removing atoms from undesired planes. In order to generate the lattice with this approach, a single light source is split into two outgoing beams, which are later recombined to interfere at the atoms' position. Particular attention must be paid to stabilizing the relative phase between the two paths, which might otherwise cause instability in the interference pattern and heat the atoms. The splitting is usually done with a combination of mirrors and beamsplitters. In our case, we have decided to adopt a novel and original approach by utilizing a *Kösters prism*, which we will describe in the next section.

Kösters prisms are rarely used in the context of ultracold atoms experiments [261]. However, they enjoy a long history of applications in precision interferometry, metrology, and testing of optical components [262–270].

Many results presented in this section have also been reported in Ref. [271], which contains additional technical details and numerical simulations.

2.1.1 Kösters prism

In our new shallow-angle vertical lattice, the source beam is split in two with a Kösters prism [272, 273], a beam splitter consisting of two identical and specially designed prisms optically contacted or cemented together (see Fig. 2.1). The incoming beam enters the prism perpendicular to one of its faces and splits in two at the interface between the halves. After a total reflection, it results in two parallel outgoing beams with symmetric properties with respect to each other. These two beams are then focused and recombined with a single lens at the atoms' position to generate the vertical lattice. With this scheme, we reduce the number of optical components necessary for the lattice to two, which is beneficial for the overall stability of the setup. The distance between the two parallel beams (and, therefore,

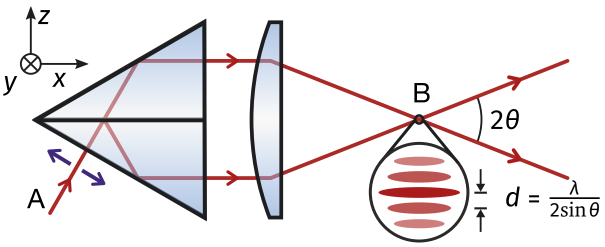

Figure 2.1 | Generation of a vertical lattice with a Kösters prism (not to scale). The source beam (A) splits into two paths at the interface between the two halves of the prism. The two beams exit parallel to each other and are focused at the atoms' position (B) to create a standing wave potential. By moving the source beam perpendicular to the entry point (purple arrows), the spacing of the lattice can be tuned. Sketch adapted from Ref. [271].

the angle and the lattice spacing) can be tuned by changing the entry point of the source beam in the prism (see Fig. 2.1). In principle, this tuning can also be done dynamically during the experiment. In this first iteration of the setup, we found it unnecessary to implement such a feature and, therefore, we have opted for a fixed configuration. However, an upgrade toward an accordion-type lattice should also be possible.

2.1.2 Lattice setup

The Kösters prism that we use has a length of 40 mm and an height of 20 mm[*]. We position the prism near the chamber (see Fig. 2.2) to minimize the beam path and improve the overall stability of the lattice. We use a lens with $f = 150\,\mathrm{mm}$ (two-inch diameter) to focus the outgoing beams at the atoms' position. The lens is half-cut to avoid overlap with the MOT beams, and it is shared with the horizontal dipole trap (hDT) beam and the in-plane retro-reflected L2 lattice.

To add the Kösters prism, we modify and adapt the hDT and L2 setups (see Fig. 2.2). In particular, we now overlap the hDT with the new vertical lattice with a dichroic mirror before the focusing lens. The hDT setup has been modified to recover similar beam waists $(w_v, w_h) \simeq (13, 88)\,\mu\mathrm{m}$ and shape ratio at the atoms' position as before the upgrade. On the backside of the chamber, we have added a symmetrically positioned defocusing lens, identical to the focusing one, to recover the two parallel beams. After this lens, most of the power is reflected through a beam splitter to a beam dump. On the other port of the beam splitter, we collect a small fraction of the power to observe and debug the interference pattern with a camera after an additional refocusing step. We initially envisioned a possible mechanism to actively stabilize the lattice based on the camera's signal. However, we have observed a very stable interference pattern without active stabilization and we currently rely solely on the passive stability.

---

[*] B. Halle Nachfl. GmbH, model IKP 040. We use the cemented version: although offering better absorption properties, the optically contacted version offered by the company specifies larger tolerances for rotational misalignments, which would result in a much worse overlap for the lattice potential. See also Ref. [271] for additional considerations on this choice.

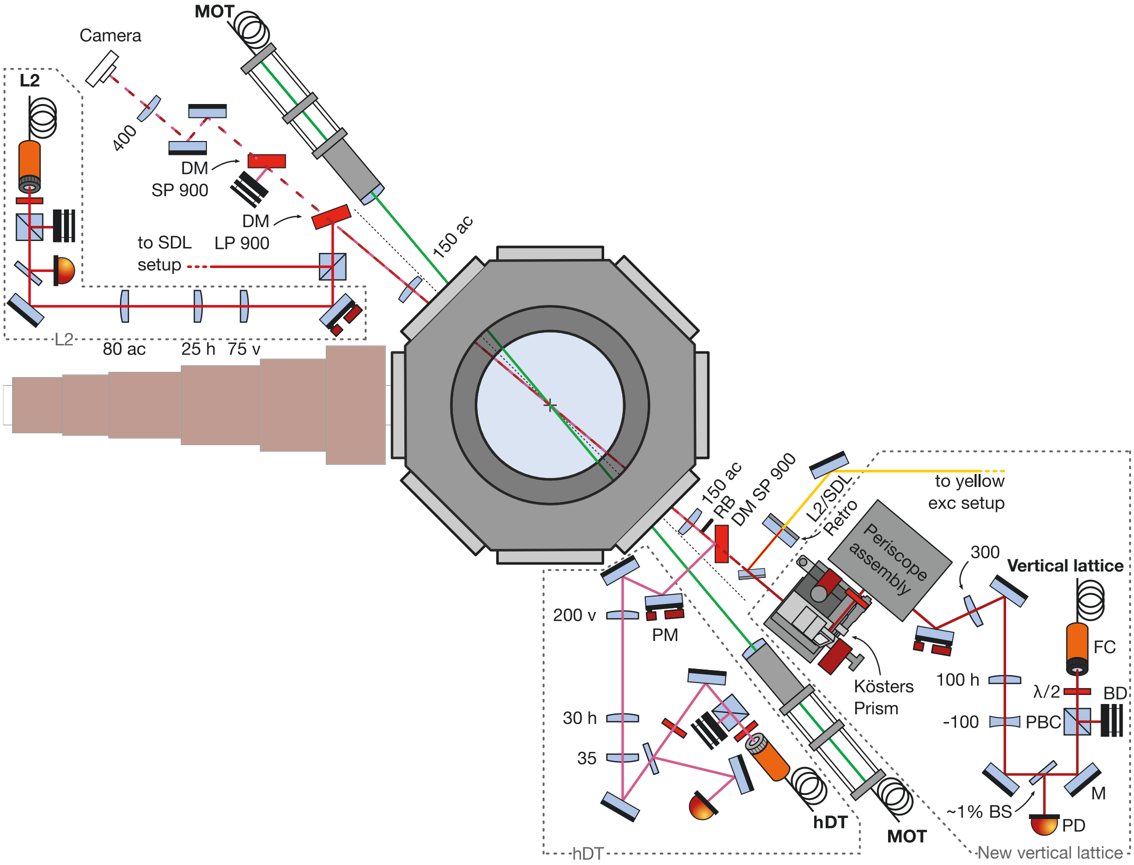

Figure 2.2 | Modifications to the experimental setup (see also Fig. 1.5) to implement the vertical lattice (not to scale). Part of the setup has been rebuilt for the horizontal dipole trap and the in-plane lattice L2 to accommodate the new vertical lattice. Abbreviations: FC - Fiber coupler, M – Mirror, BD – Beam dump, PBC – polarizing beamsplitter cube, PD – Photodiode, BS – Beam sampler, DM – Dichroic mirror, PM – Piezo-actuated mirror, RB - Razor blades. Sketch adapted from Ref. [271].

The focusing and defocusing lenses are also shared with the in-plane lattices L2 and SDL-2 and with the clock excitation's beam along this axis. The corresponding setups have been partially rebuilt to fit the new geometry. In particular, the beam-shaping telescope of L2 has been modified, and the new beam waists at the atoms are $(w_v, w_h) \simeq (30, 160)\,\mu\text{m}$ [they were $(w_v, w_h) \simeq (40, 160)\,\mu\text{m}$ before the upgrade].

Multi-axis stage and control of the degrees of freedom

The Kösters prism is mounted on a custom multi-axis stage made out of aluminum (see Fig. 2.3), which shields the prism from dust and air currents as well as possible. The mount is equipped with goniometers and translation stages, which allow us to tune all its four degrees of freedom: roll, yaw, pitch, and vertical displacement [see Fig. 2.3(b,c)]. While designing this mount, particular care has been put into disentangling each degree of freedom from other movements and facilitating their mapping to the lattice's relevant degrees of freedom. In this regard, we took care of positioning the point where the incoming beam

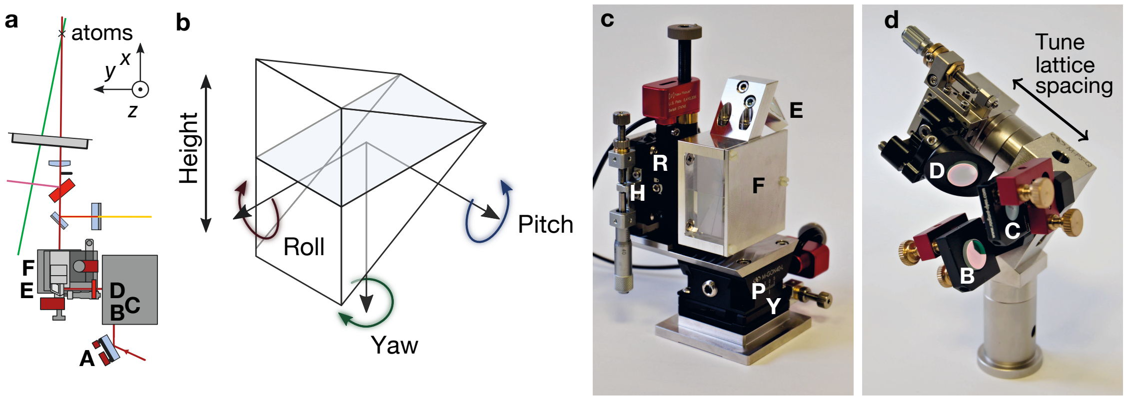

Figure 2.3 | Kösters prism's multi-axis mount and its degrees of freedom. (**a**) Sketch (rotated inset of Fig. 2.2) showing the beam path from the top. After beam shaping, the beam pointing is optimized by a motorized mirror (A), enters the periscope (B-D), and goes through the Kösters mount (E-F) to the atoms' position. (**b**) Degrees of freedom of the Kösters prism. (**c**) Kösters prism mounted on the custom-made multi-axis stage. After polarization cleaning, the beam from (D) is reflected to the mirror (E) and enters the prism (F). The degrees of freedom of the prism can be controlled with the translation stages (P, Y, R, H) corresponding to pitch, yaw, roll, and height. (**d**) Periscope before the Kösters prism. The lattice spacing can be changed by tuning the position of the mirror (D) with a translation stage. Photos and sketches adapted from Ref. [271].

splits in the Fourier plane and in trying to overlap it with the geometric center of the prism and the rotation center of the goniometers. Pitch and roll can be tuned with piezoelectric actuators, while the other two degrees of freedom are controlled by manual translation stages. The lattice spacing can be tuned by displacing a mirror in the periscope before the prism [see Fig. 2.3(d)]. Once the lattice spacing has been fixed, optimizing the degrees of freedom of the multi-axis stage and the pointing of the beam before the periscope does not induce any appreciable change in the lattice spacing. Additional technical information on the multi-axis stage can be found in Ref. [271].

Stability of the setup

A measurement of the phase fluctuations in a test setup in a closed box where a camera was positioned at the atoms' position returned a standard deviation around 0.004π for a measurement time window of 90 minutes [271]. In the final setup, the lattice setup and the single plane loading scheme have proven stable and require some minor alignment roughly once per day. For this purpose, we usually tune the piezoelectric actuators of the mirror before the periscope [(A) in Fig. 2.3(a)]. The pitch and the roll of the multi-axis stage are tuned more rarely, e.g., once a few weeks, while we hardly need to tune the yaw and the height.

2.2 Loading into a single plane

The loading into the vertical lattice follows the 3D evaporation in the crossed dipole trap described in Sec. 1.6. During the loading, we rely on the large lattice spacing to prevent the atoms from populating multiple planes.

In the experiment, we see that the population fraction of the central plane is higher than 90 % for less than 3×10^5 atoms [271]. Moreover, numerical simulations [271] confirm that we are loading up to about 10^5 atoms into the central plane with negligible spillover into the neighboring planes. However, they also indicate that the phase between the vertical lattice and the hDT (the shift between the trap centers along the propagation direction) might affect the loading.

By displacing the hDT with respect to the lattice in the vertical direction, we can change the loading plane and move from a singly populated plane to a 50:50 mixture between neighboring planes. We control this displacement by optimizing the vertical position of the hDT with the help of a piezoelectric actuator.

The method we use to detect the population in each plane is a *momentum refocusing* technique, which we describe in Sec. 2.2.1. In Sec. 2.2.2, we discuss the calibration of the lattice depth and the in-plane confinement by looking at the response of the atoms. In Sec. 2.2.3, we treat the problem of undesired optical reflexes, which initially induced anharmonic corrections to the potential, and how we solved it. Finally, in Sec. 2.2.4, we discuss the cooling scheme that allows us to reach a deep degenerate regime in the single plane.

2.2.1 Momentum refocusing

The population of each vertical plane cannot be easily distinguished by imaging the cloud in situ on a vertical plane because our camera does not have a good enough resolution[†]. As a consequence, we measure the population of each plane with a so-called *momentum refocusing* (or *kick and probe*) technique [274]. A sketch of the scheme is shown in Fig. 2.4(a-c). The idea is to give a different momentum “kick” to the atoms in each plane so that they will distribute in different spatial regions after time of flight (tof). This kick is given, in our case, by a quarter-of-period oscillation of the atoms in the hDT after switching off the vertical lattice. During this oscillation, the potential energy is transformed into kinetic energy. After tof, the resulting spatial spread allows us to resolve the population of each plane. In Fig. 2.4(d), we show the momentum refocusing technique as we displace the hDT along the vertical axis. The images show a cloud of spin-unpolarized ^{173}Yb atoms after a tof of 10 ms. On the left, we show a cloud in the central plane of the vertical lattice. As we shift the hDT, a neighboring plane gets populated. As we continue, the population of the central plane decreases until only the neighboring plane is populated. From the distance Δz between the two planes in tof, we can determine the lattice spacing

$$\Delta z = \omega_{v,\mathrm{hDT}} d_{\mathrm{lat}} t_{\mathrm{tof}}, \tag{2.1}$$

where $\omega_{v,\mathrm{hDT}}$ is the angular frequency of the hDT, d_{lat} is the lattice spacing, and t_{tof} is

---

[†] We have an AVT Manta camera with resolution 3.9 µm.

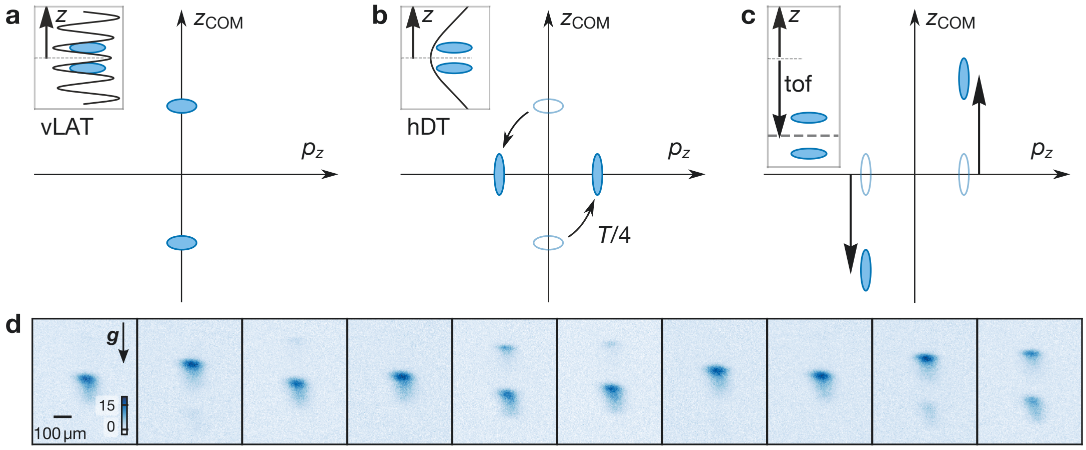

Figure 2.4 | Momentum refocusing technique. (**a**) We start with two planes populated in the vertical lattice (vLAT). In phase space (center of mass frame), the two clouds have well-defined positions (vertical axis) and a small momentum spread (horizontal axis). (**b**) We switch off the vertical lattice and switch on the horizontal dipole trap (hDT) centered in between the two clouds. After a quarter of the oscillation period, the clouds have maximized their momentum. (**c**) We switch off the hDT and let the system evolve in time of flight. The distance between the two clouds increases and becomes larger than the camera's resolution. The insets in (**a-c**) represent the potential along the vertical axis in real space. (**d**) Density measured with the momentum refocusing technique after a time of flight of 10 ms for a spin-unpolarized ^{173}Yb cloud. From left to right, we scan the relative phase between the vertical lattice and the hDT by changing the vertical position of the hDT with a pico-actuator. The distance from the first to the last image corresponds to about 3.6 µm. On the left, we populate the central plane. As we increase the phase, the neighboring plane is populated. The color bar is in units of counts/µm^2, and it is the same for all images.

the time of flight. For $\omega_{v,\mathrm{hDT}} = 2\pi \cdot 1.16(2)\,\mathrm{kHz}$ and $t_{\mathrm{tof}} = 10\,\mathrm{ms}$, we find a lattice spacing of 3.9(3) µm, which implies a half-angle of $\theta = 5.6(4)°$. The large error bar on the lattice spacing is due to the skewed distribution of the atoms after tof in the vertical direction. The origin of this skewness is not entirely understood, but it is likely due to a lensing effect induced by inhomogeneities in the "kick" given by the hDT. We observe a similar effect also with spin-polarized clouds, which suggests that this is not an interaction-driven effect.

2.2.2 Lattice depth and in-plane confinement

A precise calibration of the lattice depth and the bandgap of the vertical lattice is important for the measurements presented in the following chapters. Even in the deep lattice regime these values can still have relevant consequences for the determination of the quasi-2D properties of the gas, both in the bulk (see Sec. 3.2) and in the square lattice (see Sec. 5.1). The lattice depth can be calibrated with a *parametric heating* technique [275], which consists in modulating the lattice at the resonance frequency between the lowest and the second excited band and observing the heating (and therefore the change in size) of the cloud

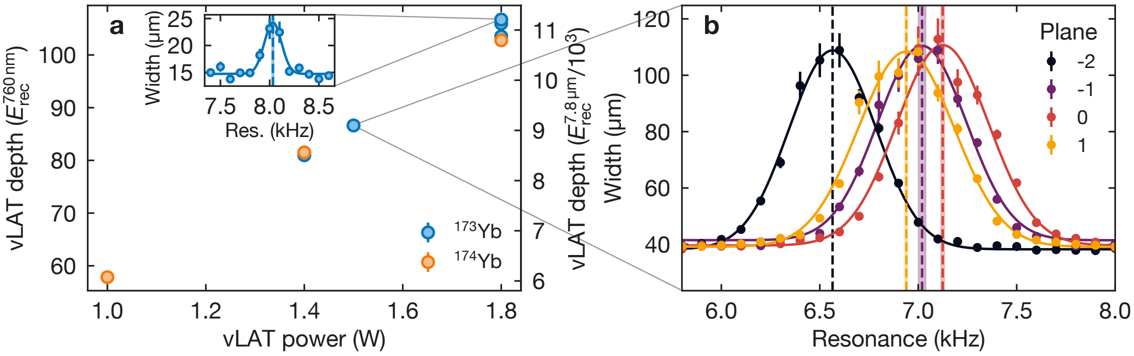

Figure 2.5 | Depth of the vertical lattice (vLAT). (**a**) Calibration of the depth in units of $E_{\mathrm{rec}}^{\lambda}$ for different values of the total power for ^{173}Yb (blue) and ^{174}Yb (orange) in the central plane. The error bars (s.e.m.) are smaller than the symbols. **Inset**: We calibrate the lattice depth with parametric modulation by measuring the change in the width of the cloud in time of flight when approaching the resonance between the lowest and the second band. With a band-structure calculation, we extract the lattice depth from the resonance position. (**b**) Parametric modulation for ^{173}Yb with a vLAT power of 1.5 W when loading into single different planes. Neighboring planes have a smaller resonance frequency than the central one (labeled with zero). Vertical lines: resonance positions returned by the fit of a Gaussian to the data. Errorbars are the s.e.m.

in time of flight [see inset of Fig. 2.5(a)]. For a lattice total power $P = 1.8\,\mathrm{W}^{\ddagger}$, we obtain a parametric heating resonance of 7.88(2) kHz, which corresponds to about $103\,E_{\mathrm{rec}}$ according to a band structure calculation. This corresponds to a bandgap of $2\pi \cdot 3.95(1)\,\mathrm{kHz}$.

Parametric heating is also useful to determine the loaded plane. Indeed, the depth of each plane is not exactly the same because of the Gaussian shape of the interfering beams, leading to the central one being deeper than the neighbors. This difference in depth can be detected with parametric heating [see Fig. 2.5(b)] and used to optimize the loading into the central plane.

The in-plane confinement in the region sampled by the atomic clouds is in first approximation harmonic (see Appendix A). Its trapping frequencies can be determined from the measurement of the center-of-mass oscillation of a spin-polarized cloud after a displacement from the rest position. With this method, we obtain $(\omega_x, \omega_y) = 2\pi\cdot[23.5(9), 30(1)]\,\mathrm{Hz}$ for the maximal depth.

From the measurement of the confinement for different depths and the knowledge of the total power and half-angle, we can calculate the beam waists. By assuming the same beam waists $w_{0,\{h,v\}}$ and Rayleigh ranges $z_{\mathrm{R},\{h,v\}}$ for the two beams and expanding the Gaussian beam profile to second order (see Appendix A) we can calculate the harmonic trapping frequencies

$$\omega_x^2 = \frac{2\alpha'}{m}\left[\frac{2}{w_{0,v}^2}\sin^2\theta + \frac{1}{2}\left(\frac{1}{z_{\mathrm{R},h}^2} + \frac{1}{z_{\mathrm{R},v}^2}\right)\cos^2\theta\right]\left(\sqrt{I_{0,a}} + \sqrt{I_{0,b}}\right)^2, \tag{2.2}$$

[‡] The total power does not split with a 1:1 ratio between the two beams due to coating imperfections. The upper beam has a power about 5 % smaller than the lower beam, and we take this difference into account for our calculations.

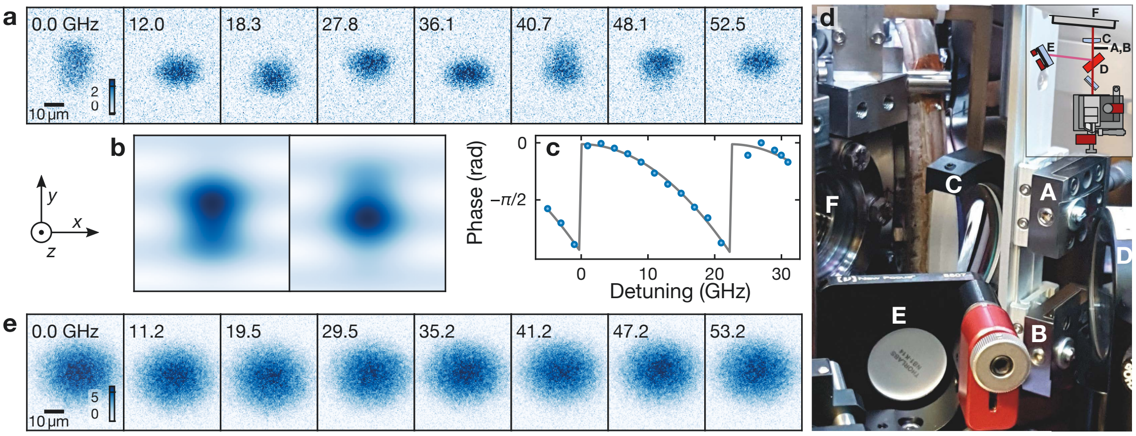

Figure 2.6 | Debugging the vertical lattice potential. (**a**) Each frame is a realization of a cloud loaded in a single plane with the same parameters but different lattice frequencies (detuning indicated at the top left). The shape of the cloud changes with the detuning, indicating the presence of a periodic pattern. (**b**) The pattern is in qualitative agreement with the shape of a cloud in a sinusoidal potential with a Gaussian envelope. The plot on the right has been obtained by changing the phase of the sinusoidal pattern on the left by $\pi/2$. The two plots are qualitative sketches with non-physical parameters. (**c**) By fitting the sinusoidal potential with a Gaussian envelope after integrating the data of (**a**) along the x-axis, we obtain a period of the pattern of 22.1(1) GHz. (**d**) We individuate the origin of the pattern in a reflex generated by the dichroic element (D) between the Kösters prism and the focusing lens (C). We block the reflexes with two razor blades (A) and (B) after the dichroic. (**e**) After blocking the reflex, the periodic pattern disappears. Images of (**a**) and (**e**) are single realizations without averaging. The detunings of (**a**,**c**,**e**) have been calculated with respect to the frequencies 394.7538 THz, 394.7656 THz and 394.7768 THz respectively. The size of the clouds in (**a**) and (**e**) is different because the total atom number is different. The color scales indicate the atoms per pixel squared, and it is the same for all the frames in the same row.

$$\omega_y^2 = \frac{4\alpha'}{m w_{0,h}^2}\left(\sqrt{I_{0,a}} + \sqrt{I_{0,b}}\right)^2, \tag{2.3}$$

where $I_{0,\{a,b\}}$ is the intensity of the beams a and b and α' is the polarizability. It can be easily verified that the ratio of the in-plane frequencies is intensity-independent.

By fitting the confinement for different depths, we obtain $(w_h, w_v) = [248(13), 32(2)]$ µm, to be compared with a preliminary measurement of $(w_h, w_v) \simeq (270, 25)$ µm which might have changed during the alignment and optimization.

2.2.3 Undesired reflexes

During the optimization of the cooling scheme, we noticed that the cloud shape was changing depending on the wavelength of the lattice laser. In particular, we observed a periodic change in the cloud shape perpendicular to the beams' propagation direction [see Fig. 2.6(a), beams propagate along the x-axis]. This pattern is in qualitative agreement with the shape of a cloud in an (unexpected) sinusoidal potential on top of the Gaussian envelope [see Fig. 2.6(b)]. A fit of the phase of the sinusoidal modulation [see Fig. 2.6(c)] returned a period of 22.1(1) GHz. This suggested that an etalon effect at the interfaces

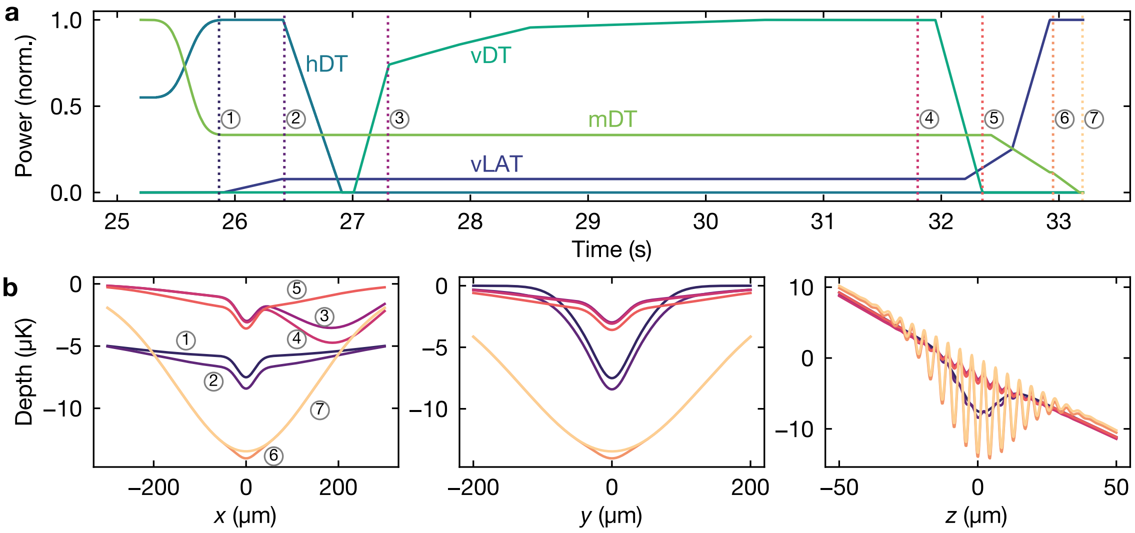

Figure 2.7 | Tilted evaporation and loading into a single plane. (**a**) Normalized power of the dipole traps and lattices as a function of the loading sequence time. The initial point in time at ≈ 25.2 s corresponds to the end of the 3D evaporation in the crossed dipole trap. From the darkest to the lightest shade of green: vertical lattice vLAT (max. power: 1.8 W), horizontal dipole trap hDT (0.3 W), vertical dipole trap vDT, displaced by about 194 μm along the *x*-axis (5.4 W), magic dipole trap mDT (0.3 W). (**b**) Numerical simulation of the trap depth along the main axes [see Fig. 2.1 or 2.3(a)] for the points indicated by the vertical lines in (**a**).

of the dichroic element combining the lattice with the hDT could originate reflexes producing an interference pattern with the main beams at the atoms' position[§]. We could not see the reflexes directly after the dichroic element neither by eye nor by using a camera. However, we blocked the optical access next to the main beams where the reflexes were to be expected with two razor blades (A) and (B) [see Fig. 2.6(d)]. After their alignment, the pattern disappeared [see Fig. 2.6(e)].

2.2.4 Cooling scheme

The measurements presented in Chap. 3 and 5 require an initial SU(N) Fermi cloud in the deep degenerate regime. Particular effort has been therefore put into optimizing the loading scheme in the vertical lattice to achieve a cold quasi-2D sample. We initially tried to load the gas directly and adiabatically from the crossed dipole trap to the vertical lattice. However, we could not achieve temperatures below $T/T_F^{2D} \approx 0.3$ for a spin-unpolarized sample starting from $T/T_F^{3D} \approx 0.1$ in the crossed dipole trap. The reason for this heating is probably a lack of adiabaticity during the loading process due to the change in the density of states between the two configurations and an inefficient entropy redistribution across the cloud. To overcome this issue, we tried to increase the final confinement along the vertical direction with another vertical dipole trap centered with the cloud in the $x - y$ plane, but we could only partially mitigate the heating.

[§] The dichroic is a Thorlabs DMSP900L, with a thickness of 5 mm, which would make it responsible for a pattern with a frequency of about 19 GHz, the same order of magnitude of the observed modulation.

The approach which proved to be the most effective was the so-called “tilted” evaporation scheme, as presented in Fig. 2.7. In this scheme, we add an in-plane optical gradient generated by a vertical dipole trap (vDT) displaced along the x-axis by about 194 µm with respect to the center of the cloud. The sequence works as follows. Starting from the end of the 3D evaporation, we first switch on the vertical lattice at low power to hold the atoms against gravity. At this point, we ramp down the hDT. We then ramp up the vDT and allow a “spillover” to the new lateral minimum, which results in the loss of the most energetic atoms. During the evaporation, the mDT (centered on the vertical lattice on the $x-y$ plane) stays constant and provides additional in-plane confinement. After the evaporation, we switch off the vDT and increase the depth of the vertical lattice. The corresponding increase of the in-plane confinement is compensated by reducing the mDT confinement. With this scheme, we could achieve a temperature of $T/T_{\mathrm{F}}^{2\mathrm{D}} \gtrsim 0.15$ for $3 \leq N \leq 6$.

2.3 Imaging techniques and calibration

In this section, we focus on the techniques used in our experiment for imaging the atoms and their calibration. In order to measure the equation of state (EoS) of a gas, it is important to have a reliable and calibrated detection mechanism that allows the extraction of the atomic density without systematic errors and with a good signal-to-noise ratio. Most measurements in the following chapters rely on in-situ, high-intensity absorption imaging. This technique measures the transmission of a probe beam through the cloud and allows the reconstruction of the atomic density with a Beer-Lambert law. In our experiment, the probe is a circularly polarized beam along the stretched $^1\mathrm{S}_0 \rightarrow {}^1\mathrm{P}_1$ transition operating above the saturation intensity and with a small bias magnetic field of $\simeq 1\,\mathrm{G}$. The pulse duration, when it is not differently specified, is 5 µs. This value has been chosen to maximize the absorption signal and simultaneously avoid excessive blurring due to the motion of the atoms during the process [180].

The imaging apparatus consists of a high-resolution custom objective[¶] with NA = 0.27 and a theoretical diffraction limit of about 1.2 µm at the imaging wavelength of 399 nm. After the objective, a system of lenses and mirrors guides the light to an EMCCD camera[‖] with a total magnification of about 28.

In Sec. 2.3.1, we discuss the non-linear correction that needs to be applied to the Beer-Lambert law in the high-intensity regime and its calibration. In Sec. 2.3.2, we discuss the calibration of the cross section for different spin mixtures and trap geometries by looking at the density fluctuations of a thermal gas. The method we use for this purpose can also be used to optimize the alignment of the imaging system. Moreover, the method allows the reconstruction of the system’s point spread function (PSF), which is crucial for EoS and thermometry measurements.

Some of the methods presented in this section have already been used in our experiment in a 3D geometry [82, 180, 207]. However, the new 2D geometry allows for an improved

---

[¶] Designed by LensOptics

[‖] Andor iXon

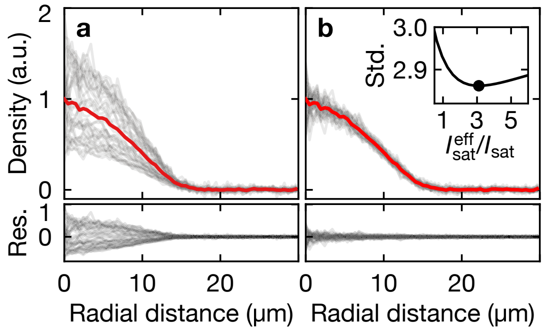

Figure 2.8 | High-intensity calibration for an SU(4) cloud in a 2D harmonic confinement. (**a**) Radial density evaluated with the uncorrected Beer Lamber law for different I_{in}/I_{sat} values between 2 and 8 (grey lines). Red line: average density. Lower panel: residuals between the average density and the data. (**b**) Same dataset of (**a**) evaluated with the Beer Lamber law corrected for high intensity [see Eq. (2.4)]. **Inset**: Relative standard deviation of the atom number measured with various imaging light intensities as a function of I_{sat}^{eff}/I_{sat}. The minimum is the value that we use for the calibration.

Dim	N	I_{sat}^{eff}/I_{sat}
2D	6	2.9(2)
2D	4	3.0(1)
2D	3	3.0(2)
2D†	6	3.0(2)
3D	6	2.8(2)
3D	4	2.80(8)

Table 2.2 | Calibrated effective saturation intensity for different SU(N) mixtures in 2D and 3D harmonic confinements. † Data taken in a Mott insulating configuration (see Chap. 5).

signal-to-noise and calibration resolution. Moreover, other experiments have shown that high-density monolayers can show significantly different imaging parameters and calibration [276, 277]. It is, therefore, important to re-evaluate the calibration and compare it with the old results.

2.3.1 High-intensity imaging calibration

We determine the density with the modified Beer-Lambert law [278], which accounts for the saturation effects of the imaging light:

$$n(x,y) = \frac{1}{\sigma}\left[\log\left(\frac{I_{\text{in}}}{I_{\text{out}}}\right) + \frac{I_{\text{in}} - I_{\text{out}}}{I_{\text{sat}}^{\text{eff}}}\right], \tag{2.4}$$

where $n(x,y)$ is the density at pixel position (x,y), σ is the cross section, and $I_{\text{in}} = I_{\text{in}}(x,y)$ and $I_{\text{out}} = I_{\text{out}}(x,y)$ are the incident light and the light after absorption, respectively. We calibrate the effective saturation intensity $I_{\text{sat}}^{\text{eff}}$ by varying $I_{\text{in}}/I_{\text{sat}}$ between 2 and 8 and minimizing the variation of the density profile as described in Ref. [278] with a least-squares method [see Fig. 2.8(a)]. The results for different spin mixtures and geometries are reported in Tab. 2.2. The effective saturation intensity $I_{\text{sat}}^{\text{eff}}$ is about three times larger than the bare $I_{\text{sat}} = \pi h c\Gamma/(3\lambda^3) \simeq 60\,\text{mW/cm}^2$ (λ and Γ are the wavelength and linewidth of the probe beam, respectively), an effect which has been observed in previous experiments and might be due to a breakdown of the two-level system approximation, imperfections in the control of the polarization or the presence of a residual magnetic field [278]. We find that the effective saturation intensity is independent of the spin mixture and overall compatible

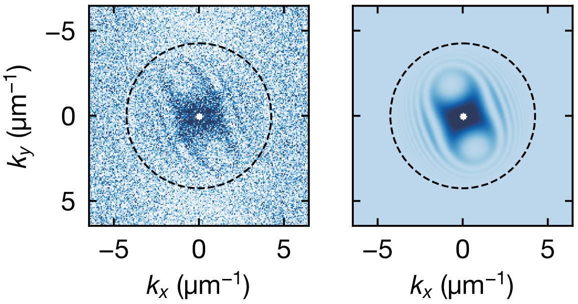

Figure 2.9 | Image response function for an SU(3) cloud in a 2D harmonic confinement. **Left**: Experimental data. **Right**: Fit of the data according to the model described in the text. The black dashed line represents the maximum $\boldsymbol{k}$-vector according to the theoretical NA of the objective. The central white region has been masked out in the fit.

Dim	N	$\sigma_{\mathrm{eff}}/\sigma_0$
2D	6	0.383(7)
2D	4	0.38(1)
2D	3	0.35(1)
3D	6	0.389(2)
3D	4	0.395(2)
3D	3	0.393(2)

Table 2.3 | Calibrated effective cross section for different SU(N) mixtures in 2D and 3D harmonic confinements.

with the 3D values within 5 %. Moreover, we find a similar agreement for a cloud in the 2D harmonic trap and the deep 2D Mott insulating regime.

2.3.2 Point spread function and absolute atom number calibration

In Sec. 2.3.1, we have calibrated the imaging system such that our measurement of the optical density is independent of the intensity of the imaging light. However, we have not discussed the calibration of the cross section σ, which is the subject of this section, together with the reconstruction of the point spread function (PSF) and the pixel calibration of our camera.

Determination of the cross section

With an independent measurement, we extract the effective cross section from the density shot noise of a thermal sample in the 2D bulk according to the method described in Ref. [279]. In particular, we make use of the relation of the local density fluctuations $\langle|\delta n|^2\rangle$ to the cross section σ, the total atom number N_p and the modulation transfer function (MTF) $\mathcal{M}$ of the imaging system in momentum space [279]

$$\langle|\delta n(\boldsymbol{k})|^2\rangle = \sigma N_p \mathcal{M}^2(\boldsymbol{k}). \tag{2.5}$$

The functional form of the MTF can be modeled with a few assumptions on the set of most relevant aberrations of the imaging system. In particular, in the low imaging intensity regime, according to the derivation presented in Ref. [280],

$$\mathcal{M}^2(\boldsymbol{k}) = \left|\mathcal{F}^{-1}\left\{\Re\left\{e^{i\delta_s}\mathcal{F}\left[p(kr_0d,\theta)\right]\right\}\right\}\right|^2, \tag{2.6}$$

where $p(r,\theta)$ is the exit pupil function:

$$p(r,\theta) = \mathrm{H}(1-r/r_0)e^{-(r/r_0)^2/\tau^2}e^{i\phi(r/r_0,\theta)}, \tag{2.7}$$

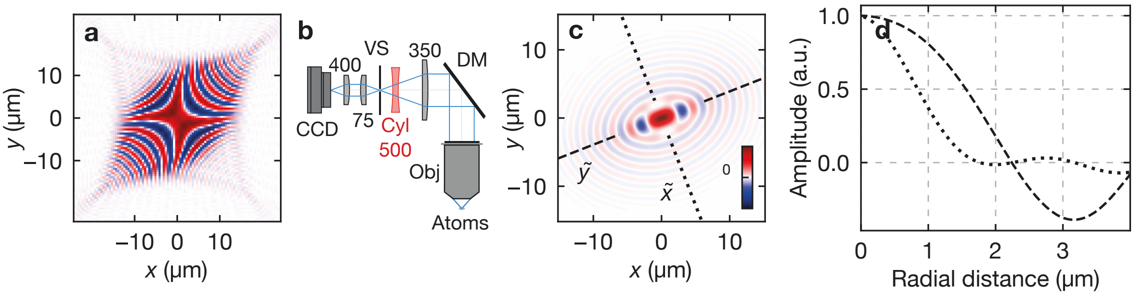

Figure 2.10 | Reconstruction and optimization of the point spread function (PSF). (**a**) Reconstructed PSF in the single 2D plane before the optimization. The PSF is strongly affected by astigmatism. (**b**) Sketch (not to scale and without mirrors) of the imaging system adapted from Ref. [180]. In order to compensate for the astigmatism, we add a cylindrical lens with a long focal length (red). The numbers in the sketch indicate the focal lengths of the lenses. Abbreviations: Obj - Objective, DM - Dichroic mirror, VS - Adjustable variable mechanical slit. (**c**) PSF after the optimization of the objective alignment and the compensation of the astigmatism, corresponding to the MTF shown in Fig. 2.9. (**d**) Cuts along the main axes (dashed and dotted lines) of the PSF in (**c**). The colormap of (**a**) and (**c**) is in arbitrary units.

$$\psi(r,\theta) = S_0 r^4 + \alpha r^2 \cos(2\theta - 2\phi) + \beta r^2. \tag{2.8}$$

In the previous equations, $\mathscr{F}$ is the Fourier transform, $d = \lambda/(2\pi\mathrm{NA})$, δ_s represents the phase shift due to the detuning of the imaging light with respect to the atomic resonance, $\mathrm{H}(x)$ the Heaviside step function, r_0 is the radius of the finite aperture, and τ the acceptance angle. $\psi(r,\theta)$ is the wavefront aberration function, which in our approximation is composed of contributions from spherical aberration S_0, astigmatism (α,ϕ) and defocussing β.

In Fig. 2.9(a) we show the measured $\langle|\delta n(\boldsymbol{k})|^2\rangle$ for an $N = 3$ sample in a 2D harmonic confinement. The best fit of the data with the model described above and free parameters $\sigma, \tau, S_0, \alpha, \phi, \beta, \delta_s$ is shown in Fig. 2.9(b). The fit returns correlated values for the aberration parameters but allows us to obtain a well-defined value for the cross section σ. In Tab. 2.3, we compare the values of σ obtained with this method for $N = 3, 4$, and 6 in the 2D and 3D cases. We observe a good agreement between most of the values. For $N = 4$ and 6, the 2D and 3D values agree within the uncertainties. For $N = 3$ the 2D value is about 11 % smaller than the 3D case. A possible explanation for this discrepancy might be a cooperative optical response similarly observed in other monolayer systems [276].

Reconstruction of the PSF

The MTF is related to the PSF according to the relation $\mathscr{M}(\boldsymbol{k}) = |\mathscr{P}(\boldsymbol{k})|$, which allows us to reconstruct the even components of the PSF, which we assume to be the predominant ones [280]:

$$\mathscr{P}(\boldsymbol{k}) \propto \Re\left[e^{i\delta_s} p(\boldsymbol{k})\right]\Big|_{k=r/(r_0 d)}. \tag{2.9}$$

In Fig. 2.10, we show the reconstructed PSF. Thanks to this method, we could note that our imaging system was not diffraction limited and was affected by astigmatism [see Fig. 2.10(a)]. Since a re-alignment of the objective could only partially mitigate the problem, we decided

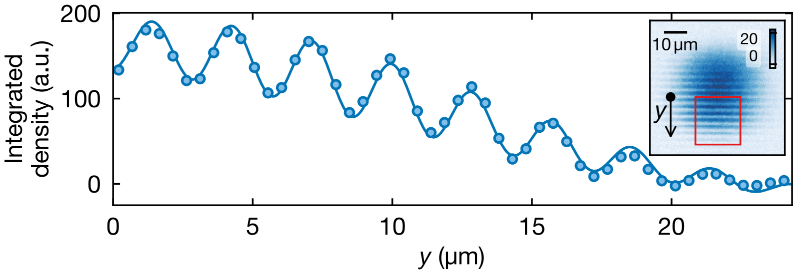

Figure 2.11 | Density modulation pattern generated by the combination of two retro-reflected lattices at 760 nm and 670 nm propagating in the same direction *y*. The density has been integrated along the in-plane direction perpendicular to the lattice propagation. Solid line: best fit of the data. **Inset**: In-situ image of the density-modulated atomic cloud. The ROI inside the red rectangle corresponds to the data shown in the main panel. The color bar is in units of atoms/µm^2.

to add a cylindrical lens with a long focal length to the imaging system to correct it [see Fig. 2.10(b)]. After this modification of the imaging system, we could obtain a smaller and more symmetric PSF with a resolution of about 2.5 µm[**] [see Fig. 2.10(c-d)].

Pixel size calibration

The absolute atom number calibration presented in Sec. 2.3.2 relies on an accurate calibration of the pixel size to the real size of the cloud. We determine this calibration by looking, in the single plane, at the density modulation pattern generated by the combination of two in-plane and co-propagating lattices with different lattice spacing. In particular, for the measurement shown in Fig. 2.11, we use the lattices L1 ($\lambda = 760$ nm) and SDL-1 ($\lambda = 670$ nm). From the fit of the modulation frequency, we obtain the camera magnification $M = 0.482(2)$ µm/pixel. This value is in good agreement with the one previously reported for our experiment in Ref. [180] with a difference between the two calibrations smaller than 1 %.

[**] The HWHM of the main axes is of approx. 0.85 µm and 1.6 µm, respectively. The location of the first minimum from the center is at approx. 1.9 µm and 3.2 µm, respectively.

CHAPTER 3

SU(*N*) Fermi gases in a quasi-2D harmonic trap

Starting from the state preparation of degenerate SU(N) gases in a single plane described in Chap. 2, we present in this chapter the results of our measurements of the EoS of a quasi-2D, weakly-interacting SU(N) Fermi gas in a harmonic trap.

From a theoretical point of view, the behavior of interacting SU(N) Fermi gases in free space is particularly intriguing and far from being fully understood. The interplay between superfluidity and magnetism is qualitatively different for $N \geq 3$ with respect to $N = 2$ because of the different pairing symmetries [66, 281]. Prethermal states similar to those observed in quark-gluon physics have been predicted [282]. The physics of the BEC-BCS crossover is richer than in the SU(2) case [283]. The probing of systems with large N might provide a better understanding of the non-analytical deviations from the Sommerfeld expansion in interacting Fermi gases [161, 284]. Moreover, the study of SU(N) gases is particularly relevant in the context of itinerant ferromagnetism (see Sec. 1.3.1).

From an experimental point of view, many of the interesting regimes considered in these theoretical studies currently cannot be easily probed. ^{173}Yb and ^{87}Sr naturally feature an SU(N) symmetry in the ground state. However, they lack a magnetic Feshbach resonance and a mechanism for tuning the interactions. Nevertheless, alternative mechanisms such as optical Feshbach resonances [165, 166] have been proposed in the past and might enable the probing of these regimes.

Some pioneering measurements of the SU(N) EoS with degenerate quantum gases have been presented, for the 3D harmonic case, in Refs. [72, 149, 180, 285, 286], usually neglecting the effect of weak interactions. More recently, the experiment of Ref. [287] has looked systematically at the EoS in the 3D case (with ^{87}Sr) and successfully developed a reliable thermometry which also accounts for weak interaction effects.

Other significant milestones for a better understanding of the SU(N) Fermi liquids in 3D (with ^{173}Yb) encompass the study of bosonization (the resemblance of Fermi gases with large N to bosonic systems) [288] and the development of machine learning techniques to distinguish between different spin multiplicities [289].

It is worth emphasizing that most of the experimental and theoretical works in the literature focus on the 3D case. In 2D, N-dependent collective excitations have been predicted and observed in stacks of layers formed by a one-dimensional optical lattice [290, 291]. However, a comprehensive theoretical treatment of the 2D weakly interacting SU(N) Fermi liquid at finite temperature is still lacking. Therefore, the measurement of this SU($N > 2$) EoS, which, to our knowledge, is reported here for the first time for a single-layer 2D ensemble, is an important milestone in the exploration of the properties of these systems.

This chapter develops as follows. In Sec. 3.1, we briefly consider the non-interacting Fermi gas. In Sec. 3.3, we consider the weakly interacting case and discuss the effect of interactions on the density profile, temperature, and entropy. In Sec. 3.2, we define the quasi-2D regime and discuss the role of the third dimension in our experiment. In Sec. 3.4, we present the experimental determination of the EoS for $N = 3, 4$ and 6 and benchmark the theory presented in the previous sections. Finally, in Sec. 3.5, we present the measurement of the local density fluctuations and their relation to the other EoS quantities through the fluctuation-dissipation theorem.

The results of this chapter, particularly the development of a reliable method for measuring the entropy per particle, will be used in Chap. 5 to cross-benchmark the in-lattice fit results. Moreover, the fluctuation-dissipation theorem and the calibration of the local density fluctuations will be used again in Chap. 5 to develop and test a theory-free thermometry for the SU(N) Fermi-Hubbard model.

3.1 The non-interacting case

In the non-interacting limit, the components of an SU(N) Fermi gas are decoupled from each other. In the grand canonical ensemble, the N-dependency factorizes in the most relevant thermodynamic quantities.

The thermodynamics of the system can be either derived by assuming a harmonic potential and using the corresponding density of states, or by assuming a homogeneous potential and using the local density approximation (LDA) to account for the effect of the trapping potential.

The density of states of a 2D harmonic oscillator $V(x,y) = \frac{1}{2}m\left(\omega_x^2 x^2 + \omega_y^2 y^2\right)$ is

$$\rho(\epsilon) = N\frac{\epsilon}{\hbar^2\bar{\omega}^2}, \tag{3.1}$$

where $\bar{\omega} = \sqrt{\omega_x \omega_y}$ and ϵ is the energy.

The density of states for a N-components homogeneous system is instead

$$\rho = N\frac{m}{2\pi\hbar^2}. \tag{3.2}$$

In LDA, the harmonic confinement is absorbed in the chemical potential:

$$\mu(x,y) = \mu_0 - V(x,y) = \mu_0 - \frac{1}{2}m\left(\omega_x^2 x^2 + \omega_y^2 y^2\right), \tag{3.3}$$

where μ_0 is the chemical potential at the trap's center.

The LDA has been verified several times in experiments with ultracold atoms [73, 186–188, 292, 293], although its use requires some additional care in the case of strongly an-

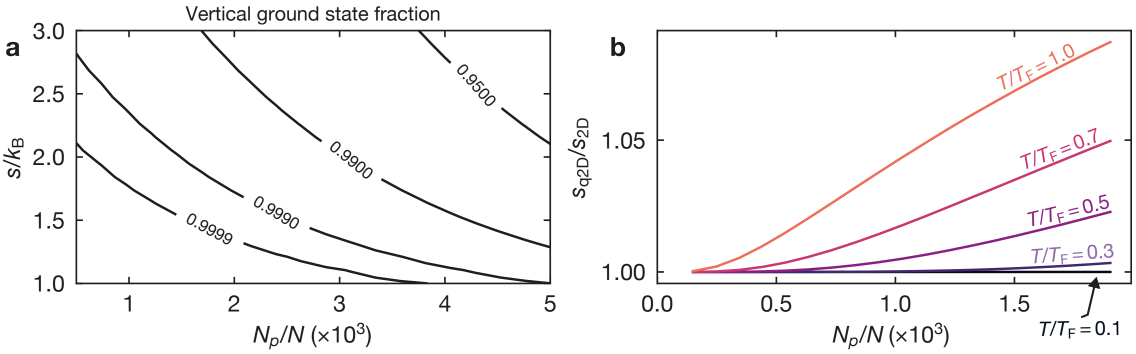

Figure 3.1 | Quasi-2D effects for the typical parameters of our experiment $(\omega_x, \omega_y, \omega_z) = 2\pi\cdot(23.5, 30, 4\times 10^3)$ Hz. (**a**) Fraction of atoms in the lowest level of the harmonic oscillator along the *z*-axis as a function of the total atom number and the entropy per particle. We perform the calculation from the discrete spectrum of the 3D anisotropic harmonic oscillator. (**b**) Ratio between the entropy of the quasi-2D system and the entropy of the pure 2D system as a function of the total atom number and temperature. The pure 2D (quasi-2D) entropy is calculated from the discrete spectrum of the 2D (3D anisotropic) harmonic oscillator.

harmonic potentials [294, 295], near unitarity [293, 294] or when looking extremely close to the interface between the metallic and the insulating phases [296, 297]. It is accurate when the energy spacing of the potential is much smaller than the other characteristic energies of the system. This is the case in the experiments that we present in the following, where we can, therefore, safely use the LDA.

From the density of states, one can calculate the grand potential Ω of the system and all the thermodynamic quantities of interest. In Appendix B, we report the derivation of the most relevant thermodynamic quantities in both the harmonic and the homogeneous cases.

3.2 Quasi-2D approximations

The system we probe in our experiment is not a pure 2D system but a 3D system where we freeze the motion along the z-axis. In this case, we talk about a *quasi-2D* system*. It is important to understand the role of the third dimension and estimate the corrections that we need to take into account when we describe our system as 2D. The most relevant effects concern the density of states (Sec. 3.2.1) and the scattering properties (Sec. 3.2.2).

3.2.1 Density of states

A possibly fragile assumption we make when we describe our system as purely 2D is that the density of states of Eq. (3.1) is correct. Our system is better described as a 3D anisotropic harmonic oscillator with $\omega_z \gg \omega_x, \omega_y$, where we assume that all the atoms are in the lowest

---

*In the case of an interacting system, a quasi-2D system is characterized by a 2D dynamics of the atoms and a 3D character of the interactions. This means that $l_z \gg a_{3D}$, with l_z the size of the harmonic oscillator in the z direction and a_{3D} the s-wave scattering length. In this framework, the dynamics in the 2D plane can be described with an effective scattering length a_{2D} which come from the 3D collisions, as we do in Sec. 3.2.2.

energy level along the z direction. This assumption requires $\mu, k_\mathrm{B}T \ll \hbar\omega_z$. By comparing $\hbar\omega_z$ with the Fermi energy, we infer a higher boundary on the total atom number that we can safely probe in our experiment without having to consider the complications of higher bands:

$$\hbar\omega_z \gg E_\mathrm{F} = \hbar\sqrt{2\omega_x\omega_y N_p/N} \qquad \Rightarrow \qquad N_p/N \ll \frac{1}{2}\left(\frac{\omega_z^2}{\omega_x\omega_y}\right), \tag{3.4}$$

which in our case corresponds to $N_p/N \lesssim 11\times10^3$. This value reduces at finite temperature. In general, we can estimate the error that we commit by treating our system as purely 2D by calculating the discrete spectrum and the distribution of the atoms in the different energy levels of the 3D anisotropic harmonic oscillator and comparing it with the 2D value. In particular, we can compare the entropy by using the identity [298]

$$S/k_\mathrm{B} = \beta(E - \mu N_p) + \sum_n \log\left[1 + e^{\beta(\mu-\epsilon_n)}\right], \tag{3.5}$$

where $E = \sum_n \epsilon_n F(\epsilon_n)$ is the total energy, $F(\epsilon_n)$ the Fermi-Dirac distribution and n the label of the energy eigenstates. The simulation of Fig. 3.1(a) shows that, assuming a vertical bandgap of about 4 kHz, more than 99.9 % of the atoms are in the ground state along the z-direction for the experiments we present in the following.

In Fig. 3.1(b), we compare different ways of calculating the entropy of the system. In particular, we compare the entropy of the quasi-2D system s_q2D calculated from the discrete spectrum of the 3D anisotropic harmonic oscillator with the entropy of the pure 2D system s_2D[†]. The two values can be significantly different for large atom numbers and high temperatures. However, for the typical parameters of our experiment, the two values are in agreement within 1 %.

3.2.2 Scattering properties

In addition to the density of states, another crucial difference between a pure 2D and a quasi-2D system concerns the scattering properties. So far, we have considered non-interacting ensembles, but in Sec. 3.3, we will consider the effect of weak interactions and therefore need a model.

In a pure 2D system, particle scattering happens in the 2D plane. At the lowest order, the scattering amplitude can be described as [299]

$$f_\mathrm{2D}(k) \simeq \frac{4\pi}{i\pi - 2\log\left(ka_\mathrm{2D}\right)}. \tag{3.6}$$

In contrast to the 3D case, where the s-wave interactions are in first approximation parametrized

---

[†] The entropy per particle in a pure 2D system s_2D can be calculated from the discrete spectrum of the 2D harmonic oscillator or from the continuous density of states of Eq. (3.1). For small atom numbers, we expect a discrepancy between the two values because of the coarseness of the discrete spectrum. For the simulation of Fig. 3.1(b), we use the discrete spectrum. The discrepancy between the two values can be as large as 2 % to 4 % for our typical atom numbers.

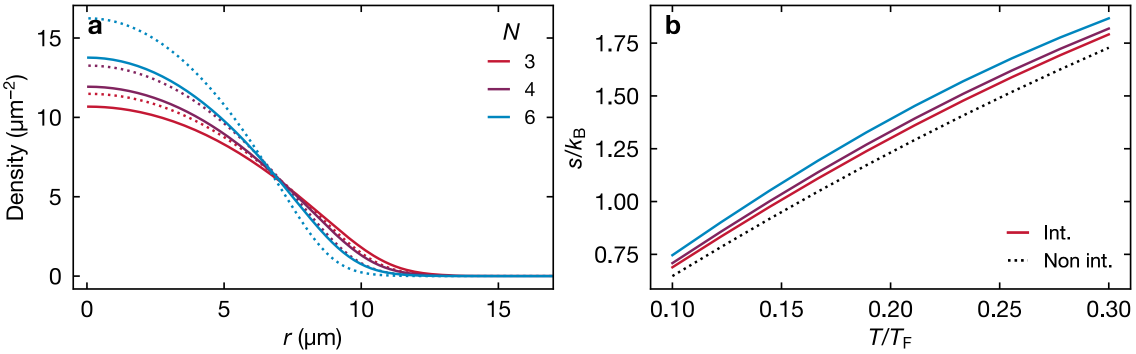

Figure 3.2 | Simulation of SU(N) Fermi gases in a 2D harmonic potential. (**a**) Density profile for $N = 3,4$ and 6, $N_p = 2\times10^3$ and $T = 0.15T_F$ in a harmonic confinement with $\omega_x = \omega_y = 2\pi\cdot 40\,\mathrm{Hz}$. Dotted lines: non-interacting profiles. Continuous lines: interacting profiles according to the model presented in Sec. 3.3 and with $a_{2D} = 0.0025\,a_0$. (**b**) Entropy per particle vs T/T_F for $N_p/N = 500$. In the non-interacting limit (dotted lines), the relation is independent of N. When we consider interactions, we observe a small N-dependency.

by the 3D scattering length only (see Sec. 1.2), the interaction parameter in 2D depends on both the scattering length a_{2D} and the momentum k. For a degenerate Fermi gas, it is natural to define the interaction parameter as the scattering amplitude at the Fermi momentum k_F [300].

The scattering amplitude in a 3D anisotropic harmonic potential is generally different from the one of Eq. (3.6). However, for a weakly interacting system, it is possible to define a 2D scattering length $a_{2D}(\omega_z, a_{3D})$ that describes the scattering behavior at low energy. Remarkably, the scattering amplitude assumes the same functional form as Eq. (3.6) if we define [300]

$$a_{2D} = l_z\sqrt{\frac{\pi}{0.905}}\exp\left(-\sqrt{\frac{\pi}{2}}\frac{l_z}{a_{3D}}\right), \tag{3.7}$$

where $l_z = \sqrt{\hbar/m\omega_z}$ is the characteristic length of the harmonic oscillator along the vertical direction. For ^{173}Yb and $\omega_z \simeq 2\pi\cdot 4\,\mathrm{kHz}$, we obtain $a_{2D} \simeq 0.0025\,\mathrm{a}_0$.

3.3 The effect of interactions

A rigorous treatment of the interactions for SU(N) Fermi liquids at finite temperature is beyond the scope of this work. Nevertheless, we can obtain a satisfactory correction to the non-interacting limit with a small set of approximations. The following derivation follows the lines of the treatment presented for the 3D case in Ref. [287].

The idea is to parametrize interactions with a density-dependent coupling constant $g(n,N)$ [301]:

$$g(n,N) = \frac{1}{\log 2 - 2\log(k_F a_{2D})}, \tag{3.8}$$

where $k_\mathrm{F} = \sqrt{4\pi n/N}$ is the local, density-dependent Fermi vector and a_2D is the 2D scattering length (see Sec. 3.2.2). At zero temperature, we can perturbatively include the interaction's contribution to the Fermi energy by extending a result presented for the SU(2) case in Ref. [301][‡]:

$$E_\mathrm{F}^\mathrm{int} = E_\mathrm{F}\left[1 + 2g(N-1) + 4g^2(N-1)(1-\log 2)\right] + O(g^3). \tag{3.9}$$

In the following, when we write E_F and T_F, we will still refer to the non-interacting Fermi energy and temperature, respectively, even when considering the interacting case.

At finite temperature, we can make use of the expression for the chemical potential in the non-interacting case (see Appendix B):

$$\mu = \frac{1}{\beta}\log\left(e^{\beta E_\mathrm{F}} - 1\right). \tag{3.10}$$

In this way, we can approximate the chemical potential in the interacting case as

$$\mu_\mathrm{int}(T,N) \approx \frac{1}{\beta}\left[1 + 2g(N-1) + 4g^2(N-1)(1-\log 2)\right]\log\left(e^{\beta E_\mathrm{F}} - 1\right). \tag{3.11}$$

In a canonical ensemble and LDA, we can therefore calculate the density profile $n(x,y)$ and the density-dependent coupling constant $g(n,N)$ by self-consistently solving the following equations:

$$\begin{cases} \mu_\mathrm{int}[n(x,y)] = \mu_0(N_p) - V(x,y) \\ N_p = \int \mathrm{d}x\,\mathrm{d}y\, n[x,y,\mu_0(N_p)]. \end{cases} \tag{3.12}$$

Once we have solved Eqs. (3.12), we can use the determined μ_int to calculate the entropy. As a first approximation, we use the non-interacting expression.

In Fig. 3.2(a), we show a simulation of how interactions lower the density in the center of the trap and reduce the differences in the density profiles between systems with different values of N. Moreover, as we see in Fig. 3.2(b), interactions increase the entropy per particle for systems with the same T/T_F, and this effect is more pronounced for larger N.

We expect the correction developed in this section to be a good approximation for $T \ll T_\mathrm{F}$ and small interactions. At higher temperatures, additional corrections might be necessary. In the "thermal gas" limit ($T \gg T_\mathrm{F}$), however, we expect the non-interacting expression to be again a good approximation for the entropy per particle.

3.4 Measurement of the EoS

In Fig. 3.3, we show the results of the measurement of the quasi-2D EoS for SU(N) Fermi gases with $N = 3, 4$, and 6. We prepare the ensembles with different N by optically pumping the unwanted spin components before the 3D forced evaporation (see Sec. 1.6). After the

---

[‡] We extend the SU(2) results on the same lines as in Ref. [287] for the 3D case.

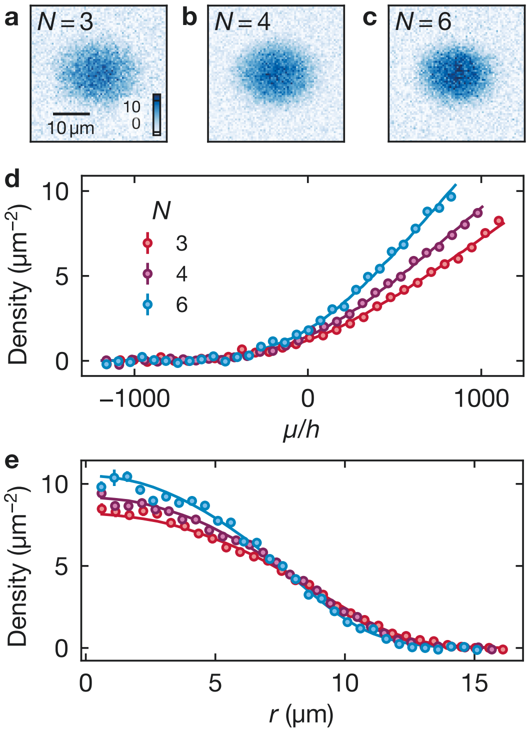

Figure 3.3 | Measurement of the EoS of an SU(N) Fermi gas in the 2D single plane without in-plane lattices. (**a-c**) 2D density profiles for $N = 3, 4$ and 6. Each profile is obtained by averaging over 3-5 experimental realizations after a postselection based on the total atom number and the value of T/T_F returned by the fit. The averaging was done after the alignment of the center of mass of the clouds. The color scale is the same for all the frames and it is in units of µm^{-2}. (**d**) EoS for the data shown in (**a-c**) against the chemical potential. (**e**) EoS as a function of the radius of the cloud. The measurement has been performed in the combined potential of the vertical lattice and the mDT. The trap frequencies are $(\omega_x, \omega_y) \simeq 2\pi \cdot (28.2, 36.2)\,\mathrm{Hz}$. The total atom number N_p and values of T/T_F and s/k_B returned by the fit are [1920(4), 0.19(1), 1.13(4)], [1923(7), 0.19(1), 1.16(3)] and [1927(12), 0.20(1), 1.20(4)] for $N = 3, 4$ and 6 respectively. Error bars are the standard error of the mean.

tilted evaporation and the loading in the 2D single plane, we perform a fit of the density profile based on the interacting model presented in Sec. 3.3 to determine the temperature. The results shown in Fig. 3.3 are obtained after a postselection of the data based on the total atom number and the value of T/T_F returned by the fit. We observe a good agreement between the data and the model. In Sec. 3.4.1, we discuss the fit model's choice and the residuals in more detail.

In Fig. 3.4, we show how the temperature of the gas changes as a function of the hold time. With this measurement, we can determine the heating rate in the 2D plane, which is important for verifying the adiabaticity condition when loading into the lattice discussed in Chap. 5. From the measurement, we can see that the heating rate has a minor effect on the entropy (increase $\lesssim 6\%$) for the lattice timescales ($\lesssim 250\,\mathrm{ms}$). For long holding times, the heating rate can be substantially larger. Nevertheless, we observe that it is largely independent of N.

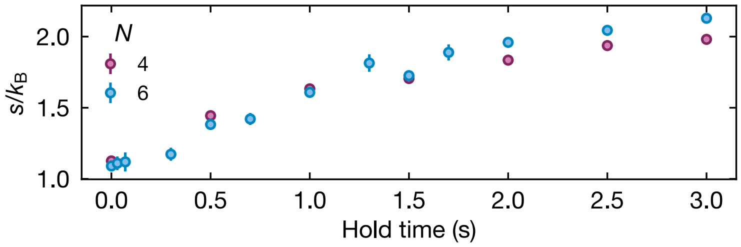

Figure 3.4 | Entropy per particle for $N = 4$ and 6 as a function of the hold time in the 2D plane before imaging. The trap configuration and frequencies are the same as those in Fig. 3.3. The entropy is calculated from the fit of the data to the weakly-interacting Fermi gas model. The average total atom number is $N_p = 2385(18)$. The error bars are the standard error of the mean.

3.4.1 Considerations on the fit method

In Sec. 3.3, we have seen that the weak interactions in our system add a non-negligible correction to the temperature and the entropy compared to the non-interacting case. In this section, we address the systematic errors we make when we fit a weakly-interacting Fermi gas with a non-interacting model.

Fitting experimental data with different models

In Fig. 3.5(a), we show the residuals of the weakly-interacting fit to the data shown in Fig. 3.3. The residuals look homogeneous for all values of N, indicating a good agreement between the data and the model.

In Fig. 3.5(b), we show the residuals of the fit of the same data with a non-interacting model. For $N = 3$, the residuals look homogeneous, but for $N = 4$ and 6, we observe the emergence of a spurious structure. Compared to the weakly-interacting fit, the results are also different: the temperature and entropy per particle returned by the fit of the non-interacting model are larger than the one returned by the weakly-interacting model. In particular, for $N = 3$, the difference is about 30 % for both the temperature and the entropy per particle. For $N = 6$, the discrepancy increases to about 75 % for the temperature and about 50 % for the entropy per particle.

Simulating the fit of a weakly-interacting Fermi gas with non-interacting models

In order to better characterize the discrepancies between the models presented in the previous section, we replicate the fits on synthetic data. We numerically generate a weakly-interacting cloud with $a_{2D} = 0.0025\,a_0$ and temperature T_{set} and fit it with non-interacting models. In Fig. 3.5(c), we show the ratio between the fitted temperature T_{fit} and T_{set} for three different implementations of a non-interacting model.

The first model (blue line) is the same as the one used in Fig. 3.5(b): we fit the temperature and the chemical potential at the center of the trap and assume the knowledge of the trap frequencies. In this case, we see a large discrepancy, which is also strongly dependent (and increases) with N.

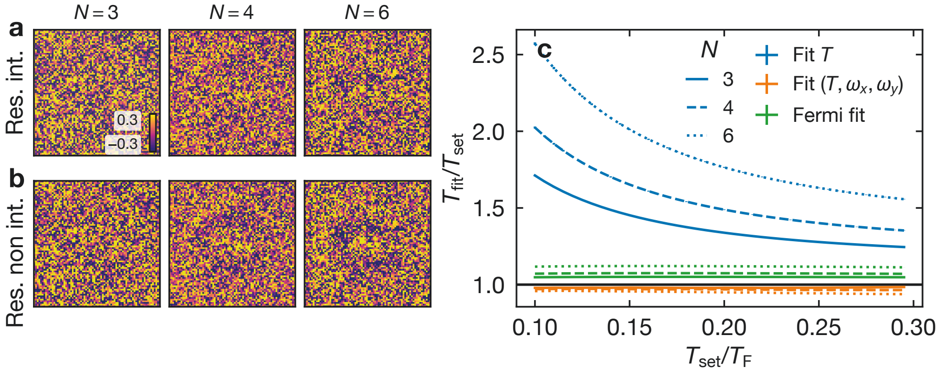

Figure 3.5 | Fitting a weakling-interacting SU(N) Fermi gas with different models. (**a**) Residuals in real space for the fit of the clouds shown in Fig. 3.3(a-c) with a weakly interacting model, corresponding to the continuous lines in Fig. 3.3(d-e). (**b**) Residuals of the fit of the clouds in Fig. 3.5(a-c) with a non-interacting model. For all fits of (**a**) and (**b**), the fit parameters are the temperature and the center of the cloud. (**c**) Fit of numerically-simulated weakly-interacting SU(N) clouds with different models. We generate clouds with different $T_{\rm set}$ and $a_{\rm 2D} = 0.0025\,a_0$ and fit them with three different implementations of a non-interacting model. We show the ratio between the fitted temperature $T_{\rm fit}$ and $T_{\rm set}$ for each fit. Blue: we fit the temperature and assume the knowledge of the trap frequencies. Orange: we fit both the temperature and the trap frequencies. Green: Fermi fit according to Eq. (3.13). We compare the simulations for $N = 3$ (continuous line), $N = 4$ (dashed line) and $N = 6$ (dotted line).

The second model (orange line) is similar to the first one, but we also fit the trap frequencies. In this case, we see that the fitted temperature is much closer to the set temperature, although the fitted frequencies are about 7 % to 10 % smaller than the set frequencies.

Finally, the third model (green line) is a Fermi fit according to the expression

$$n(x,y) = A\frac{\log\left[1+z\,\mathrm{gsn}(x,y)\right]}{\log\left(1+z\right)}+b, \tag{3.13}$$

where $\mathrm{gsn}(x,y)$ is a Gaussian function with free parameters center, width, and angle. A and b are also free parameters and z is the fugacity. From the fugacity, we directly obtain $T/T_{\rm F}$ [see Eq. (B.7)]. The trap frequencies relate to the cloud width and the normalization factor A. In this case, the fitted temperatures are close to the set temperature (about 5 % higher). However, the fitted trap frequencies are unmatched as in the previous case.

For the first two methods, we verify that fitting the chemical potential at the trap's center μ_0 or calculating it self-consistently from the fixed total atom number N_p does not significantly alter the results.

Systematic errors due to imaging imperfections

For the fit of the experimental data, we take into account the effect of the imaging imperfections of our system. In particular, we correct the theoretical model by convolving the 2D density profiles with the PSF (see Sec. 2.3.2). The systematic errors that we commit by not taking into account the PSF are small but not negligible in the deep degenerate limit. In Fig. 3.6, we show a simulation where we fit a weakly-interacting cloud after the

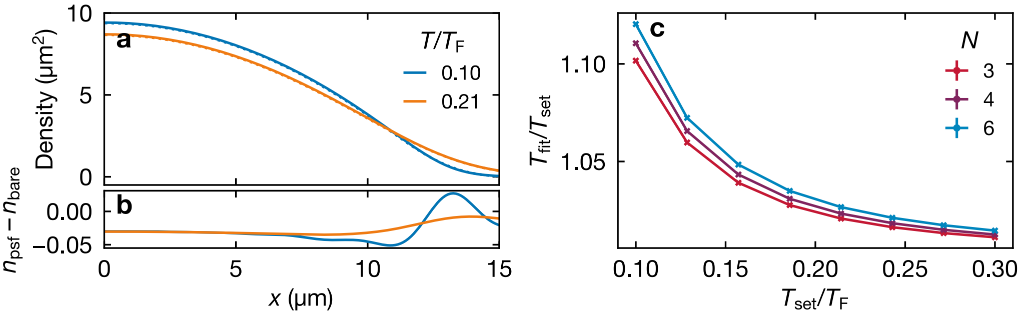

Figure 3.6 | Simulating the effect of the PSF on a weakly-interacting SU(N) Fermi gas. (**a**) Simulated density profiles with $N = 6$ and $T/T_F = 0.10$ (blue) and 0.21 (orange). Continuous lines: bare density profiles. Dashed lines (overlapping with continuous lines with the same color): convolution of the bare density profiles with the PSF. (**b**) residuals between the profiles shown in (**a**). (**c**) We generate weakly-interacting clouds with different T_{set}, convolve them with the PSF, and fit them with a weakly-interacting model to obtain T_{fit}. We show the ratio between T_{fit} and T_{set} for each fit.

convolution with the PSF. The temperature that we obtain can be up to 10 % higher than the initial temperature depending on the temperature itself and N. By taking the PSF into account for our modeling, we estimate the systematic errors on the temperature due to imaging imperfections to be less than 2 %.

3.5 Local density fluctuations and fluctuation-dissipation theorem

The ability to access the density in a 2D single atomic layer allows us to measure the local density fluctuations, which in the 3D case are not directly accessible§.

For a Fermi gas, we expect the anti-bunching effect due to the Pauli exclusion principle to suppress the density fluctuations compared to a classical gas which obeys Poissonian statistics. This can be seen as a consequence of the fluctuation-dissipation theorem (FDT) [302], which relates the fluctuations of a system to its response to an external perturbation.

The FDT can be derived in the grand canonical ensemble in local density approximation starting from the definition of the density operator in the second quantization formalism:

$$n(\boldsymbol{r},T,\mu) = \frac{\mathrm{Tr}\left[\hat{n}(\boldsymbol{r})e^{-\beta\left(\hat{H}-\mu\hat{N}_p\right)}\right]}{\mathrm{Tr}\left[e^{-\beta\left(\hat{H}-\mu\hat{N}_p\right)}\right]} \equiv \langle\hat{n}(\boldsymbol{r})\rangle, \tag{3.14}$$

which implies [302]

$$k_\mathrm{B}T\frac{\partial\langle\hat{n}(\boldsymbol{r})\rangle}{\partial\mu} = \int \mathrm{d}\boldsymbol{r}' \left[\langle\hat{n}(\boldsymbol{r})\hat{n}(\boldsymbol{r}')\rangle - \langle\hat{n}(\boldsymbol{r})\rangle\langle\hat{n}(\boldsymbol{r}')\rangle\right]. \tag{3.15}$$

The FDT can be applied to single-layer cold atoms experiments by measuring the average density $\tilde{n}$ and the density variance $\delta\tilde{n}^2$ in a probe region of the cloud across several

---

§Although a kinetic approach can be used [287].

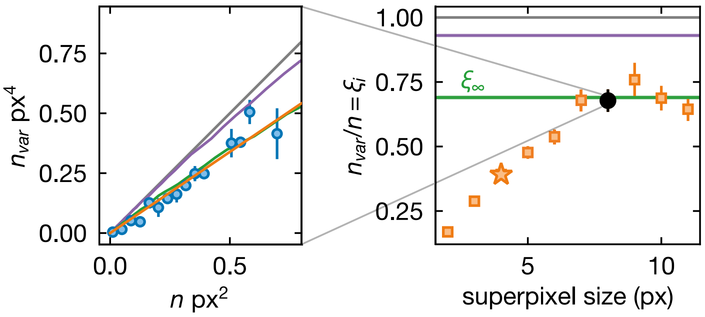

Figure 3.7 | Density fluctuations for a high-temperature Fermi gas (N = 6). **Left**: Density variance calculated for a probe area of $8 \times 8\,\mathrm{px}^2$ against the average density in the same area. Blue points: measured density variance after the subtraction of the photon shot noise. Grey line: classical limit $\delta\tilde{n}^2/\tilde{n} = 1$. Purple line: theoretical prediction estimated from the temperature returned by a non-interacting fit [$T/T_\mathrm{F} = 1.37(1)$]. Green line: theoretical prediction according to a weakly-interacting fit [$T/T_\mathrm{F} = 1.02(1)$]. Orange line: linear fit of the blue points. **Right**: Slope $\delta\tilde{n}^2/\tilde{n} = \xi_i$ returned by the fit as a function of the probe area. i is the size length in pixels of the square probe area. Star (i = 4): probe size used in Chap. 5.

identical experimental realizations. When the size of the probe region is large enough (thermodynamic limit), we recover the FDT in the form [303]

$$\frac{\delta\tilde{n}^2}{\tilde{n}} = \frac{k_\mathrm{B} T \kappa}{\langle\hat{n}\rangle}, \tag{3.16}$$

where $\kappa = \partial\langle\hat{n}\rangle/\partial\mu$ is the isothermal compressibility.

For an ideal classical gas, $\kappa = n/(k_\mathrm{B}T)$ [304]. Hence, the FDT predicts that the density fluctuations in the thermodynamic limit are given by

$$\frac{\delta\tilde{n}^2}{\tilde{n}} = \frac{k_\mathrm{B} T \kappa}{n} = 1, \tag{3.17}$$

indicating Poissonian statistics.

This is not the case for a Fermi gas, which is characterized by sub-Poissonian statistics. The compressibility and the density fluctuations are given by [see Eq. (B.16)]

$$\frac{(\delta\tilde{n})^2}{\tilde{n}} = \frac{k_\mathrm{B} T \kappa}{n} = \frac{k_\mathrm{B} T}{n}\rho\left[1 - e^{-\beta n/\rho}\right]. \tag{3.18}$$

For $(\beta n) \to 0$ the expression on the right becomes $1 + O(\beta n/N)$, which gives back the classical limit of Eq. (3.17). The correction to the unitary slope is negative for a Fermi gas. This anti-bunching, sub-Poissionian effect has been measured with ultracold atoms [305, 306], also in the SU(N) case in a 3D trap geometry [287].

From an experimental point of view, it is important to choose a probe region that is large enough to include the most important contributions to the correlations of Eq. (3.15). However, the probe region should also be small enough to sample the total density profile with enough points, ensure that the average density across it has a small standard deviation, and provide a good signal-to-noise ratio. The choice of a small probe region effectively

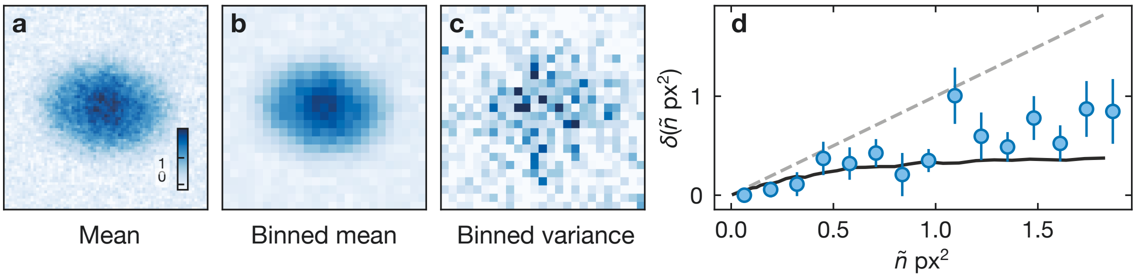

Figure 3.8 | Density fluctuations for a degenerate SU(6) Fermi gas in a 2D harmonic confinement. (**a**) Average density profile of the 10 frames used for the measurement after c.o.m. alignment. $N_p = 1523(37)$ and $T/T_\mathrm{F} = 0.21(1)$. (**b**) Average density [same as in (**a**)] binned in probe areas with size $3{\times}3\,\mathrm{px}^2$. (**c**) Density variance calculated for each probe area. The photon shot noise has been corrected and the value linearly scaled according to the method discussed in the text. (**d**) Density fluctuations plotted against average density values [same binning size of (**b**) and (**c**)]. Blue points: corrected experimental data. Black line: theoretical prediction from the EoS fit of the mean density profile. Dashed line: classical limit. The color bar is the same for (**a**)-(**c**) and it indicates the density in units of px^2.

decreases the measured variance with respect to the thermodynamic limit, but this effect can be characterized and corrected.

In our case, we calibrate this correction by measuring the density fluctuations of a cloud with $T/T_\mathrm{F} \gtrsim 1$. In this case, the density fluctuations are expected to be close to the classical temperature-independent limit of Eq. (3.17). We can calibrate the correction for different probe sizes by enforcing this equation. However, we also consider corrections due to the finite temperature and the weak interactions. In this case, for low densities, we still expect a linear relation between the variance and the average density but with a slope smaller than one. In particular, we fit a temperature $T/T_\mathrm{F} = 1.02(1)$ for the sample we use for the calibration. For this temperature and a weakly-interacting model, a numerical simulation of the FDT returns a slope $\delta\tilde{n}^2/\tilde{n} \equiv \xi_\infty = 0.69(1)$ for small densities. The binning to small probe areas introduces an additional correction $\xi_\infty \to \xi_i$. In the following, we will consider only square probe areas, and i indicates the side of the square in units of pixels. In Fig. 3.7, we show the measured slopes ξ_i for different probe sizes. Remarkably, we observe that the slope converges to ξ_∞ for $i \gtrsim 7$, which consistently confirms that the weakly-interacting theory we use to fit the data is valid in this regime. This calibration is also used for the measurements of the density fluctuations in the lattice described in Sec. 5.4.

Once we have calibrated the correction for the finite probe size, we can use the FDT to measure the density fluctuations of the degenerate Fermi gas. In Fig. 3.8, we show the measured density fluctuations for an SU(6) Fermi gas. We consider 10 post-selected frames with similar atom number and temperature. To obtain the blue data points in Fig. 3.8(c), we align their center of mass, bin the cloud with a probe size of $3 \times 3\,\mathrm{px}^2$, subtract the photon shot noise and correct for the finite probe size. If the FDT holds, the fluctuations should equal $\kappa k_\mathrm{B} T$ (black curve), as in Eq. (3.18). We obtain T from the fit of the EoS of the mean density profile and κ from a three-point numerical differentiation of the density with respect to the chemical potential. In Fig. 3.8, we can see a good agreement between the two sides of the FDT for low densities. At high densities, the small number of pixels sampling the cloud results in a much larger uncertainty on the density fluctuations. Nevertheless, we observe, as expected, a substantial deviation from the classical Poissonian statistics of Eq. (3.17) (dashed line).

CHAPTER 4

Thermodynamics of the 2D SU(*N*) Fermi-Hubbard model

In this chapter, we present a theoretical description of the thermodynamic properties of the SU(N) Fermi-Hubbard model. We introduce the model, its symmetries, and the observables of interest in Sec. 4.1. In Sec. 4.2, we review some simple limits of the model, namely the non-interacting and the atomic limits, which give us a first intuitive understanding of some of its properties. Away from these two limits, no analytical solution is known, and we resort to numerical methods such as high-temperature series expansion (HTSE), numerical linked-cluster expansion (NLCE), and determinant quantum Monte Carlo (DQMC). These methods are described in Sec. 4.3. The properties of the model according to the numerical simulations are discussed in Sec. 4.4, where we focus in particular on the observables and the cases that are relevant for the experiments presented in Chap. 5.

4.1 The SU(*N*) Fermi-Hubbard model

The SU(N) Fermi-Hubbard Hamiltonian is defined as

$$\hat{H} = -t \sum_{\langle i,j\rangle,\sigma} \left(\hat{c}^{\dagger}_{i\sigma} \hat{c}_{j\sigma} + \text{h.c.} \right) + \frac{U}{2} \sum_{i,\sigma\neq\tau} \hat{n}_{i\sigma} \hat{n}_{i\tau} - \sum_{i,\sigma} \mu_i \hat{n}_{i\sigma}, \tag{4.1}$$

where $\hat{c}^{\dagger}_{i\sigma}$ and $\hat{c}_{i\sigma}$ represent the fermionic creation and annihilation operators at site i with spin $\sigma \in \{1 \ldots N\}$, $\hat{n}_{i\sigma} = \hat{c}^{\dagger}_{i\sigma} \hat{c}_{i\sigma}$ is the number operator, $\langle i,j\rangle$ denotes next-neighbor lattice sites, t is the hopping amplitude, U is the on-site interaction strength and μ denotes the chemical potential.

Here, we restrict ourselves to the two-dimensional case of a square (bipartite) lattice, which is the system that we probe in our experiments in Chap. 5. For the same reason, we focus on the thermodynamic properties of the model and the observables that we can measure in our experiments. In particular, these include:

- The local density

$$n \equiv \langle \hat{n} \rangle = \frac{1}{N_s} \sum_{i,\sigma} \langle \hat{n}_{i\sigma} \rangle, \tag{4.2}$$

where N_s is the number of lattice sites.

- The components of the site-occupation distribution

  $$p_\alpha \equiv \langle \hat{p}_\alpha \rangle = \langle n = \alpha \rangle, \qquad \forall\, \alpha \in \{0 \dots N\}, \tag{4.3}$$

  which give the probability of finding a site with α particles and satisfy the normalization condition $n = \sum_\alpha \alpha p_\alpha$.

- The isothermal compressibility

  $$\kappa = \left.\frac{\partial \langle \hat{n} \rangle}{\partial \mu}\right|_T. \tag{4.4}$$

- The local density fluctuations*

  $$\mathrm{var}(\hat{n}) = \langle \hat{n}^2 \rangle - \langle \hat{n} \rangle^2, \tag{4.5}$$

  and in particular, their value in a probe area A, which can be related to the compressibility κ and temperature T of the system through the fluctuation-dissipation theorem (FDT, see Sec. 3.5):

  $$\mathrm{var}\left(\int_A n\, dA \right) = k_\mathrm{B} T A \kappa = k_\mathrm{B} T A \left.\frac{\partial n}{\partial \mu}\right|_T. \tag{4.6}$$

- The entropy per site and the entropy per particle, respectively

  $$s_0 = S/N_s, \qquad s = S/N_p, \tag{4.7}$$

  where S is the system's entropy, N_s is the number of lattice sites, and N_p is the total number of particles.

The components of the site-occupation distribution p_α for $\alpha = 1$ and 2 contain the information on the *singlons* and *doublons* in the system, respectively. Here, it is worth emphasizing that the extension of the definition of *doublons* from the SU(2) to the SU(N) case is not straightforward and might be ambiguous. In the SU(2) case, where the spin can be up or down, doublons are often defined as

$$\mathcal{D} = \frac{1}{N_s} \sum_i \langle \hat{n}_{i\uparrow} \hat{n}_{i\downarrow} \rangle. \tag{4.8}$$

This definition can be generalized to the SU(N) case as

$$\mathcal{D} = \frac{1}{N_s} \sum_i \left[\frac{1}{2} \sum_{\sigma \neq \tau} \langle \hat{n}_{i\sigma} \hat{n}_{i\tau} \rangle \right], \tag{4.9}$$

---

[*] This observable is not treated directly in this chapter, but in Chap. 5 together with the discussion of the experimental results.

indicating the number of on-site pairs per site. However, this expression differs from the number of doubly-occupied sites p_2[†]. From an experimental point of view, $2p_2$ is the most easily accessible quantity, and we will use it as the definition of the doublon density in the following.

4.1.1 Symmetries of the SU(*N*) FHM

The SU(N) FHM possesses some symmetries that allow us to focus on a smaller part of the parameter space and obtain the results for the whole model by simple transformations. In particular, we focus here on the SU(N) spin symmetry and the particle-hole symmetry.

The SU(*N*) symmetry refers to the fact that the spin permutation operators

$$\hat{S}^{\sigma}_{\tau} = \sum_i \hat{S}^{\sigma}_{\tau}(i) = \sum_i \hat{c}^{\dagger}_{i\sigma}\hat{c}_{i\tau} \tag{4.10}$$

satisfy the SU(N) algebra

$$[\hat{S}^{\sigma}_{\tau}, \hat{S}^{\xi}_{\rho}] = \delta_{\sigma\rho}\hat{S}^{\xi}_{\tau} - \delta_{\tau\xi}\hat{S}^{\sigma}_{\rho}, \tag{4.11}$$

and are the generators of the respective group ($\delta_{\alpha\beta}$ is the Kronecker delta). These operators commute with the Hamiltonian:

$$[\hat{S}^{\sigma}_{\tau}, \hat{H}] = 0 \qquad \forall\, \tau, \sigma \in \{1 \dots N\}, \tag{4.12}$$

and the spin isotropy of the system is, therefore, preserved. From Eq. (4.12) it follows that also $\hat{S}^{\sigma}_{\sigma} = \sum_i \hat{c}^{\dagger}_{i\sigma}\hat{c}_{i\sigma} = \hat{n}_{\sigma}$ commutes with the Hamiltonian. This means that if we prepare the system with a fixed number of particles per spin state, the number of particles per spin state will remain constant. Moreover, if we prepare a state populating $N' < N$ spin components, the system will remain in this subspace and obey an SU(N') symmetry.

The particle-hole symmetry relates the properties of the system below half-filling to the ones above half-filling. It can be seen by the particle-hole transformation (PHT), which exchanges the creation and annihilation operators:

$$\hat{d}^{\dagger}_{\ell\sigma} = (-1)^{\ell}\hat{c}_{\ell\sigma}. \tag{4.13}$$

It follows that for the new fermionic operators $\hat{d}^{\dagger}_{\ell\sigma}$ and $\hat{d}_{\ell\sigma}$ holds

$$\hat{d}^{\dagger}_{\ell\sigma}\hat{d}_{\ell\sigma} = 1 - \hat{c}^{\dagger}_{\ell\sigma}\hat{c}_{\ell\sigma}, \tag{4.14}$$

and, therefore, the corresponding density operator is

$$\hat{n}'_{\ell} \equiv \sum_{\sigma} \hat{d}^{\dagger}_{\ell\sigma}\hat{d}_{\ell\sigma} = N - \sum_{\sigma} \hat{c}^{\dagger}_{\ell\sigma}\hat{c}_{\ell\sigma} = N - \hat{n}_{\ell}. \tag{4.15}$$

[†] For $N > 2$, $\langle \hat{n}_{i\sigma}\hat{n}_{i\tau} \rangle$, which is naturally related to the total potential energy, is not enough to discriminate between the presence of doublons, triplons, etc. For example, an energy increase of $3U$ could be due to a triplon or to the existence of three doublons in the system. $\mathscr{D}$ indicates the number of on-site pairs (e.g. a triplon forms 3 pairs).

On the other hand, the hopping term in Eq. (4.1) remains unchanged:

$$\hat{c}^{\dagger}_{i\sigma}\hat{c}_{j\sigma} = (-1)^{i+j}\hat{d}^{\dagger}_{i\sigma}\hat{d}_{j\sigma} = \hat{d}^{\dagger}_{i\sigma}\hat{d}_{j\sigma}, \tag{4.16}$$

In the SU(N) case, we define half-filling as where the number of particles per site is $N/2$. The particle-hole symmetry becomes more evident if we write Eq. (4.1) as

$$\hat{H} = -t\sum_{\langle i,j\rangle,\sigma}\left(\hat{c}^{\dagger}_{i\sigma}\hat{c}_{j\sigma} + \text{h.c.}\right) + \sum_i\left[\frac{U}{2}\left(\hat{n}_i - \frac{N}{2}\right)^2 - \mu_i\hat{n}_i\right], \tag{4.17}$$

This is often referred to as the *particle-hole symmetric* (PHS) form of the Hamiltonian, and it is equivalent to Eq. (4.1) up to a shift in the chemical potential. As a consequence of the particle-hole symmetry, we can calculate the properties for $\mu < 0$ and obtain those for $\mu > 0$ with a simple transformation. In particular, we find that

$$n(\mu) = N - n(-\mu), \tag{4.18}$$

$$\kappa(\mu) = \kappa(-\mu), \tag{4.19}$$

$$s(\mu) = s(-\mu), \tag{4.20}$$

$$p_{\alpha}(\mu) = p_{N-\alpha}(-\mu). \tag{4.21}$$

The particle-hole symmetry breaks down for non-bipartite lattices or if we include next-nearest neighbor hopping terms [307].

4.2 Limits of the SU(N) Fermi-Hubbard model

This section reviews some fundamental limits of the SU(N) FHM. In Sec. 4.2.1, we consider the *atomic limit*, where $t = 0$. In Sec. 4.2.2, we consider the non-interacting limit with $U = 0$, which captures the metallic behavior of the model. These limits can be exactly solved and provide a useful starting point for discussing the numerical results in the following sections.

4.2.1 Atomic limit

In the case of strong interactions ($U \gg t$), the kinetic term can be, in first approximation, neglected ($t = 0$). This is the so-called *atomic limit* (AL). The Hamiltonian becomes

$$\hat{H}_{\text{al}} = \frac{U}{2}\sum_{i,\sigma\neq\tau}\hat{n}_{i\sigma}\hat{n}_{i\tau} - \mu\sum_{i\sigma}\hat{n}_{i\sigma}. \tag{4.22}$$

In this case, the system can be described as a set of independent (uncoupled) sites, and the grand canonical partition function becomes $\mathcal{Z} = z_0^{N_s}$, where N_s is the number of the lattice sites and z_0 the single-site partition function

$$z_0(\mu, T, U, N) = \sum_{n=0}^{N}\binom{N}{n}e^{-\beta\left[\frac{U}{2}n(n-1)-\mu n\right]}, \tag{4.23}$$

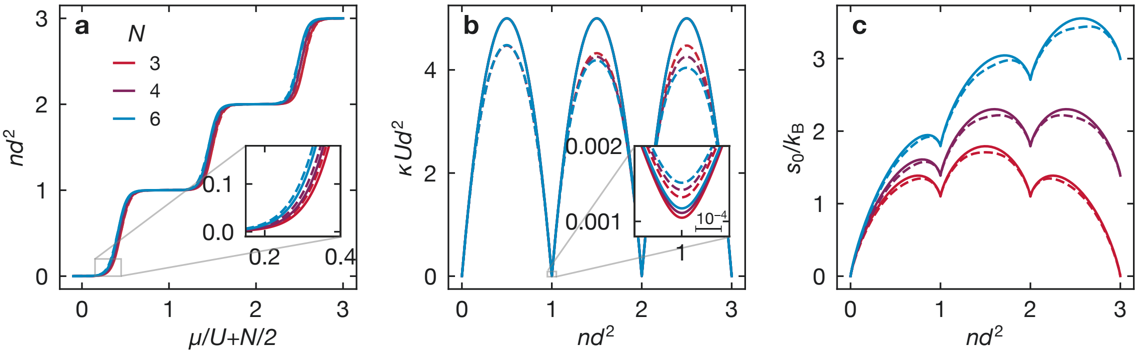

Figure 4.1 | Equation of state for the strongly-interacting SU(N) FHM. (**a**) Density per lattice site. (**b**) Compressibility per lattice site. (**c**) Entropy per lattice site. Continuous lines: atomic limit for $T/U = 0.05$ and $N = 3$ (red), 4 (purple), and 6 (blue). Dashed line: HTSE-2 correction for $T/t = 3$ (the same color corresponds to the same N). We define $\mu = 0$ at half filling ($nd^2 = N/2$). Positive chemical potentials can be obtained with a particle-hole transformation (see Sec. 4.1).

where we are considering all the permutations of $0 \leq n \leq N$ particles on the site. The grand potential is

$$\Omega_0(\mu, T, U, N) = -\frac{1}{\beta}\log\left[z_0(\mu, T, U, N)\right]. \tag{4.24}$$

From the partition function or the grand potential, it is possible to derive the most relevant thermodynamic quantities similarly to what we presented in Sec. 3.1 for the bulk. Their calculation and exact dependency on the natural variables are reported in Appendix C.1. Here, we will focus on a qualitative description of the most relevant ones.

The density $n = -\partial\Omega_0/\partial\mu$ [see Fig. 4.1(a)] distributes as a function of the chemical potential in insulating plateaus at integer values up to N (the so-called Mott shells [292, 308]). At zero temperature, the spectrum is gapped, and the density “jumps” between integer values when the chemical potential μ changes by U. Increasing the temperature, metallic phases emerge around the jump positions, and the density profile gets “smoother”. The isothermal compressibility $\kappa = \partial n/\partial\mu$ shows local minima at the plateaus [see Fig. 4.1(b)]. At zero temperature, these minima are zero. The entropy per site $s_0 = -\partial\Omega_0/\partial T$ also shows local minima at the plateaus, [see Fig. 4.1(c)]. In Fig. 4.1 we show the observables for $N = 3, 4$ and 6.

In addition to density, compressibility, and entropy, other important observables we can probe in our experiment are the components of the site-occupation distribution p_α (see Sec. 4.1.1). $\langle\hat{p}_1\rangle$, $\langle\hat{p}_2\rangle$ and $\langle\hat{p}_3\rangle$ represent the amount of singly, doubly, and triply occupied sites of the system, respectively. These observables represent additional coordinates of the equation of state and contain information on the number squeezing to a high atom density which is not directly accessible from the sole measurement of $\langle\hat{n}\rangle$. In Fig. 4.2, we show an example of their scaling as a function of the chemical potential and the temperature (see Appendix C.1 for the analytical expressions).

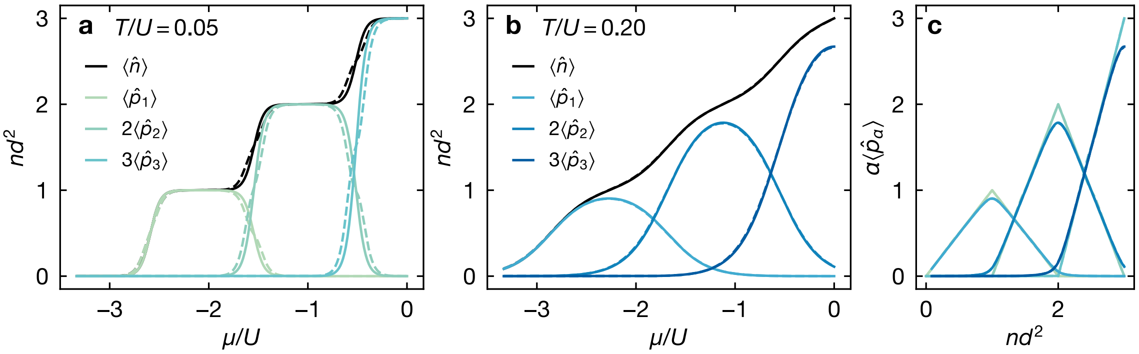

Figure 4.2 | Site-occupation distributions $\langle \hat{p}_\alpha \rangle$ for $N = 6$ and $\alpha = 1, 2, 3$. Continuous lines represent atomic limit; dashed lines are HTSE-2 corrections for $U/t = 30$. In (**a**) and (**b**) $\alpha\langle \hat{p}_\alpha \rangle$ are plotted as a function of the chemical potential for two temperatures, respectively. The black lines represent the total density $\langle \hat{n} \rangle = \sum_{\alpha=1}^{N} \alpha\langle \hat{p}_\alpha \rangle$. In (**c**), the curves of (**a**) and (**b**) are plotted against the total density. The color code is the same as in (**a**) and (**b**).

4.2.2 Non-interacting limit

In the non-interacting limit $U = 0$, the SU(N) FHM Hamiltonian becomes diagonal in momentum space:

$$\hat{H} = -t \sum_{\langle i,j\rangle,\sigma} \left(\hat{c}^\dagger_{i\sigma}\hat{c}_{j\sigma} + \text{h.c.}\right) - \mu \sum_{i\sigma} \hat{n}_{i\sigma} = \sum_{k,\sigma} (\epsilon_k - \mu)\hat{n}_{k\sigma}, \tag{4.25}$$

with $\hat{n}_{k,\sigma} = \hat{c}^\dagger_{k,\sigma}\hat{c}_{k,\sigma}$ and $\hat{c}_{r,\sigma} = (1/N_s)\sum_k e^{-ik\cdot\frac{r}{|r|}d}\hat{c}_{k\sigma}$. $\boldsymbol{k} = (k_x, k_y)$ is the wave vector, N_s is the number of lattice sites, d is the lattice spacing and ϵ_k is the dispersion relation

$$\epsilon_k = -2t\left[\cos(k_x d) + \cos(k_y d)\right]. \tag{4.26}$$

The analytical expression for some of the most relevant thermodynamic quantities in this limit is reported in Appendix C.4. In Fig. 4.3, we show the density as a function of the chemical potential and the compressibility and the entropy as a function of the density (continuous lines). In the same figure, we show the comparison with a non-interacting calculation in bulk (dotted lines). The parameters of this simulation match the same absolute temperature and volume of the in-lattice calculation for our specific lattice spacing and an arbitrary value of t/h, allowing for a qualitative comparison of the two models. In particular, we observe that the compressibility and the entropy per volume do not saturate at high density but show a maximum at half-filling, a consequence of the Pauli blocking and the particle-hole symmetry. The figure also shows a determinant Quantum Monte Carlo simulation for small U/t (dashed lines). Here we observe that the interactions strongly suppress the compressibility while the entropy per lattice site is only slightly affected.

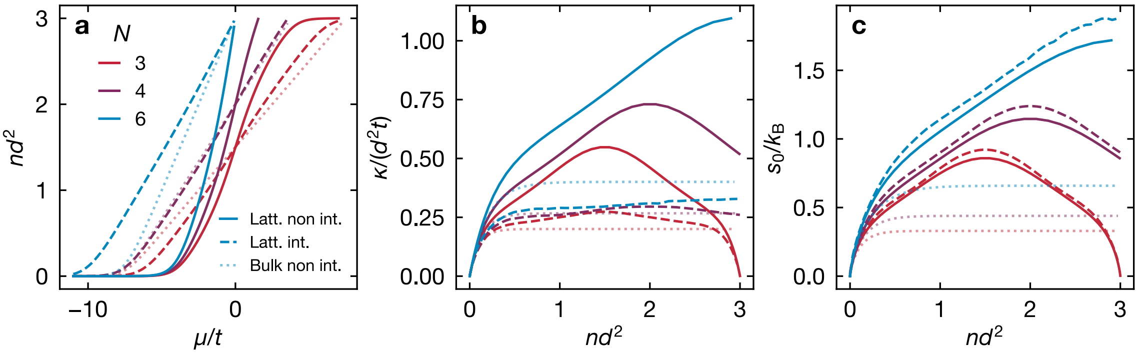

Figure 4.3 | Equation of state of the SU(N) FHM in the non-interacting limit for $N = 3$ (red), $N = 4$ (purple), and $N = 6$ (blue). (**a**) Density as a function of the chemical potential. The zero of the chemical potential is defined as half-filling. (**b**) Compressibility as a function of the density. (**c**) Entropy per lattice site as a function of the density. Continuous lines: non-interacting model for $T/t = 0.5$. Dashed lines: DQMC simulations (see Sec. 4.3.3) for $U/t = 2.34$ and $T/t = 0.5$. Dotted lines: non-interacting model in bulk (see Sec. 3.1) matching the same absolute temperature and volume for our specific lattice spacing $d \approx 380\,\mathrm{nm}$ and for $t/h = 170\,\mathrm{Hz}$. DQMC curves are reworkings of simulations courtesy of the Hazzard group at Rice University.

4.3 Methods to simulate the SU(N) FHM at intermediate interactions

Ideally, the complete description of the equation of state could be obtained straightforwardly with the exact diagonalization (ED) of the Hamiltonian of Eq. (4.1). This is, however, very difficult because of the exponential scaling of the size of the Hilbert space with the number of lattice sites N_s and the number of spin components N. A smart use of the symmetries of the system described in Sec. 4.1.1 and a truncation of the Hilbert space to the most relevant states helps to reduce the computational complexity, but only to a limited extent [309]. State-of-the-art ED algorithms can treat only few sites and spin components [309], which quickly reduce with N [50].

Alternative methods have been developed to study the properties of the model in specific regimes and under a certain set of assumptions and approximations. In this section, we focus on the methods we use in Chap. 5 to fit the experimentally measured equation of state. At the same time, we restrict our attention to the observables which we probe in our experiment.

In Sec. 4.3.1, we present the high-temperature series expansion (HTSE), which treats the kinetic energy as a perturbation to the atomic limit. In Sec. 4.3.2 and 4.3.3, we briefly describe numerical linked-cluster expansion (NLCE) and determinant quantum Monte Carlo (DQMC), respectively. Our theory collaborators use these methods to simulate the thermodynamic properties of the model for $N \geq 2$ and a wide range of interaction strengths and temperatures.

In addition to ED, HTSE, NLCE, and DQMC, several other numerical techniques can be used to probe the equation of state of the SU(2) FHM. A review and comparison of the results obtained with different methods can be found in Ref. [309]. Among these methods, dynamical mean field theory (DMFT) [310, 311] has been successfully applied to study the SU(N)-symmetric and the degenerate multiorbital extensions of the FHM in several regimes [41, 43–45, 47, 51, 312–316]. Furthermore, the density-matrix renormalization group (DMRG) [317, 318] has also been successfully extended to the SU(N) case [57, 319, 320].

4.3.1 High-temperature series expansion

In the strongly-interacting limit, instead of completely neglecting the kinetic energy as discussed in Sec. 4.2.1, we can treat it as a perturbation and perform a series expansion in powers of (βt). In particular, it is possible to calculate a leading correction to the grand potential [70, 321]:

$$\Omega = \Omega_0 + \Delta\Omega\{O[N,(\beta t)^2]\} + O(\beta t)^4. \tag{4.27}$$

The truncation at the second order is often called HTSE-2[‡]. The analytical expressions for $\Delta\Omega$ and the most relevant observables are reported in Appendix C.3. In Fig. 4.1 and 4.2, we show an example of how the kinetic term in HTSE-2 modifies the atomic limit. The main corrections affect the metallic regions, where the compressibility and the entropy per site decrease [see Fig. 4.1(b,c)]. At the plateaus, instead, the compressibility slightly increases [see inset of Fig. 4.1(b)].

HTSE-2 is very easy to compute and implement, but being a perturbative correction, it has a limited range of validity $T/t \gtrsim 1$. At lower temperatures, HTSE-2 is inaccurate and eventually diverges (see Fig. 4.5). In order to describe lower temperatures, the calculation of higher orders is required. This has been done for the $N = 2$ case up to $O\left[(\beta t)^{10}\right]$ [322–324]. An expansion up to the 4th order has been calculated for $N = 4$ on a honeycomb lattice [325]. For the generic N case, high-order terms have been calculated only near $nd^2 = 1$ and for the strongly-interacting limit $w = e^{-\beta U} \to \infty$ [326, 327]. These calculations evaluate the perturbation on small clusters of n sites and calculate the result in the thermodynamic limit by weighting the contribution of each cluster in a similar way to what NLCE does (see Sec. 4.3.2). Calculating high orders is rather cumbersome, and alternative numerical methods such as NLCE and DQMC, which we will describe in the following sections, are considered more convenient.

4.3.2 Numerical linked-cluster expansion

Numerical linked-cluster expansion (NLCE) [328, 329] works similarly to high-order HTSE. The general idea is to consider clusters of k sites, group them according to point-group or topological equivalence, evaluate the thermodynamic property of interest in the representative clusters, and take a weighted sum to describe the property in the full-size lattice.

More in detail, if $\mathscr{P}$ is the property that we want to evaluate on the lattice $\mathscr{L}$ with N_s lattice sites,

$$\mathscr{P}(\mathscr{L})/N_s = \sum_c L(c) \times \mathscr{W}_P(c), \tag{4.28}$$

[‡] The atomic limit is sometimes referred to as HTSE-0. Odd terms of the expansion do not contribute on bipartite lattices [322].

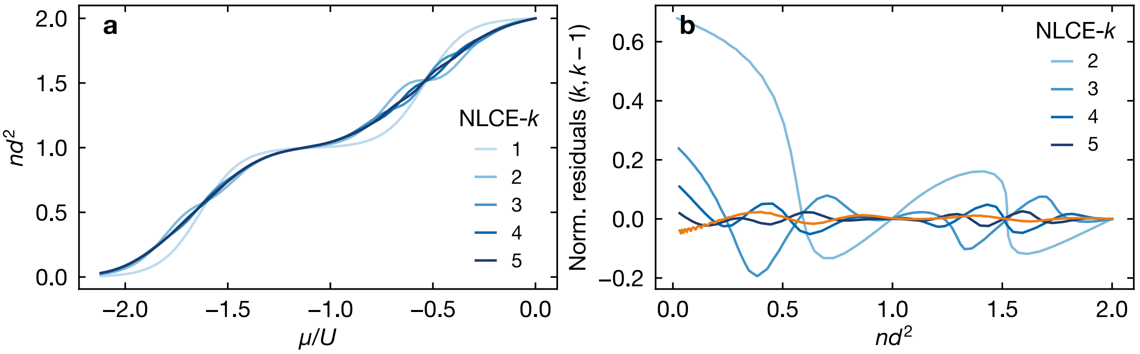

Figure 4.4 | Comparison of different NLCE orders for $N = 4$, $U/t = 10.38$ and $T/t = 1.0$. (**a**) Density as a function of the chemical potential. (**b**) Normalized residuals for the density between orders k and $k-1$. Orange line: normalized residuals between NLCE-2 and HTSE-2, showing that the two methods at this order are in good agreement. NLCE curves are reworkings of simulations courtesy of the Hazzard group at Rice University.

with

$$\mathscr{W}_P(c) = \mathscr{P}(c) - \sum_{s\subset c} \mathscr{W}_P(c), \tag{4.29}$$

$$\mathscr{P}(c) = \frac{\mathrm{Tr}\left[\hat{\mathscr{P}}(c)e^{-\beta \hat{H}_c}\right]}{\mathrm{Tr}\left[e^{-\beta \hat{H}_c}\right]}. \tag{4.30}$$

$\mathscr{P}(c)$ is the property evaluated in the cluster c, s is the sum running on all the subclusters of c and $\hat{H}_c$ is the Hamiltonian of c. The second term of Eq. (4.29) is necessary to ensure that $\mathscr{P}(c)$ is given by the sum of the weights of c and the weights of its subclusters. k (the number of sites) is also the NLCE order: if $k = 4$, for example, we talk about 4th order NLCE or NLCE-4.

The key feature distinguishing NLCE from high-order HTSE is the use of exact diagonalization instead of thermodynamic perturbation theory to evaluate Eq. (4.30). This means that the property of interest is calculated to all orders in (βt) and can be described at arbitrary small temperatures. The convergence temperature of NLCE is limited by the size of the longest cluster that can be probed, which determines the cut to the correlation range captured by the model. A nice feature of NLCE is the presence of a convergence control parameter: the simulation has converged if order k and order $k-1$ return the same result. This convergence criterion depends on the observable and the chemical potential. Empirically, we see that the density converges faster than the entropy and the site-occupation probabilities and that lower chemical potentials generally converge faster than higher ones. Furthermore, insulating phases converge faster than metallic ones because their wavefunctions are more localized.

In Fig. 4.4(a) we show a comparison of different NLCE orders for $N = 4$, $U/t = 10.38$ and $T/t = 1$. In Fig. 4.4(b), we show the normalized residuals between neighboring orders and a comparison with the HTSE-2 calculation with the same parameters. We point out that NLCE-1 is exactly equal to AL by definition. On the other hand, NLCE-2 usually agrees well with HTSE-2 but converges to lower T/t values [50].

The NLCE calculations presented in this chapter and the next one have been performed for fixed U/t and N on a dense $(\mu/t, T/t)$-grid by our theory collaborators in Kaden Hazzard's group at Rice University, in particular by Sohail Dasgupta and Eduardo Ibarra García Padilla. A detailed discussion of their implementation, which allowed the application of NLCE to $N > 2$ systems for the first time, can be found in Refs. [50, 87]. In order to fit the experimental data of Ref. [87] and Chap. 5, they calculated NLCE up to order 7 for $N = 3$, order 5 for $N = 4$ and order 4 for $N = 6$ for arbitrary chemical potentials, temperatures $T/t \gtrsim 0.5$ and a selected choice of U/t values.

4.3.3 Determinant quantum Monte Carlo

Determinant quantum Monte Carlo (DQMC) [330, 331] is one of the numerical techniques which have been most successful in the exploration of the EoS for the SU(2) FHM [17, 332, 333]. In this section, we will briefly summarize its working principle for the SU(2) case by taking inspiration from Ref. [334] and then hint at the generalization to the SU(N) case. A detailed discussion of the method and its limits, such as the famous sign-problem [60, 335, 336], falls outside the scope of this thesis.

The idea behind DQMC is to approximate the partition function with a Trotter-Suzuki decomposition by splitting the imaginary time $[0, \beta]$ into L subintervals of width $\Delta\tau = \beta/L$, such that

$$\mathcal{Z} = \mathrm{Tr}(e^{-\beta\hat{H}}) = \mathrm{Tr}\prod_{l=1}^{L} e^{-\Delta\tau\hat{H}} \simeq \mathrm{Tr}\left(\prod_{l=1}^{L} e^{-\Delta\tau\hat{H}_k} e^{-\Delta\tau\hat{H}_U}\right), \tag{4.31}$$

where $\hat{H}_k$ and $\hat{H}_U$ represent the kinetic and interaction terms of the SU(2) FHM, and the chemical potential has been set to zero for simplicity. The kinetic term $\hat{H}_k$ can be easily diagonalized (see Sec. 4.2.2). Instead, the interaction term $\hat{H}_U$ cannot be easily diagonalized in a single-particle eigenbasis. The approach used in DQMC is then to apply a discrete Hubbard-Stratonovich transformation [17] which replaces the quartic term in the creation/annihilation operators with a quadratic one. This is possible by adding auxiliary variables $\{h\}$ and increasing the dimensionality of the problem. After the transformation, the partition function assumes a computable form

$$\mathcal{Z}_h \propto \mathrm{Tr}_h \left\{\det\left[M_\uparrow(h)\right]\det\left[M_\downarrow(h)\right]\right\}. \tag{4.32}$$

By writing Eq. (4.32), we want to emphasize how the partition function can now be computed as a product of two determinants (we will not further discuss the exact form of the two fermionic matrices $M_{\uparrow,\downarrow}$). h is a matrix of entries ± 1 and size $2^{N_s L}$ and its configurations are sampled according to a classical Monte Carlo method (using a Metropolis-Hastings model [337] for example). The resulting probability distribution can be used as a Boltzmann weight to compute observables.

For the SU(N) case, the algorithm can be generalized by independently treating the

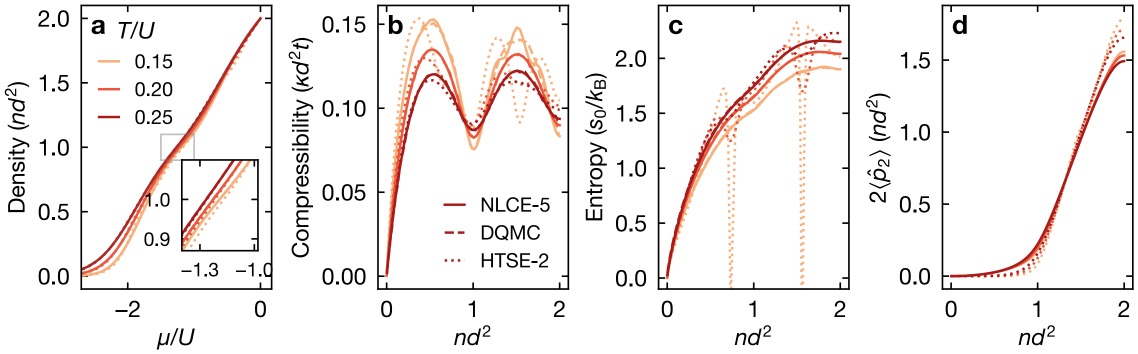

Figure 4.5 | Equation of state for $N = 4$ and $U/t = 7.43$ as a function of the temperature T/U (shades of red). (**a**) Density per site vs. chemical potential. (**b**) Compressibility vs. density. (**c**) Entropy per site vs. density. (**d**) Density of doubly-occupied sites vs. total density. The continuous line is an NLCE calculation; the dashed line, which most of the time overlaps with the continuous line, is a DQMC simulation, and the dotted line is the HTSE-2 approximation. NLCE and DQMC curves are reworkings of simulations courtesy of the Hazzard group at Rice University.

interaction terms for each pair of spin components and introducing $N(N-1)/2$ auxiliary fields[§]. Additional details about the method can be found in Refs. [50, 75, 87, 340].

The DQMC simulations shown in this chapter and the next one have been performed by our theory collaborators in Kaden Hazzard's group at Rice University and Richard Scalettar's group at UC Davis, and in particular by Eduardo Ibarra García Padilla. Their implementation allows for simulation on a dense (μ, T)-grid, arbitrary U/t, $N \geq 2$, and temperatures a fraction of the hopping energy.

4.4 Thermodynamics of the SU(N) FHM at intermediate temperatures and interactions

In Sec. 4.2.1 and 4.2.2, we have discussed the EoS in the limits $t = 0$ and $U = 0$, respectively. In this section, we focus on the intermediate regime, where no analytical model is available, and we resort to the HTSE, NLCE, and DQMC methods and calculations presented in Sec. 4.3.

In Fig. 4.5, we show some of the most experimentally relevant observables for $N = 4$ and $U/t = 7.43$ as a function of the temperature. This interaction strength is near the critical point for the phase transition between metal and Mott insulator [44]. The Mott plateaus in the density cannot be clearly identified at these temperatures. The compressibility shows minima at integer densities less pronounced than in the strongly-interacting case. The contrast with the metallic regions decreases as a function of the temperature. Compared to the strongly-interacting case, the local minima of the entropy can hardly be seen. In

---

[§] For $N > 2$, the choice of decoupling is not unique. One possibility consists in introducing $N(N-1)/2$ real auxiliary Hubbard Stratonovich fields; another one is using one complex auxiliary field. Although the latter one is free of the sign problem at half-filling for even N [40, 42, 53, 338], it hasn't been explored for odd values of N [339].

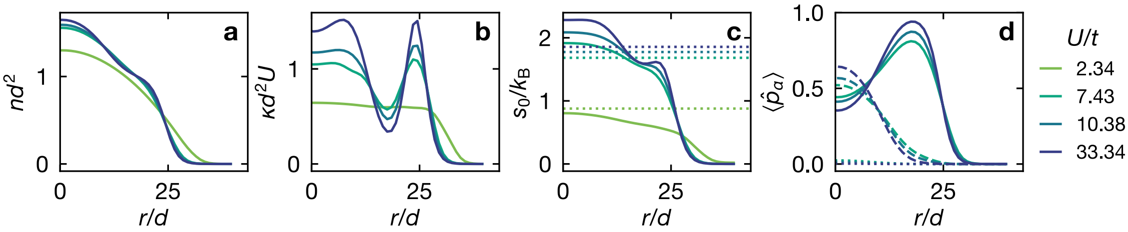

Figure 4.6 | Spatial radial profiles for (**a**) the density, (**b**) the compressibility, (**c**) the entropy per lattice site and (**d**) the occupation probabilities (continuous line: $\langle \hat{p}_1 \rangle$, dashed line: $\langle \hat{p}_2 \rangle$, dotted line: $\langle \hat{p}_3 \rangle$). The profiles have been calculated for a cloud of fixed atom number $N_p = 2 \times 10^3$ in a harmonic trap with $\kappa_x d^2/U = \kappa_y d^2/U = 0.0045$ in local density approximation for $N = 4$ and fixed temperature $T/U = 0.15$. The dotted lines in (**c**) represent the average entropy per particle $s = \left(\sum_i s_{0,i}\right)/\left(\sum_i n_i\right)$, with i running on the lattice sites. Curves are reworkings of DQMC ($U/t = 2.34$) and NLCE (other U/t values) simulations courtesy of the Hazzard group at Rice University.

this regime, the EoS has been calculated with NLCE (continuous line) and DQMC (dashed line), showing excellent agreement. The only visible discrepancy is in the compressibility for $T/U = 0.15$ and $nd^2 \simeq 1.5$, where NLCE has not fully converged. HTSE-2 instead (dotted line) shows some discrepancy at low temperatures in the density, presents unphysical wiggles in the compressibility at half-integer densities, and diverges in the entropy. Some deviations from NLCE can also be seen in the doubly-occupied fraction.

The convergence range of each method varies as a function of $N, \mu/t, U/t$, and T/U and needs to be estimated case by case. In general, we observe that NLCE and DQMC are rather complementary techniques. We expect DQMC to perform better for smaller U/t and NLCE for larger U/t, with a good overlap between $U/t \sim 7$ and 12[¶].

4.4.1 Local density approximation

Up to now, we have considered the equation of state in a grand canonical ensemble with natural variables (T, μ, U, N). The EoS-dependence on the chemical potential is significant for the experimental realization described in Chap. 5. There, we implement the SU(N) FHM with an additional harmonic confinement V, such that

$$H = -t \sum_{\langle i,j \rangle, \sigma} \left(\hat{c}^\dagger_{i\sigma} \hat{c}_{j\sigma} + \text{h.c.} \right) + \frac{U}{2} \sum_{i, \sigma \neq \tau} \hat{n}_{i\sigma} \hat{n}_{i\tau} + \sum_{i,\sigma} V_i \hat{n}_{i\sigma}. \tag{4.33}$$

In local density approximation (LDA), the harmonic confinement term can be reabsorbed in the chemical potential term, which becomes spatially dependent:

$$\mu(x,y) = \mu_0 - V(x,y) = \mu_0 - \frac{1}{2}\left(\kappa_x x^2 + \kappa_y y^2 \right), \tag{4.34}$$

where μ_0 is the chemical potential at the center of the trap, κ_x and κ_y are the parame-

---

[¶] On the one hand, DQMC is less prone to Trotter errors (proportional to $U\Delta\tau^2$) and non-ergodicity issues at small U/t. On the other hand, NLCE is more performant at large U/t because the system is more localized and the finite-size errors are smaller [339].

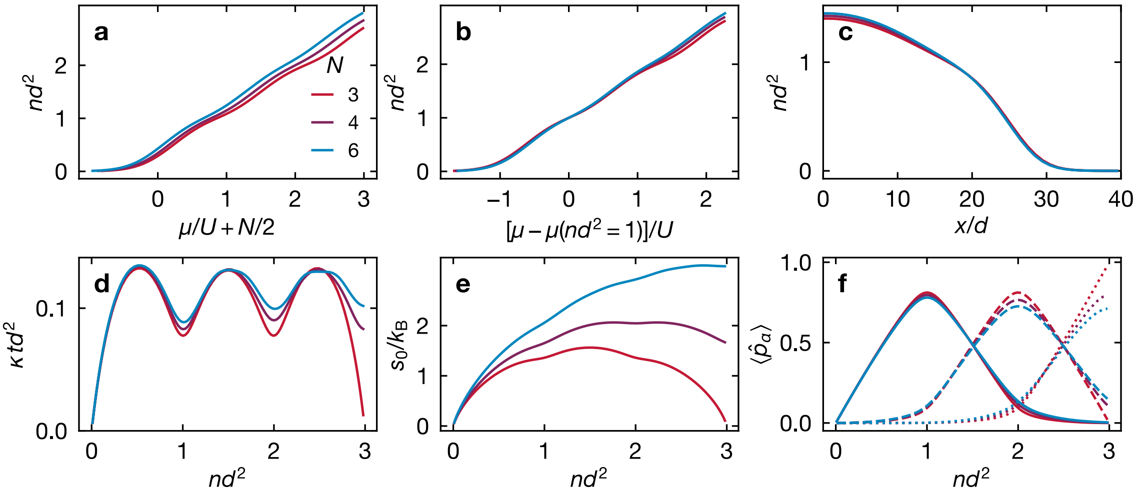

Figure 4.7 | N-dependency of the equation of state for fixed $U/t = 7.43$, $T/t = 1.5$, and $N = 3$ (red), 4 (purple), and 6 (blue). (**a**) Density after a shift of the chemical potential of $U \cdot N/2$. (**b**) Density after setting the zero of the chemical potential at the plateau $nd^2 = 1$. (**c**) Density profiles in local density approximation for $N_p = 2 \times 10^3$ and $\kappa_x d^2/t = \kappa_y d^2/t = 0.03$. (**d**) Compressibility. (**e**) Entropy per lattice site. (**f**) Occupation probabilities (continuous line: $\langle \hat{p}_1 \rangle$, dashed line: $\langle \hat{p}_2 \rangle$, dotted line: $\langle \hat{p}_3 \rangle$). Curves are reworkings of NLCE simulations courtesy of the Hazzard group at Rice University.

ters of the harmonic trap, and we have moved from the discrete set of indices $\{i\}$ to the continuous variables (x, y).

The trap shape plays an important role in the experiment. From the knowledge of the trap and the total atom number N_p, we can calculate the chemical potential at the trap's center μ_0 and simulate the cloud's shape in the experiment. In Fig. 4.6, we simulate a cloud with fixed atom number and temperature in a harmonic trap similar to the one used for the experiments described in Chap. 5. As the chemical potential varies as a function of the radius, we probe the entire equation of state for $\mu < \mu_0$. We can clearly identify the Mott plateaus and the (in)compressible regimes in real space for strong interactions.

The LDA is a powerful tool to probe the EoS across different phases. It is accurate when the energy spacing of V is much smaller than the other characteristic energies of the system. In the case of the experiments presented in Chap. 5, $\kappa_x d^2, \kappa_y d^2 \leq 0.15t, 0.006U, 0.07T$ and we can therefore safely apply LDA.

4.4.2 The dependence on *N* and the Pomeranchuk effect

The study of the N-dependency of the EoS shines some light on Pauli blocking and how the thermodynamic properties of the system are affected by it. If we consider intermediate temperatures and fixed (T, U, N_p), a shift of $N/2$ in the chemical potential causes a collapse of the density profiles $n(\mu, N)$ on top of each other, with only minor discrepancies [see Fig. 4.7(a)]. In particular, the Mott region becomes less sharp with increasing N. These discrepancies come from the fact that the particle-hole symmetry holds with respect to half-filling $(N/2)$. In real space [see Fig. 4.7(c)], we observe a similar situation, and the shape of the clouds shows minimal deviations as a function of N to each other. These

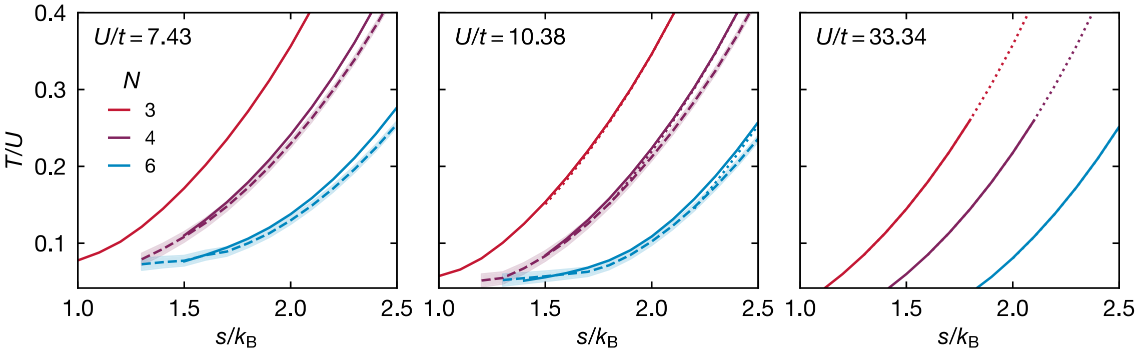

Figure 4.8 | Pomeranchuk effect for the SU(N) FHM. Relation between the average entropy per particle s and the temperature T in the lattice for different N and U/t ratios. Continuous line: NLCE. Dashed line: DQMC. Dotted line: HTSE. Shadowed area: estimated DQMC uncertainty. The relation has been calculated for a cloud with $N_p = 2 \times 10^3$ in a harmonic potential with the $\kappa_{x,y}$ coefficients reported in Tab. 5.1. NLCE and DQMC curves are derived from simulations courtesy of the Hazzard group at Rice University.

discrepancies are nevertheless intriguing because they allow, in principle, to access the system's statistics from a macroscopic observable such as the density. The differences are more pronounced in the compressibility [see Fig. 4.7(d)]. Although it is comparable for all values of N in the metallic phase, it significantly increases with N in the Mott regions. This is expected since the density fluctuations also increase with N. The entropy per lattice site [see Fig. 4.7(e)] encodes the information of the internal degree of freedom and shows, therefore, a significant N-dependency. Finally, we also observe that the lower occupation probabilities $\langle \hat{p}_\alpha \rangle$ become smaller for larger N because of the increasing suppression of Pauli blocking and the possibility of having more atoms per lattice site [see Fig. 4.7(f)].

More dramatic is the contrast between systems with different N and fixed (s, U, N_p). This comparison can be experimentally probed by preparing SU(N) mixtures with the same T/T_F (equivalent to the same entropy per particle s in the non-interacting regime, see Sec. 3.1) in the dipole trap. This scheme will be used and discussed in more detail in Chap. 5.

For fixed temperature, we have just seen that the entropy per particle is higher for larger N because additional entropy is stored in the spin degree of freedom. Conversely, this implies that the temperature must be lower for larger N at fixed entropy. This phenomenon is called *Pomeranchuk effect* because it presents analogies with the pioneering proposal of similar behavior in ^{3}He presented by Isaak Pomeranchuk in 1950 [341] and later demonstrated by Anufriev in 1965 [342, 343]. In ^{3}He, it is, in fact, possible to cool down a sample in the liquid phase to the solid phase with an adiabatic transformation [343–345]. Similarly, in our experiment, we "cool" down a cloud of ultracold atoms with large N when we adiabatically load it into the lattice and compare the result with a system with a smaller N [70, 73, 346].

In Fig. 4.8, we show a numerical simulation emphasizing the Pomeranchuk effect for our typical experimental parameters. For a fixed average entropy per particle, there is a clear hierarchy of temperatures as a function of N. However, we also observe a reduction of the “cooling” effect for low entropies. This reduction happens when approaching the superexchange energy $J \simeq 4t^2/U$ and it has been reported first in Ref. [50] (looking at this relation for a fixed chemical potential instead of total atom number). At lower temperatures, it seems possible that the curves for different N and the same entropy collapse on top of each other [50].

CHAPTER 5

Measurement of the Equation of State of the 2D SU(*N*) Fermi-Hubbard model

This chapter presents the experimental measurements of the equation of state (EoS) of the two-dimensional SU(N) Fermi-Hubbard model (FHM) in a square lattice. We realize this system starting from an SU(N) mixture of ^{173}Yb atoms in a single 2D plane as described in Chaps. 2 and 3 and ramping up two orthogonal in-plane lattices. First, we describe in Sec. 5.1 the optical lattice setup and the loading scheme. In Sec. 5.2, we illustrate the photoassociation scheme that allows us to probe the components of the site-occupation distribution. Then, in Sec. 5.3, we present our measurement of the EoS and discuss its agreement with the numerical simulations presented in Chap. 4. We characterize the EoS as functions of the chemical potential, the interaction strength, the temperature, the entropy, and the number of spin components. In Sec. 5.4, we show our measurement of the density fluctuations and use the fluctuation-dissipation theorem to determine the temperature with a theory-free model and verify its consistency with the temperature obtained from the fit of the EoS. Finally, in Sec. 5.5, we present some more technical details about the calibration and characterization of the systematic effects in our measurements.

The central results of this chapter have been submitted for publication and can be found in Ref. [87].

5.1 Lattice loading and Hubbard parameters

In our experiment, we perform a quantum simulation of the SU(N) FHM (see Chap. 4) by mapping the atoms in the Zeeman states of the ground state manifold of ^{173}Yb to the spin states of the Hubbard model. The Hamiltonian of the system, already introduced in Eq. (4.1), is given by

$$\hat{H} = -t \sum_{\langle i,j \rangle,\sigma} \left(\hat{c}^{\dagger}_{i\sigma} \hat{c}_{j\sigma} + \text{h.c.} \right) + \frac{U}{2} \sum_{i,\sigma \neq \tau} \hat{n}_{i\sigma} \hat{n}_{i\tau} - \sum_{i,\sigma} \mu_i \hat{n}_{i\sigma}. \tag{5.1}$$

The atoms are all contained in the central plane of a deep vertical lattice (vLAT, see Chap. 2), which provides the confinement along the z-direction and ensures a quasi-2D geometry (see

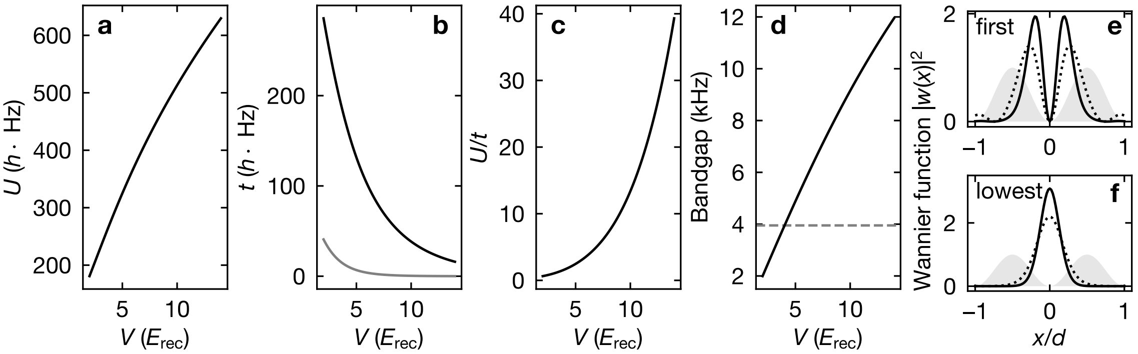

Figure 5.1 | Hubbard parameters for a homogeneous lattice potential as a function of the lattice depth V. (**a**) On-site interaction U calculated from the Wannier overlap. We also consider the contribution of a vertical lattice with a bandgap of 3.95 kHz. (**b**) Hopping energy t. The black line indicates the tunneling between nearest-neighboring sites, and the grey line indicates the next-nearest-neighbor hopping. (**c**) On-site interaction ratio U/t. (**d**) Bandgap between the first excited and the lowest bands. The dashed line corresponds to the bandgap of the vertical lattice. (**e**) and (**f**) Wannier overlap $|w(x)|^2$ for the first excited and the lowest bands, respectively, for $V = 12\,E_{\rm rec}$ (continuous line) and $V = 4\,E_{\rm rec}$ (dotted line).

Chap. 3). Two orthogonal lattices along the x- and y-axes generate the in-plane lattice potential. These lattices originate from retro-reflected Gaussian beams, and the potential in the (x, y) plane is given by

$$V(x,y) \simeq V_x \cos^2(kx) + V_y \cos^2(ky) + \frac{1}{2}\left(\kappa_{x,\rm lat}x^2 + \kappa_{y,\rm lat}y^2\right) + O(x^4, y^4), \qquad (5.2)$$

where $V_{x,y}$ are proportional to the intensity of the beams, $k = 2\pi/\lambda$ is the wavevector of the lattice light with magic wavelength $\lambda \simeq 760\,\rm nm$ and $\kappa_{x,y,\rm lat}$ are the coefficients of the harmonic confinement. They are related to the trap frequencies $\omega_{x,y,\rm lat}$ by $\kappa_{x,y,\rm lat} = m\omega^2_{x,y,\rm lat}d^2$, where m is the atomic mass and $d = \lambda/2$ is the lattice spacing. In addition to the in-plane lattices, the vertical lattice vLAT, and the magic dipole trap mDT (see Chap. 2) provide additional in-plane confinement, such that the coefficients of the combined harmonic confinement are given by

$$\kappa_i = \kappa_{i,\rm lat} + \kappa_{i,\rm vLAT} + \kappa_{i,\rm mDT}, \qquad i \in \{x, y\}. \qquad (5.3)$$

The Hubbard parameters t and U can be calculated according to Eqs. (1.6) and (1.7), respectively. In practice, this is done by numerically solving the band structure. In Fig. 5.1(a-c), we show the numerically calculated values of t and U and their ratio as a function of the lattice depth. The chemical potential of Eq. (5.1) absorbs instead the in-plane harmonic confinement in local density approximation (LDA) as described in Sec. 4.4.1.

The ratio U/t, which is a measure of the interaction strength, can be therefore tuned by changing the intensity of the beams that generate the in-plane lattices. By doing so, the system can be driven from the weakly interacting regime to the strongly interacting regime through the metal-insulator transition. Furthermore, because of the harmonic confinement, points at a different distance from the center of the cloud correspond to different

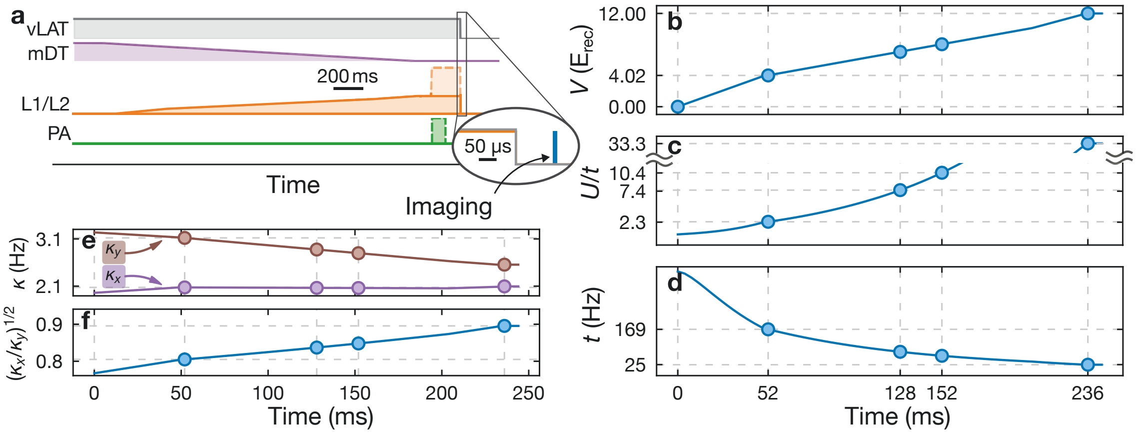

Figure 5.2 | Loading sequence from the 2D bulk to the square lattice with $U/t = 33(2)$. (**a**) Power (in arbitrary units) of the most relevant beams: vertical lattice (vLAT), dipole trap (mDT), in-plane lattices (L1/L2), photoassociation beam (PA). Dashed lines: values toggled for photoassociation measurements (see Sec. 5.2). (**b**), (**c**), (**d**) Time dependency of the lattice depth V and the Hubbard parameters U and t during the loading to $U/t = 33(2)$. (**e**), (**f**) Time dependency of the harmonic confinement parameters and the cloud aspect ratio.

chemical potentials, allowing us to explore a vast portion of the EoS of the system in a single realization.

When loading the atoms into the lattice, the tuning of U/t should be adiabatic, such that the system remains in the ground state of the Hamiltonian. This means the ramp speed must be slow enough to avoid heating. In Fig. 5.1(d), we show the bandgap between the first excited band and the lowest band as a function of the lattice depth, which sets the timescale for avoiding excitations to higher bands. Furthermore, the in-plane confinement and aspect ratio of the cloud should also stay as constant as possible during the tuning of U/t to avoid a nonadiabatic suppression of the mass flow [73].

In Fig. 5.2, we show the time evolution of the Hubbard parameters in our experiment over time as we switch on the lattices and tune the interaction strength to the strongly interacting regime $U/t = 33(2)$. We start in the 2D bulk in the central plane generated by the vertical lattice (vLAT) with additional confinement provided by the magic dipole trap (mDT). Then, we ramp up the two orthogonal in-plane lattices simultaneously and to the same depth. We implement three linear ramps with different slopes, such that the slope near the metal-insulator transition is smaller. During the ramps, we lower the mDT power to zero to balance the lattice-induced increase in the harmonic confinement and keep the aspect ratio as constant as possible. After we reach the desired depth, we switch off all the lattices to avoid light-assisted collisions and to perform in-situ imaging. In Tab. 5.1, we report the relevant Hubbard and confinement parameters for the other U/t ratios we will consider in the following. When ramping to a different U/t ratio, we tune the lattice depth by following the same curves of Fig. 5.2 up to the desired point. The mDT power, instead, is always ramped down to zero (with a different speed).

U/t	$V\ (E_{\mathrm{rec}})$	U/h (Hz)	t/h (Hz)	$\kappa_x d^2/t\,(10^{-3})$	$\kappa_y d^2/t\,(10^{-3})$
2.3(1)	4.0(1)	398(6)	170(4)	10(1)	13(1)
7.5(4)	7.1(1)	582(9)	78(3)	26(1)	35(1)
10.4(6)	8.0(2)	634(9)	61(2)	38(1)	50(1)
33(2)	12.0(2)	816(11)	25(1)	135(1)	174(1)

Table 5.1 | Hubbard and confinement parameters for our system after loading the atoms into the square lattice. V is the lattice depth along one direction (both lattices have the same depth). For $U/t = 2.3(1)$, the next-nearest-neighbor hopping is 12 Hz.

5.2 Parity-projected density

The typical observable that we can access in our experiment is the total density $n = \langle \hat{n} \rangle$. Another observable that we can measure is the parity-projected density, which we define in this section. The parity-projected density is an observable related to the components of the site-occupation distribution described in Chap. 4. In particular, it is defined as

$$\langle \hat{n}_{\mathrm{PR}} \rangle = \sum_{\alpha=1}^{N} (\alpha \bmod 2) \langle \hat{p}_\alpha \rangle, \tag{5.4}$$

where p_α is the probability of having α particles on a given site*. At low density, the parity-projected density consists of the removal of doublons, and it is, therefore, a measurement of the number of singlons in the system. At higher density, it also contains the contribution of triplons and higher-order site-occupation components.

This observable is measured after the application of a photoassociation technique. We use a photoassociation beam working on the ${}^1\mathrm{S}_0 \rightarrow {}^3\mathrm{P}_1$ transition, resonant with a molecular transition detuned by $-599.28(8)$ MHz with respect to the single-particle transition with a bias magnetic field of 1 G. The beam is coplanar with the lattices (see Fig. 1.5) and has a power of 30 mW. The sequences for measuring the pair-removal and the total density are very similar. The sequences are the same up to the point where we ramp the lattice to the desired U/t value. Then, before switching off the lattices and performing in-situ imaging, we quench the lattice to $30\,E_{\mathrm{rec}}$ to suppress the motion of the atoms and apply the photoassociation pulse (see dashed lines in Fig. 5.2).

The typical duration of the photoassociation pulse is 10 ms. In this way, we remove most of the doublons in the system. However, some doublons remain after the finite duration of the photoassociation pulse, and some singlons are removed due to experimental imperfections. Eq. (5.4) needs, therefore, to be corrected to

$$\langle \hat{n}_{\mathrm{PR}}^{\mathrm{eff}} \rangle \simeq e^{-\gamma_s t} \left[\sum_\alpha (\alpha \bmod 2) \langle \hat{p}_\alpha \rangle + e^{-\gamma_d t} \left(\sum_\alpha 2 \lfloor \alpha/2 \rfloor \langle \hat{p}_\alpha \rangle \right) \right], \tag{5.5}$$

where $\lfloor \cdot \rfloor$ represents the floor function and γ_s and $\gamma_s + \gamma_d$ represent the decay rate of the singlons and the doublons, respectively. Here, we neglect the fast decay of the states with more than two particles per site. For $\gamma_s, \gamma_d \rightarrow 0$ we recover $\langle \hat{n}_{\mathrm{PR}}^{\mathrm{eff}} \rangle \rightarrow \langle \hat{n}_{\mathrm{PR}} \rangle$. In the following,

---

[*] $\alpha \langle \hat{p}_\alpha \rangle$ is the number of particles and $\langle \hat{n} \rangle = \sum_{\alpha=0}^{N} \alpha \langle \hat{p}_\alpha \rangle$, see also Sec. 4.1.

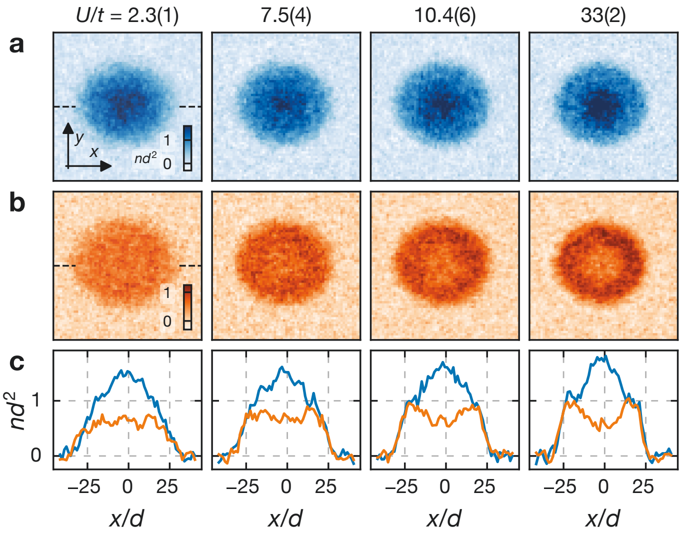

Figure 5.3 | Probing the EoS of the FHM for $N = 6$. (**a**) In-situ absorption images of the density $\langle \hat{n}(x,y) \rangle$ in a single layer 2D square lattice with harmonic confinement. Each horizontal frame has been prepared with the same initial entropy in the 2D bulk and loaded into the lattice to a different U/t ratio. (**b**) Singly-occupied sites $\langle \hat{n}^{\mathrm{eff}}_{\mathrm{PR}}(x,y) \rangle$ measured with the parity-projection method (see Sec. 5.2). Each horizontal frame corresponds to the same state shown in the same column of (**a**). (**c**) Density profiles for the data shown in (**a**) and (**b**) along the dashed lines in the first column. Each image is averaging eight realizations after total atom number postselection and c.o.m. alignment.

whenever it is not specified, we plot the experimental data and use the calibration of γ_s and γ_d to adapt the theoretical prediction for $\langle \hat{n}^{\mathrm{eff}}_{\mathrm{PR}} \rangle$ to the experimental values.

When comparing the measurement of the total density with the pair removal taken under the same conditions, we assume that we can neglect the tunneling during the quench of the lattice depth. The calibration of γ_s and γ_d is discussed in Sec. 5.5.5.

5.3 Measurement and fit of the SU(*N*) equation of state

In Fig. 5.3(a), we show a spatially resolved measurement of the density for $N = 6$ and different U/t ratios. Each frame is characterized by the same total atom number and entropy per particle before switching on the in-plane lattices. For increasing interaction strengths, we can clearly identify the formation of a plateau at density $nd^2 \simeq 1$, which signals the emergence of an insulating phase between two metallic phases. In Fig. 5.3(b), we show the corresponding measurement of the parity-projected density. Here, we see a depletion of atoms in the center associated with the removal of doublons. As a function of the interaction strength, we observe an increase in the contrast between the center and the edge of the cloud. This indicates a higher localization of doubly-occupied sites in the center and an increase in the number squeezing at higher densities.

In local density approximation (see Sec. 4.4.1), the knowledge of the shape of the trap allows us to map the real-space coordinates to the chemical potential. In Fig. 5.4(a), we show the measured density (circles) and the singly-occupied sites (diamonds) as a function

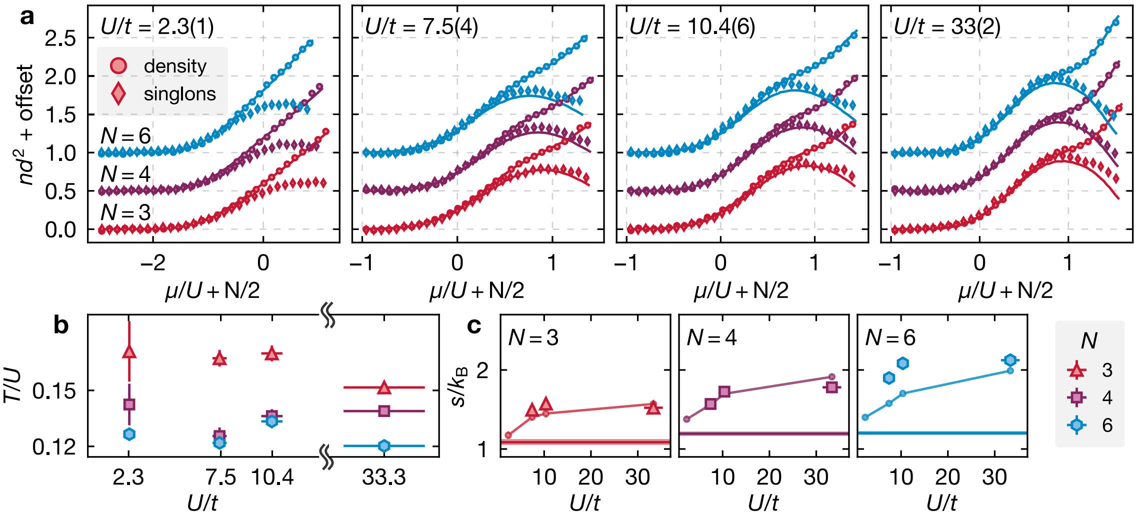

Figure 5.4 | Measuring the EoS of the SU(N) FHM. (**a**) Density $\langle \hat{n} \rangle$ (circles) and singly-occupied sites $\langle \hat{n}_{\mathrm{PR}}^{\mathrm{eff}} \rangle$ (diamonds) as a function of the chemical potential μ for $N = 3, 4$ and 6. The continuous lines correspond to a fit of the data for the density [DQMC for $U/t = 2.3(1)$ and NLCE for the other cases] and a prediction (NLCE) from the fit results of the density for the singly-occupied sites. The curves for $N = 4$ and $N = 6$ are vertically shifted for clarity. The chemical potential is computed with respect to the reference half-filling [$nd^2(\mu = 0) = N/2$]. For each U/t and N, we fit the average of 15 frames with similar atom number after c.o.m. alignment. Error bars are the standard error of the mean (s.e.m.). (**b**) Temperature returned from the fits shown in (**a**). (**c**) Entropy per particle. Triangles, squares, and hexagons correspond to the in-lattice values determined by the fits of (**a**) for $N = 3, 4$ and 6, respectively. The horizontal lines indicate the entropy in the 2D bulk before ramping up the in-plane lattices. The small circles indicate the entropy after a round-trip experiment (the connecting lines are a guide to the eye). The bulk entropy takes into account the effect of interactions (see Chap 3). Error bars correspond to the s.e.m. of the fit results. DQMC and NLCE theory for the fit courtesy of the Hazzard group at Rice University.

of the chemical potential. Here, we also compare realizations for $N = 3, 4$ and 6 with similar initial entropy and total atom number.

The data of 5.4(a) can be compared with the DQMC and NLCE simulations presented in Chap. 4. In particular, we can use these theoretical models to fit the data and determine the system's temperature and entropy. The continuous lines in Fig. 5.4(a) associated with the density data points correspond to the fit of the density with DQMC for $U/t = 2.3(1)$ and NLCE for the other cases. The theory curves agree well with the data. From these fit results, we predict the theoretical curves for the singly-occupied sites. These curves, computed with NLCE without any degree of freedom and shown in Fig. 5.4(a) as continuous lines associated with the singlons, are also in reasonable agreement with the data. A comparison of the data and the fit results in real space can be found in Appendix E.

In Fig. 5.4, the three datasets for $N = 3, 4$ and 6 have been prepared with the same entropy per particle $s/k_{\mathrm{B}} \simeq 1.2(1)$ in the 2D bulk before ramping up the in-plane lattices (see Chap. 2 for the entropy measurement method). This allows us to directly compare them and verify the presence of a Pomeranchuk effect (see Sec. 4.4.2). In Fig. 5.4(b), we compare the in-lattice temperatures returned by the fit for different values of N. Here, we observe a decrease in the temperature for increasing N compatible with the Pomeranchuk effect. The "cooling" effect is apparent when we compare $N = 3$ with $N = 4$ or the strongest interaction strength for all values of N. However, we observe that the temperatures for $N = 4$ and $N = 6$ and intermediate U/t values are similar within 10 % and their difference is smaller than what we would have expected (see, for example, Fig. 4.8). This weakening of the Pomeranchuk effect can be partially explained by looking at the entropy per particle in the lattice, as shown in Fig. 5.4(c). We observe that the entropy in the lattice (large data points) is larger than the one measured in the 2D bulk (horizontal line) and that this increase is more significant for larger N. This phenomenon is corroborated by the entropy measurement after a round-trip experiment (small circles). For this experiment, after loading into the lattice to the desired U/t value, we add a symmetric and inverted ramp back to the 2D bulk system and measure the entropy again. We observe that the entropy after the round-trip experiment is always larger than the initial one and shows a N-dependency similar to the one measured in the lattice. The round-trip and in-lattice values are in good agreement for $N = 3$ and 4 and show some deviations for $N = 6$.

In determining the exact shape, slope, and duration of the lattice ramps, we put particular care into minimizing the round-trip entropy. However, the lack of complete adiabaticity when loading into the lattice is not a complete surprise since it has been reported several times in the literature for different systems and geometries [73, 186, 217, 292, 347]. Moreover, the N-dependency of the heating is not an entirely new phenomenon since similar discrepancies for $N = 6$ have been observed in the measurement of the EoS in a 3D cubic lattice [73]. We will return to this point in Sec. 5.5.3.

5.3.1 Equation of state for higher temperatures

In addition to comparing the EoS for fixed entropy per particle s/k_B and different N as described in Sec. 5.3, we also explore the EoS for other combinations of parameters. In this section, we focus on the EoS as a function of the entropy per particle, which we tune by adding a hold time in the 2D bulk before ramping up the lattices (see Sec. 3.4). In Fig. 5.5(a), we show the measured density profiles as a function of the hold time for different values of U/t and $N = 6$. In the strongly interacting regime, we observe the fading of the Mott plateau at density $nd^2 \simeq 1$. By fitting the density profiles with DQMC [for $U/t = 2.2(1)$] and NLCE (for the other cases), we see that the theory curves agree well with the data.

In Fig. 5.5(b), we show the temperatures returned by the fits. They are, as expected, monotonic and increase gradually with the hold time. In Fig. 5.5(c), we show the entropy per particle returned by the fit, and we compare it with the bulk entropy measured before the lattice loading and after a round trip experiment. For finite hold time and when applicable[†], we observe some agreement between the in-lattice entropy and the bulk entropy after the round-trip experiment. This is especially true for longer hold times, where the discrepancy between the two values becomes comparable with the error bars. However, for $U/t = 10.0(5)$, we observe that the in-lattice entropy is systematically larger than the

---

[†] For $U/t = 2.2(1)$ and low temperatures, the range of convergence of the entropy curves with DQMC is limited, and we cannot reliably compute the in-lattice entropy for all the hold times.

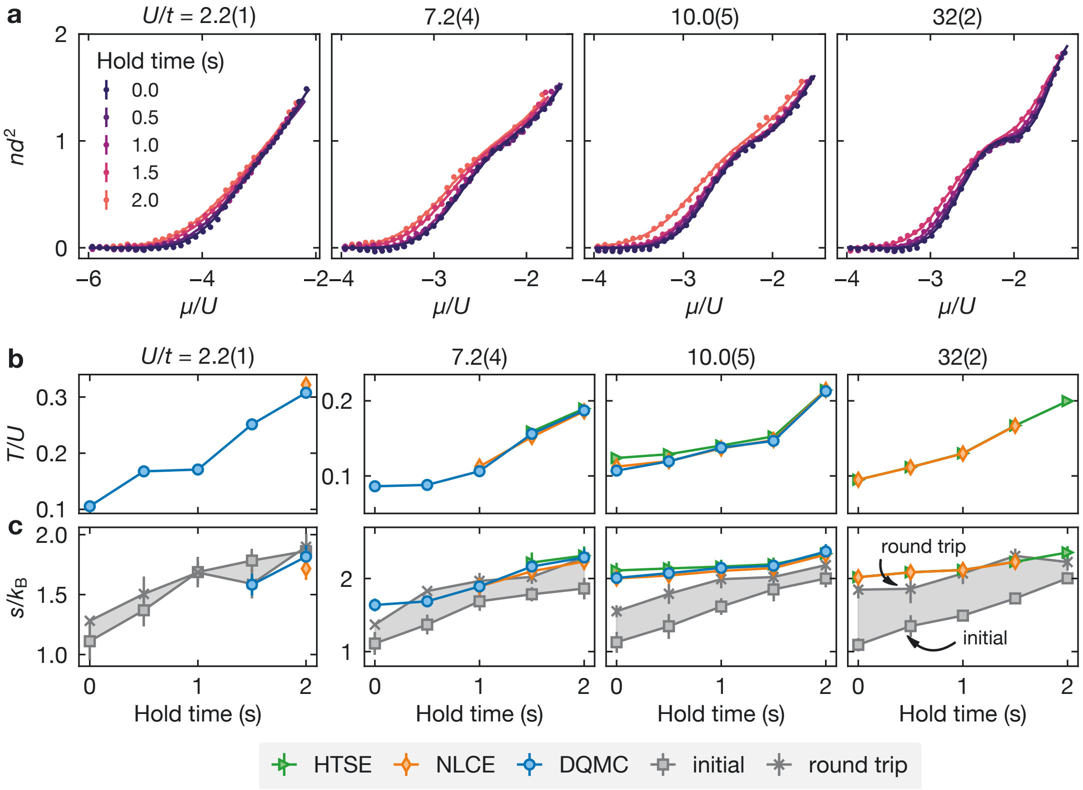

Figure 5.5 | Temperature dependence of the equation of state for $N = 6$. (**a**) Density profiles as a function of the hold time in the 2D bulk before ramping up the lattices for different values of U/t. The data correspond to the average of 15 frames with $N_p \approx 2.2 \times 10^3$ and a s.e.m. of 15 to 35 for each combination of U/t and hold time, after total atom number postselection and c.o.m. alignment. The continuous lines are the results of the fit with NLCE [for $U/t = 33(2)$] and DQMC (for the other cases). (**b**) Temperature returned by the fit as a function of the hold time. We compare the results of the fits with different methods: DQMC (circles), NLCE (diamonds), and HTSE (triangles). The lines are a guide to the eye. (**c**) Entropy per particle in the lattice as a function of the hold time. We compare the results of the fits with different methods [same markers and colors as in (**b**)]. The in-lattice results are compared with the entropy measured in the 2D bulk before loading to the lattice (squares) and after a round-trip experiment (crosses). The lines and the shaded areas are a guide to the eye. The error bars in (**b**) and (**c**) are the s.e.m. of the fit. DQMC and NLCE theory for the fit courtesy of the Hazzard group at Rice University.

bulk entropy. This discrepancy is not fully understood, and it might relate to the relatively strongly interacting regime at temperatures approaching the superexchange energy $J \sim 4t^2/U$[‡].

5.3.2 Compressibility

From the density and the knowledge of the chemical potential, we can compute the isothermal compressibility $\kappa = \partial n/\partial\mu$. The compressibility contains information about the insulating properties of the system (see Chap. 4). In Fig. 5.6, we show the measured com-

---

[‡] In this regime, it has been reported that, at $\langle\hat{n}\rangle = 1$, the entropy measures $\approx \log N$ and shows only a weak dependency on the temperature [50].

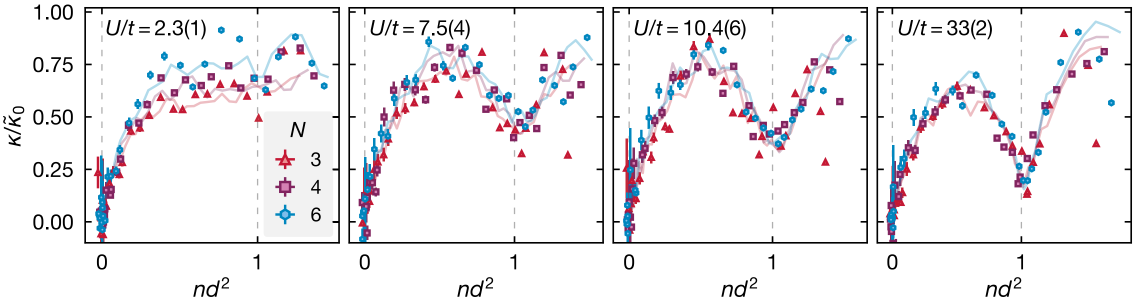

Figure 5.6 | Compressibility as a function of the density for the same datasets shown in Fig. 5.4. Points: data numerically derived from the experimental density profiles with three-point differentiation. Lines: compressibility computed from the numerical differentiation of the theoretical curves shown in Fig. 5.4. The values are normalized to the compressibility $\tilde{\kappa}_0$ of a non-interacting Fermi gas with $N = 6$.

pressibility as a function of the density for the same datasets of Fig. 5.4. As U/t increases, we can clearly see a suppression of the compressibility at densities $nd^2 \simeq 1$, a clear signature of the insulating behavior. When we compare the curves with the same U/t ratio and different N, we observe that they almost collapse on each other. The same temperature would result in higher compressibility at $nd^2 \simeq 1$ for larger N [see Fig. 4.7(d)]. The fact that the compressibility looks almost independent of N indicates, therefore, that a lower temperature compensates for the statistics-induced additional stiffness of the system, a consequence of the Pomeranchuk effect.

5.3.3 Gap estimation

In Fig. 5.7(a), we show the compressibility for different values of U/t and $N = 6$ as a function of the temperature. Qualitatively, it can be seen that the compressibility has a stronger dependence on the temperature for larger U/t. This behavior is associated with the opening of a charge gap Δ in the excitation spectrum of the system. More quantitatively, we can estimate the gap by fitting the minimum of the compressibility at the plateau with the expression $\kappa_{\mathrm{min}}(T) \propto \exp(-\Delta/T)$ [348] [see Fig. 5.7(b)]. In Fig. 5.7(c), we show the gap as a function of U/t. We observe that the gap becomes very small around $U/t \sim 7$. A linear fit to the data returns a zero crossing of $(7.8 \pm 1.2)\,t$. However, we should point out that it is not clear whether a linear scaling is the correct functional form for the gap. In particular, $O(t)$ terms might play an important role near the closure of the gap [349]. Further studies are, therefore, needed to determine the point where the gap opens and its functional dependency with respect to the interaction strength. With an accurate modeling, this technique might nevertheless provide valuable insights on the transition from the metallic to the insulating regime for $N > 2$[§].

[§] For $N = 2$ the existence of a perfect nesting causes a smooth crossover [17].

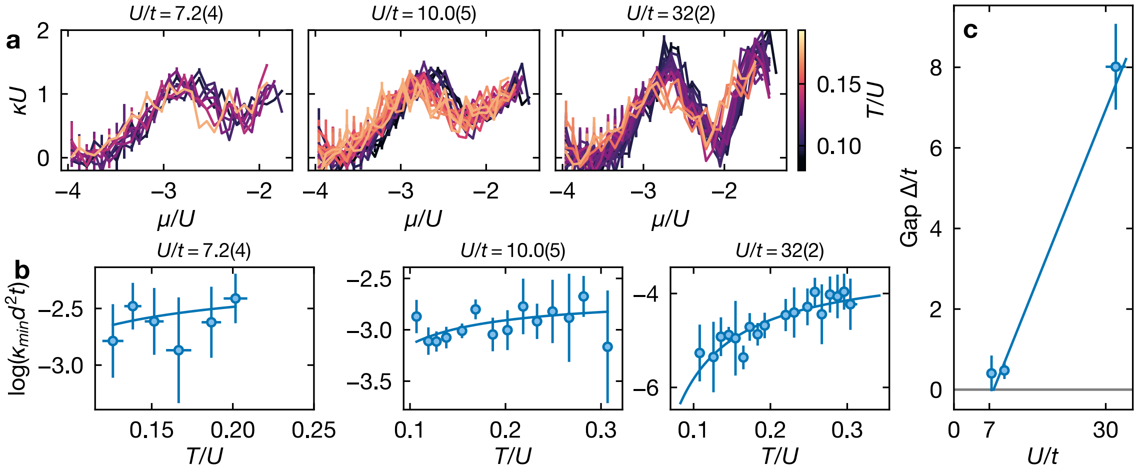

Figure 5.7 | Estimating the charge gap Δ emerging in the Mott insulating regime around $nd^2 \simeq 1$. (**a**) Compressibility as a function of the chemical potential and the temperature (color scale) for different values of U/t and $N = 6$. (**b**) Minimum of the compressibility around $nd^2 \simeq 1$ as a function of the temperature. Continuous line: fit of the data with the expression $\log(\kappa_{\mathrm{min}}) = \mathrm{const} - \Delta/T$. (**c**) Gap Δ obtained from the fits of (**b**) as a function of U/t. Continuous line: linear fit to the data.

5.4 Density fluctuations and model-free thermometry

Complementary to the density profiles, the 2D single-plane geometry allows us to access the local density fluctuations[¶] without the need for complex reconstruction techniques. Similarly to what we have discussed in Sec. 3.5, we compute the density variance in spatially-binned probe areas. There, we illustrated a method to correct the raw data for the PSF and the photon shot noise. Here, we apply the same method and calibration parameters. A measurement of the local density fluctuations is shown in Fig. 5.8(a-c) for $N = 3$, 4 and 6, respectively (data points). It corresponds to the variance of several frames measured under the same conditions computed in spatially-binned probe areas of size $4\times4\,\mathrm{px}^2 \approx 5.1\times5.1\,d^2$. The local density fluctuations are compared to the numerically-differentiated compressibility κ times the temperature T_{EoS} obtained from the EoS-fit of the averaged data (green lines). We observe that the two quantities are in good agreement with each other. This comparison is enabled by the fluctuation-dissipation theorem (FDT) [302], which, in the form derived in Eq. (3.15), states that the density fluctuations are proportional to the compressibility times the temperature. In Eq. (3.15), the fluctuations are

---

[¶] The use of the word *local* requires some care and explanation. Unfortunately, it is used in the literature with different meanings even in the same context of EoS and FDT in cold atoms experiments with optical lattices [186, 188, 189]. Here, we use *local* to indicate the fluctuations measured on a finite probe area A. They converge to the *thermodynamic* fluctuations if the correlation lengths are much smaller than $\sqrt{A}$ (as in our case). We distinguish between *local* and *on-site* density fluctuations, which are computed on an area $A \gg d^2$ and corresponding to a single lattice site, respectively. Furthermore, to avoid other ambiguities, we prefer to write about *off-site* fluctuations instead of *nonlocal* fluctuations to indicate the terms at the origin of the differences between the *local* and the *on-site* fluctuations.

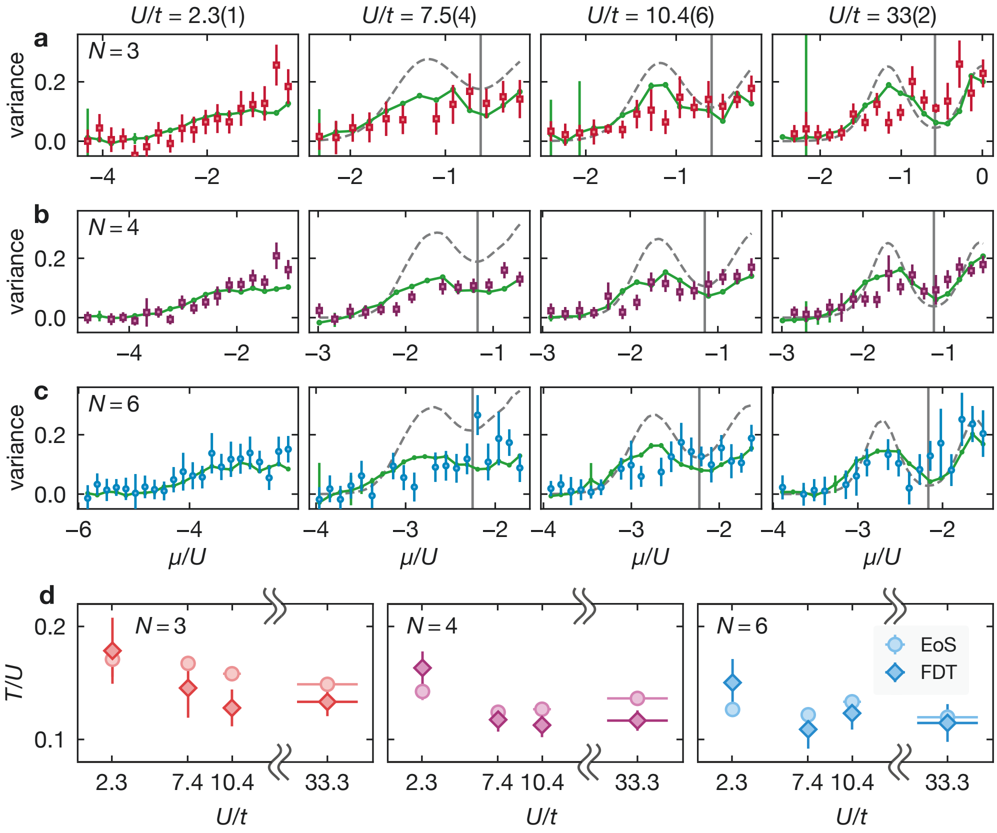

Figure 5.8 | Density fluctuations as a function of the chemical potential for (**a**) $N = 3$, (**b**) $N = 4$ and (**c**) $N = 6$. For $N = 3$ and 6, data points correspond to the variance of the same dataset of Fig. 5.4 and are computed in spatially-binned probe areas of size $4 \times 4\,\mathrm{px}^2 \approx 5.1 \times 5.1\, d^2$. For $N = 4$, 35 frames have been used instead of 15 to improve the statistics. The photon shot noise has been subtracted, and a PSF correction has been applied as described in Sec. 3.5. The green lines correspond to the numerically-differentiated compressibility κ times the temperature T_{EoS} obtained from the EoS-fit of the averaged data. The grey dashed lines correspond to the on-site density fluctuations $\delta n_0^2 = \langle \hat{n}^2 \rangle - \langle \hat{n} \rangle^2$ calculated with NLCE for T_{EoS}. The vertical lines correspond to $nd^2 \simeq 1$. (**d**) Comparison of the temperatures T_{FDT} (diamonds) and T_{EoS} (circles). Error bars are the s.e.m.

calculated from the density-density correlation function on all length scales. This is equivalent in our case to the measurement of the fluctuations in a finite-size probe area $A \gg d^2$:

$$\mathrm{var}\left(\int_A n\, dA\right) = k_{\mathrm{B}} T \kappa A. \tag{5.6}$$

The effect of the large probe area is better understood when comparing the local density fluctuations with the on-site density fluctuations

$$\delta n_0^2 = \langle \hat{n}^2 \rangle - \langle \hat{n} \rangle^2. \tag{5.7}$$

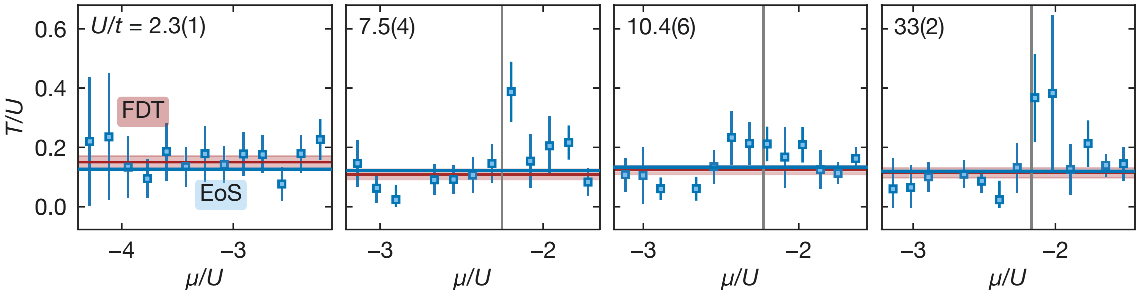

Figure 5.9 | Local temperature for the $N = 6$ dataset of Figs. 5.4 and 5.8. Data points: local temperature obtained as a ratio between the local density fluctuations and the compressibility as a function of the chemical potential. Blue line: temperature according to the fit of the EoS. Red line: temperature according to the fit of the FDT. Vertical line: chemical potential corresponding to $nd^2 \simeq 1$.

By transcribing the integral in Eq. (3.15) to a sum over lattice sites, we rewrite the FDT as [189]

$$\kappa d^2 k_{\mathrm{B}} T = \delta n_0^2 + \sum_{i \neq j} \Big(\langle \hat{n}_i \hat{n}_j \rangle - \langle \hat{n}_i \rangle \langle \hat{n}_j \rangle \Big). \tag{5.8}$$

The on-site density fluctuations are generally higher than the local ones, as shown in Fig. 5.8(a-c) (grey dashed lines). The difference between the two is given by the off-site density fluctuations [second term on the right side of Eq. (5.8)], which give a negative contribution.

The relationship between the local density fluctuations and the compressibility in the FDT can be used to measure the system's temperature without relying on a theoretical model for the EoS. In particular, we compute the temperature T_{FDT} as the (weighted) mean of the ratio between the local density fluctuations and the compressibility as a function of the chemical potential for $nd^2 > 0.05$. In Fig. 5.8(d), we compare T_{FDT} with the temperature T_{EoS} obtained from the EoS-fit of the averaged data. We observe a good agreement between the two temperatures for all interaction strengths and values of N.

The FDT can also be used to measure the *local* temperature of the system and verify the global equilibrium hypothesis that we implicitly make when we fit the EoS. This is done by calculating the ratio between the local density fluctuations and the compressibility in different regions of the trap or as a function of the chemical potential. In Fig. 5.9, we show the local temperature as a function of the chemical potential for $N = 6$. We observe that the local temperature is overall constant across the trap. In the strongly-interacting regime near the plateau, we measure local temperatures slightly higher than the global one. However, measuring the local temperature in this region is particularly challenging because of the low compressibility and the small signal-to-noise ratio in the density fluctuations. We see instead an excellent agreement between the values at small and large densities, a strong hint suggesting global thermal equilibrium across the cloud.

5.5 Calibration and systematic errors

The determination of the EoS from experimental data is a sensitive procedure. Small calibration errors or incorrect handling of systematic effects might result in imprecise or inaccurate temperatures and other thermodynamic quantities. It is therefore important to characterize the experimental setup, document the fit procedures and individuate possible causes of systematics errors. This is the goal of this section. In Sec. 5.5.1, we first document the fit procedure used to determine the EoS from the measured density profiles. In Sec. 5.5.2, we discuss the determination of the trap potential and the harmonic assumption. In Sec. 5.5.3, we discuss the adiabaticity of the lattice loading and the global thermal equilibrium hypothesis. In Sec. 5.5.4, we return to the Hubbard parameters' calibration and the systematic errors we commit when we fit a theoretical model to the data with a fixed U/t ratio without considering its uncertainty. In Sec. 5.5.5, we discuss the calibration of the photoassociation technique associated with the parity-projection operation. Finally, in Sec. 5.5.6, we discuss the role of the point spread function (PSF) and other imaging imperfections.

Additional information is reported in Appendix E, where we compare different fitting models and discuss the systematic errors due to the numerics.

5.5.1 Fit method

This section illustrates the fit procedure used in Sec. 5.3 to determine the EoS from the measured density profiles. This is a multi-step procedure, described in detail in the following.

The fit is done starting from the density profile $n(x,y)$, which is obtained by averaging the density profiles of several frames after total atom number postselection and center of mass alignment[‖]. Afterward, the procedure is the following:

1. Determination of the cross section.

   - Consider the $U/t = 33(2)$ dataset only.
   - For each N, fit separately $\left\{T, \mu_0, \kappa_x, \kappa_y, \sigma_{\text{corr}}^{(N)}\right\}$.
   - This fit is used to determine $\sigma_{\text{corr}}^{(N)}$, the correction of the cross section compared to the calibration in the 2D bulk described in Sec. 2.3.2, for $N = 3, 4$ and 6.
   - We use $\sigma_{\text{corr}}^{(N)}$ to update the cross section of all the lattice datasets before fitting the EoS in the following steps.

   This first step is necessary because we observe a substantial change in the cross section between the bulk and the lattice. Without a correction, the Mott plateau at $nd^2 \simeq 1$ would appear at a higher density value, incorrectly determining the temperature and the chemical potential. To determine the correction, we fit the density profiles for

---

[‖] The center of mass alignment is done by fitting the density profiles with an EoS model and shifting the images to align their centers with linear interpolation. We use the same model used to determine the temperature (step 3 of the following). We have observed this to lead to substantially more accurate results than calculating the weighted average of the density across the cloud or using a Gaussian fit function.

$U/t = 33(2)$ because the larger Mott plateau makes this dataset particularly sensitive to a cross section mismatch. Furthermore, we fit the density profiles for each N separately because the cross section correction might depend on the statistics. This discrepancy is presented and further discussed in Sec. 5.5.6.

2. Determination of the trap frequencies.
    - Consider the datasets for each U/t separately.
    - Perform a combined fit for all Ns, and simultaneously determine $\left\{T^{(N)}, \mu_0^{(N)}\right\}$ for $N = 3, 4$ and 6 and values of $\left\{\kappa_x, \kappa_y\right\}$ independent of N.
    - This fit is used to determine the values of $\left\{\kappa_x, \kappa_y\right\}$ defining the harmonic confinement for each U/t ratio.

    Here, we assume the trap is harmonic (see Sec. 5.5.2 for the discussion of this hypothesis). We perform a combined fit because the harmonic coefficients depend on the lattice depth, which is a trap property, but not on N. The combined fit is more robust and reduces their uncertainty. As a sanity check, we verify that separate fits for each N give compatible results.

3. Determination of the EoS.
    - Consider the datasets for each N and U/t separately.
    - Fit $\{T, \mu_0\}$ and determine the best matching of the theoretical model to the data.

    This third step returns the temperature and chemical potential values and determines the EoS. Given these two values, we can calculate the entropy per particle and the parity-projected profiles shown in Fig. 5.4.

Each fit is done with the implementation of the trust region reflective algorithm of the `scipy` library[**]. The fit function minimizes the distance between the data and the theoretical curve calculated in a two-dimensional grid and convolved with the PSF (see Sec. 5.5.6).

5.5.2 Trap frequencies and anharmonicities

In Eq. (5.2), we have modeled the lattice envelope with a harmonic potential with coefficients κ_x and κ_y. In Sec. 5.5.1, we have described how we determine these coefficients by fitting the EoS. We verify that adding third and fourth order anharmonic terms to the potential as free fit parameters does not significantly affect the results.

[**] We found out that, for our specific implementation, the trust region reflective algorithm (`trf`) is slightly faster and more robust than the Levenberg-Marquardt (`lm`) algorithm. This is particularly true for $U/t \sim 2.3$ and $U/t \sim 33$, where the `lm` algorithm sometimes converges to local optima. When we use `trf`, we specify boundaries to the temperature $T/t \gtrsim 0.167$ for $U/t \sim 2.3$ and $T/t \gtrsim 0.5$ for the other U/t values. We use `scipy` 1.9.3.

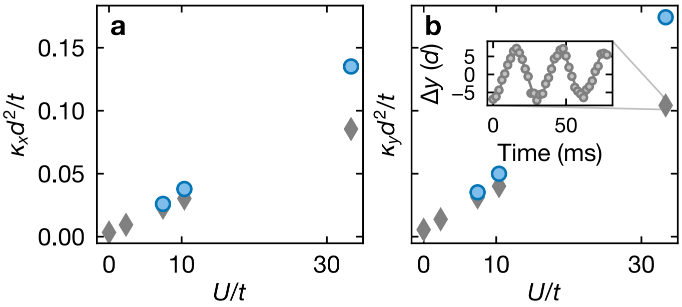

Figure 5.10 | Coefficients of the harmonic confinement along the main axes (x, y). Circles correspond to the harmonic confinement determined from the fit of the EoS described in Sec. 5.5.1. Diamonds correspond to an independent calibration measuring the frequencies of the center of mass (c.o.m.) oscillations around the trap's center. Inset: example of c.o.m. oscillations for $U/t = 33(2)$.

However, the values obtained for κ_x and κ_y do not fully agree with the independent measurement of the frequency of the oscillatory motion of the atoms in the combined potential. More specifically, we measure the trap frequencies in the following way. We load a spin-polarized cloud in the combined potential of the vertical lattice and one in-plane lattice at the time. We measure the c.o.m. oscillation after an initial displacement of $\sim 5\,d$ along the lattice direction. We then calculate the trap frequencies in the combined potential from the individual contribution of each lattice in the perpendicular direction of propagation. Before doing so, we verify that the Rayleigh range contribution to the combined potential is negligible[††]. A comparison between the two sets of values can be found in Fig. 5.10. The origin of this discrepancy, which is about 13 % for $U/t \sim 7$ and 40 % for $U/t \sim 33$, is not completely clear. In Sec. 5.5.3, we discuss the possibility that the discrepancy is due to non-adiabaticities of the loading process and present arguments against this hypothesis.

In order to verify that the harmonic approximation is valid, we try to characterize the anharmonicities of the potential. We do so by loading a hot cloud ($T/t \gg 1$) in the lattice. In this regime, the cloud can be fitted with an atomic limit model (see Sec. 4.2.1). This way, we can generate a spatial map of the chemical potential and observe that the functional modeling as a harmonic trap is a good approximation[‡‡]. In particular, we estimate the anharmonic corrections being less than $0.03\mu_0$ over the whole region of interest in the deep Mott insulating regime.

5.5.3 Considerations on adiabaticity

A possible explanation for the discrepancy in the shape of the inferred potential described in Sec. 5.5.2 might be a lack of adiabaticity and equilibration during the tuning of U/t [350]. However, the temperatures measured with the FDT (see Sec. 5.4) match those obtained from the fit of the EoS. In particular, we verify that for $N = 6$ and $U/t = 33(2)$, if we use the chemical potential coming from the oscillatory-motion calibration to calculate the

---

[††] About 1 % in the trap frequencies.

[‡‡] We do so by describing the potential with Hermite functions up to the 8th order instead of polynomial powers and fitting their parameters. We verify that the potential sampled by the cloud is not significantly different from the one obtained from the harmonic approximation.

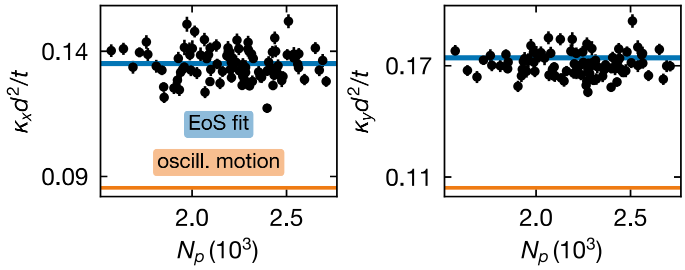

Figure 5.11 | Dependency of the harmonic coefficients κ_x and κ_y with the total atom number N_p. Each point corresponds to a single realization with $N = 6$ and $U/t = 33(2)$. For each realization we fit (T, κ_x, κ_y, μ_0) with NLCE. Blue lines: values determined from the EoS fit as described in Sec. 5.5.1 for this U/t ratio. Orange lines: values determined with the independent “oscillatory motion” calibration.

compressibility and the FDT relation to fit the temperature, we get a temperature inside the regime of convergence of our theoretical models but mismatching the temperature returned by the fit of the EoS with the same potential.

Moreover, we verify that the values of κ_x and κ_y determined by the EoS fit are robust against atom number variation (see Fig. 5.11).

Finally, we observe that κ_x and κ_y are also insensitive to the lattice ramp time duration. In Fig. 5.12, we show an experiment that consists of tuning the lattice depth to $13\,E_{\mathrm{rec}}$ ($U/t \approx 44$) with a linear ramp of different duration Δt between 300 ms and 1 s [see Fig. 5.12(a)]. For each Δt, we fit the EoS with HTSE and leave (T, κ_x, κ_y, μ_0) as free fit parameters. As shown in Fig. 5.12(b), we observe that the values of κ_x and κ_y returned by the fit for different Δt are compatible among each other [$\kappa_x d^2/t = 0.151(2)$, $\kappa_y d^2/t = 0.204(3)$]. However, they are incompatible with the ones predicted by the independent “oscillatory-motion” calibration described in Sec. 5.5.2 ($\kappa_x^{\mathrm{osc}}/t \simeq 0.109$, $\kappa_y^{\mathrm{osc}} \simeq 0.131$). If we assume these values and fit the EoS with free parameters $\{T, \mu_0\}$, the fit fails for $\Delta t = 0.3$ s and returns high residuals for $\Delta t = 0.5$ s and 1 s, failing to reproduce the cloud shape, especially in the center [see Fig. 5.12(c)]. We conclude that if the mismatch between the two different harmonic potential parameters comes from a lack of equilibration during the tuning of the lattice depth, the time scale to achieve this equilibration significantly exceeds the experimentally accessible timescales.

5.5.4 Calibration of the Hubbard parameters and uncertainties

As we have seen in Sec. 5.1, the ratio U/t is determined by the lattice depth V. We calibrate the lattice depth by measuring the resonance between the lowest band and the second excited band with parametric modulation [275]. The uncertainty on U/t is given by the error propagation on this measurement.

As a cross-check for the calibration with parametric modulation, we use clock-line spectroscopy along the ${}^1\mathrm{S}_0 \rightarrow {}^3\mathrm{P}_0$ transition to measure the bandgap between the lowest and the first band, which is consistent with the value obtained from the parametric modulation.

In addition to calibrating U/t, we directly measure U for deep lattice depths. This measurement consists in modulating the lattice depth with an amplitude of 2% to 6%

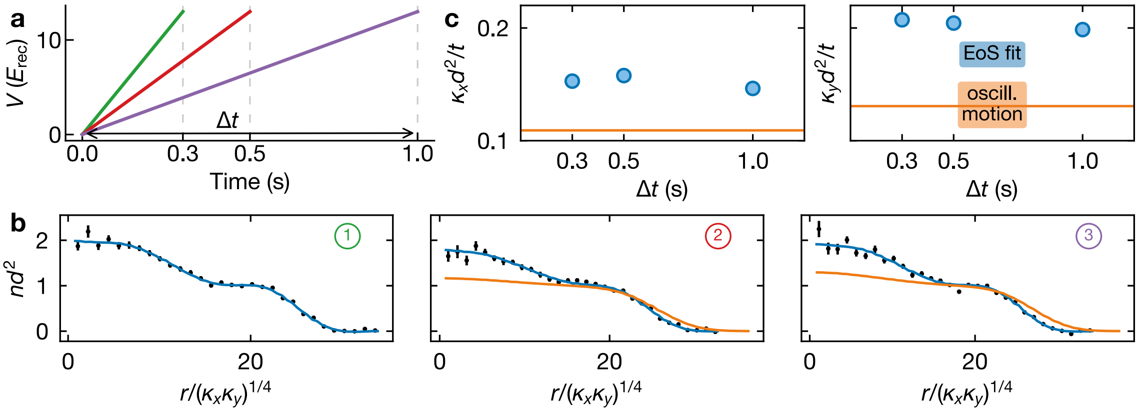

Figure 5.12 | Robustness of the EoS fit as a function of the ramp duration. (**a**) We tune the interaction strength of a sample with $N = 6$ to $U/t \approx 44$ with a linear ramp of duration $\Delta t = 0.3$ s (green), 0.5 s (red), 1 s (purple). (**b**) For each ramp duration Δt, we fit the density profile with HTSE assuming a harmonic potential with coefficients determined by the "oscillatory-motion" calibration (orange) and by leaving the coefficients free in the EoS fit (blue). Here, we plot the fit results as a function of the spacial radial profile. For the first frame, the "oscillatory-motion" fit fails. (**c**) Comparison of the harmonic potential coefficients returned by the fits [same color code as (**b**)]. Error bars are s.e.m. from the fit (smaller than markers).

and, at the same time, applying a pair removal pulse (see Sec. 5.2). When the modulation frequency is resonant with U, atom losses are enhanced. The measurement results can be seen in Fig. 5.13, and they agree with the values expected from a band structure calculation. In particular, for $V = 13\,E_{\mathrm{rec}}$ ($U/t \approx 43$) we measure $U = h \cdot 886(8)\,\mathrm{Hz}$ for an expected value of $h \cdot 856(8)\,\mathrm{Hz}$ and for $V = 19\,E_{\mathrm{rec}}$ ($U/t \approx 178$) we measure $U = h \cdot 1065(8)\,\mathrm{Hz}$ for an expected value of $h \cdot 1069(9)\,\mathrm{Hz}$.

We now consider the systematic errors associated to U in the fit of the EoS. When we perform the fit, we use the fixed value of U/t obtained from the band structure calculation. However, the fit does not consider the uncertainty on U/t. We can estimate the systematic error in the temperature and the entropy per particle due to the uncertainty on U/t by repeating the fit for different values of U/t. In Fig. 5.14, we show the results of this test for the dataset of Fig. 5.5. We estimate that the systematic error on the entropy is about 1 %, and it is comparable with the statistical error. The systematic error on the temperature is instead of the order of $0.015\,U$, making it one of the dominant ones.

5.5.5 PA efficiency calibration

In Sec. 5.2, we have introduced the parity projection technique. In Eq. (5.5), we have seen that the photoassociation beam that we use to remove pairs of atoms from the lattice is not perfect and requires an efficiency correction parametrized by the factors γ_s and γ_d. We calibrate the efficiency by looking at the atom losses as a function of the pulse duration in the deep Mott insulating regime [$U/t = 33(2)$]. The measurement is shown in Fig. 5.15(a). Neglecting the sites occupied by more than two particles, we fit a double-exponential model:

$$N_p = e^{-\gamma_s t}\left(N_s + N_d e^{-\gamma_d t}\right), \tag{5.9}$$

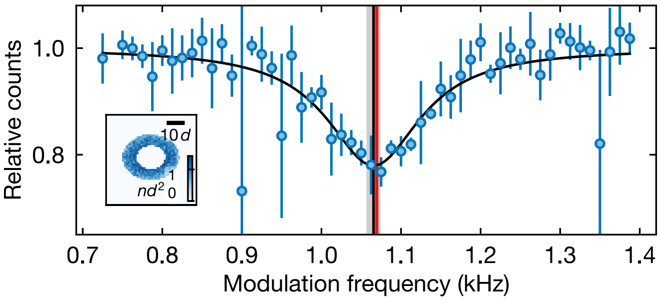

Figure 5.13 | Direct measurement of U with modulation spectroscopy for $U/t \approx 178$. Data points: normalized atom number after a pair removal pulse as a function of the modulation frequency. Red line: expected value of U according to the Wannier overlap. Black line: fit of a Lorentzian function. The vertical black line and the shaded area indicate the position of the resonance according to this fit and its uncertainty, respectively. **Inset**: To enhance the signal-to-noise ratio, the data have been evaluated in an elliptical shell where the cloud is mainly in the insulating phase.

where $N_p = N_s + N_d$ is the total atom number, N_s the number of singlons, N_d the number of doublons. We obtain $1/\gamma_d = 1.2(2)\,\mathrm{ms}$ and $1/\gamma_s = 200(11)\,\mathrm{ms}$, which we find to be independent of N inside the uncertainties. We cross-check the value of γ_s by repeating the same experiment in a small Mott insulator with $\approx 1 \times 10^3$ atoms where negligible doublon decay is expected. For the typical pulse duration of 10 ms, we remove all the doublons within our detection sensitivity and about 5 % of the singlons. This factor is taken into account when we calculate the theoretical curves in Fig. 5.4. In Fig. 5.15(b), we compare the ideal and corrected parity-projected density for some reference configurations.

5.5.6 Imaging effects

Calibration of the cross section

In the lattice, we calibrate the effective cross section σ for each spin mixture by the fit of the EoS as described in Sec. 5.5.1. We obtain $\sigma/\sigma_0 = \{0.310(3), 0.320(3), 0.321(3)\}$ respectively for $N = \{3,4,6\}$, where $\sigma_0 = 3\lambda^2/(2\pi)$ is the photon resonant cross section. The result is in agreement within the uncertainties with the determination of minimum of the compressibility $\kappa = \partial n/\partial\mu$ near the insulating regime at $nd^2 \simeq 1$ (see Fig. 5.6). However, there is a discrepancy of 10 % to 20 % with the values obtained for the quasi-2D bulk in Sec. 2.3.2. The origin of this discrepancy is not clear. We attribute the differences between the values to cooperative optical response effects at high densities [276, 277] and use the values obtained from the fit to analyze the in-lattice data. We take into account this difference in the cross section when calculating the PSF correction to the density fluctuations in Sec. 5.4.

PSF effect on the EoS

In Fig. 5.16, we show the effect of the PSF on a simulated density profile. The PSF blurs the density profile and significantly affects the fit of the EoS. A simulation shows that without taking into account the PSF, the fit of the EoS overestimates the temperature by 10 % to

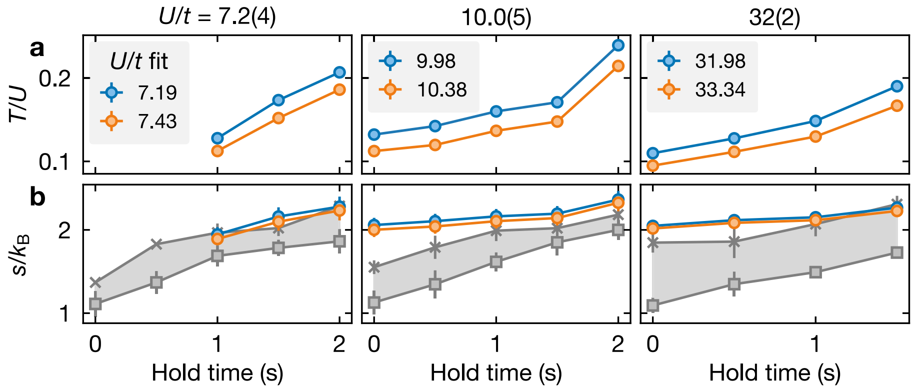

Figure 5.14 | Estimate of the systematic error on (**a**) the temperature and (**b**) the entropy per particle due to the uncertainty on U/t. We repeat the fit of the EoS for the dataset of Fig. 5.5 with NLCE for different values of U and compare the results. The error bars are the statistical error on the fit (smaller than the markers). Grey points and lines correspond to the bulk entropy as in Fig. 5.5. NLCE theory courtesy of the Hazzard group at Rice University.

20 % for T/U between 0.15 and 0.3 (larger overestimation for colder samples). We also estimate that the fit of a cloud in atomic limit with $T_{\text{set}}/U \to 0$ would return a temperature $T_{\text{fit}}/U \approx 0.07$. In order to correct these effects, we convolve the simulated density with the PSF inside the EoS fitting routine.

Since the PSF has been determined experimentally, we need to estimate the systematic error due to its uncertainty when determining the EoS. We do so by varying the HWHM of the reconstructed PSF. Testing the sensitivity of the fit parameter results, we find that, in the deep Mott insulating regime[§§], where the effects of the PSF are most relevant, a variation of 50 % in the size of the HWHM causes a change of ≈ 10% to 15% in the temperature and ≈ 4% in the entropy per particle.

[§§] for $U/t \sim 33$ and $N = 6$.

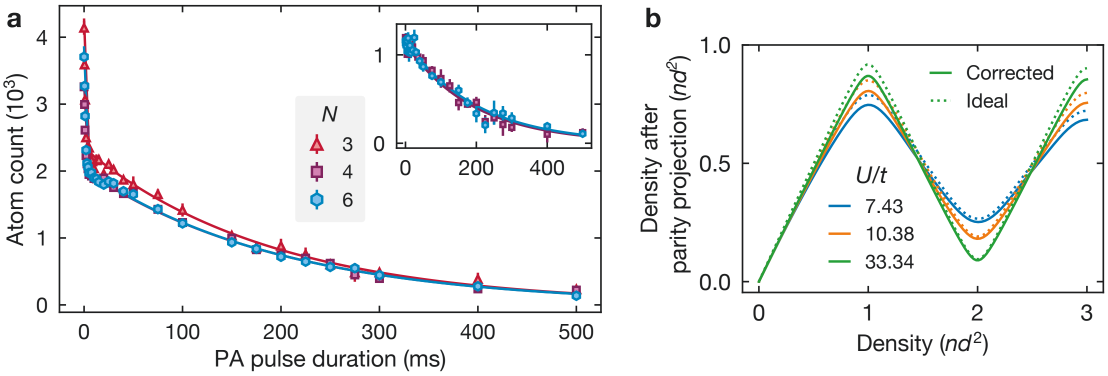

Figure 5.15 | (**a**) Calibration of the photoassociation efficiency. We first tune the lattice depth to $12\,E_{\text{rec}}$ [$U/t = 33(2)$] and then quench it to $30\,E_{\text{rec}}$. We then apply the photoassociation beam for different durations and measure the atom number loss for $N = 3$ (red), $N = 4$ (purple), and $N = 6$ (blue). The losses are fitted with a double-exponential model (solid lines), corresponding to the doublons and singlons decay. **Inset**: Same experiment repeated for a smaller atom number, such that $nd^2 \simeq 1$ in the center. (**b**) Comparison of the ideal [dotted line, Eq. (5.4)] and corrected [continuous line, Eq. (5.5)] parity-projected density as a function of the total density for $N = 6$, $T/U = 0.18$ and different U/t ratios. Curves are reworkings of NLCE simulations courtesy of the Hazzard group at Rice University.

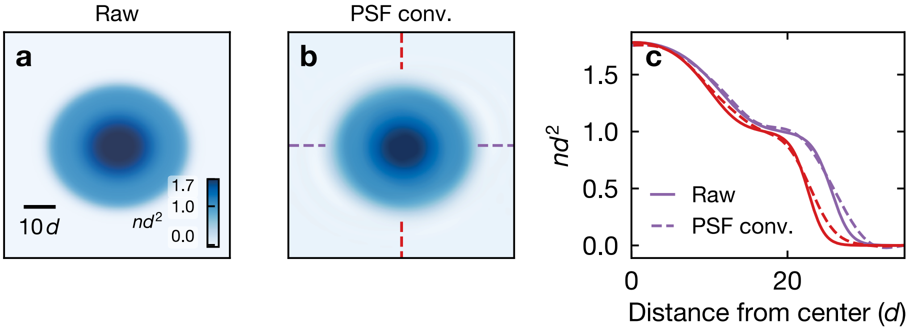

Figure 5.16 | Effect of the PSF on the measurement of the EoS. (**a**) HTSE simulation of the density for $N = 6$, $U/t = 33.34$ and $T/U = 0.12$ in a harmonic trap. (**b**) Simulation of (**a**) convolved with the PSF. (**c**) Cuts along the main axes [along the lines with the same color in (**b**)] for the density in (**a**) (solid lines) and in (**b**) (dashed lines).

Conclusions and outlook

In this thesis, we have reported the first experimental studies of SU(N) Fermi gases in a 2D single-layer system. This has been made possible by the SU($N \leq 6$) symmetry of ^{173}Yb in the ground state and by the implementation of a novel shallow-angle optical lattice enabling the loading of the atoms into a single plane.

We have first characterized the equation of state (EoS) of the system in a quasi-2D harmonic oscillator as a function of the number of spin components N, and modeled and investigated the interaction effects to obtain a reliable thermometry and entropy measurement.

We have then studied the SU(N) Fermi gases in a square lattice, probing the 2D SU(N) Fermi-Hubbard model (FHM). Our work constitutes the first experimental measurement of the SU(4) FHM in a non-dimerized geometry and the first measurement of the SU(3) and SU(6) FHM in a single-layer geometry. With high-resolution absorption imaging, we have locally probed the density, the compressibility, the components of the site-occupation distribution, and the local density fluctuations across the metal-to-Mott-insulator transition. By taking advantage of the local density approximation, it was possible to determine the EoS of the system for a large range of fillings in the same realization. In particular, we have characterized the formation of an incompressible Mott-insulating phase around unitary density surrounded by compressible metallic phases as a function of the interaction strength.

These measurements have been harnessed to benchmark state-of-the-art numerical methods, including determinant quantum Monte Carlo (DQMC), numerical linked-cluster expansion (NLCE), and high-temperature series expansion (HTSE). We have observed an excellent agreement between our measurements and fits to the data, allowing the determination of the system's temperature and entropy with high precision, and the observation of the Pomeranchuk effect.

Finally, we have used the fluctuation-dissipation theorem (FDT) to determine the system's temperature from the density fluctuations and the compressibility with a theory-free method. The results are in excellent agreement with the EoS-fit results, confirming the fit models' validity and the thermometry's reliability. The FDT also allows for determining the local temperature, which has been found reasonably uniform across the system, strongly hinting at global equilibration.

We believe that our results are an important milestone in exploring the properties of SU(N) Fermi gases and validating theoretical models. In the future, we believe that quantum simulation with alkaline-earth-like atoms such as ^{173}Yb or ^{87}Sr will allow for the exploration of SU(N)-symmetric models beyond the limits of state-of-the-art numerical methods [65]. In this regard, the determination of theory-free thermometry techniques and cross-check methods for verifying the reliability of numerical simulations presented in this thesis constitute a promising step towards self-validating quantum simulations [64].

Many exciting directions for future studies are open. In the 2D bulk system, the possibility of tuning the interaction strength between the spin components would pave the way to the study of SU(N) itinerant ferromagnetism [33, 34, 66, 153] and help to understand the non-analytic behavior of thermodynamic quantities in interacting Fermi gases [284].

In the square lattice, there are numerous intriguing properties that await exploration across all temperature ranges. At temperatures already accessible in the type of experiments presented in this thesis, it would be interesting to verify the universal scaling with N of certain observables, such as the energy and the number of on-site pairs [50]. Furthermore, the transition from the metallic phase to the Mott insulator phase is yet to be fully comprehended. For $N = 2$, the perfect nesting of the Fermi surface at half-filling leads to a crossover between the two phases [15, 17]. However, for larger N, the Fermi surface is not perfectly nested, and phase transitions have been predicted [44]. By analyzing the system's compressibility as a function of temperature and interaction strength, as outlined in Sec. 5.3.3, we might gain further insights into the opening of the gap in the Mott-insulating phase.

For temperatures below the superexchange energy, there are additional aspects to investigate. The Pomeranchuk effect in the Mott-insulating phase is expected to break [50]. Moreover, the phase diagram for $N > 2$ is still largely under debate, and quantum simulations could serve as a valuable instrument for its exploration. This applies to both the SU(N) Fermi-Hubbard model and the SU(N) Heisenberg model, its strong-coupling limit. Specifically, the magnetic ordering predicted for some phases could be examined by measuring the spin-spin correlations in the system. To achieve this, enhancements in imaging resolution and the implementation of spin-resolved imaging techniques are essential. Quantum gas microscopes with alkaline-earth-like atoms have already been demonstrated for bosonic species [252, 351–353], and fermionic microscopes are under development.

Beyond thermodynamics, the application of more sophisticated potential shaping techniques, as demonstrated in other cold atom experiments [354, 355], could facilitate the study of the dynamics of SU(N) Fermi gases. Specifically, our understanding of the transport properties of the SU($N > 2$) FHM is currently limited, and it remains uncertain how the diffusive behavior observed in SU(2) cases [356] alters for larger N.

Another promising avenue for future research involves investigating the breaking of the SU(N) symmetry in the models of interest, both in bulk and in the lattice. The SU(N) symmetry can be broken in our experiment by opportune optical state manipulation or by using state-dependent potentials [67, 76, 357]. The controlled breaking of the symmetry would allow for verifying the validity of the SU(N) models to represent real materials, where the SU(N) symmetry is usually only approximate.

Finally, the clock state allows the study of more complex interorbital models [67]. By populating the clock state in a controlled manner in state-dependent lattices, we can study systems with two species of fermions with different masses and tunable interactions. In particular, adequate state preparation, e.g., by using optical tweezers [358–360] to trap and localize single atoms in the clock state, would allow for the probing of Kondo-type physics [67–69, 83, 84].

In summary, the exploration of the physics of SU(N) Fermi gases presents a promising trajectory for the future of quantum simulation with alkaline-earth(-like) atoms. The exponential scaling of the Hilbert space with N makes these systems particularly challenging for numerical methods. Consequently, quantum simulation is anticipated to offer a valuable tool for investigating their properties and demonstrating significant advantages over classical simulations in the near future.

Appendices

Appendix A Potential of the vertical lattice

In this appendix, we derive the approximate harmonic potential given by the shallow-angle vertical lattice described in Chap. 2.

The electric field of a single beam with wavelength λ propagating along the x-axis is given by

$$E(x,y,z) = \sqrt{\frac{2P}{\pi w_y(x) w_z(y)}} e^{-\frac{y^2}{w_y^2(x)} - \frac{z^2}{w_z^2(x)}} e^{-i\left[kx + k\left(\frac{y^2}{2R_y(x)} + \frac{z^2}{2R_z(x)}\right) - \arctan\left(\frac{z}{z_R(x)}\right)\right]}, \tag{A.1}$$

where P is the beam's power, $w_{y,z}(x)$ are the beam's waists, $R_{y,z}(x)$ are the beam's radii of curvature and $z_R(x)$ is the beam's Rayleigh range. They are defined with respect of the $1/e^2$ beam's waists $w_{0,y,z}$ at the focus point $x = 0$ as

$$w_{y,z}(x) = w_{0,y,z}\sqrt{1 + \left(\frac{x}{z_{R,y,z}}\right)^2}, \tag{A.2}$$

$$z_{R,y,z} = \frac{\pi w_{0,y,z}^2}{\lambda}, \tag{A.3}$$

$$R_{y,z}(x) = x\left[1 + \left(\frac{z_{R,y,z}}{x}\right)^2\right]. \tag{A.4}$$

At the interference point, the electric fields $\mathbf{E}_{a,b}$ of the two beams forming the vertical lattice sum and the total intensity I and trap depth U_0 are

$$I(x,y,z) = \frac{1}{2} c\epsilon_0 \,|E_a(x_a, y_a, z_a) + E_b(x_b, y_b, z_b)|^2, \tag{A.5}$$

$$U_0 = -\alpha' I(x,y,z), \qquad \alpha' = \frac{\alpha}{2\epsilon_0 c}, \tag{A.6}$$

where α is the polarizability.

If the two beams are propagating along x with a small angle with respect to the z-axis, we transform the coordinate system of the two beams:

$$\begin{cases} x_a = x\cos\theta + z\sin\theta, \\ y_a = y, \\ z_a = -x\sin\theta + z\cos\theta, \end{cases} \qquad \begin{cases} x_b = x\cos\theta - z\sin\theta, \\ y_b = y, \\ z_b = x\sin\theta + z\cos\theta. \end{cases} \tag{A.7}$$

By assuming the same beam waists $w_{0,\{h,v\}}$ and Rayleigh ranges $z_{\mathrm{R},\{h,v\}}$ for the two beams and expanding the electric fields to second order we can calculate the harmonic trapping frequencies:

$$\omega_x^2 = \frac{2\alpha'}{m}\left[\frac{2}{w_{0,v}^2}\sin^2\theta + \frac{1}{2}\left(\frac{1}{z_{\mathrm{R},h}^2} + \frac{1}{z_{\mathrm{R},v}^2}\right)\cos^2\theta\right]\left(\sqrt{I_{0,a}} + \sqrt{I_{0,b}}\right)^2, \tag{A.8}$$

$$\omega_y^2 = \frac{4\alpha'}{m w_{0,h}^2}\left(\sqrt{I_{0,a}} + \sqrt{I_{0,b}}\right)^2, \tag{A.9}$$

$$\omega_z^2 = \frac{2\alpha'}{m}\left[\frac{2}{w_{0,v}^2}\cos^2\theta + \frac{1}{2}\left(\frac{1}{z_{\mathrm{R},h}^2} + \frac{1}{z_{\mathrm{R},v}^2}\right)\sin^2\theta\right]\left(\sqrt{I_{0,a}} + \sqrt{I_{0,b}}\right)^2, \tag{A.10}$$

where $I_{0,\{a,b\}}$ is the intensity of the beams a and b:

$$I_{0,\{a,b\}} = \frac{2P_{\{a,b\}}}{\pi w_{0,h} w_{0,v}}. \tag{A.11}$$

Appendix B Analytical models in the bulk

In this appendix, we derive the thermodynamics of non-interacting Fermi gases in free space. In Sec. B.1, we focus on the description of 2D Fermi gases in homogeneous and harmonic potentials. These models are relevant for the determination of the EoS described in Chap. 3. In Sec. B.2, we present a similar derivation for the 3D case, which is relevant for the description of the 3D Fermi gases described in Chap. 1, Fig. 1.6.

B.1 Non-interacting 2D Fermi gas

Harmonic potential

In this section, we consider the case of an SU(N) non-interacting gas in a harmonic potential $V = \frac{1}{2}m\left(\omega_x^2 x^2 + \omega_y^2 y^2\right)$, where m is the mass of the atoms and (ω_x, ω_y) are the trapping frequencies. In this case, the density of states for a N-components gas is

$$\rho(\epsilon) = N\frac{\epsilon}{\hbar^2\bar{\omega}^2}, \tag{B.1}$$

where $\bar{\omega} = \sqrt{\omega_x\omega_y}$ and ϵ is the energy. The total number of particles is obtained by integrating the density of states up to the Fermi energy E_F

$$N_p = \int_0^\infty \rho(\epsilon)\mathrm{Pr}(\epsilon)\mathrm{d}\epsilon = \int_0^\infty \rho(\epsilon)\mathrm{H}(E_\mathrm{F} - \epsilon)\mathrm{d}\epsilon = N\frac{1}{2}\frac{E_\mathrm{F}^2}{\hbar^2\bar{\omega}^2}, \tag{B.2}$$

where H(x) is the Heaviside function. From Eq. (B.2), we see that the Fermi energy is:

$$E_\mathrm{F} = \hbar\bar{\omega}\sqrt{2N_p/N}. \tag{B.3}$$

In the grand canonical ensemble, the grand potential Ω can be calculated as

$$\Omega(\mu,T) = N k_{\mathrm{B}} T \int_0^{\infty} \mathrm{d}\epsilon \rho(\epsilon) \log[1 - F(\epsilon)], \qquad \text{with } F(\epsilon) = \frac{1}{\frac{1}{z} e^{\beta\epsilon} + 1}. \tag{B.4}$$

After integrating by parts, we get

$$\Omega(\mu,T) = \frac{N}{\hbar^2 \bar{\omega}^2 \beta^3} \mathrm{Li}_3(-z), \tag{B.5}$$

where $z = e^{\beta\mu}$ is the fugacity, $\beta = 1/(k_{\mathrm{B}} T)$ and $\mathrm{Li}_s(z)$ is the polylogarithm of order s and argument z (see Appendix D for some properties of the polylogarithm). The most relevant thermodynamic quantities can be derived from the grand potential. The number of particles is

$$N_p(\mu,T) = -\frac{\partial \Omega}{\partial \mu} = -\frac{N}{\hbar^2 \bar{\omega}^2 \beta^2} \mathrm{Li}_2(-z). \tag{B.6}$$

Combining Eqs. (B.3) and (B.6), we get an analytical expression which relates $T_{\mathrm{F}} = E_{\mathrm{F}}/k_{\mathrm{B}}$ to the fugacity z:

$$\frac{T}{T_{\mathrm{F}}} = \frac{1}{\sqrt{-2\mathrm{Li}_2(-z)}}. \tag{B.7}$$

The entropy is

$$S(\mu,T) = -\frac{\partial \Omega}{\partial T} = -\frac{N k_{\mathrm{B}}}{\hbar^2 \bar{\omega}^2 \beta} \left[\frac{3}{\beta} \mathrm{Li}_3(-z) - \mu \mathrm{Li}_2(-z) \right]. \tag{B.8}$$

Expanding the polylogarithms for low temperatures ($T \ll T_{\mathrm{F}}$) and using Eq. (B.3), we get the approximate relation for the entropy per particle:

$$s \equiv S/N_p \approx k_{\mathrm{B}} \frac{2}{3} \pi^2 \left(\frac{T}{T_{\mathrm{F}}} \right). \tag{B.9}$$

Homogeneous potential

In this section, we consider the case of a gas in a homogeneous potential. The density of states for a N-components homogeneous system is

$$\rho = N \frac{m}{2\pi\hbar^2}. \tag{B.10}$$

The derivation of the grand potential Ω and the thermodynamic quantities is similar to the one in the previous section, and we report here the main results:

$$\Omega(\mu,T) \;=\; N \frac{m}{2\pi\hbar^2 \beta^2} \mathrm{Li}_2(-z), \tag{B.11}$$

$$n(\mu,T) = -\frac{\partial\Omega}{\partial\mu} = -N\frac{m}{2\pi\hbar^2\beta}\mathrm{Li}_1(-z), \tag{B.12}$$

$$\kappa(\mu,T) = \frac{\partial n}{\partial\mu} = N\frac{m}{2\pi\hbar^2}\frac{z}{z+1}, \tag{B.13}$$

$$S(\mu,T) = -\frac{\partial\Omega}{\partial T} = -N\frac{mk_\mathrm{B}}{2\pi\hbar^2}\left[\frac{2}{\beta}\mathrm{Li}_2(-z) - \mu\mathrm{Li}_1(-z)\right]. \tag{B.14}$$

By relating the density of Eq. (B.12) with the Fermi energy calculated similarly to what has been done in Eq. (B.2), we get an analytical result that relates the chemical potential at finite temperature to the Fermi energy:

$$\mu = \frac{1}{\beta}\log\left(e^{\beta E_\mathrm{F}} - 1\right). \tag{B.15}$$

Concerning the compressibility, we note that, by combining Eq. (B.12) with Eq. (B.13), it can also be expressed as a function of the density as

$$\kappa(n,T) = \rho\left[1 - e^{-\beta n/\rho}\right]. \tag{B.16}$$

B.2 Non-interacting 3D Fermi gas

Harmonic potential

In the 3D harmonic trap, the density of state is

$$\rho(\epsilon) = \frac{\epsilon^2}{2\hbar^3\bar{\omega}^3}, \tag{B.17}$$

where we define $\bar{\omega} = (\omega_x\omega_y\omega_z)^{1/3}$ Following the same procedure of the 2D case, we get that

$$\Omega = N\frac{1}{\hbar^3\bar{\omega}^3\beta^4}\mathrm{Li}_4(-z), \tag{B.18}$$

$$N_p = -N\frac{1}{\hbar^3\bar{\omega}^3\beta^3}\mathrm{Li}_3(-z), \tag{B.19}$$

$$S = N\frac{k_\mathrm{B}}{\hbar^3\bar{\omega}^3\beta^2}\left[\mu\mathrm{Li}_3(-z) - \frac{4}{\beta}\mathrm{Li}_4(-z)\right]. \tag{B.20}$$

(B.21)

The Fermi temperature is related to the total atom number and the fugacity by the following equations:

$$T_\mathrm{F} = \hbar\bar{\omega}\,(6N_p/N)^{1/3}, \tag{B.22}$$

$$T/T_\mathrm{F} = \left[-\frac{1}{6\mathrm{Li}_3(-z)}\right]^{1/3}. \tag{B.23}$$

Homogeneous potential

In the 3D case, for a homogeneous potential, the density of state is

$$\rho(\epsilon) = \frac{2\pi(2m)^{3/2}V}{h^3}\sqrt{\epsilon}, \tag{B.24}$$

where ϵ is the energy, V is the volume, m the mass. Following the same procedure of the 2D case, we get that

$$\Omega = N\frac{V}{\lambda_T^3\beta}\mathrm{Li}_{5/2}(-z), \tag{B.25}$$

$$n = -N\frac{1}{\lambda_T^3}\mathrm{Li}_{3/2}(-z), \tag{B.26}$$

$$\kappa = -N\frac{\beta}{\lambda_T^3}\mathrm{Li}_{1/2}(-z), \tag{B.27}$$

$$S = \frac{NVk_\mathrm{B}^2\beta^2}{\lambda_T^3}\left[2\mu\mathrm{Li}_{3/2}(-z) - \frac{5}{\beta}\mathrm{Li}_{5/2}(-z)\right], \tag{B.28}$$

where $\lambda_T = h/\sqrt{2\pi mk_\mathrm{B}T}$ is the thermal de Broglie wavelength.

In LDA, for a harmonic oscillator, $\mu = \mu_0 - \frac{1}{2}m\left(\omega_x^2x^2 + \omega_y^2y^2 + \omega_z^2z^2\right)$. We can integrate along the z direction by using Eq. (D.7) to get the density in the $x-y$ plane:

$$n(x,y) = -N\frac{2\pi\hbar}{\omega_z m\lambda_T^4}\mathrm{Li}_2\left\{-e^{-\beta\left[\mu_0-\frac{1}{2}m\left(\omega_x^2x^2+\omega_y^2y^2\right)\right]}\right\}. \tag{B.29}$$

Interactions

Interactions can be included in the 3D case in a similar way of what we have done in the 2D case in Sec. 3.3. Ref. [287] gives the following expression for the chemical potential of an SU(N) weakly-interacting Fermi gas in 3D in the homogeneous case:

$$\mu(n,T,a) \simeq E_\mathrm{F}\left[1 - \frac{\pi^2}{12}\left(\frac{T}{T_\mathrm{F}}\right)^2 + \frac{4}{3\pi}(N-1)k_\mathrm{F}a + \frac{4(11-2\log 2)}{15\pi^2}(k_\mathrm{F}a)^2(N-1)\right] + CT^2a^2, \tag{B.30}$$

where C is a constant independent of the density n, a is the 3D scattering length and the Fermi parameters depend on n.

Furthermore, Refs. [161, 284, 361] contain analytical corrections to some relevant thermodynamic quantities.

Appendix C Analytical models in the lattice

In this appendix, we present the derivation of some analytical models describing the thermodynamics of the SU(N) FHM.

C.1 Atomic limit

By setting $t = 0$, the SU(N) FHM Hamiltonian (Eq. 4.1) becomes

$$\hat{H} = \frac{U}{2} \sum_{i,\sigma \neq \tau} \hat{n}_{i\sigma} \hat{n}_{i\tau} - \mu \sum_{i,\sigma} \hat{n}_{i\sigma}. \tag{C.1}$$

Its eigenenergies are

$$\epsilon(n) = \frac{U}{2} n(n-1) - \mu n. \tag{C.2}$$

The total partition function $\mathcal{Z} = \mathrm{Tr}\left[e^{-\beta \hat{H}}\right]$ can be expressed as product of the single-site partition function z_0 such that $\mathcal{Z} = z_0^{N_s}$ (N_s is the number of lattice sites). The single-site partition function is

$$z_0(\mu, T, U, N) = \sum_{m=0}^{N} \binom{N}{m} e^{-\beta \epsilon(m)}. \tag{C.3}$$

The grand potential is

$$\Omega(\mu, T, U, N) = -\frac{1}{\beta} \log\left[z_0(\mu, T, U, N)\right]. \tag{C.4}$$

The expectation value of observable $\langle \hat{A} \rangle$ can be calculated as

$$\langle \hat{A} \rangle = \mathrm{Tr}\left[e^{-\beta \hat{H}} \hat{A}\right] / z_0. \tag{C.5}$$

The internal energy per lattice site is

$$\varepsilon = \langle \hat{\epsilon} + \mu \hat{n} \rangle = \frac{1}{z_0} \sum_{m=0}^{N} \frac{U}{2} m(m-1) \binom{N}{m} e^{-\beta \epsilon(m)}. \tag{C.6}$$

The entropy per lattice site is

$$s_0 = -\frac{\partial \Omega}{\partial T} = k_{\mathrm{B}} \log z_0 + \frac{1}{T} \langle \hat{\epsilon} \rangle. \tag{C.7}$$

The density per lattice site is

$$n = \langle \hat{n} \rangle = -\frac{\partial \Omega}{\partial \mu} = \frac{1}{z_0} \sum_{m=0}^{N} m \binom{N}{m} e^{-\beta \epsilon(m)}. \tag{C.8}$$

The compressibility is

$$\begin{aligned} \kappa &= \frac{\partial n}{\partial \mu} = \beta \left[\frac{1}{z_0} \sum_{m=0}^{N} m^2 \binom{N}{m} e^{-\beta \epsilon(m)} - \left(\frac{1}{z_0} \sum_{m=0}^{N} m \binom{N}{m} e^{-\beta \epsilon(m)} \right)^2 \right] && \text{(C.9)} \\ &= \beta \left[\langle \hat{n}^2 \rangle - \langle \hat{n} \rangle^2 \right] = \beta \mathrm{var}(\hat{n}). && \text{(C.10)} \end{aligned}$$

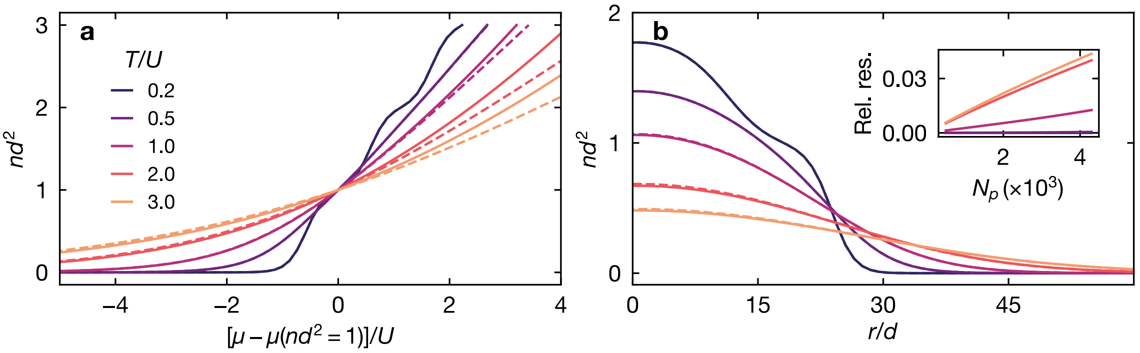

Figure C.1 | Two-bands atomic limit for $N = 6$. **a** Total density per lattice site as a function of the chemical potential (the zero of the chemical potential has been set at $nd^2 = 1$). **b** Radial profiles for $N_p = 2 \times 10^3$ atoms in a harmonic potential with $\kappa_{x,y} = 0.005\,U$. The continuous line corresponds to the atomic limit model assuming all the atoms in the lowest band. The dashed line corresponds to the correction to the atomic limit including the first excited band in the vertical direction ($n = n_0 + n_1$). **Inset**: relative residuals at the center of the cloud between the two-bands and the single-band atomic limit models as a function of the total atom number. The vertical bandgap is $\Delta = 3.95\,\mathrm{kHz}$.

The components of the site-occupation distribution p_α are

$$\langle \hat{p}_\alpha \rangle = \frac{1}{z_0} \binom{N}{\alpha} e^{-\beta\epsilon(\alpha)}, \tag{C.11}$$

and they fulfill the normalization condition $\langle \hat{n} \rangle = \sum_\alpha \alpha \langle \hat{p}_\alpha \rangle$.

C.2 Two-bands atomic limit

In this section, we consider the extension of the atomic limit model to higher bands. In our experiment, we operate in the central plane of a vertical lattice with a typical bandgap of ca. 4 kHz. At low temperatures, we are reasonably sure to operate in the lowest band (see Sec. 3.2), but at high enough temperatures the first excited band may be populated. We therefore expand the atomic limit to consider two bands and we verify that the contribution of the excited one is negligible for our experimental parameters.

In this case, the eigenenergies are

$$\epsilon(n_0, n_1) = \frac{U_{00}}{2} n_0(n_0 - 1) + \frac{U_{01}}{2} n_0 n_1 + \frac{U_{11}}{2} n_1(n_1 - 1) + \Delta n_1 - \mu(n_0 + n_1) \tag{C.12}$$

where n_0 and n_1 represent the density in the lowest and the first vertical band, respectively. Δ is the bandgap between the two bands and

$$U_{ij} = \frac{4\pi\hbar^2}{m} a \int |w_{00}(x)|^2 |w_{00}(y)|^2 |w_{ij}(z)|^2 \, \mathrm{d}\boldsymbol{x} \tag{C.13}$$

is the on-site interaction considering the lowest in-plane bands and vertical bands i and

j (w_{ij} is the corresponding Wannier overlap, a is the scattering length, m is the mass). The partition function is

$$z_0' = \sum_{n_0=0}^{N} \sum_{n_1=0}^{N} \binom{N}{n_0} \binom{N}{n_1} e^{-\beta\epsilon(n_0,n_1)} \tag{C.14}$$

And the total density per lattice site is

$$\langle \hat{n} \rangle = \frac{1}{z_0'} \sum_{n_0,n_1} \left[(n_0+n_1) \binom{N}{n_0} \binom{N}{n_1} e^{-\beta\epsilon(n_0,n_1)} \right]. \tag{C.15}$$

In Fig. C.1 we compare the equation of state with all the atoms in the lowest band with its two-band extension for the values of U_{ij} and Δ calculated for our experimental parameters. The correction becomes first relevant at high temperatures ($T \gtrsim U$) and high densities ($nd^2 \gtrsim 2$). For the experiments presented in Chap. 5 the correction is therefore negligible.

C.3 High-temperature series expansion

In high-temperature series expansion (HTSE), we start from the atomic limit Hamiltonian of Eq. (C.1) and we add the kinetic energy K as a perturbation:

$$K = -t \sum_{\langle ij \rangle,\sigma} \left(\hat{c}_{i,\sigma}^{\dagger} \hat{c}_{j,\sigma} + \text{h.c.} \right). \tag{C.16}$$

By performing a second order expansion in βt and using the formalism of thermodynamic perturbation theory [322, 324], the total partition function $\mathcal{Z}$ becomes

$$\mathcal{Z} \simeq z_0^{N_s} \left[1 + \int_0^{\beta} \mathrm{d}\tau_1 \int_0^{\tau_2} \mathrm{d}\tau_2 \langle \tilde{K}(\tau_1) \tilde{K}(\tau_2) \rangle \right], \tag{C.17}$$

with $\tilde{K}(\tau) = e^{\tau H_0} K e^{-\tau H_0}$. By taking the logarithm, the grand potential can therefore be written as $\Omega \simeq \Omega_0 + \Delta\Omega$. Ω_0 is the grand potential in the atomic limit and

$$\begin{aligned} -\beta\Delta\Omega = zN \left(\frac{\beta t}{z_0} \right)^2 \Bigg[& \frac{1}{2} \sum_{n=1}^{N} \binom{N-1}{n-1}^2 x^{2n-1} y^{(n-1)^2} \\ & - \frac{1}{\beta U} \sum_{n \neq m} \binom{N-1}{n-1} \binom{N-1}{m-1} \frac{x^{n+m-1} y^{\frac{1}{2}[n(n-1)+(m-1)(m-2)]}}{n-m} \Bigg], \end{aligned} \tag{C.18}$$

where z is the number of next neighbors in the lattice, $x = e^{\beta\mu}$ and $y = e^{-\beta U}$. This equation can be rewritten in a more convenient form as

$$-\beta\Delta\Omega = zN \left(\frac{\beta t}{z_0} \right) (F[1] + G[1]), \tag{C.19}$$

with

$$F[f(n,m)] = \frac{1}{2}\sum_{n=1}^{N}\binom{N-1}{n-1}x^{2n-1}y^{(n-1)^2}f(n,m), \tag{C.20}$$

$$G[f(n,m)] = -\frac{1}{\beta U}\sum_{n\neq m}\binom{N-1}{n-1}\binom{N-1}{m-1}\frac{x^{n+m-1}y^{\frac{1}{2}[n(n-1)+(m-1)(m-2)]}}{n-m}f(n,m). \tag{C.21}$$

We then get the correction to the density

$$\langle\Delta\hat{n}\rangle = zN\left(\frac{\beta t}{z_0}\right)\left[-2\langle n\rangle_0\left(F[1]+G[1]\right)+F[2n-1]+G[n+m-1]\right], \tag{C.22}$$

where $\langle\cdot\rangle_0$ is the expectation value in the atomic limit. To calculate the correction to the site-occupation distribution Δp_α, we consider a small coupling in the eigenenergies as a perturbation:

$$\epsilon(n,\alpha) = \frac{U}{2}n(n-1)-\mu n+g\delta_{n,\alpha}. \tag{C.23}$$

We can now calculate

$$\langle\Delta\hat{p}_\alpha\rangle = \lim_{g\to 0}\frac{\partial\Delta\Omega}{\partial g}, \tag{C.24}$$

and we get

$$\langle\Delta\hat{p}_\alpha\rangle = zN\left(\frac{\beta t}{z_0}\right)^2\left[-2\langle\hat{p}_\alpha\rangle_0\left(F[1]+G[1]\right)+F[\delta_{\alpha,n}+\delta_{\alpha,n-1}]+G[\delta_{\alpha,n}+\delta_{\alpha,m-1}]\right], \tag{C.25}$$

where $\langle p_\alpha\rangle_0$ is the unperturbed value from Eq. (C.11). The full derivation can be found in Refs. [87, 340].

C.4 Non-interacting limit

In the non-interacting limit $U=0$ the SU(N) FHM becomes

$$\hat{H} = -t\sum_{\langle i,j\rangle,\sigma}\left(\hat{c}^\dagger_{i\sigma}\hat{c}_{j\sigma}+\text{h.c.}\right)-\mu\sum_{i,\sigma}\hat{n}_{i\sigma}. \tag{C.26}$$

By applying the transformation $\hat{c}_{r,\sigma} = 1/N_s\sum_{\boldsymbol{k}}e^{-i\boldsymbol{k}\cdot\boldsymbol{r}}\hat{c}_{\boldsymbol{k}\sigma}$ with $\boldsymbol{k}=(k_x,k_y)$ we diagonalize the Hamiltonian, which becomes

$$\hat{H} = \sum_{\boldsymbol{k},\sigma}(\epsilon_{\boldsymbol{k}}-\mu)\hat{n}_{\boldsymbol{k}\sigma}, \tag{C.27}$$

with the dispersion relation

$$\epsilon_{\boldsymbol{k}} = -2t\left[\cos(k_x d)+\cos(k_y d)\right], \tag{C.28}$$

where d is the lattice spacing. The partition function is

$$\mathcal{Z} = \mathrm{Tr}\left[e^{-\beta\hat{H}}\right] = \sum_{\boldsymbol{k}}\left[1 + e^{-\beta(\epsilon_k-\mu)}\right]^N. \tag{C.29}$$

The grand potential is

$$\begin{aligned} \Omega &= -\frac{1}{\beta}\log Z = -\frac{N}{\beta}\sum_{\boldsymbol{k}}\log\left[1+e^{-\beta(\epsilon_k-\mu)}\right] && \text{(C.30)} \\ &= -\frac{N}{\beta(2\pi)^2}\int_{-\pi}^{\pi}\mathrm{d}^2\boldsymbol{k}\log\left[1+e^{-\beta(\epsilon_k-\mu)}\right]. && \text{(C.31)} \end{aligned}$$

The density per lattice site is

$$\begin{aligned} n = \langle\hat{n}\rangle &= \frac{1}{\mathcal{Z}}\mathrm{Tr}\left[\hat{n}e^{-\beta\hat{H}}\right] && \text{(C.32)} \\ &= \frac{N}{(2\pi)^2}\int_{-\pi}^{\pi}\mathrm{d}^2\boldsymbol{k}\frac{1}{1+e^{\beta(\epsilon_k-\mu)}}. && \text{(C.33)} \end{aligned}$$

The compressibility is

$$\kappa = \frac{\partial n}{\partial\mu} = \frac{N\beta}{(2\pi)^2}\int_{-\pi}^{\pi}\mathrm{d}^2\boldsymbol{k}\frac{e^{\beta(\epsilon_k-\mu)}}{1+e^{\beta(\epsilon_k-\mu)}}. \tag{C.34}$$

The entropy per lattice site is

$$s_0 = -\frac{\partial\Omega}{\partial T} = \frac{N}{(2\pi)^2}\int_{-\pi}^{\pi}\mathrm{d}^2\boldsymbol{k}\left\{\log\left[1+e^{-\beta(\epsilon_k-\mu)}\right] + \beta\frac{\epsilon_k-\mu}{1+e^{\beta(\epsilon_k-\mu)}}\right\}. \tag{C.35}$$

Appendix D Thermodynamic integrals and polylogarithm identities

In this appendix, we report some identities and series expansions useful when calculating thermodynamic properties of degenerate gases. In particular, these expressions have been used to derive some results presented in Chap. 3 and Appendix B.

Integrals of the Fermi-Dirac (or Bose-Dirac) distribution function across a density of states function of the energy ϵ can be solved analytically:

$$\int\frac{\epsilon^s}{\frac{1}{z}e^{\beta\epsilon}\mp 1}\mathrm{d}\epsilon = \pm\left(\frac{1}{\beta}\right)^{s+1}\Gamma(s+1)\mathrm{Li}_{s+1}(\pm z), \tag{D.1}$$

where $\Gamma(x)$ is the gamma function and $\mathrm{Li}_s(z)$ is the polylogarithm function of order s and argument z. The polylogarithm is defined by a power series:

$$\mathrm{Li}_s(z) = \sum_{k=1}^{\infty}\frac{z^k}{k^s}. \tag{D.2}$$

Polylogarithms of low order can be expressed in a simple form:

$$\begin{aligned} \mathrm{Li}_0(z) &= \frac{z}{1-z}, & \text{(D.3)} \\ \mathrm{Li}_1(z) &= -\log(1-z). & \text{(D.4)} \end{aligned}$$

When integrating and deriving the polylogarithm, the following identities hold:

$$z\frac{\partial \mathrm{Li}_s(z)}{\partial z} = \mathrm{Li}_{s-1}(z), \tag{D.5}$$

$$\frac{\partial \mathrm{Li}_s(e^\mu)}{\partial \mu} = \mathrm{Li}_{s-1}(e^\mu). \tag{D.6}$$

Another useful identity is the following:

$$\int_{-\infty}^{\infty} \mathrm{d}z\, \mathrm{Li}_n\left(-e^{\beta\mu}e^{-z^2}\right) = \sqrt{\pi}\mathrm{Li}_{n+1/2}\left(-e^{\beta\mu}\right). \tag{D.7}$$

Finally, when calculating thermodynamic properties at low temperatures, the following series expansions can be useful:

$$\begin{aligned} \lim_{x\to\infty} x\mathrm{Li}_2(-e^x) &= -\frac{x^3}{2} - \frac{\pi^2}{6}x + O\left(\frac{1}{x}\right)^7, & \text{(D.8)} \\ \lim_{x\to\infty} \mathrm{Li}_3(-e^x) &= -\frac{x^3}{6} - \frac{\pi^2}{6}x + O\left(\frac{1}{x}\right)^7. & \text{(D.9)} \end{aligned}$$

Appendix E Benchmarking numerical methods

E.1 Comparison of fit results with different numerical methods

In Tab. E.1, we compare the results of fits performed on the data of Fig. 5.4 with different numerical methods. For NLCE, the agreement between two consecutive orders indicates that the method has converged. In Fig. E.1, we compare the fits of the density profiles for $N = 6$ in real space coordinates.

E.2 Systematic errors from the numerics

In this section, we estimate the systematic errors in the determination of the EoS due to the numerics. A more detailed discussion of the technical implementation of the DQMC and NLCE methods and their systematic errors can be found in Refs. [50, 87]. Here, we only summarize the main points.

For DQMC simulations, we estimate the systematic error due to the Trotter approximation of about $0.03\,t$ in the temperature and $0.06\,k_\mathrm{B}$ in the entropy per particle. The error made by the finite-size extrapolation is estimated to be $0.07\,t$ in the temperature and $0.13\,k_\mathrm{B}$ in the entropy per particle for $U/t = 2.34$. For other values of U/t, the error is $0.04\,t$ in the temperature and $0.03\,k_\mathrm{B}$ in the entropy. The error due to the grid size and interpolation is estimated to be $0.007\,t$ in the temperature and $0.05\,k_\mathrm{B}$ in the entropy per particle.

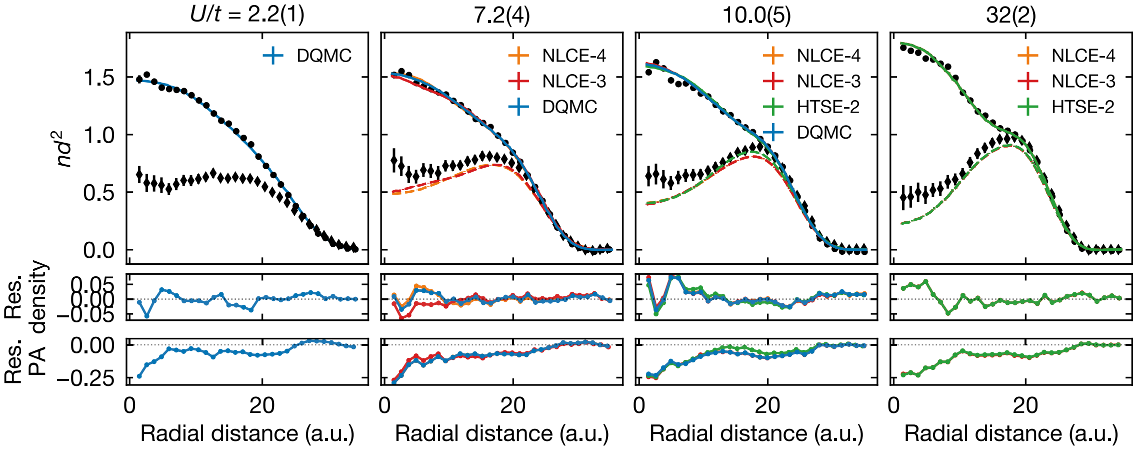

Figure E.1 | Radial density profiles for $N = 6$ (same dataset of Fig. 5.4) and comparison of the fit with different methods. **First row** Black circles: radially averaged measured density profiles. Black diamonds: radially averaged parity-projected density profiles. Continuous lines: fit of the density profiles with different methods. Dashed lines: plot of the expected parity-projected density profiles according to the fit of the density (same color code). **Second row** Residuals of the fit of the density profiles. **Third row** Residuals of the parity-projected density profiles. The second and third rows have the same color code as the first one.

For NLCE simulations, the computation of the observables is performed on a dense grid of chemical potential values and temperatures and we estimate the relative error to be negligible. For HTSE and AL simulations, the chemical potential is also computed on a dense grid and the error is estimated to be negligible.

N	U/t	N_p ($\times 10^3$)	Method	T/t	T/U	s/k_B
3	2.3(1)	1.98(2)	DQMC	0.40(4)	0.17(2)	
	7.5(4)	1.96(2)	NLCE-6	1.24(3)	0.167(4)	1.50(6)
			NLCE-7	1.24(3)	0.167(4)	1.50(6)
	10.4(6)	1.94(3)	NLCE-6	1.69(4)	0.163(4)	1.55(6)
			NLCE-7	1.69(4)	0.163(4)	1.55(6)
			HTSE-2	1.69(4)	0.163(4)	1.56(6)
	33(2)	1.99(2)	NLCE-6	5.0(1)	0.149(3)	1.51(4)
			NLCE-7	5.0(1)	0.149(3)	1.51(4)
			HTSE-2	5.0(1)	0.149(3)	1.51(4)
4	2.3(1)	1.99(1)	DQMC	0.32(3)	0.13(1)	
	7.5(4)	1.99(1)	DQMC	0.97(3)	0.130(4)	1.61(7)
			NLCE-4	0.98(3)	0.131(3)	1.59(6)
			NLCE-5	0.94(3)	0.126(4)	1.57(7)
	10.4(6)	1.99(1)	DQMC	1.36(4)	0.131(4)	1.73(6)
			NLCE-4	1.42(4)	0.137(4)	1.73(6)
			NLCE-5	1.41(4)	0.136(4)	1.72(6)
			HTSE-2	1.43(4)	0.138(3)	1.76(7)
	33(2)	1.99(1)	NLCE-4	4.62(9)	0.139(3)	1.78(5)
			NLCE-5	4.62(9)	0.139(3)	1.78(5)
			HTSE-2	4.63(9)	0.139(3)	1.78(5)
6	2.3(1)	1.99(1)	DQMC	0.30(1)	0.127(1)	
	7.5(4)	1.99(1)	DQMC	0.91(3)	0.122(4)	1.95(9)
			NLCE-3	0.94(3)	0.126(4)	1.97(8)
			NLCE-4	0.91(2)	0.122(3)	1.90(7)
	10.4(6)	2.05(1)	DQMC	1.35(4)	0.131(4)	2.11(8)
			NLCE-3	1.40(4)	0.135(3)	2.10(8)
			NLCE-4	1.38(4)	0.133(4)	2.08(8)
			HTSE-2	1.48(3)	0.142(3)	2.15(9)
	33(2)	2.00(1)	NLCE-3	3.99(8)	0.120(2)	2.12(6)
			NLCE-4	3.99(8)	0.120(2)	2.12(6)
			HTSE-2	4.06(8)	0.122(2)	2.13(6)

Table E.1 | Comparison of the parameters returned by the fit of the data in Fig. 5.4. For HTSE and NLCE methods, the number indicates the order. The uncertainties correspond to the values returned by the fit and do not take into account additional systematic errors.

References

[1] P. W. Anderson, *More Is Different*, Science **177**, 393 (1972) (cit. on p. 1).

[2] J. Bardeen, L. N. Cooper, and J. R. Schrieffer, *Theory of Superconductivity*, Physical Review **108**, 1175 (1957) (cit. on p. 1).

[3] J. Kondo, *Resistance Minimum in Dilute Magnetic Alloys*, Progress of Theoretical Physics **32**, 37 (1964) (cit. on pp. 1, 20).

[4] H. K. Onnes, *The Superconductivity of Mercury*, Communications from the Physical Laboratory of the University of Leiden, 122 (1911) (cit. on p. 1).

[5] W. J. de Haas, J. de Boer, and G. J. van dën Berg, *The Electrical Resistance of Gold, Copper and Lead at Low Temperatures*, Physica **1**, 1115 (1934) (cit. on pp. 1, 20).

[6] P. Coleman, *Introduction to Many-Body Physics* (Cambridge University Press, 2015) (cit. on p. 1).

[7] Y. Tokura and N. Nagaosa, *Orbital Physics in Transition-Metal Oxides*, Science **288**, 462 (2000) (cit. on pp. 1, 2, 11).

[8] P. Coleman, *Heavy Fermions: Electrons at the Edge of Magnetism*, in *Handbook of magnetism and advanced magnetic materials* (John Wiley & Sons, Ltd, 2007) (cit. on pp. 1, 20, 21).

[9] H.-H. Wen and S. Li, *Materials and Novel Superconductivity in Iron Pnictide Superconductors*, Annual Review of Condensed Matter Physics **2**, 121 (2011) (cit. on p. 1).

[10] B. Keimer, S. A. Kivelson, M. R. Norman, S. Uchida, and J. Zaanen, *From Quantum Matter to High-Temperature Superconductivity in Copper Oxides*, Nature **518**, 179 (2015) (cit. on p. 1).

[11] P. A. Lee, N. Nagaosa, and X.-G. Wen, *Doping a Mott Insulator: Physics of High-Temperature Superconductivity*, Rev. Mod. Phys. **78**, 17 (2006) (cit. on pp. 1, 11).

[12] F. Steglich and S. Wirth, *Foundations of Heavy-Fermion Superconductivity: Lattice Kondo Effect and Mott Physics*, Reports on Progress in Physics **79**, 084502 (2016) (cit. on pp. 1, 21).

[13] M. Yi, Y. Zhang, Z.-X. Shen, and D. Lu, *Role of the Orbital Degree of Freedom in Iron-Based Superconductors*, npj Quantum Materials **2**, 1 (2017) (cit. on p. 1).

[14] E. Dagotto, T. Hotta, and A. Moreo, *Colossal Magnetoresistant Materials: The Key Role of Phase Separation*, Physics Reports **344**, 1 (2001) (cit. on pp. 1, 2, 11).

[15] M. Imada, A. Fujimori, and Y. Tokura, *Metal-Insulator Transitions*, Rev. Mod. Phys. **70**, 1039 (1998) (cit. on pp. 1, 11, 91).

[16] J. Hubbard, *Electron Correlations in Narrow Energy Bands*, Proceedings of the Royal Society of London. Series A, Mathematical and Physical Sciences **276**, 238 (1963) (cit. on p. 1).

[17] J. E. Hirsch, *Two-Dimensional Hubbard Model: Numerical Simulation Study*, Phys. Rev. B **31**, 4403 (1985) (cit. on pp. 1, 11, 12, 64, 78, 91).

[18] P. W. Anderson, *The Resonating Valence Bond State in* $\mathrm{La_2CuO_4}$, Science **235**, 1196 (1987) (cit. on pp. 1, 11).

[19] F. C. Zhang and T. M. Rice, *Effective Hamiltonian for the Superconducting* Cu *Oxides*, Phys. Rev. B **37**, 3759 (1988) (cit. on pp. 1, 11).

[20] I. Affleck, *Large-N Limit of* SU(N) *Quantum "Spin" Chains*, Phys. Rev. Lett. **54**, 966 (1985) (cit. on pp. 1, 2, 12).

[21] I. Affleck and J. B. Marston, *Large-n Limit of the Heisenberg-Hubbard Model: Implications for High-*T_c *Superconductors*, Phys. Rev. B **37**, 3774 (1988) (cit. on pp. 1, 2).

[22] J. B. Marston and I. Affleck, *Large-N Limit of the Hubbard-Heisenberg Model*, Phys. Rev. B **39**, 11538 (1989) (cit. on pp. 1, 2).

[23] Y. Q. Li, M. Ma, D. N. Shi, and F. C. Zhang, SU(4) *Theory for Spin Systems with Orbital Degeneracy*, Phys. Rev. Lett. **81**, 3527 (1998) (cit. on pp. 2, 11).

[24] A. C. Hewson, *The Kondo Problem to Heavy Fermions* (Cambridge University Press, 1993) (cit. on pp. 2, 20, 21).

[25] S. Florens and A. Georges, *Quantum Impurity Solvers Using a Slave Rotor Representation*, Phys. Rev. B **66**, 165111 (2002) (cit. on pp. 2, 11).

[26] L. de'Medici, A. Georges, and S. Biermann, *Orbital-Selective Mott Transition in Multiband Systems: Slave-spin Representation and Dynamical Mean-Field Theory*, Phys. Rev. B **72**, 205124 (2005) (cit. on pp. 2, 11).

[27] P. O. Sprau, A. Kostin, A. Kreisel, A. E. Böhmer, V. Taufour, P. C. Canfield, S. Mukherjee, P. J. Hirschfeld, B. M. Andersen, and J. C. S. Davis, *Discovery of Orbital-Selective Cooper Pairing in* FeSe, Science **357**, 75 (2017) (cit. on pp. 2, 11).

[28] M. O. Goerbig, *Electronic Properties of Graphene in a Strong Magnetic Field*, Rev. Mod. Phys. **83**, 1193 (2011) (cit. on pp. 2, 11).

[29] X. Y. Xu, K. T. Law, and P. A. Lee, *Kekulé Valence Bond Order in an Extended Hubbard Model on the Honeycomb Lattice with Possible Applications to Twisted Bilayer Graphene*, Phys. Rev. B **98**, 121406 (2018) (cit. on pp. 2, 11).

[30] Y.-Z. You and A. Vishwanath, *Superconductivity from Valley Fluctuations and Approximate* SO(4) *Symmetry in a Weak Coupling Theory of Twisted Bilayer Graphene*, npj Quantum Materials **4**, 1 (2019) (cit. on pp. 2, 11).

[31] Y. Da Liao, J. Kang, C. N. Breiø, X. Y. Xu, H.-Q. Wu, B. M. Andersen, R. M. Fernandes, and Z. Y. Meng, *Correlation-Induced Insulating Topological Phases at Charge Neutrality in Twisted Bilayer Graphene*, Phys. Rev. X **11**, 011014 (2021) (cit. on pp. 2, 11).

[32] H. Katsura and A. Tanaka, *Nagaoka States in the* SU(N) *Hubbard Model*, Phys. Rev. A **87**, 013617 (2013) (cit. on p. 2).

[33] Y. Li, E. H. Lieb, and C. Wu, *Exact Results for Itinerant Ferromagnetism in Multiorbital Systems on Square and Cubic Lattices*, Phys. Rev. Lett. **112**, 217201 (2014) (cit. on pp. 2, 10, 91).

[34] E. Bobrow, K. Stubis, and Y. Li, *Exact Results on Itinerant Ferromagnetism and the 15-Puzzle Problem*, Phys. Rev. B **98**, 180101 (2018) (cit. on pp. 2, 10, 91).

[35] N. D. Mermin and H. Wagner, *Absence of Ferromagnetism or Antiferromagnetism in One- or Two-Dimensional Isotropic Heisenberg Models*, Phys. Rev. Lett. **17**, 1133 (1966) (cit. on p. 2).

[36] M. Hermele, V. Gurarie, and A. M. Rey, *Mott Insulators of Ultracold Fermionic Alkaline Earth Atoms: Underconstrained Magnetism and Chiral Spin Liquid*, Phys. Rev. Lett. **103**, 135301 (2009) (cit. on pp. 2, 13, 19).

[37] C. Honerkamp and W. Hofstetter, *Ultracold Fermions and the* SU(N) *Hubbard Model*, Phys. Rev. Lett. **92**, 170403 (2004) (cit. on pp. 2, 12, 13, 19).

[38] I. Titvinidze, A. Privitera, S.-Y. Chang, S. Diehl, M. A. Baranov, A. Daley, and W. Hofstetter, *Magnetism and Domain Formation in* SU(N)*-Symmetric Multi-Species Fermi Mixtures*, New Journal of Physics **13**, 035013 (2011) (cit. on p. 2).

[39] Z. Cai, H.-H. Hung, L. Wang, and C. Wu, *Quantum Magnetic Properties of the* SU($2N$) *Hubbard Model in the Square Lattice: A Quantum Monte Carlo Study*, Phys. Rev. B **88**, 125108 (2013) (cit. on pp. 2, 12).

[40] D. Wang, Y. Li, Z. Cai, Z. Zhou, Y. Wang, and C. Wu, *Competing Orders in the 2D Half-Filled* SU($2N$) *Hubbard Model through the Pinning-Field Quantum Monte Carlo Simulations*, Phys. Rev. Lett. **112**, 156403 (2014) (cit. on pp. 2, 65).

[41] A. Sotnikov and W. Hofstetter, *Magnetic Ordering of Three-Component Ultracold Fermionic Mixtures in Optical Lattices*, Phys. Rev. A **89**, 063601 (2014) (cit. on pp. 2, 12, 62).

[42] Z. Zhou, Z. Cai, C. Wu, and Y. Wang, *Quantum Monte Carlo Simulations of Thermodynamic Properties of* SU($2N$) *Ultracold Fermions in Optical Lattices*, Phys. Rev. B **90**, 235139 (2014) (cit. on pp. 2, 65).

[43] A. Sotnikov, *Critical Entropies and Magnetic-Phase-Diagram Analysis of Ultracold Three-Component Fermionic Mixtures in Optical Lattices*, Phys. Rev. A **92**, 023633 (2015) (cit. on pp. 2, 12, 13, 62).

[44] H. Yanatori and A. Koga, *Finite-Temperature Phase Transitions in the* SU(N) *Hubbard Model*, Phys. Rev. B **94**, 041110 (2016) (cit. on pp. 2, 12, 62, 65, 91).

[45] A. Golubeva, A. Sotnikov, A. Cichy, J. Kuneš, and W. Hofstetter, *Breaking of* SU(N) *Symmetry and Interplay between Strongly Correlated Phases in the Hubbard Model*, Phys. Rev. B **95**, 125108 (2017) (cit. on pp. 2, 62).

[46] A. Koga and H. Yanatori, *Spontaneously Symmetry Breaking States in the Attractive* SU(N) *Hubbard Model*, Journal of the Physical Society of Japan **86**, 034702 (2017) (cit. on p. 2).

[47] S.-S. B. Lee, J. von Delft, and A. Weichselbaum, *Filling-Driven Mott Transition in* SU(N) *Hubbard Models*, Phys. Rev. B **97**, 165143 (2018) (cit. on pp. 2, 62).

[48] D. Wang, L. Wang, and C. Wu, *Slater and Mott Insulating States in the* SU(6) *Hubbard Model*, Phys. Rev. B **100**, 115155 (2019) (cit. on pp. 2, 12).

[49] H. Yoshida and H. Katsura, *Rigorous Results on the Ground State of the Attractive* SU(N) *Hubbard Model*, Phys. Rev. Lett. **126**, 100201 (2021) (cit. on p. 2).

[50] E. Ibarra-García-Padilla, S. Dasgupta, H.-T. Wei, S. Taie, Y. Takahashi, R. T. Scalettar, and K. R. A. Hazzard, *Universal Thermodynamics of an* SU(N) *Fermi-Hubbard Model*, Phys. Rev. A **104**, 043316 (2021) (cit. on pp. 2, 3, 12, 61, 64, 65, 69, 77, 91, 103).

[51] V. Unukovych and A. Sotnikov, SU(4)*-Symmetric Hubbard Model at Quarter Filling: Insights from the Dynamical Mean-Field Approach*, Phys. Rev. B **104**, 245106 (2021) (cit. on pp. 2, 12, 13, 62).

[52] N. Read and S. Sachdev, *Some Features of the Phase Diagram of the Square Lattice* SU(N) *Antiferromagnet*, Nuclear Physics B **316**, 609 (1989) (cit. on p. 2).

[53] F. F. Assaad, *Phase Diagram of the Half-Filled Two-Dimensional* SU(N) *Hubbard-Heisenberg Model: A Quantum Monte Carlo Study*, Phys. Rev. B **71**, 075103 (2005) (cit. on pp. 2, 65).

[54] T. A. Tóth, A. M. Läuchli, F. Mila, and K. Penc, *Three-Sublattice Ordering of the* SU(3) *Heisenberg Model of Three-Flavor Fermions on the Square and Cubic Lattices*, Phys. Rev. Lett. **105**, 265301 (2010) (cit. on pp. 2, 13).

[55] M. Hermele and V. Gurarie, *Topological Liquids and Valence Cluster States in Two-Dimensional* SU(N) *Magnets*, Phys. Rev. B **84**, 174441 (2011) (cit. on pp. 2, 13).

[56] P. Corboz, A. M. Läuchli, K. Penc, M. Troyer, and F. Mila, *Simultaneous Dimerization and* SU(N) *Symmetry Breaking of 4-Color Fermions on the Square Lattice*, Phys. Rev. Lett. **107**, 215301 (2011) (cit. on p. 2).

[57] B. Bauer, P. Corboz, A. M. Läuchli, L. Messio, K. Penc, M. Troyer, and F. Mila, *Three-Sublattice Order in the* SU(3) *Heisenberg Model on the Square and Triangular Lattice*, Phys. Rev. B **85**, 125116 (2012) (cit. on pp. 2, 13, 62).

[58] P. Nataf and F. Mila, *Exact Diagonalization of Heisenberg* SU(N) *Models*, Phys. Rev. Lett. **113**, 127204 (2014) (cit. on pp. 2, 13).

[59] C. Romen and A. M. Läuchli, *Structure of Spin Correlations in High-Temperature* SU(N) *Quantum Magnets*, Physical Review Research **2**, 043009 (2020) (cit. on p. 2).

[60] G. G. Batrouni and R. T. Scalettar, *Anomalous Decouplings and the Fermion Sign Problem*, Phys. Rev. B **42**, 2282 (1990) (cit. on pp. 2, 64).

[61] I. Bloch, *Ultracold Quantum Gases in Optical Lattices*, Nat. Phys. **1**, 23 (2005) (cit. on p. 2).

[62] I. Bloch, J. Dalibard, and S. Nascimbène, *Quantum Simulations with Ultracold Quantum Gases*, Nat. Phys. **8**, 267 (2012) (cit. on p. 2).

[63] C. Gross and I. Bloch, *Quantum Simulations with Ultracold Atoms in Optical Lattices*, Science **357**, 995 (2017) (cit. on pp. 2, 13).

[64] A. J. Daley, I. Bloch, C. Kokail, S. Flannigan, N. Pearson, M. Troyer, and P. Zoller, *Practical Quantum Advantage in Quantum Simulation*, Nature **607**, 667 (2022) (cit. on pp. 2, 91).

[65] Y. Takahashi, *Quantum Simulation of Quantum Many-Body Systems with Ultracold Two-Electron Atoms in an Optical Lattice*, Proceedings of the Japan Academy, Series B **98**, 141 (2022) (cit. on pp. 2, 6, 7, 14, 21, 90).

[66] M. A. Cazalilla, A. F. Ho, and M. Ueda, *Ultracold Gases of Ytterbium: Ferromagnetism and Mott States in an* SU(6) *Fermi System*, New Journal of Physics **11**, 103033 (2009) (cit. on pp. 2, 9, 10, 12, 42, 91).

[67] A. V. Gorshkov, M. Hermele, V. Gurarie, C. Xu, P. S. Julienne, J. Ye, P. Zoller, E. Demler, M. D. Lukin, and A. M. Rey, *Two-Orbital* SU(N) *Magnetism with Ultracold Alkaline-Earth Atoms*, Nat. Phys. **6**, 289 (2010) (cit. on pp. 2, 3, 7, 8, 10, 15, 18, 20, 21, 91, 92).

[68] M. Foss-Feig, M. Hermele, and A. M. Rey, *Probing the Kondo Lattice Model with Alkaline-Earth-Metal Atoms*, Phys. Rev. A **81**, 051603 (2010) (cit. on pp. 2, 3, 18, 20, 21, 92).

[69] M. Foss-Feig, M. Hermele, V. Gurarie, and A. M. Rey, *Heavy Fermions in an Optical Lattice*, Phys. Rev. A **82**, 053624 (2010) (cit. on pp. 2, 3, 18, 20, 21, 92).

[70] S. Taie, R. Yamazaki, S. Sugawa, and Y. Takahashi, *An* SU(6) *Mott Insulator of an Atomic Fermi Gas Realized by Large-Spin Pomeranchuk Cooling*, Nat. Phys. **8**, 825 (2012) (cit. on pp. 2, 9, 12, 14, 62, 68).

[71] X. Zhang, M. Bishof, S. L. Bromley, C. V. Kraus, M. S. Safronova, P. Zoller, A. M. Rey, and J. Ye, *Spectroscopic Observation of* SU(N)*-Symmetric Interactions in* Sr *Orbital Magnetism*, Science **345**, 1467 (2014) (cit. on pp. 2, 9).

[72] G. Pagano, M. Mancini, G. Cappellini, P. Lombardi, F. Schäfer, H. Hu, X.-J. Liu, J. Catani, C. Sias, M. Inguscio, and L. Fallani, *A One-Dimensional Liquid of Fermions with Tunable Spin*, Nat. Phys. **10**, 198 (2014) (cit. on pp. 2, 9, 42).

[73] C. Hofrichter, L. Riegger, F. Scazza, M. Höfer, D. R. Fernandes, I. Bloch, and S. Fölling, *Direct Probing of the Mott Crossover in the* SU(N) *Fermi-Hubbard Model*, Phys. Rev. X **6**, 021030 (2016) (cit. on pp. 2, 9, 14, 27, 43, 68, 72, 76).

[74] H. Ozawa, S. Taie, Y. Takasu, and Y. Takahashi, *Antiferromagnetic Spin Correlation of* SU(N) *Fermi Gas in an Optical Superlattice*, Phys. Rev. Lett. **121**, 225303 (2018) (cit. on pp. 2, 14).

[75] S. Taie, E. Ibarra-García-Padilla, N. Nishizawa, Y. Takasu, Y. Kuno, H.-T. Wei, R. T. Scalettar, K. R. A. Hazzard, and Y. Takahashi, *Observation of Antiferromagnetic Correlations in an Ultracold* SU(N) *Hubbard Model*, Nat. Phys. **18**, 1356 (2022) (cit. on pp. 2, 14, 65).

[76] D. Tusi, L. Franchi, L. F. Livi, K. Baumann, D. Benedicto Orenes, L. Del Re, R. E. Barfknecht, T.-W. Zhou, M. Inguscio, G. Cappellini, M. Capone, J. Catani, and L. Fallani, *Flavour-Selective Localization in Interacting Lattice Fermions*, Nat. Phys. **18**, 1201 (2022) (cit. on pp. 2, 14, 26, 91).

[77] W. F. McGrew, X. Zhang, R. J. Fasano, S. A. Schäffer, K. Beloy, D. Nicolodi, R. C. Brown, N. Hinkley, G. Milani, M. Schioppo, T. H. Yoon, and A. D. Ludlow, *Atomic Clock Performance Enabling Geodesy below the Centimetre Level*, Nature **564**, 87 (2018) (cit. on pp. 3, 7).

[78] L. Riegger, N. Darkwah Oppong, M. Höfer, D. R. Fernandes, I. Bloch, and S. Fölling, *Localized Magnetic Moments with Tunable Spin Exchange in a Gas of Ultracold Fermions*, Phys. Rev. Lett. **120**, 143601 (2018) (cit. on pp. 3, 20, 27).

[79] G. Cappellini, M. Mancini, G. Pagano, P. Lombardi, L. Livi, M. Siciliani de Cumis, P. Cancio, M. Pizzocaro, D. Calonico, F. Levi, C. Sias, J. Catani, M. Inguscio, and L. Fallani, *Direct Observation of Coherent Interorbital Spin-Exchange Dynamics*, Phys. Rev. Lett. **113**, 120402 (2014) (cit. on pp. 3, 20).

[80] F. Scazza, C. Hofrichter, M. Höfer, P. C. De Groot, I. Bloch, and S. Fölling, *Observation of Two-Orbital Spin-Exchange Interactions with Ultracold* SU(N)*-Symmetric Fermions*, Nat. Phys. **10**, 779 (2014) (cit. on pp. 3, 20, 27).

[81] K. Ono, Y. Saito, T. Ishiyama, T. Higomoto, T. Takano, Y. Takasu, Y. Yamamoto, M. Tanaka, and Y. Takahashi, *Observation of Nonlinearity of Generalized King Plot in the Search for New Boson*, Phys. Rev. X **12**, 021033 (2022) (cit. on p. 3).

[82] O. Bettermann, N. Darkwah Oppong, G. Pasqualetti, L. Riegger, I. Bloch, and S. Fölling, *Clock-Line Photoassociation of Strongly Bound Dimers in a Magic-Wavelength Lattice*, Phys. Rev. A **108**, L041302 (2023) (cit. on pp. 3, 16, 17, 20, 27, 37).

[83] M. Kanász-Nagy, Y. Ashida, T. Shi, C. P. Moca, T. N. Ikeda, S. Fölling, J. I. Cirac, G. Zaránd, and E. A. Demler, *Exploring the Anisotropic Kondo Model in and out of Equilibrium with Alkaline-Earth Atoms*, Phys. Rev. B **97**, 155156 (2018) (cit. on pp. 3, 20, 92).

[84] S. Goto and I. Danshita, *Quasiexact Kondo Dynamics of Fermionic Alkaline-Earth-Like Atoms at Finite Temperatures*, Phys. Rev. Lett. **123**, 143002 (2019) (cit. on pp. 3, 20, 92).

[85] S. Doniach, *The Kondo Lattice and Weak Antiferromagnetism*, Physica B+C **91**, 231 (1977) (cit. on pp. 3, 20, 21).

[86] Autumn School on Correlated Electrons, E. Pavarini, E. Koch, P. Coleman, Institute for Advanced Simulation, and German Research School for Simulation Sciences, eds., *Many-Body Physics: From Kondo to Hubbard: Lecture Notes of the Autumn School on Correlated Electrons 2015* (2015) (cit. on pp. 3, 20, 21).

[87] G. Pasqualetti, O. Bettermann, N. Darkwah Oppong, E. Ibarra-García-Padilla, S. Dasgupta, R. T. Scalettar, K. R. A. Hazzard, I. Bloch, and S. Fölling, *Equation of State and Thermometry of the 2D* SU(N) *Fermi-Hubbard Model*, Phys. Rev. Lett. **132**, 083401 (2024) (cit. on pp. 4, 64, 65, 70, 101, 103).

[88] E. Ibarra-García-Padilla, C. Feng, G. Pasqualetti, S. Fölling, R. T. Scalettar, E. Khatami, and K. R. A. Hazzard, *Metal-insulator Transition and Magnetism of* SU(3) *Fermions in the Square Lattice*, Phys. Rev. A **108**, 053312 (2023) (cit. on p. 4).

[89] N. Darkwah Oppong, G. Pasqualetti, O. Bettermann, P. Zechmann, M. Knap, I. Bloch, and S. Fölling, *Probing Transport and Slow Relaxation in the Mass-Imbalanced Fermi-Hubbard Model*, Phys. Rev. X **12**, 031026 (2022) (cit. on pp. 4, 19, 20, 27).

[90] J. Meija, T. B. Coplen, M. Berglund, W. A. Brand, P. De Bièvre, M. Gröning, N. E. Holden, J. Irrgeher, R. D. Loss, T. Walczyk, and T. Prohaska, *Isotopic Compositions of the Elements 2013 (IUPAC Technical Report)*, Pure and Applied Chemistry **88**, 293 (2016) (cit. on p. 5).

[91] M. Kitagawa, K. Enomoto, K. Kasa, Y. Takahashi, R. Ciuryło, P. Naidon, and P. S. Julienne, *Two-Color Photoassociation Spectroscopy of Ytterbium Atoms and the Precise Determinations of s-Wave Scattering Lengths*, Phys. Rev. A **77**, 012719 (2008) (cit. on pp. 5, 9).

[92] T. Fukuhara, S. Sugawa, and Y. Takasu, *Quantum Degenerate Gases and the Mixtures of Ytterbium Atoms*, in *Ultra-cold Fermi Gases* (IOS Press, 2008) (cit. on p. 5).

[93] T. Fukuhara, S. Sugawa, Y. Takasu, and Y. Takahashi, *All-Optical Formation of Quantum Degenerate Mixtures*, Phys. Rev. A **79**, 021601 (2009) (cit. on p. 5).

[94] K. Konishi and G. Paffuti, *Quantum Mechanics: A New Introduction* (Oxford University Press, 2009) (cit. on pp. 6, 9).

[95] A. Lurio, M. Mandel, and R. Novick, *Second-Order Hyperfine and Zeeman Corrections for an* (sl) *Configuration*, Physical Review **126**, 1758 (1962) (cit. on p. 6).

[96] N. Lemke, A. Ludlow, Z. Barber, T. Fortier, S. Diddams, Y. Jiang, S. Jefferts, T. Heavner, T. Parker, and C. Oates, *Spin-1/2 Optical Lattice Clock*, Phys. Rev. Lett. **103**, 063001 (2009) (cit. on pp. 6, 15).

[97] A. D. Ludlow, M. M. Boyd, J. Ye, E. Peik, and P. O. Schmidt, *Optical Atomic Clocks*, Rev. Mod. Phys. **87**, 637 (2015) (cit. on pp. 6–8, 15).

[98] M. S. Safronova, D. Budker, D. DeMille, D. F. J. Kimball, A. Derevianko, and C. W. Clark, *Search for New Physics with Atoms and Molecules*, Rev. Mod. Phys. **90**, 025008 (2018) (cit. on p. 6).

[99] A. J. Daley, M. M. Boyd, J. Ye, and P. Zoller, *Quantum Computing with Alkaline-Earth-Metal Atoms*, Phys. Rev. Lett. **101**, 170504 (2008) (cit. on pp. 6, 8, 14, 15).

[100] A. M. Kaufman and K.-K. Ni, *Quantum Science with Optical Tweezer Arrays of Ultracold Atoms and Molecules*, Nat. Phys. **17**, 1324 (2021) (cit. on p. 6).

[101] A. Jenkins, J. W. Lis, A. Senoo, W. F. McGrew, and A. M. Kaufman, *Ytterbium Nuclear-Spin Qubits in an Optical Tweezer Array*, Phys. Rev. X **12**, 021027 (2022) (cit. on p. 6).

[102] S. Ma, A. P. Burgers, G. Liu, J. Wilson, B. Zhang, and J. D. Thompson, *Universal Gate Operations on Nuclear Spin Qubits in an Optical Tweezer Array of* ^{171}Yb *Atoms*, Phys. Rev. X **12**, 021028 (2022) (cit. on p. 6).

[103] S. Ma, G. Liu, P. Peng, B. Zhang, S. Jandura, J. Claes, A. P. Burgers, G. Pupillo, S. Puri, and J. D. Thompson, *High-Fidelity Gates with Mid-Circuit Erasure Conversion in a Metastable Neutral Atom Qubit*, Nature **622**, 279 (2023) (cit. on p. 6).

[104] Y. Takasu, K. Komori, K. Honda, M. Kumakura, T. Yabuzaki, and Y. Takahashi, *Photoassociation Spectroscopy of Laser-Cooled Ytterbium Atoms*, Phys. Rev. Lett. **93**, 123202 (2004) (cit. on p. 6).

[105] K. Pandey, A. K. Singh, P. V. K. Kumar, M. V. Suryanarayana, and V. Natarajan, *Isotope Shifts and Hyperfine Structure in the* 555.8 nm $^1S_0 \rightarrow ^3 P_1$ *Line of* Yb, Phys. Rev. A **80**, 022518 (2009) (cit. on pp. 6, 7).

[106] S. G. Porsev and A. Derevianko, *Hyperfine Quenching of the Metastable* $^3P_{0,2}$ *States in Divalent Atoms*, Phys. Rev. A **69**, 042506 (2004) (cit. on pp. 6, 7).

[107] J. W. Cho, H.-g. Lee, S. Lee, J. Ahn, W.-K. Lee, D.-H. Yu, S. K. Lee, and C. Y. Park, *Optical Repumping of Triplet-*P *States Enhances Magneto-Optical Trapping of Ytterbium Atoms*, Phys. Rev. A **85**, 035401 (2012) (cit. on p. 6).

[108] K. Beloy, J. A. Sherman, N. D. Lemke, N. Hinkley, C. W. Oates, and A. D. Ludlow, *Determination of the* 5d6s $^3D_1$ *State Lifetime and Blackbody-Radiation Clock Shift in* Yb, Phys. Rev. A **86**, 051404 (2012) (cit. on pp. 6, 7).

[109] M. S. Safronova, S. G. Porsev, C. Sanner, and J. Ye, *Two Clock Transitions in Neutral* Yb *for the Highest Sensitivity to Variations of the Fine-Structure Constant*, Phys. Rev. Lett. **120**, 173001 (2018) (cit. on pp. 6, 8).

[110] V. A. Dzuba, V. V. Flambaum, and S. Schiller, *Testing Physics beyond the Standard Model through Additional Clock Transitions in Neutral Ytterbium*, Phys. Rev. A **98**, 022501 (2018) (cit. on pp. 6, 8).

[111] M. Kleinert, M. E. Gold Dahl, and S. Bergeson, *Measurement of the* Yb *I* $^1S_0 \rightarrow ^1 P_1$ *Transition Frequency at* 399 nm *Using an Optical Frequency Comb*, Phys. Rev. A **94**, 052511 (2016) (cit. on p. 6).

[112] M. M. Boyd, T. Zelevinsky, A. D. Ludlow, S. Blatt, T. Zanon-Willette, S. M. Foreman, and J. Ye, *Nuclear Spin Effects in Optical Lattice Clocks*, Phys. Rev. A **76**, 022510 (2007) (cit. on p. 7).

[113] A. V. Taichenachev, V. I. Yudin, C. W. Oates, C. W. Hoyt, Z. W. Barber, and L. Hollberg, *Magnetic Field-Induced Spectroscopy of Forbidden Optical Transitions with Application to Lattice-Based Optical Atomic Clocks*, Phys. Rev. Lett. **96**, 083001 (2006) (cit. on p. 7).

[114] A. Yamaguchi, *Metastable State of Ultracold and Quantum Degenerate Ytterbium Atoms: High-Resolution Spectroscopy and Cold Collisions*, PhD Thesis, Kyoto University (2008).

[115] S. G. Porsev, Y. G. Rakhlina, and M. G. Kozlov, *Electric-Dipole Amplitudes, Lifetimes, and Polarizabilities of the Low-Lying Levels of Atomic Ytterbium*, Phys. Rev. A **60**, 2781 (1999) (cit. on p. 7).

[116] B. Hundt, *Optical Potentials for the Realization of Dissipative Fermi-Hubbard Models with Ultracold Ytterbium Atoms*, PhD Thesis, Universität Hamburg (2017).

[117] W. Meggers, *The First Spectrum of Ytterbium (*Yb I*)*, Journal of Research of the National Bureau of Standards **83** (1978) (cit. on p. 7).

[118] G. Pasqualetti, *Design and Characterization of a Repump Laser for Clock State Detection Using the* $^3P_0 \rightarrow ^3 D_1$ *Transition in* ^{173}Yb, Technical Report (Ludwig-Maximilians-Universität München, 2017) (cit. on p. 7).

[119] A. Yamaguchi, S. Uetake, and Y. Takahashi, *A Diode Laser System for Spectroscopy of the Ultranarrow Transition in Ytterbium Atoms*, Applied Physics B **91**, 57 (2008) (cit. on p. 8).

[120] A. Yamaguchi, S. Uetake, D. Hashimoto, J. M. Doyle, and Y. Takahashi, *Inelastic Collisions in Optically Trapped Ultracold Metastable Ytterbium*, Phys. Rev. Lett. **101**, 233002 (2008) (cit. on p. 8).

[121] S. Kato, K. Shibata, R. Yamamoto, Y. Yoshikawa, and Y. Takahashi, *Optical Magnetic Resonance Imaging with an Ultra-Narrow Optical Transition*, Applied Physics B **108**, 31 (2012) (cit. on p. 8).

[122] Y. Takasu, Y. Fukushima, Y. Nakamura, and Y. Takahashi, *Magnetoassociation of a Feshbach Molecule and Spin-Orbit Interaction between the Ground and Electronically Excited States*, Phys. Rev. A **96**, 023602 (2017) (cit. on p. 8).

[123] K. Shibata, R. Yamamoto, Y. Seki, and Y. Takahashi, *Optical Spectral Imaging of a Single Layer of a Quantum Gas with an Ultranarrow Optical Transition*, Phys. Rev. A **89**, 031601 (2014) (cit. on pp. 8, 27).

[124] S. Taie, S. Watanabe, T. Ichinose, and Y. Takahashi, *Feshbach-Resonance-Enhanced Coherent Atom-Molecule Conversion with Ultranarrow Photoassociation Resonance*, Phys. Rev. Lett. **116**, 043202 (2016) (cit. on p. 8).

[125] S. Kato, K. Inaba, S. Sugawa, K. Shibata, R. Yamamoto, M. Yamashita, and Y. Takahashi, *Laser Spectroscopic Probing of Coexisting Superfluid and Insulating States of an Atomic Bose-Hubbard System*, Nature Communications **7**, 11341 (2016) (cit. on p. 8).

[126] T. Ishiyama, K. Ono, T. Takano, A. Sunaga, and Y. Takahashi, *Observation of an Inner-Shell Orbital Clock Transition in Neutral Ytterbium Atoms*, Phys. Rev. Lett. **130**, 153402 (2023) (cit. on p. 8).

[127] A. Kawasaki, T. Kobayashi, A. Nishiyama, T. Tanabe, and M. Yasuda, *Observation of the* $4f^{14}6s^2\ ^1S_0 \rightarrow 4f^{13}5d6s^2$ *(*$J = 2$*) Clock Transition at* 431 nm *in* ^{171}Yb, Phys. Rev. A **107**, L060801 (2023) (cit. on p. 8).

[128] Z.-M. Tang, Y.-m. Yu, B. K. Sahoo, C.-Z. Dong, Y. Yang, and Y. Zou, *Simultaneous Magic Trapping Conditions for Three Additional Clock Transitions in Yb to Search for Variation of the Fine-Structure Constant*, Phys. Rev. A **107**, 053111 (2023) (cit. on p. 8).

[129] R. Lange, N. Huntemann, J. M. Rahm, C. Sanner, H. Shao, B. Lipphardt, C. Tamm, S. Weyers, and E. Peik, *Improved Limits for Violations of Local Position Invariance from Atomic Clock Comparisons*, Phys. Rev. Lett. **126**, 011102 (2021) (cit. on p. 8).

[130] A. Hees, J. Guéna, M. Abgrall, S. Bize, and P. Wolf, *Searching for an Oscillating Massive Scalar Field as a Dark Matter Candidate Using Atomic Hyperfine Frequency Comparisons*, Phys. Rev. Lett. **117**, 061301 (2016) (cit. on p. 8).

[131] C. J. Kennedy, E. Oelker, J. M. Robinson, T. Bothwell, D. Kedar, W. R. Milner, G. E. Marti, A. Derevianko, and J. Ye, *Precision Metrology Meets Cosmology: Improved Constraints on Ultralight Dark Matter from Atom-Cavity Frequency Comparisons*, Phys. Rev. Lett. **125**, 201302 (2020) (cit. on p. 8).

[132] T. Kobayashi, A. Takamizawa, D. Akamatsu, A. Kawasaki, A. Nishiyama, K. Hosaka, Y. Hisai, M. Wada, H. Inaba, T. Tanabe, and M. Yasuda, *Search for Ultralight Dark Matter from Long-Term Frequency Comparisons of Optical and Microwave Atomic Clocks*, Phys. Rev. Lett. **129**, 241301 (2022) (cit. on p. 8).

[133] M. Filzinger, S. Dörscher, R. Lange, J. Klose, M. Steinel, E. Benkler, E. Peik, C. Lisdat, and N. Huntemann, *Improved Limits on the Coupling of Ultralight Bosonic Dark Matter to Photons from Optical Atomic Clock Comparisons*, Phys. Rev. Lett. **130**, 253001 (2023) (cit. on p. 8).

[134] N. Sherrill et al., *Analysis of Atomic-Clock Data to Constrain Variations of Fundamental Constants*, New Journal of Physics **25**, 093012 (2023) (cit. on p. 8).

[135] D. Antypas, A. Fabricant, J. E. Stalnaker, K. Tsigutkin, V. V. Flambaum, and D. Budker, *Isotopic Variation of Parity Violation in Atomic Ytterbium*, Nat. Phys. **15**, 120 (2019) (cit. on p. 8).

[136] I. Counts, J. Hur, D. P. L. Aude Craik, H. Jeon, C. Leung, J. C. Berengut, A. Geddes, A. Kawasaki, W. Jhe, and V. Vuletić, *Evidence for Nonlinear Isotope Shift in* Yb^{+} *Search for New Boson*, Phys. Rev. Lett. **125**, 123002 (2020) (cit. on p. 8).

[137] N. L. Figueroa, J. C. Berengut, V. A. Dzuba, V. V. Flambaum, D. Budker, and D. Antypas, *Precision Determination of Isotope Shifts in Ytterbium and Implications for New Physics*, Phys. Rev. Lett. **128**, 073001 (2022) (cit. on p. 8).

[138] J. Hur, D. P. L. Aude Craik, I. Counts, E. Knyazev, L. Caldwell, C. Leung, S. Pandey, J. C. Berengut, A. Geddes, W. Nazarewicz, P.-G. Reinhard, A. Kawasaki, H. Jeon, W. Jhe, and V. Vuletić, *Evidence of Two-Source King Plot Nonlinearity in Spectroscopic Search for New Boson*, Phys. Rev. Lett. **128**, 163201 (2022) (cit. on p. 8).

[139] K. Ono, Y. Saito, T. Ishiyama, T. Higomoto, T. Takano, Y. Takasu, Y. Yamamoto, M. Tanaka, and Y. Takahashi, *Observation of Nonlinearity of Generalized King Plot in the Search for New Boson*, Phys. Rev. X **12**, 021033 (2022) (cit. on p. 8).

[140] A. Sotnikov, A. Cichy, and J. Kuneš, *Suppression and Revival of Long-Range Ferromagnetic Order in the Multiorbital Fermi-Hubbard Model*, Phys. Rev. B **97**, 235157 (2018) (cit. on p. 8).

[141] I. Kuzmenko, T. Kuzmenko, Y. Avishai, and G. B. Jo, *Multipolar Kondo Effect in* $^1\mathrm{S}_0 \rightarrow ^3\mathrm{P}_2$ *Mixture of* $^{173}\mathrm{Yb}$ *Atoms*, Phys. Rev. B **97**, 075124, eprint: 1611.08673 (cit. on pp. 8, 20).

[142] A. J. Daley, *Quantum Computing and Quantum Simulation with Group-II Atoms*, Quantum Information Processing **10**, 865 (2011) (cit. on p. 8).

[143] A. V. Gorshkov, A. M. Rey, A. J. Daley, M. M. Boyd, J. Ye, P. Zoller, and M. D. Lukin, *Alkaline-Earth-Metal Atoms as Few-Qubit Quantum Registers*, Phys. Rev. Lett. **102**, 110503 (2009) (cit. on p. 8).

[144] K. Shibata, S. Kato, A. Yamaguchi, S. Uetake, and Y. Takahashi, *A Scalable Quantum Computer with Ultranarrow Optical Transition of Ultracold Neutral Atoms in an Optical Lattice*, Applied Physics B **97**, 753 (2009) (cit. on p. 8).

[145] A. J. Daley, J. Ye, and P. Zoller, *State-Dependent Lattices for Quantum Computing with Alkaline-Earth-Metal Atoms*, The European Physical Journal D **65**, 207 (2011) (cit. on p. 8).

[146] J. T. M. Walraven, *Quantum Gases-Collisions and Statistics*, Lecture course at University of Vienna (2013) (cit. on pp. 8, 9).

[147] T.-L. Ho, *Spinor Bose Condensates in Optical Traps*, Phys. Rev. Lett. **81**, 742 (1998) (cit. on p. 9).

[148] D. M. Stamper-Kurn and M. Ueda, *Spinor Bose Gases: Symmetries, Magnetism, and Quantum Dynamics*, Rev. Mod. Phys. **85**, 1191 (2013) (cit. on p. 9).

[149] S. Taie, Y. Takasu, S. Sugawa, R. Yamazaki, T. Tsujimoto, R. Murakami, and Y. Takahashi, *Realization of a* SU(6) × SU(2) *System of Fermions in a Cold Atomic Gas*, Phys. Rev. Lett. **105**, 190401 (2010) (cit. on pp. 9, 25, 42).

[150] S. Stellmer, R. Grimm, and F. Schreck, *Detection and Manipulation of Nuclear Spin States in Fermionic Strontium*, Phys. Rev. A **84**, 043611 (2011) (cit. on p. 9).

[151] E. C. Stoner, *LXXX. Atomic Moments in Ferromagnetic Metals and Alloys with Non-Ferromagnetic Elements*, The London, Edinburgh, and Dublin Philosophical Magazine and Journal of Science **15**, 1018 (1933) (cit. on p. 10).

[152] E. C. Stoner, *Collective Electron Ferromagnetism*, Proceedings of the Royal Society of London. Series A. Mathematical and Physical Sciences **165**, 372 (1938) (cit. on p. 10).

[153] J. Pera, J. Casulleras, and J. Boronat, *Itinerant Ferromagnetism in Dilute* SU(N) *Fermi Gases*, SciPost Physics **14**, 038 (2023) (cit. on pp. 10, 26, 91).

[154] G. Grosso and G. Pastori Parravicini, *Solid State Physics*, Second edition (Academic Press, 2014) (cit. on p. 10).

[155] G.-B. Jo, Y.-R. Lee, J.-H. Choi, C. A. Christensen, T. H. Kim, J. H. Thywissen, D. E. Pritchard, and W. Ketterle, *Itinerant Ferromagnetism in a Fermi Gas of Ultracold Atoms*, Science **325**, 1521 (2009) (cit. on p. 10).

[156] W. Zwerger, *Itinerant Ferromagnetism with Ultracold Atoms*, Science **325**, 1507 (2009) (cit. on p. 10).

[157] G. Valtolina, F. Scazza, A. Amico, A. Burchianti, A. Recati, T. Enss, M. Inguscio, M. Zaccanti, and G. Roati, *Exploring the Ferromagnetic Behaviour of a Repulsive Fermi Gas through Spin Dynamics*, Nat. Phys. **13**, 704 (2017) (cit. on p. 10).

[158] H. Zhai, *Correlated versus Ferromagnetic State in Repulsively Interacting Two-Component Fermi Gases*, Phys. Rev. A **80**, 051605 (2009) (cit. on p. 10).

[159] C. Sanner, E. J. Su, W. Huang, A. Keshet, J. Gillen, and W. Ketterle, *Correlations and Pair Formation in a Repulsively Interacting Fermi Gas*, Phys. Rev. Lett. **108**, 240404 (2012) (cit. on p. 10).

[160] L. He, X.-J. Liu, X.-G. Huang, and H. Hu, *Stoner Ferromagnetism of a Strongly Interacting Fermi Gas in the Quasirepulsive Regime*, Phys. Rev. A **93**, 063629 (2016) (cit. on p. 10).

[161] P. T. How and S.-K. Yip, *Nonanalytic Crossover Behavior of* SU(N) *Fermi Liquid*, Phys. Rev. A **97**, 063623 (2018) (cit. on pp. 10, 42, 97).

[162] P. H. Chankowski, J. Wojtkiewicz, and S. Augustynowicz, *Third Order Corrections to the Ground State Energy of the Gas of Spin* s *Fermions with Arbitrary Densities of Different Spin Projections*, Phys. Rev. A **107**, 063311 (2023) (cit. on p. 10).

[163] J. Pera, J. Casulleras, and J. Boronat, *Beyond Universality in Repulsive* SU(N) *Fermi Gases*, arXiv:2206.06932 (cit. on p. 10).

[164] G. J. Conduit, *Itinerant Ferromagnetism in a Two-Dimensional Atomic Gas*, Phys. Rev. A **82**, 043604 (2010) (cit. on p. 10).

[165] P. O. Fedichev, Y. Kagan, G. V. Shlyapnikov, and J. T. M. Walraven, *Influence of Nearly Resonant Light on the Scattering Length in Low-Temperature Atomic Gases*, Phys. Rev. Lett. **77**, 2913 (1996) (cit. on pp. 11, 42).

[166] R. Ciuryło, E. Tiesinga, and P. S. Julienne, *Optical Tuning of the Scattering Length of Cold Alkaline-Earth-Metal Atoms*, Phys. Rev. A **71**, 030701 (2005) (cit. on pp. 11, 42).

[167] K. Enomoto, K. Kasa, M. Kitagawa, and Y. Takahashi, *Optical Feshbach Resonance Using the Intercombination Transition*, Phys. Rev. Lett. **101**, 203201 (2008) (cit. on p. 11).

[168] S. Blatt, T. L. Nicholson, B. J. Bloom, J. R. Williams, J. W. Thomsen, P. S. Julienne, and J. Ye, *Measurement of Optical Feshbach Resonances in an Ideal Gas*, Phys. Rev. Lett. **107**, 073202 (2011) (cit. on p. 11).

[169] H. Kajueter, G. Kotliar, and G. Moeller, *Doped Mott Insulator: Results from Mean-Field Theory*, Phys. Rev. B **53**, 16214 (1996) (cit. on p. 11).

[170] B. Johansson, *The α-γ Transition in Cerium Is a Mott Transition*, Philosophical Magazine **30**, 469 (1974) (cit. on p. 11).

[171] J. W. Allen and R. M. Martin, *Kondo Volume Collapse and the $\gamma \to \alpha$ Transition in Cerium*, Phys. Rev. Lett. **49**, 1106 (1982) (cit. on p. 11).

[172] K. Held, A. K. McMahan, and R. T. Scalettar, *Cerium Volume Collapse: Results from the Merger of Dynamical Mean-Field Theory and Local Density Approximation*, Phys. Rev. Lett. **87**, 276404 (2001) (cit. on p. 11).

[173] M. J. Lipp, Z. Jenei, H. Cynn, Y. Kono, C. Park, C. Kenney-Benson, and W. J. Evans, *Anomalous Elastic Properties across the γ to α Volume Collapse in Cerium*, Nature Communications **8**, 1198 (2017) (cit. on p. 11).

[174] S. Florens and A. Georges, *Slave-Rotor Mean-Field Theories of Strongly Correlated Systems and the Mott Transition in Finite Dimensions*, Phys. Rev. B **70**, 035114 (2004) (cit. on p. 11).

[175] W. M. H. Natori, R. Nutakki, R. G. Pereira, and E. C. Andrade, SU(4) *Heisenberg Model on the Honeycomb Lattice with Exchange-Frustrated Perturbations: Implications for Twistronics and Mott Insulators*, Phys. Rev. B **100**, 205131 (2019) (cit. on p. 11).

[176] N. Read and D. M. Newns, *On the Solution of the Coqblin-Schreiffer Hamiltonian by the Large-N Expansion Technique*, Journal of Physics C: Solid State Physics **16**, 3273 (1983) (cit. on p. 12).

[177] N. E. Bickers, *Review of Techniques in the Large-N Expansion for Dilute Magnetic Alloys*, Rev. Mod. Phys. **59**, 845 (1987) (cit. on p. 12).

[178] A. Auerbach, *Interacting Electrons and Quantum Magnetism*, edited by J. L. Birman, J. W. Lynn, M. P. Silverman, H. E. Stanley, and M. Voloshin (Springer, 1994) (cit. on p. 12).

[179] P. W. Anderson, *Localized Magnetic States in Metals*, Physical Review **124**, 41 (1961) (cit. on p. 12).

[180] C. Hofrichter, *Probing the* SU(N) *Fermi-Hubbard Model with Ytterbium Atoms in an Optical Lattice*, PhD Thesis, Ludwig-Maximilians-Universität München (2016).

[181] M. A. Cazalilla and A. M. Rey, *Ultracold Fermi Gases with Emergent* SU(N) *Symmetry*, Reports on Progress in Physics **77**, 124401 (2014) (cit. on p. 13).

[182] J. E. Hirsch, *Metallic Ferromagnetism in a Single-Band Model*, Phys. Rev. B **40**, 2354 (1989) (cit. on p. 12).

[183] E. Ibarra-García-Padilla and al., *In preparation* (cit. on p. 12).

[184] N. W. Ashcroft and N. D. Mermin, *Solid State Physics* (Harcourt College Publishers, 1976) (cit. on pp. 14, 20).

[185] B. Abeln, K. Sponselee, M. Diem, N. Pintul, K. Sengstock, and C. Becker, *Interorbital Interactions in an* SU(2) × SU(6)*-Symmetric Fermi-Fermi Mixture*, Phys. Rev. A **103**, 033315 (2021) (cit. on p. 14).

[186] D. Greif, M. F. Parsons, A. Mazurenko, C. S. Chiu, S. Blatt, F. Huber, G. Ji, and M. Greiner, *Site-Resolved Imaging of a Fermionic Mott Insulator*, Science **351**, 953 (2016) (cit. on pp. 14, 43, 76, 79).

[187] E. Cocchi, L. A. Miller, J. H. Drewes, M. Koschorreck, D. Pertot, F. Brennecke, and M. Köhl, *Equation of State of the Two-Dimensional Hubbard Model*, Phys. Rev. Lett. **116**, 175301 (2016) (cit. on pp. 14, 43).

[188] L. W. Cheuk, M. A. Nichols, K. R. Lawrence, M. Okan, H. Zhang, and M. W. Zwierlein, *Observation of 2D Fermionic Mott Insulators of* ^{40}K *with Single-Site Resolution*, Phys. Rev. Lett. **116**, 235301 (2016) (cit. on pp. 14, 43, 79).

[189] J. H. Drewes, E. Cocchi, L. A. Miller, C. F. Chan, D. Pertot, F. Brennecke, and M. Köhl, *Thermodynamics versus Local Density Fluctuations in the Metal-Mott-Insulator Crossover*, Phys. Rev. Lett. **117**, 135301 (2016) (cit. on pp. 14, 79, 81).

[190] M. Boll, T. A. Hilker, G. Salomon, A. Omran, J. Nespolo, L. Pollet, I. Bloch, and C. Gross, *Spin- and Density-Resolved Microscopy of Antiferromagnetic Correlations in Fermi-Hubbard Chains*, Science **353**, 1257 (2016) (cit. on p. 14).

[191] M. F. Parsons, A. Mazurenko, C. S. Chiu, G. Ji, D. Greif, and M. Greiner, *Site-Resolved Measurement of the Spin-Correlation Function in the Fermi-Hubbard Model*, Science **353**, 1253 (2016) (cit. on p. 14).

[192] L. W. Cheuk, M. A. Nichols, K. R. Lawrence, M. Okan, H. Zhang, E. Khatami, N. Trivedi, T. Paiva, M. Rigol, and M. W. Zwierlein, *Observation of Spatial Charge and Spin Correlations in the 2D Fermi-Hubbard Model*, Science **353**, 1260 (2016) (cit. on p. 14).

[193] J. H. Drewes, L. A. Miller, E. Cocchi, C. F. Chan, N. Wurz, M. Gall, D. Pertot, F. Brennecke, and M. Köhl, *Antiferromagnetic Correlations in Two-Dimensional Fermionic Mott-Insulating and Metallic Phases*, Phys. Rev. Lett. **118**, 170401 (2017) (cit. on p. 14).

[194] A. Mazurenko, C. S. Chiu, G. Ji, M. F. Parsons, M. Kanász-Nagy, R. Schmidt, F. Grusdt, E. Demler, D. Greif, and M. Greiner, *A Cold-Atom Fermi-Hubbard Antiferromagnet*, Nature **545**, 462 (2017) (cit. on p. 14).

[195] E. Cocchi, L. A. Miller, J. H. Drewes, C. F. Chan, D. Pertot, F. Brennecke, and M. Köhl, *Measuring Entropy and Short-Range Correlations in the Two-Dimensional Hubbard Model*, Phys. Rev. X **7**, 031025 (2017) (cit. on p. 14).

[196] T. A. Hilker, G. Salomon, F. Grusdt, A. Omran, M. Boll, E. Demler, I. Bloch, and C. Gross, *Revealing Hidden Antiferromagnetic Correlations in Doped Hubbard Chains via String Correlators*, Science **357**, 484 (2017) (cit. on p. 14).

[197] M. A. Nichols, L. W. Cheuk, M. Okan, T. R. Hartke, E. Mendez, T. Senthil, E. Khatami, H. Zhang, and M. W. Zwierlein, *Spin Transport in a Mott Insulator of Ultracold Fermions*, Science **363**, 383 (2019) (cit. on p. 14).

[198] C. S. Chiu, G. Ji, A. Bohrdt, M. Xu, M. Knap, E. Demler, F. Grusdt, M. Greiner, and D. Greif, *String Patterns in the Doped Hubbard Model*, Science **365**, 251 (2019) (cit. on p. 14).

[199] J. Koepsell, J. Vijayan, P. Sompet, F. Grusdt, T. A. Hilker, E. Demler, G. Salomon, I. Bloch, and C. Gross, *Imaging Magnetic Polarons in the Doped Fermi-Hubbard Model*, Nature **572**, 358 (2019) (cit. on p. 14).

[200] T. Hartke, B. Oreg, N. Jia, and M. Zwierlein, *Doublon-Hole Correlations and Fluctuation Thermometry in a Fermi-Hubbard Gas*, Phys. Rev. Lett. **125**, 113601 (2020) (cit. on p. 14).

[201] G. Ji, M. Xu, L. H. Kendrick, C. S. Chiu, J. C. Brüggenjürgen, D. Greif, A. Bohrdt, F. Grusdt, E. Demler, M. Lebrat, and M. Greiner, *Coupling a Mobile Hole to an Antiferromagnetic Spin Background: Transient Dynamics of a Magnetic Polaron*, Phys. Rev. X **11**, 021022 (2021) (cit. on p. 14).

[202] J. Koepsell, D. Bourgund, P. Sompet, S. Hirthe, A. Bohrdt, Y. Wang, F. Grusdt, E. Demler, G. Salomon, C. Gross, and I. Bloch, *Microscopic Evolution of Doped Mott Insulators from Polaronic Metal to Fermi Liquid*, Science **374**, 82 (2021) (cit. on p. 14).

[203] L. Riegger, *Interorbital Spin Exchange in a State-Dependent Optical Lattice*, PhD Thesis, Ludwig-Maximilians-Universität München (2019).

[204] V. A. Dzuba and A. Derevianko, *Dynamic Polarizabilities and Related Properties of Clock States of the Ytterbium Atom*, Journal of Physics B: Atomic, Molecular and Optical Physics **43**, 074011 (2010) (cit. on p. 15).

[205] A. Heinz, A. J. Park, N. Šantić, J. Trautmann, S. G. Porsev, M. S. Safronova, I. Bloch, and S. Blatt, *State-Dependent Optical Lattices for the Strontium Optical Qubit*, Phys. Rev. Lett. **124**, 203201 (2020) (cit. on p. 15).

[206] T. O. Höhn, E. Staub, G. Brochier, N. Darkwah Oppong, and M. Aidelsburger, *State-Dependent Potentials for the* $^1\mathrm{S}_0$ *and* $^3\mathrm{P}_0$ *Clock States of Neutral Ytterbium Atoms*, Phys. Rev. A **108**, 053325 (2023) (cit. on p. 15).

[207] N. Darkwah Oppong, L. Riegger, O. Bettermann, M. Höfer, J. Levinsen, M. M. Parish, I. Bloch, and S. Fölling, *Observation of Coherent Multiorbital Polarons in a Two-Dimensional Fermi Gas*, Phys. Rev. Lett. **122**, 193604 (2019) (cit. on pp. 16, 27, 37).

[208] O. Bettermann, *Interorbital Interactions in Ytterbium-171*, PhD Thesis, Ludwig-Maximilians-Universität München (2022).

[209] F. Scazza, *Probing* SU(N)*-Symmetric Orbital Interactions with Ytterbium Fermi Gases in Optical Lattices*, PhD Thesis, Ludwig-Maximilians-Universität München (2015).

[210] G. Pagano, M. Mancini, G. Cappellini, L. Livi, C. Sias, J. Catani, M. Inguscio, and L. Fallani, *Strongly Interacting Gas of Two-Electron Fermions at an Orbital Feshbach Resonance*, Phys. Rev. Lett. **115**, 265301 (2015) (cit. on p. 17).

[211] M. Höfer, L. Riegger, F. Scazza, C. Hofrichter, D. R. Fernandes, M. M. Parish, J. Levinsen, I. Bloch, and S. Fölling, *Observation of an Orbital Interaction-Induced Feshbach Resonance in* Yb-*173*, Phys. Rev. Lett. **115**, 265302 (2015) (cit. on pp. 17, 22, 27).

[212] K. Ono, J. Kobayashi, Y. Amano, K. Sato, and Y. Takahashi, *Antiferromagnetic Interorbital Spin-Exchange Interaction of* ^{171}Yb, Phys. Rev. A **99**, 032707 (2019) (cit. on pp. 17, 20).

[213] M. Höfer, *A Two-Orbital Quantum Gas with Tunable Interactions*, PhD Thesis, Ludwig-Maximilians-Universität München (2017).

[214] R. Zhang, Y. Cheng, H. Zhai, and P. Zhang, *Orbital Feshbach Resonance in Alkali-Earth Atoms*, Phys. Rev. Lett. **115**, 135301 (2015) (cit. on p. 17).

[215] P. Ketterer, *A Stable Laser Setup for the* 578 nm *Clock Transition of Ytterbium*, Diploma Thesis, Ludwig-Maximilians-Universität München (2012).

[216] S. S. Kondov, W. R. McGehee, W. Xu, and B. DeMarco, *Disorder-Induced Localization in a Strongly Correlated Atomic Hubbard Gas*, Phys. Rev. Lett. **114**, 083002 (2015) (cit. on p. 19).

[217] M. Schreiber, S. S. Hodgman, P. Bordia, H. P. Lüschen, M. H. Fischer, R. Vosk, E. Altman, U. Schneider, and I. Bloch, *Observation of Many-Body Localization of Interacting Fermions in a Quasirandom Optical Lattice*, Science **349**, 842 (2015) (cit. on pp. 19, 76).

[218] J. Smith, A. Lee, P. Richerme, B. Neyenhuis, P. W. Hess, P. Hauke, M. Heyl, D. A. Huse, and C. Monroe, *Many-Body Localization in a Quantum Simulator with Programmable Random Disorder*, Nat. Phys. **12**, 907 (2016) (cit. on p. 19).

[219] P. Roushan et al., *Spectroscopic Signatures of Localization with Interacting Photons in Superconducting Qubits*, Science **358**, 1175 (2017) (cit. on p. 19).

[220] Y. Kagan and L. A. Maksimov, *Localization in a System of Interacting Particles Diffusing in a Regular Crystal*, J. Exp. Theor. Phys. **60**, 201 (1984) (cit. on p. 19).

[221] W. De Roeck and F. Huveneers, *Asymptotic Quantum Many-Body Localization from Thermal Disorder*, Communications in Mathematical Physics **332**, 1017 (2014) (cit. on p. 19).

[222] M. Schiulaz and M. Müller, *Ideal Quantum Glass Transitions: Many-body Localization without Quenched Disorder*, in International Conference on Analysis and Applied Mathematics 2014 (2014), 11 (cit. on p. 19).

[223] M. Schiulaz, A. Silva, and M. Müller, *Dynamics in Many-Body Localized Quantum Systems without Disorder*, Phys. Rev. B **91**, 184202 (2015) (cit. on p. 19).

[224] Z. Papić, E. M. Stoudenmire, and D. A. Abanin, *Many-Body Localization in Disorder-Free Systems: The Importance of Finite-Size Constraints*, Annals of Physics **362**, 714 (2015) (cit. on p. 19).

[225] N. Y. Yao, C. R. Laumann, J. I. Cirac, M. D. Lukin, and J. E. Moore, *Quasi-Many-Body Localization in Translation-Invariant Systems*, Phys. Rev. Lett. **117**, 240601 (2016) (cit. on p. 19).

[226] J. Sirker, *Exploration of the Existence of a Distinct Quasi Many-Body Localized Phase: Numerical Study of a Translationally Invariant System in the Thermodynamic Limit*, Phys. Rev. B **99**, 075162 (2019) (cit. on p. 19).

[227] N. Darkwah Oppong, *Probing Many-Body Physics with Multiorbital Quantum Gases*, PhD Thesis, Ludwig-Maximilians-Universität München (2021).

[228] Á. Rapp, W. Hofstetter, and G. Zaránd, *Trionic Phase of Ultracold Fermions in an Optical Lattice: A Variational Study*, Phys. Rev. B **77**, 144520 (2008) (cit. on p. 19).

[229] Y. Zhong, Y. Liu, and H.-G. Luo, *Simulating Heavy Fermion Physics in Optical Lattice: Periodic Anderson Model with Harmonic Trapping Potential*, Frontiers of Physics **12**, 127502 (2017) (cit. on p. 20).

[230] M. Nakagawa, N. Kawakami, and M. Ueda, *Non-Hermitian Kondo Effect in Ultracold Alkaline-Earth Atoms*, Phys. Rev. Lett. **121**, 203001 (2018) (cit. on p. 20).

[231] M. Raczkowski and F. F. Assaad, *Phase Diagram and Dynamics of the* $\mathrm{SU}(N)$*-Symmetric Kondo Lattice Model*, Physical Review Research **2**, 013276 (2020) (cit. on pp. 20, 21).

[232] K. Totsuka, *Ferromagnetism in the* $\mathrm{SU}(N)$ *Kondo lattice model:* $\mathrm{SU}(N)$ *double exchange and supersymmetry*, Phys. Rev. A **107**, 033317 (2023) (cit. on pp. 20, 21).

[233] P. Nozières, *A "Fermi-Liquid" Description of the Kondo Problem at Low Temperatures*, Journal of Low Temperature Physics **17**, 31 (1974) (cit. on p. 20).

[234] M. A. Ruderman and C. Kittel, *Indirect Exchange Coupling of Nuclear Magnetic Moments by Conduction Electrons*, Physical Review **96**, 99 (1954) (cit. on p. 21).

[235] T. Kasuya, *A Theory of Metallic Ferro- and Antiferromagnetism on Zener's Model*, Progress of Theoretical Physics **16**, 45 (1956) (cit. on p. 21).

[236] K. Yosida, *Magnetic Properties of* Cu – Mn *Alloys*, Physical Review **106**, 893 (1957) (cit. on p. 21).

[237] N. F. Mott, *Rare-Earth Compounds with Mixed Valencies*, Philosophical Magazine **30**, 403 (1974) (cit. on p. 21).

[238] H. Prüser, P. E. Dargel, M. Bouhassoune, R. G. Ulbrich, T. Pruschke, S. Lounis, and M. Wenderoth, *Interplay between the Kondo Effect and the Ruderman – Kittel – Kasuya – Yosida Interaction*, Nature Communications **5**, 5417 (2014) (cit. on p. 21).

[239] F. Steglich, J. Aarts, C. D. Bredl, W. Lieke, D. Meschede, W. Franz, and H. Schäfer, *Superconductivity in the Presence of Strong Pauli Paramagnetism:* $CeCu_2Si_2$, Phys. Rev. Lett. **43**, 1892 (1979) (cit. on p. 21).

[240] C. Petrovic, P. G. Pagliuso, M. F. Hundley, R. Movshovich, J. L. Sarrao, J. D. Thompson, Z. Fisk, and P. Monthoux, *Heavy-Fermion Superconductivity in* $CeCoIn_5$ *at* 2.3 K, Journal of Physics: Condensed Matter **13**, L337 (2001) (cit. on p. 21).

[241] P. Coleman, $1/N$ *Expansion for the Kondo Lattice*, Phys. Rev. B **28**, 5255 (1983) (cit. on p. 21).

[242] G. Pasqualetti, *Isotopic Mixtures of Ytterbium for Quantum Simulation of Kondo Physics*, Master Thesis, Ludwig-Maximilians-Universität München (2018).

[243] D. A. Steck, *Quantum and Atom Optics*, revision 0.12.0 (May 2017) (cit. on p. 25).

[244] T. Sleator, T. Pfau, V. Balykin, O. Carnal, and J. Mlynek, *Experimental Demonstration of the Optical Stern-Gerlach Effect*, Phys. Rev. Lett. **68**, 1996 (1992) (cit. on p. 25).

[245] M. Vojta, *Orbital-Selective Mott Transitions: Heavy Fermions and Beyond*, Journal of Low Temperature Physics **161**, 203 (2010) (cit. on p. 26).

[246] A. Georges, L. de'Medici, and J. Mravlje, *Strong Correlations from Hund's Coupling*, Annual Review of Condensed Matter Physics **4**, 137 (2013) (cit. on p. 26).

[247] L. Del Re and M. Capone, *Selective Insulators and Anomalous Responses in Three-Component Fermionic Gases with Broken* SU(3) *Symmetry*, Phys. Rev. A **98**, 063628 (2018) (cit. on p. 26).

[248] A. Görlitz, J. M. Vogels, A. E. Leanhardt, C. Raman, T. L. Gustavson, J. R. Abo-Shaeer, A. P. Chikkatur, S. Gupta, S. Inouye, T. Rosenband, and W. Ketterle, *Realization of Bose-Einstein Condensates in Lower Dimensions*, Phys. Rev. Lett. **87**, 130402 (2001) (cit. on p. 27).

[249] N. L. Smith, W. H. Heathcote, G. Hechenblaikner, E. Nugent, and C. J. Foot, *Quasi-2D Confinement of a BEC in a Combined Optical and Magnetic Potential*, Journal of Physics B: Atomic, Molecular and Optical Physics **38**, 223 (2005) (cit. on p. 27).

[250] S. P. Rath, T. Yefsah, K. J. Günter, M. Cheneau, R. Desbuquois, M. Holzmann, W. Krauth, and J. Dalibard, *Equilibrium State of a Trapped Two-Dimensional Bose Gas*, Phys. Rev. A **82**, 013609 (2010) (cit. on p. 27).

[251] C. Weitenberg, *Single-Atom Resolved Imaging and Manipulation in an Atomic Mott Insulator*, PhD Thesis, Ludwig-Maximilians-Universität München (2011).

[252] R. Yamamoto, J. Kobayashi, T. Kuno, K. Kato, and Y. Takahashi, *An ytterbium quantum gas microscope with narrow-line laser cooling*, New Journal of Physics **18**, 023016 (2016) (cit. on pp. 27, 91).

[253] J. Trautmann, D. Yankelev, V. Klüsener, A. J. Park, I. Bloch, and S. Blatt, $^1S_0$–$^3P_2$ *magnetic quadrupole transition in neutral strontium*, Phys. Rev. Res. **5**, 013219 (2023) (cit. on p. 27).

[254] D. Rychtarik, B. Engeser, H.-C. Nägerl, and R. Grimm, *Two-Dimensional Bose-Einstein Condensate in an Optical Surface Trap*, Phys. Rev. Lett. **92**, 173003 (2004) (cit. on p. 27).

[255] J. I. Gillen, W. S. Bakr, A. Peng, P. Unterwaditzer, S. Fölling, and M. Greiner, *Two-Dimensional Quantum Gas in a Hybrid Surface Trap*, Phys. Rev. A **80**, 021602 (2009) (cit. on p. 27).

[256] M. Miranda, A. Nakamoto, Y. Okuyama, A. Noguchi, M. Ueda, and M. Kozuma, *All-Optical Transport and Compression of Ytterbium Atoms into the Surface of a Solid Immersion Lens*, Phys. Rev. A **86**, 063615 (2012) (cit. on p. 27).

[257] R. Scheunemann, F. S. Cataliotti, T. W. Hänsch, and M. Weitz, *Resolving and Addressing Atoms in Individual Sites of a* CO_2*-Laser Optical Lattice*, Phys. Rev. A **62**, 051801 (2000) (cit. on p. 27).

[258] O. Morsch, J. H. Müller, M. Cristiani, D. Ciampini, and E. Arimondo, *Bloch Oscillations and Mean-Field Effects of Bose-Einstein Condensates in 1D Optical Lattices*, Phys. Rev. Lett. **87**, 140402 (2001) (cit. on p. 27).

[259] T. C. Li, H. Kelkar, D. Medellin, and M. G. Raizen, *Real-Time Control of the Periodicity of a Standing Wave: An Optical Accordion*, Optics Express **16**, 5465 (2008) (cit. on p. 27).

[260] R. Saint-Jalm, *Exploring Two-Dimensional Physics with Bose Gases in Box Potentials: Phase Ordering and Dynamical Symmetry*, PhD Thesis, Université Paris Sciences et Lettres (2019).

[261] R. F. Capellmann, J. Bewerunge, F. Platten, and S. U. Egelhaaf, *Note: Using a Kösters Prism to Create a Fringe Pattern*, Review of Scientific Instruments **88**, 056102 (2017) (cit. on p. 28).

[262] J. W. Gates, *The Measurement of Comatic Aberrations by Interferometry*, Proceedings of the Physical Society. Section B **68**, 1065 (1955) (cit. on p. 28).

[263] C. F. Bruce, *A Kösters-type Interferometer*, Journal of Scientific Instruments **33**, 478 (1956) (cit. on p. 28).

[264] J. Saunders, *The Kosters Interferometer*, Journal of Research of the National Bureau of Standards **58**, 27 (1957) (cit. on p. 28).

[265] G. H. Lovins, *High-Precision Pointing Interferometer*, Applied Optics **3**, 883 (1964) (cit. on p. 28).

[266] Y. Ohtsuka, A. Tanone, and K. Itoh, *New Visualization Method of Progressive Acoustic Wavefronts Using a Köster Prism*, Optics Communications **31**, 9 (1979) (cit. on p. 28).

[267] M. S. Brown, *A Kosters Prism Acousto-Optic Interferometer for Radio-Frequency Direction of Arrival Measurements*, Journal of Physics E: Scientific Instruments **20**, 164 (1987) (cit. on p. 28).

[268] H. Darnedde, *High-Precision Calibration of Long Gauge Blocks Using the Vacuum Wavelength Comparator*, Metrologia **29**, 349 (1992) (cit. on p. 28).

[269] Y. Ohtsuka, F. Nagaoka, and S. Tanaka, *White-Light Frequency-Domain Interferometry Using a Köosters Prism*, Optical Review **5**, 21 (1998) (cit. on p. 28).

[270] J. E. Decker, R. Schodel, and G. Bonsch, *Next-Generation Kosters Interferometer*, in Optical Science and Technology, SPIE's 48th Annual Meeting, edited by J. E. Decker and N. Brown (Nov. 2003), 14 (cit. on p. 28).

[271] A. Impertro, *Preparation and Study of 1D and 2D Many-Body Systems with Fermionic Ytterbium*, Master Thesis, Ludwig-Maximilians-Universität München (2020).

[272] W. Kösters, *Ein Neuer Interferenzkomparator f. Unmittelbaren Wellenlängenanschluß*, Zeitschrift für Feinmechanik und Präzision **34**, 55 (1926) (cit. on p. 28).

[273] W. Kösters, *Interferenzdoppelprisma Für Messzwecke*, Patent DE595211C (Apr. 1934) (cit. on p. 28).

[274] K. M. Hueck, *A Homogeneous, Two-Dimensional Fermi Gas*, PhD Thesis, University of Hamburg (2017).

[275] R. Jáuregui, N. Poli, G. Roati, and G. Modugno, *Anharmonic Parametric Excitation in Optical Lattices*, Phys. Rev. A **64**, 033403 (2001) (cit. on pp. 33, 85).

[276] L. Chomaz, L. Corman, T. Yefsah, R. Desbuquois, and J. Dalibard, *Absorption Imaging of a Quasi-Two-Dimensional Gas: A Multiple Scattering Analysis*, New Journal of Physics **14**, 055001 (2012) (cit. on pp. 38, 40, 87).

[277] J. Rui, D. Wei, A. Rubio-Abadal, S. Hollerith, J. Zeiher, D. M. Stamper-Kurn, C. Gross, and I. Bloch, *A Subradiant Optical Mirror Formed by a Single Structured Atomic Layer*, Nature **583**, 369 (2020) (cit. on pp. 38, 87).

[278] G. Reinaudi, T. Lahaye, Z. Wang, and D. Guéry-Odelin, *Strong Saturation Absorption Imaging of Dense Clouds of Ultracold Atoms*, Optics Letters **32**, 3143 (2007) (cit. on p. 38).

[279] C.-L. Hung and C. Chin, *In Situ Imaging of Atomic Quantum Gases*, Vol. 3, 6 (Imperial College Press, 2014), 101 (cit. on p. 39).

[280] C.-L. Hung, X. Zhang, L.-C. Ha, S.-K. Tung, N. Gemelke, and C. Chin, *Extracting Density – Density Correlations from* in Situ *Images of Atomic Quantum Gases*, New Journal of Physics **13**, 075019 (2011) (cit. on pp. 39, 40).

[281] R. W. Cherng, G. Refael, and E. Demler, *Superfluidity and Magnetism in Multicomponent Ultracold Fermions*, Phys. Rev. Lett. **99**, 130406 (2007) (cit. on p. 42).

[282] C.-H. Huang, Y. Takasu, Y. Takahashi, and M. A. Cazalilla, *Suppression and Control of Prethermalization in Multicomponent Fermi Gases Following a Quantum Quench*, Phys. Rev. A **101**, 053620 (2020) (cit. on p. 42).

[283] T. Ozawa and G. Baym, *Population Imbalance and Pairing in the BCS-BEC Crossover of Three-Component Ultracold Fermions*, Phys. Rev. A **82**, 063615 (2010) (cit. on p. 42).

[284] C.-H. Cheng and S.-K. Yip, SU(N) *Fermi Liquid at Finite Temperature*, Phys. Rev. A **95**, 033619 (2017) (cit. on pp. 42, 91, 97).

[285] S. Stellmer, R. Grimm, and F. Schreck, *Production of Quantum-Degenerate Strontium Gases*, Phys. Rev. A **87**, 013611 (2013) (cit. on p. 42).

[286] A. Thobe, *Ultracold* Yb *Gases with Control over Spin and Orbital Degrees of Freedom*, PhD Thesis, Universität Hamburg (2014).

[287] L. Sonderhouse, C. Sanner, R. B. Hutson, A. Goban, T. Bilitewski, L. Yan, W. R. Milner, A. M. Rey, and J. Ye, *Thermodynamics of a Deeply Degenerate* SU(N)*-Symmetric Fermi Gas*, Nat. Phys., 1216 (2020) (cit. on pp. 42, 46, 47, 51, 52, 97).

[288] B. Song, Y. Yan, C. He, Z. Ren, Q. Zhou, and G.-B. Jo, *Evidence for Bosonization in a Three-Dimensional Gas of* SU(N) *Fermions*, Phys. Rev. X **10**, 041053 (2020) (cit. on p. 42).

[289] E. Zhao, J. Lee, C. He, Z. Ren, E. Hajiyev, J. Liu, and G.-B. Jo, *Heuristic Machinery for Thermodynamic Studies of* SU(N) *Fermions with Neural Networks*, Nature Communications **12**, 2011 (2021) (cit. on p. 42).

[290] C. He, Z. Ren, B. Song, E. Zhao, J. Lee, Y.-C. Zhang, S. Zhang, and G.-B. Jo, *Collective Excitations in Two-Dimensional* SU(N) *Fermi Gases with Tunable Spin*, Physical Review Research **2**, 012028 (2020) (cit. on p. 42).

[291] S. Choudhury, K. R. Islam, Y. Hou, J. A. Aman, T. C. Killian, and K. R. A. Hazzard, *Collective Modes of Ultracold Fermionic Alkaline-Earth-Metal Gases with* SU(N) *Symmetry*, Phys. Rev. A **101**, 053612 (2020) (cit. on p. 42).

[292] R. Jördens, N. Strohmaier, K. Günter, H. Moritz, and T. Esslinger, *A Mott Insulator of Fermionic Atoms in an Optical Lattice*, Nature **455**, 204 (2008) (cit. on pp. 43, 59, 76).

[293] S. Giorgini, L. P. Pitaevskii, and S. Stringari, *Theory of Ultracold Atomic Fermi Gases*, Rev. Mod. Phys. **80**, 1215 (2008) (cit. on pp. 43, 44).

[294] M. W. Zwierlein and W. Ketterle, *Comment on "Pairing and Phase Separation in a Polarized Fermi Gas" by G. B. Partridge, W. Li, R. I. Kamar, Y. Liao, R. G. Hulet, Science 311, 503 (2006)*, Sept. 2006, arXiv:cond-mat/0603489 (cit. on p. 44).

[295] A. Imambekov, C. J. Bolech, M. Lukin, and E. Demler, *Breakdown of the Local Density Approximation in Interacting Systems of Cold Fermions in Strongly Anisotropic Traps*, Phys. Rev. A **74**, 053626 (2006) (cit. on p. 44).

[296] R. W. Helmes, T. A. Costi, and A. Rosch, *Mott Transition of Fermionic Atoms in a Three-Dimensional Optical Trap*, Phys. Rev. Lett. **100**, 056403 (2008) (cit. on p. 44).

[297] R. W. Helmes, T. A. Costi, and A. Rosch, *Kondo Proximity Effect: How Does a Metal Penetrate into a Mott Insulator?* Phys. Rev. Lett. **101**, 066802 (2008) (cit. on p. 44).

[298] K. Huang, *Statistical Mechanics*, Second Edition (John Wiley & Sons, Inc, 1963) (cit. on p. 45).

[299] D. S. Petrov and G. V. Shlyapnikov, *Interatomic Collisions in a Tightly Confined Bose Gas*, Phys. Rev. A **64**, 012706 (2001) (cit. on p. 45).

[300] J. Levinsen and M. M. Parish, *Strongly Interacting Two-Dimensional Fermi Gases*, in *Annual Review of Cold Atoms and Molecules*, Vol. 3 (World Scientific, May 2015), 1 (cit. on p. 46).

[301] J. R. Engelbrecht, M. Randeria, and L. Zhang, *Landau f Function for the Dilute Fermi Gas in Two Dimensions*, Phys. Rev. B **45**, 10135 (1992) (cit. on pp. 46, 47).

[302] Q. Zhou and T.-L. Ho, *Universal Thermometry for Quantum Simulation*, Phys. Rev. Lett. **106**, 225301 (2011) (cit. on pp. 51, 79).

[303] M. Klawunn, A. Recati, L. P. Pitaevskii, and S. Stringari, *Local Atom-Number Fluctuations in Quantum Gases at Finite Temperature*, Phys. Rev. A **84**, 033612 (2011) (cit. on p. 52).

[304] D. Goodstein, *States of Matter* (Dover, 2002) (cit. on p. 52).

[305] C. Sanner, E. J. Su, A. Keshet, R. Gommers, Y.-i. Shin, W. Huang, and W. Ketterle, *Suppression of Density Fluctuations in a Quantum Degenerate Fermi Gas*, Phys. Rev. Lett. **105**, 040402 (2010) (cit. on p. 52).

[306] T. Müller, B. Zimmermann, J. Meineke, J.-P. Brantut, T. Esslinger, and H. Moritz, *Local Observation of Antibunching in a Trapped Fermi Gas*, Phys. Rev. Lett. **105**, 040401 (2010) (cit. on p. 52).

[307] M. Eckstein, M. Kollar, M. Potthoff, and D. Vollhardt, *Phase Separation in the Particle-Hole Asymmetric Hubbard Model*, Phys. Rev. B **75**, 125103 (2007) (cit. on p. 58).

[308] U. Schneider, L. Hackermüller, S. Will, T. Best, I. Bloch, T. A. Costi, R. W. Helmes, D. Rasch, and A. Rosch, *Metallic and Insulating Phases of Repulsively Interacting Fermions in a 3D Optical Lattice*, Science **322**, 1520 (2008) (cit. on p. 59).

[309] J. P. F. LeBlanc et al. (Simons Collaboration on the Many-Electron Problem), *Solutions of the Two-Dimensional Hubbard Model: Benchmarks and Results from a Wide Range of Numerical Algorithms*, Phys. Rev. X **5**, 041041 (2015) (cit. on p. 61).

[310] A. Georges, G. Kotliar, W. Krauth, and M. J. Rozenberg, *Dynamical Mean-Field Theory of Strongly Correlated Fermion Systems and the Limit of Infinite Dimensions*, Rev. Mod. Phys. **68**, 13 (1996) (cit. on p. 61).

[311] G. Kotliar, S. Y. Savrasov, K. Haule, V. S. Oudovenko, O. Parcollet, and C. A. Marianetti, *Electronic Structure Calculations with Dynamical Mean-Field Theory*, Rev. Mod. Phys. **78**, 865 (2006) (cit. on p. 61).

[312] M. J. Rozenberg, *Integer-Filling Metal-Insulator Transitions in the Degenerate Hubbard Model*, Phys. Rev. B **55**, R4855 (1997) (cit. on p. 62).

[313] J. E. Han, M. Jarrell, and D. L. Cox, *Multiorbital Hubbard Model in Infinite Dimensions: Quantum Monte Carlo Calculation*, Phys. Rev. B **58**, R4199 (1998) (cit. on p. 62).

[314] G. Kotliar, S. Murthy, and M. J. Rozenberg, *Compressibility Divergence and the Finite Temperature Mott Transition*, Phys. Rev. Lett. **89**, 046401 (2002) (cit. on p. 62).

[315] E. V. Gorelik and N. Blümer, *Mott Transitions in Ternary Flavor Mixtures of Ultracold Fermions on Optical Lattices*, Phys. Rev. A **80**, 051602 (2009) (cit. on p. 62).

[316] N. Blümer and E. V. Gorelik, *Mott Transitions in the Half-Filled* SU($2M$) *Symmetric Hubbard Model*, Phys. Rev. B **87**, 085115 (2013) (cit. on p. 62).

[317] S. R. White, *Density Matrix Formulation for Quantum Renormalization Groups*, Phys. Rev. Lett. **69**, 2863 (1992) (cit. on p. 62).

[318] U. Schollwöck, *The Density-Matrix Renormalization Group*, Rev. Mod. Phys. **77**, 259 (2005) (cit. on p. 62).

[319] Y. Yamashita, N. Shibata, and K. Ueda, SU(4) *Spin-Orbit Critical State in One Dimension*, Phys. Rev. B **58**, 9114 (1998) (cit. on p. 62).

[320] S. R. Manmana, K. R. A. Hazzard, G. Chen, A. E. Feiguin, and A. M. Rey, SU(N) *Magnetism in Chains of Ultracold Alkaline-Earth-Metal Atoms: Mott Transitions and Quantum Correlations*, Phys. Rev. A **84**, 043601 (2011) (cit. on p. 62).

[321] K. R. A. Hazzard, V. Gurarie, M. Hermele, and A. M. Rey, *High-Temperature Properties of Fermionic Alkaline-Earth-Metal Atoms in Optical Lattices*, Phys. Rev. A **85**, 041604 (2012) (cit. on p. 62).

[322] J. Oitmaa, C. Hamer, and W. Zheng, *Series Expansion Methods for Strongly Interacting Lattice Models* (Cambridge University Press, 2006) (cit. on pp. 62, 100).

[323] D. F. B. ten Haaf and J. M. J. van Leeuwen, *High-Temperature Series Expansions for the Hubbard Model*, Phys. Rev. B **46**, 6313 (1992) (cit. on p. 62).

[324] J. A. Henderson, J. Oitmaa, and M. C. B. Ashley, *High-Temperature Expansion for the Single-Band Hubbard Model*, Phys. Rev. B **46**, 6328 (1992) (cit. on pp. 62, 100).

[325] R. Hingorani, J. Oitmaa, and R. R. P. Singh, *Onset of Charge Incompressibility and Mott Gaps in the Honeycomb-Lattice* SU(4) *Hubbard Model: Lessons for Twisted Bilayer Graphene Systems*, Phys. Rev. B **105**, L241410 (2022) (cit. on p. 62).

[326] R. R. P. Singh and J. Oitmaa, *Finite-Temperature Strong-Coupling Expansions for the* SU(N) *Hubbard Model*, Phys. Rev. A **105**, 033317 (2022) (cit. on p. 62).

[327] R. R. P. Singh and J. Oitmaa, *Divergence of Magnetic Susceptibility in the* SU(N) *Nagaoka-Thouless Ferromagnet*, Phys. Rev. B **106**, 014424 (2022) (cit. on p. 62).

[328] M. Rigol, T. Bryant, and R. R. P. Singh, *Numerical Linked-Cluster Approach to Quantum Lattice Models*, Phys. Rev. Lett. **97**, 187202 (2006) (cit. on p. 62).

[329] B. Tang, E. Khatami, and M. Rigol, *A Short Introduction to Numerical Linked-Cluster Expansions*, Computer Physics Communications **184**, 557 (2013) (cit. on p. 62).

[330] R. Blankenbecler, D. J. Scalapino, and R. L. Sugar, *Monte Carlo Calculations of Coupled Boson-Fermion Systems. I*, Phys. Rev. D **24**, 2278 (1981) (cit. on p. 64).

[331] S. Sorella, S. Baroni, R. Car, and M. Parrinello, *A Novel Technique for the Simulation of Interacting Fermion Systems*, Europhysics Letters (EPL) **8**, 663 (1989) (cit. on p. 64).

[332] S. R. White, D. J. Scalapino, R. L. Sugar, E. Y. Loh, J. E. Gubernatis, and R. T. Scalettar, *Numerical Study of the Two-Dimensional Hubbard Model*, Phys. Rev. B **40**, 506 (1989) (cit. on p. 64).

[333] T. Paiva, R. Scalettar, M. Randeria, and N. Trivedi, *Fermions in 2D Optical Lattices: Temperature and Entropy Scales for Observing Antiferromagnetism and Superfluidity*, Phys. Rev. Lett. **104**, 066406 (2010) (cit. on p. 64).

[334] Z. Bai, W. Chen, R. Scalettar, and I. Yamazaki, *Numerical Methods for Quantum Monte Carlo Simulations of the Hubbard Model*, in *Multi-Scale Phenomena in Complex Fluids*, Vol. 12 (2009), 1 (cit. on p. 64).

[335] G. G. Batrouni and P. de Forcrand, *Fermion Sign Problem: Decoupling Transformation and Simulation Algorithm*, Phys. Rev. B **48**, 589 (1993) (cit. on p. 64).

[336] V. I. Iglovikov, E. Khatami, and R. T. Scalettar, *Geometry Dependence of the Sign Problem in Quantum Monte Carlo Simulations*, Phys. Rev. B **92**, 045110 (2015) (cit. on p. 64).

[337] W. K. Hastings, *Monte Carlo Sampling Methods Using Markov Chains and Their Applications*, Biometrika **57**, 97 (1970) (cit. on p. 64).

[338] F. F. Assaad, SU(N)*-Spin Invariant Auxiliary Field Quantum Monte Carlo Algorithm for Hubbard Models*, June 1998, arXiv:cond-mat/9806307 (cit. on p. 65).

[339] E. Ibarra-García-Padilla and S. Dasgupta, private communications, Apr. 2023 (cit. on pp. 65, 66).

[340] E. Ibarra-García-Padilla, *Quantum Simulation of the Hubbard Model: Higher Symmetry Fermions and New Architectures*, PhD Thesis, Rice University (2022).

[341] I. Pomeranchuk, *On the Theory of* ^{3}He, Zh. Eksp.Teor. Fiz **20** (1950) (cit. on p. 68).

[342] Y. Anufriev, *Use of the Pomeranchuk Effect to Obtain Infralow Temperatures*, JETP Letters **1**, 155 (1965) (cit. on p. 68).

[343] D. M. Lee, *The Extraordinary Phases of Liquid* ^{3}He, Rev. Mod. Phys. **69**, 645 (1997) (cit. on p. 68).

[344] D. D. Osheroff, *Superfluidity in* ^{3}He*: Discovery and Understanding*, Nobel Lecture, 1996 (cit. on p. 68).

[345] R. C. Richardson, *The Pomeranchuk Effect*, Rev. Mod. Phys. **69**, 683 (1997) (cit. on p. 68).

[346] L. Bonnes, K. R. A. Hazzard, S. R. Manmana, A. M. Rey, and S. Wessel, *Adiabatic Loading of One-Dimensional* SU(N) *Alkaline-Earth-Atom Fermions in Optical Lattices*, Phys. Rev. Lett., 5 (2012) (cit. on p. 68).

[347] T. Esslinger, *Fermi-Hubbard Physics with Atoms in an Optical Lattice*, Annual Review of Condensed Matter Physics **1**, 129 (2010) (cit. on p. 76).

[348] D. Garwood, J. Mongkolkiattichai, L. Liu, J. Yang, and P. Schauss, *Site-Resolved Observables in the Doped Spin-Imbalanced Triangular Hubbard Model*, Phys. Rev. A **106**, 013310 (2022) (cit. on p. 78).

[349] E. Ibarra-García-Padilla, S. Dasgupta, R. Scalettar, and K. Hazzard, private communications, Dec. 2022 (cit. on p. 78).

[350] M. Dolfi, A. Kantian, B. Bauer, and M. Troyer, *Minimizing Nonadiabaticities in Optical-Lattice Loading*, Phys. Rev. A **91**, 033407 (2015) (cit. on p. 84).

[351] M. Miranda, R. Inoue, Y. Okuyama, A. Nakamoto, and M. Kozuma, *Site-Resolved Imaging of Ytterbium Atoms in a Two-Dimensional Optical Lattice*, Phys. Rev. A **91**, 063414 (2015) (cit. on p. 91).

[352] R. Yamamoto, J. Kobayashi, K. Kato, T. Kuno, Y. Sakura, and Y. Takahashi, *Site-Resolved Imaging of Single Atoms with a Faraday Quantum Gas Microscope*, Phys. Rev. A **96**, 033610 (2017) (cit. on p. 91).

[353] M. Miranda, R. Inoue, N. Tambo, and M. Kozuma, *Site-Resolved Imaging of a Bosonic Mott Insulator Using Ytterbium Atoms*, Phys. Rev. A **96**, 043626 (2017) (cit. on p. 91).

[354] G. Gauthier, I. Lenton, N. M. Parry, M. Baker, M. J. Davis, H. Rubinsztein-Dunlop, and T. W. Neely, *Direct Imaging of a Digital-Micromirror Device for Configurable Microscopic Optical Potentials*, Optica **3**, 1136 (2016) (cit. on p. 91).

[355] P. M. Preiss, *Atomic Bose-Hubbard Systems with Single-Particle Control*, PhD Thesis, Harvard University (2016).

[356] P. T. Brown, D. Mitra, E. Guardado-Sanchez, R. Nourafkan, A. Reymbaut, C.-D. Hébert, S. Bergeron, A.-M. S. Tremblay, J. Kokalj, D. A. Huse, P. Schauß, and W. S. Bakr, *Bad Metallic Transport in a Cold Atom Fermi-Hubbard System*, Science **363**, 379 (2019) (cit. on p. 91).

[357] W. Yi, A. J. Daley, G. Pupillo, and P. Zoller, *State-Dependent, Addressable Subwavelength Lattices with Cold Atoms*, New Journal of Physics **10**, 073015 (2008) (cit. on p. 91).

[358] A. Cooper, J. P. Covey, I. S. Madjarov, S. G. Porsev, M. S. Safronova, and M. Endres, *Alkaline-Earth Atoms in Optical Tweezers*, Phys. Rev. X **8**, 041055 (2018) (cit. on p. 91).

[359] M. A. Norcia, A. W. Young, and A. M. Kaufman, *Microscopic Control and Detection of Ultracold Strontium in Optical-Tweezer Arrays*, Phys. Rev. X **8**, 041054 (2018) (cit. on p. 91).

[360] S. Saskin, J. T. Wilson, B. Grinkemeyer, and J. D. Thompson, *Narrow-Line Cooling and Imaging of Ytterbium Atoms in an Optical Tweezer Array*, Phys. Rev. Lett. **122**, 143002 (2019) (cit. on p. 91).

[361] S.-K. Yip, B.-L. Huang, and J.-S. Kao, *Theory of* SU(N) *Fermi Liquids*, Phys. Rev. A **89**, 043610 (2014) (cit. on p. 97).

Acknowledgements

Ich möchte Immanuel Bloch dafür danken, mir die Chance gegeben zu haben, in einer derart inspirierenden und motivierenden Gruppe mein Dissertationsprojekt voranzutreiben. Seine physikalische Intuition sowie seine positive Haltung haben mich stets motiviert.

Ein besonderer Dank gilt Simon Fölling für seine durchgehende Betreuung und Unterstützung in den vergangenen Jahren. Seine ständige Bereitschaft, sich Zeit zu nehmen, um meine Fragen zu beantworten, und die Fähigkeit, anregende Diskussionen sowohl zu technischen und labor-spezifischen Themen, als auch zu weitreichenden Fragen der Physik und darüber hinaus zu führen, sind von unschätzbarem Wert gewesen.

Ich möchte mich ebenfalls bei meinem IMPRS-Co-Supervisor Jan von Delft für die inspirierenden Diskussionen bedanken.

Ich möchte mich bei den Doktoranden, den ehemaligen Kollegen Nelson Darkwah Oppong, Luis Riegger, Moritz Höfer und Oscar Bettermann bedanken, die mich auf meinem Weg begleitet haben, durch Höhen und Tiefen gleichermaßen. Ihnen und Simon verdanke ich das Erlernen vieler technischer Fähigkeiten, einschließlich Atomphysik, Optik, Elektronik, Programmierung, CAD-Konstruktion, sowie alles andere, das man wissen muss, um das Labor am Laufen zu halten. Ich möchte auch Francesco Scazza und Christian Hofrichter danken, die zu den frühen Phasen des Experiments beigetragen haben und die, obwohl ich nicht direkt mit ihnen zusammengearbeitet habe, meine Arbeit tiefgreifend beeinflusst haben. Ein Dankeschön an die Studenten, die ihre Bachelor- oder Masterarbeit oder ein Praktikum in unserem Labor absolviert haben: Benjamin Schiffer, Florian Fertig, Alexander Impertro, Caroline Tornow und Ben Röcken. Vielen Dank an allen anderen Mitgliedern der Bloch-Gruppe für den interessanten Austausch und die angenehme gemeinsame Zeit. Besonderer Dank gilt den Mitarbeitern der LMU und des MPQ, darunter: Ildiko Kecskesi, Kristina Schuldt, Sonya Gzyl, Bodo Hecker, Doreen Seidl, Anton Mayer, Jürgen Aust, Reinhard Grottenthaler.

I would like to thank Kaden Hazzard, Eduardo Ibarra García Padilla, Sohail Dasgupta and Richard Scalettar for the intense collaboration and insightful discussions both in person and remotely, across the ocean. I am thankful to them for sharing their numerical results, which have been incorporated and showcased within this thesis.

A big thanks to all the proofreaders: Simon, Nelson, Alex, Raphaël, Tim, Eduardo, Sohail.

I also acknowledge the fruitful collaboration with Michael Knap and Philip Zechmann and the inspiring discussions with Monika Aidelsburger, Matthias Punk, Trey Porto, Andrew Ludlow, Chun-Chia Chen, William Milner, and many others.

Infine, vorrei ringraziare la mia famiglia per il loro supporto incondizionato, senza il quale questo traguardo non sarebbe stato possibile.

近藤は今度でしょう。